Artificial Micro-Devices: Armoured Microbubbles and a Magnetically Driven Cilium

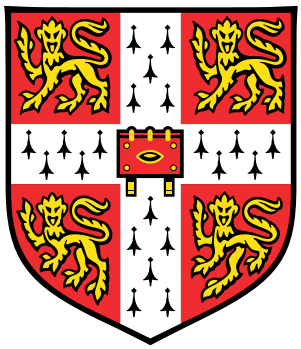

Tamsin Anne Spelman

Department of Applied Mathematics and Theoretical Physics

University of Cambridge

This dissertation is submitted for the degree of

Doctor of Philosophy

Queens' College

April 2017

Declaration

I hereby declare that except where specific reference is made to the work of others, the contents of this dissertation are original and have not been submitted in whole or in part for consideration for any other degree or qualification in this, or any other University. This dissertation is the result of my own work and includes nothing which is the outcome of work done in collaboration, except where specifically stated in the text and acknowledgements.

Tamsin Anne Spelman
April 2017

Acknowledgements

I would like to thank my supervisor Dr Eric Lauga, for his ideas, advice and continual support over the last three and a half years. Discussions with members of the biophysics group at Cambridge University have been invaluable, and I am very grateful that they have made my PhD so rewarding.

The part of my PhD on Armoured Microbubbles was collaborative work undertaken with experimentalists, specifically the group of Dr Philippe Marmottant based at the University Grenoble Alpes, Grenoble, France. All experimental work on the Armoured Microbubbles was performed by the group of Dr Philippe Marmottant, and more specifically mostly by the postdoctoral researcher Dr Nicolas Bertin. All theoretical and numerical work discussed is my own. If this is anywhere not the case, it will be specifically stated. I would like to thank Dr Nicolas Bertin and Dr Philippe Marmottant for a very rewarding collaboration, and their welcoming reception when I visited their labs.

This work was funded by an EPSRC grant provided through, DAMTP, University of Cambridge.

Abstract

Micro-devices are developed for uses in targeted drug delivery and microscale manipulation. Here we numerically and analytically study two promising devices in early stages of development. Firstly, we study Armoured Microbubbles (AMBs) which can self-propel as artificial microswimmers or facilitate microfluidic mixing in a channel when held stationary on a wall. Secondly, we study an artificial cilium, which due to its unique design, when placed in an array, easily produces a metachronal wave for fluid transportation.

The Armoured Microbubble was designed by our experimental collaborators (group of Philippe Marmottant, University Grenoble Alpes) and consists of a partial hollow sphere, inside which a bubble is caught. Under ultrasound the bubble oscillates, generating a streaming flow in the surrounding fluid and producing a net force. Motivated by the AMB but considering initially a general setup, using matched asymptotic expansions we calculate the streaming flow around a spherical body undergoing arbitrary, but known, small-amplitude surface shape oscillations.

We then specialise back to the AMB and consider its excitation under ultrasound, using a potential flow model with mixed boundary conditions, to identify the resonant frequencies and mode shapes, including the dependence of the resonance on the AMB shape parameters. Returning to our general streaming model, we applied the mixed boundary conditions directly to this model, calculating the streaming around the AMB, in good agreement with experiments. Using hydrodynamic images and linear superposition, this model was extended to incorporate one wall, and AMB compounds.

We then study the streaming flows generated by arrays of AMBs in confined channels, by modelling each AMB as its leading order behaviour (with corrections where required) and superposing the individual flow fields of all the AMBs. We identified the importance of two confining walls on the streaming flow around the array, and compared these flows to experiments in five cases. Motivated by this setup, we theoretically considered the extension of a two fluid interface passing through an AMB array to quickly identify good AMB arrays for mixing.

We then studied the second artificial micro-device: an artificial cilium. Tsumori et. al. produced a cilium of PDMS containing aligned ferromagnetic filings, which beat under a rotating magnetic field. We modelled a similar cilium but assumed paramagnetic filings, using a force model balancing elastic, magnetic and hydrodynamic forces identifying the cilium beat pattern. This agreed with our equilibrium model and asymptotic analysis. We then successfully identified that the cilium applies the most force to the surrounding fluid at an intermediate value of the two dimensionless numbers quantifying the dynamics.

Contents

List of Figures

Part I

Introduction

The behaviour of engineered microscopic actuators and microswimmers, whose size is of the order of $1\,\mu$m-$1000\,\mu$m, is the focus of this thesis. The long-term goal of microdevice development is medical equipment, in the form of micro-diagnostic appliances and also tools used for targetted drug delivery, [2, 3] as well as for biodetoxification [4]. In the short-term, the aim is to develop efficient designs for microfluidic mixing [5], fluid transportation [6], particle transportation [7] and self-propulsion [8]. Initially these will be used in lab-on-chip micro-devices. These offer many advantages over laboratory testing in the form of automation, low cost, less risk of contamination, reduced reagent consumption, fast response times and control of flow over small length scales [3, 9, 10]. However, developing devices at this micro-scale provides a number of challenges including power supply, control mechanism, life span and stability.

Power supply is an interesting conundrum for a micro-device. Even small batteries are millimetres in size [11], which is still too large, and biological chemical conversion to kinetic energy is too complex to reproduce artificially. Therefore, different methods are required. One option is to use the surrounding environment. Janus particles consist of two parts which react differently with the environment, and self-propel by generating an asymmetric distribution of charge or solute which propels the particle by electrophoresis [12, 13] or diffusiophoresis [14]. If the environment is active matter, and thus contains many moving microorganisms, this random motion can be harnessed and asymmetric gears will rotate [15].

An effective alternative option is to use an external forcing. Two examples are an ultrasound field and a magnetic field, which both need to be used slightly differently and on suitable objects to provide continuous power. More specifically, an ultrasound field can drive oscillations of microbubbles [16–18] and thin beams [8, 19, 20], which act as a focusing agent for the ultrasound so that the ultrasound wave, with a wavelength on the order of 1mm, can control behaviour on the micrometer scale. A magnetic field can be used to actuate artificial cilia [1, 21–23], which are hair like appendages, for which the cilium needs to be made of a magnetic material and the magnetic field itself needs to be either oscillating [24] or rotating [6, 23]. However, there are also undesirable side effects of using an external forcing such as temperature rises and bubble formation, which need to be carefully monitored and controlled. In this thesis an ultrasound field and a magnetic field are used to power the two devices.

It is not just the power supply of these machines which is different on the microscale. Their behaviour and the difficulties our designs have to overcome are significantly different to those on the macroscale, where fish swim with a repetitive motion, and mixing is achieved through stirring. At the microscale the Reynolds number is low so viscous effects dominate over inertial effects. The Scallop Theorem [25] says time irreversible body motion is necessary for propulsion, so the fish would go nowhere, and indeed unstirring the liquid (time reversing)

would return it to its unmixed state.

Nature has had millions of years to evolve optimal methods to overcome these microscale difficulties so can act as good blueprints when designing artificial products. A natural appendage that has motivated the development of a similar artificial product, are natural flagella and cilia. The green alga *Chlamydomonas* [26] has two slender flexible rod appendages whose length is of the same order of magnitude as its body length, called flagella, which beat to propel the microorganisms. *Rabbit Tracheal Epithelium* [27] has thousands of tiny cilia, small hair-like appendages, on its surface, which beat in a pattern to generate net flow.

Where the artificial design is based off a natural mechanism and there are significant physical similarities, modelling mechanisms for both are related so the biological models are helpful when studying the man-made systems. Also whereas micro-devices have only been being built for a few decades, study of the biological system dates back a lot further, sixty years or more, and thus forms the foundation of work on these systems. This is the case for our flagella and cilia, and additionally the modelling mechanisms for a flagellum and cilium are similar but with different boundary conditions. The earliest analytic models of biological flagella by G. I. Taylor [28] considered the swimming speed of an infinite waving sheet and how adjacent sheets interact. More modern methods assume cilium slenderness and a 2D stroke shape to model the beat pattern and force applied by a single finite length flagellum [29] and cilium [30]. But sometimes very simple theoretical models are sufficient, with a three Stokeslet (point force) model giving the flow field around *Chlamydomonas* [31]. At the other extreme using large computational models, boundary element methods has shown the flow field around long thin waving microrganisms [32], and arrays of cilia in more complicated geometries [33].

When densely packed cilia beat, there is a phase delay between adjacent cilia, which causes a metachronal wave to form. A standard modelling approach then consists of considering the dynamics of the enclosing envelope of the cilia. For microorganisms covered with these cilia (e.g the multicellular alga *Volvox* or the protozoon *Opalina*) that are approximately spherical, this reduces the problem to that of a spherical body inducing a surface wave of deformation [34, 35]. The first of such analytic models was proposed by Lighthill [36] and later corrected by Blake [34], who calculated the net flow generated by small-amplitude axisymmetric oscillations of a spherical surface in a Stokes flow. This model is now refereed to as the "squirmer" model. More recent studies have extended this model to include non-axisymmetric motion [37], the presence of nearby boundaries [38, 39] and large-amplitude oscillations [40].

While most microsystems are low Reynolds number, inertial effects are significant when an ultrasound forcing is applied. The kilohertz driving frequency of ultrasound increases the local Reynolds number, making inertia important locally, and thus allowing time-reversible oscillatory motion to generate net flow. This motion is the classical phenomenon of steady

(or acoustic) streaming, whereby a time-periodic forcing is non-linearly rectified by inertia to induce a non-zero net flow [41]. Theoretical studies of steady streaming flows have focused on shape oscillations in simple geometries, including a translating sphere [42], a translating bubble [43, 44], a bubble both translating and pulsating [44], and more recently a bubble both pulsating and oscillating with one higher-order Legendre mode [45]. For free microbubbles, the external acoustic energy is focused into the first few surface modes of oscillation hence these classical studies are sufficient to model streaming. However, as setups become more complicated, for example in the case of solid capsules partially enclosing three-dimensional bubbles [46–48], it is important to be able to model the complex shape dynamics and accurately compute the resulting streaming flows and forces.

In this thesis two micro-devices are studied in detail: an armoured microbubble (AMB) and an artificial cilium. We will thus now briefly discuss the uses and development of microbubbles and artificial cilia separately.

Early experiments on microbubbles were performed by Elder in 1958 looking at the streaming flow generated by oscillating microbubbles [49]. Since then they have been used to transport particles either in the streaming flow when the microbubble is held stationary [7, 16] or where the microbubble carries the particle [3, 46]. They can be fixed on the edge of channels in small indents and interactions between multiple oscillating bubbles may be used to increase mixing flows [18, 50, 51]. In the last couple of years microbubbles have been used for micropropulsion by containing them within small solid capsules [46–48]. The experimental armoured microbubble we study in this thesis consists of a hollow partial sphere inside which a microbubble is captured (see Fig.1a), which is different from other similar devices in that it is far smaller, of $20\,\mu$m diameter rather than with a length of 150 or $250\,\mu$m [47] or $750\,\mu\text{m} \times (2-4)\,\text{mm}$ in size [46].

One of the earliest artificial cilia was a curled filament actuated with electrostatics, which had a symmetric stroke but non-negligible local inertia, so the different speeds of the effective and recovery stroke generate a net force [5]. Since then, driving mechanisms have moved away from electrostatics as the voltage necessary can be problematic in biological settings and if the surrounding fluid is conductive, it interferes with the operation of the device. More recently a number of magnetic artificial cilia have been designed experimentally for pumping and mixing, actuated by a rotating magnetic field [52] (with such systems having been studied solely analytically and numerically too [53]), or actuated by more complex or asymmetric motions of the magnetic field [54, 55]. A particularly promising artificial cilium consists of superparamagnetic particles, which are guided to trenches allowing self-assembly, and are then actuated under a rotating magnetic field [22]. However, generating a metachronal wave for an array of cilia, as found in nature, is difficult without having a different driver for each

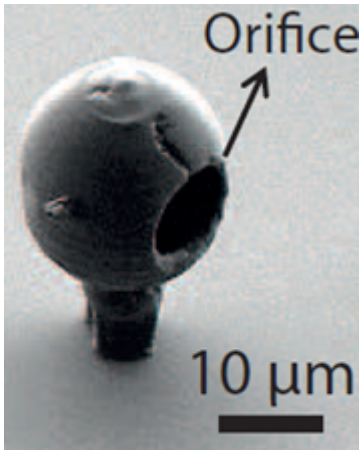

(a) The armoured microbubble (by Nicolas Bertin)

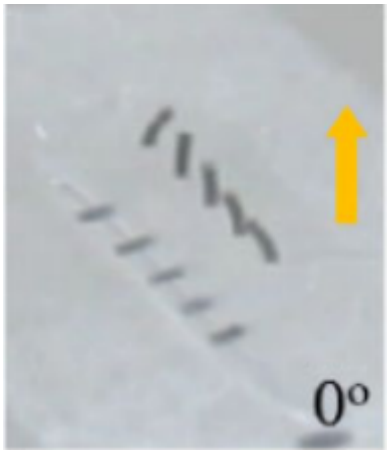

(b) The artificial cilium reproduced from: Metachronal wave of artificial cilia array actuated by applied magnetic field, F. Tsumori, R. Marume, A. Saijou, K. Kudo, T. Osado and H. Miura, Jpn. J Appl. Phys., 2016, 55:06GP19. [6]. Copyright 2016 The Japan Society of Applied Physics.

Figure 1: Experimental designs motivating this thesis.

cilium. The artificial cilium motivating the study in this thesis overcomes this difficulty. It is a PDMS cilium with aligned magnetic filings, and by changing the angle of the filings in adjacent cilia, a metachronal wave will appear when a rotating magnetic field is applied [1, 6].

In this thesis, part II focuses on our first micro-device, the Armoured Microbubble (AMB). We will first consider the streaming flow generated by arbitrary but known small amplitude oscillations of a spherical body in Chapter 1. We will then study the resonances and streaming flow generated by a single armoured microbubble, and multipropulsor compounds in Chapter 2. Next, we consider arrays of AMBs and the shape of the large collective flows they can generate in Chapter 3 and their mixing ability in Chapter 4. Then we move to our second micro-device in part III and study the beat pattern of a paramagnetic cilium in Chapter 5. We finish with a conclusion and discuss the direction of future studies in part IV.

Part II

Armoured Microbubble

Chapter 1

Acoustic Streaming around a Spherical Body

This chapter, with some edits, was published in: "Arbitrary axisymmetric steady streaming: flow, force and propulsion", Tamsin A. Spelman and Eric Lauga, Journal of Engineering Mathematics, 1-35, 2016 (reproduced with permission of Springer).

In this first chapter, we develop the mathematical framework to quantify the steady streaming of a spherical body with arbitrary axisymmetric time-periodic boundary conditions (see Fig.1.1 for setup). We compute the flow asymptotically under two assumption: (1) the amplitude of surface oscillations are small relative to the size of the body (ratio of amplitude $\varepsilon \ll 1$); and (2) the acoustic frequency is large such that the viscous penetration length scale is small compared to the body size (ratio penetration length to body size $\delta \ll 1$). Mathematically, we solve the problem as a regular perturbation expansion in ε, with each term expended in turn in powers of δ. We thus focus implicitly on the limit $\varepsilon \ll \delta \ll 1$, which is the relevant one for micron-size bubbles forced by ultrasound (frequencies in the hundreds of kHz range) and millimetre-sized organisms. Similarly to classical work, the flow is shown to have a boundary layer structure and the problem is solved by asymptotic matching. Our results, which assume that the body is fixed in space, are presented in the case of no-slip boundary conditions and extended to include the motion of vibrating free surfaces, also recover classical work as particular cases. We then illustrate the flow structure given by our solution and propose one application of our results, discussing the adaptation for a force-free body, on small-scale force-generation and synthetic locomotion.

This chapter is organised as follows. In §1.1 we set up the problem of the fluid flow generated by arbitrary surface motion of a no-slip spherical body. In §1.2, we derive the first-order solution. The second-order Eulerian steady streaming is derived in §1.3, which is extended to give the Lagrangian steady streaming in §1.4. The special case of a squirming microor-

ganism is then discussed in §1.5. This no-slip general model can be extended to incorporate other surface motion such as a no tangential stress boundary as shown in §1.6. The special case of a bubble is then considered in §1.7. In §1.8 our general solution is validated against classical results for spheres and bubbles. In §1.9, we illustrate examples of streaming flows. In all previous sections, the body was assumed to be held stationary at the origin. In §1.10 the time-averaged force induced by the flow on the fixed body is calculated, along with the translational velocity of the spherical body if it was instead free to move.

1.1 Axisymmetric steady streaming: setup

In this first section we present the general setup for our calculation. The body is taken to be spherical with an imposed axisymmetric, radial and tangential time-periodic deformation of its surface. In the following sections we will use asymptotic matching to first characterise the flow in the case of no-slip between the fluid and the surface, and then we generalise to allow the formulation to be adapted to other boundary conditions, in particular no tangential stress for a clean bubble.

1.1.1 Statement of the Mathematical Problem

The sphere has mean radius a and is contained within an unbounded Newtonian fluid of constant kinematic viscosity ν and uniform density ρ (Fig.1.1). Working in a spherical coordinate system centred on the sphere, with radial distance r and polar angle θ, the axis $\theta = 0$ is the axis of rotational symmetry. The surface of the body is assumed to oscillate at angular frequency ω with small amplitude εa, where $\varepsilon \ll 1$ is formally specified below. We define $\mu \equiv \cos\theta$ and since the flow is axisymmetric, a stream function ψ can be introduced to give radial u_r and angular u_θ velocities as

$$u_r = -\frac{1}{r^2}\frac{\partial \psi}{\partial \mu}, \tag{1.1}$$

$$u_\theta = \frac{-1}{r(1-\mu^2)^{\frac{1}{2}}}\frac{\partial \psi}{\partial r}. \tag{1.2}$$

The governing equation is then given by the vorticity equation [56]

$$\frac{\partial (D^2\psi)}{\partial t} + \frac{1}{r^2}\left[\frac{\partial(\psi, D^2\psi)}{\partial(r,\mu)} + 2D^2\psi L\psi\right] = \nu D^2\left(D^2\psi\right), \tag{1.3}$$

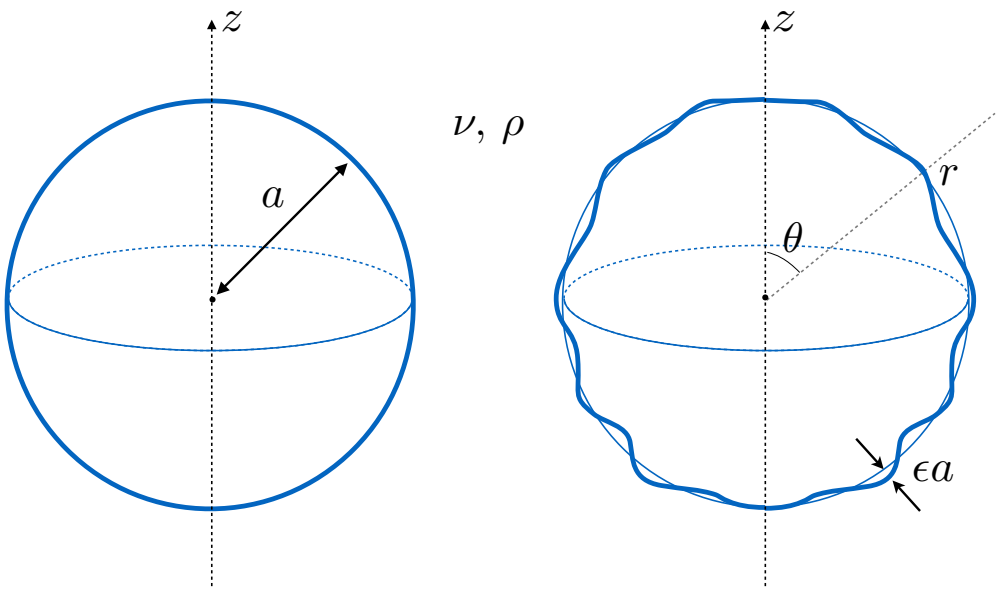

Figure 1.1: A sphere of rest radius a (left) undergoes arbitrary axisymmetric vibrations of amplitude εa, with $\varepsilon \ll 1$ (right). Spherical coordinates are used with radial distance r and polar angle θ. The surrounding fluid is Newtonian with kinematic viscosity ν and density ρ.

where we have defined the operators

$$D^2 \equiv \frac{\partial^2}{\partial r^2} + \frac{(1-\mu^2)}{r^2}\frac{\partial^2}{\partial \mu^2}, \tag{1.4}$$

$$L \equiv \frac{\mu}{(1-\mu^2)}\frac{\partial}{\partial r} + \frac{1}{r}\frac{\partial}{\partial \mu}, \tag{1.5}$$

and

$$\frac{\partial(\psi, D^2\psi)}{\partial(r,\mu)} = \frac{\partial \psi}{\partial r}\frac{\partial (D^2\psi)}{\partial \mu} - \frac{\partial (D^2\psi)}{\partial r}\frac{\partial \psi}{\partial \mu}. \tag{1.6}$$

In order to non-dimensionalise the problem, we take the relevant time scale to be ω^{-1} and the relevant length scale to be a, so that the sphere now has a rest radius of 1. The stream function thus has dimensions $a^3\omega$ and the vorticity equation becomes

$$\frac{\partial (D^2\psi)}{\partial t} + \frac{1}{r^2}\left[\frac{\partial(\psi, D^2\psi)}{\partial(r,\mu)} + 2D^2\psi L\psi\right] = \left(\frac{\nu}{\omega a^2}\right) D^2\left(D^2\psi\right). \tag{1.7}$$

Eq.1.7 introduces a non-dimensional quantity: the ratio of the viscous penetration length scale, $\sim (\nu/\omega)^{1/2}$, to the radius of the body, a. Specifically, we define a dimensionless number δ as

$$\delta \equiv \frac{(2\nu/\omega)^{\frac{1}{2}}}{a}, \tag{1.8}$$

thus reducing the governing equation to

$$\frac{\partial(D^2\psi)}{\partial t} + \frac{1}{r^2}\left[\frac{\partial(\psi, D^2\psi)}{\partial(r,\mu)} + 2D^2\psi L\psi\right] = \left(\frac{\delta^2}{2}\right) D^2\left(D^2\psi\right). \tag{1.9}$$

The second dimensionless quantity in this problem is the ratio ε between the amplitude of oscillation and the body radius. To use notations similar to those in classical steady streaming calculations, we use U to denote the maximum velocity at the surface of the oscillating body, such that ε can be defined as

$$\varepsilon = \frac{U}{a\omega}. \tag{1.10}$$

We will look to solve this problem as a regular expansion in ε for small values of δ, and then take a regular expansion in δ. We will thus assume the asymptotic limit $\varepsilon \ll \delta \ll 1$. Importantly, this assumption is sufficient for our asymptotic solution to be valid. As explained below, we will solve this problem using asymptotic matching between an inner solution (boundary layer of size δ) and an outer solution. For the inner asymptotic solution, ψ^i, we will have an expansion of the form

$$\psi^i = \varepsilon(\psi_1^{i(0)} + \delta\psi_1^{i(1)} + ... + \delta^n\psi_1^{i(n)}) + \varepsilon^2(\psi_2^{i(0)} + \delta\psi_2^{i(1)}) + O(\varepsilon\delta^{n+1}, \varepsilon^2\delta^2, \varepsilon^3), \tag{1.11}$$

with $n \geq 2$. The solution in Eq.1.11 is a valid approximation provided the errors are smaller than the order of our solution $O(\varepsilon^2\delta)$. So we require $\delta \ll 1$, $\varepsilon \ll \delta$ and $\delta^n \ll \varepsilon$. But n can be chosen to be as large as required, thus reducing down to the condition $\varepsilon \ll \delta \ll 1$ only. We note that we can easily obtain the $O(\varepsilon)$ solution up to order n in δ since ε is introduced into our equations only through assuming ψ is a power series in ε so mathematically higher orders of ε cannot effect lower orders in ε.

Physically, a small value of ε indicates small-amplitude motion while a small value of δ means that the viscous penetration length is small compared to the rest size of the body. For which practical situations will these limits be relevant? To fix ideas, let us take a value for the relative amplitude of $\varepsilon \sim 10^{-2}$. A ciliated microorganism in water ($\nu = 10^{-6}\,\mathrm{m^2/s}$) would have intrinsic frequencies of about 50 Hz, so $\omega \approx 300\,\mathrm{rad/s}$, leading to a penetration length of $(2\nu/\omega)^{\frac{1}{2}} \approx 80\,\mu\mathrm{m}$. In order to satisfy the limit $\varepsilon \ll \delta \ll 1$, the organism size would need to be just below 1 mm, which is achieved for the largest ciliated organisms such as *Spirostomum*

which can grow up to 4 mm in length [57]. For a micro bubble actuated by ultrasound the frequency is about $\omega \sim 10^6$ rad/s, so the penetration length is $(2\nu/\omega)^{\frac{1}{2}} \approx 1\,\mu$m and thus the bubble would have to be about $10\,\mu$m in diameter.

1.1.2 Boundary conditions

We apply, in this first part of the chapter, the no-slip boundary condition. Thus, the fluid velocity has to match the velocity of the material points on the surface of the body, which is arbitrary and decomposed along an infinite sum of surface modes. Using a Lagrangian formulation, the motion of the boundary can be described by its radial position, $\tilde{R}$, and angular position measured from the axis of axisymmetry, $\tilde{\Theta}$, which are functions of time t and the rest angular position θ (through μ) as

$$\tilde{R} = 1 - \varepsilon \sum_{n=0}^{\infty} V_n P_n(\mu) e^{i(t+\frac{\pi}{2})} + O(\varepsilon^2), \tag{1.12}$$

$$\tilde{\Theta} = \theta + \varepsilon \sum_{n=1}^{\infty} W_n \left(\frac{\int_\mu^1 P_n(x)dx}{(1-\mu^2)^{\frac{1}{2}}} \right) e^{i(t+\frac{\pi}{2})} + O(\varepsilon^2), \tag{1.13}$$

where V_n and W_n are arbitrary complex constants determined by the surface motion of the spherical body and $P_n(x)$ is the Legendre Polynomial of degree n. Throughout this chapter, complex notation will be used and it will always be implied that only the real part is taken; when an explicit real part appears we will denote it $\Re$.

The μ-dependence of $\tilde{R}$ and $\tilde{\Theta}$ was chosen in order to match the form of the first-order solution, as seen below. More specifically, assuming $\tilde{R}$ and hence u_r has Legendre polynomial μdependence, Eq. 1.1 suggests the μ-dependence ψ should have and hence, from Eq. 1.2, the dependence u_θ (and so $\tilde{\Theta}$) should have. Therefore, this form of $\tilde{\Theta}$ is suggested by the relationship between u_r, u_θ and ψ. We also note $\left(\int_\mu^1 P_n(x)dx\right)/(1-\mu^2)^{\frac{1}{2}} = P_n^1(\mu)/(n(n+1))$ so our formulation for $\tilde{\Theta}$ gives its μ-dependence as Associated Legendre Polynomials of order one. Additionally, $\tilde{\Theta}$ has the same μ-dependence at leading order as u_θ on the boundary, and this form of u_θ is consistent with the classical work of Riley [42] and Longuet-Higgins [44].

Since V_n and W_n can each take any value within the complex plane, a wide range of boundary motions can be studied. At leading order, $\tilde{R}(\theta)$ is equivalent to the radial position of the surface at an angle θ from the axis of symmetry. As such, V_n will be determined by the shape of the surface oscillation, and since the Legendre polynomials form a basis, any arbitrary axisymmetric small amplitude radial oscillation can be written in this form. At leading order, $\tilde{\Theta}(\theta)$ captures the tangential motion at an angle θ from the axis of symmetry, and thus

W_n will be determined by the appropriate in-surface motion. We note that the use of Legendre polynomials as a basis for μ was expected due to the axisymmetry of the problem and such a basis has appeared in other work based in similar regimes [34].

At $O(\varepsilon^2)$ only terms in $\tilde{R}$ and $\tilde{\Theta}$, which time-average to a non-zero value, would contribute to the streaming. However, such terms would indicate that the body was slowly growing or shrinking over time, and would also stretch or contract tangentially, violating the small-amplitude assumption on long time scales. We therefore do not allow for steady Lagrangian terms at order $O(\varepsilon^2)$. The boundary condition can thus be written in a Lagrangian form as

$$u_r = \frac{\partial \tilde{R}}{\partial t} = \varepsilon \sum_{n=0}^{\infty} V_n P_n(\mu) e^{it} + O(\varepsilon^3), \tag{1.14}$$

$$\begin{aligned} u_\theta &= \tilde{R} \frac{\partial \tilde{\Theta}}{\partial t} \\ &= \Re\left[-\varepsilon \sum_{n=1}^{\infty} W_n \left(\frac{\int_\mu^1 P_n(x)dx}{(1-\mu^2)^{\frac{1}{2}}} \right) e^{it} \right] \Re\left[1 - \varepsilon i \sum_{n=0}^{\infty} V_n P_n(\mu) e^{it} \right] + O(\varepsilon^3), \end{aligned} \tag{1.15}$$

and both of which have to be evaluated at $(r,\theta) = (\tilde{R}(\mu,t), \tilde{\Theta}(\mu,t))$.

Finally, we require that the flow decays to zero from the body and thus $u_{r,\theta} \to 0$ as $r \to \infty$.

We note here that we are assuming the spherical body is fixed in space and as such is not force free. A force-free condition may be incorporated with the same setup in a suitable reference frame, whereby it limits the possible surface shape oscillations through restrictions on the choice of constants V_n and W_n. This is discussed in detail in § 1.10.

1.1.3 Rearranging the surface boundary conditions

The current Lagrangian form of the surface conditions of the body Eqs.1.14–1.15 needs to be transformed into Eulerian boundary conditions of the fluid motion. This is achieved by Taylor expanding them about the average oscillation position $(1,\theta)$ so

$$\underline{u}_L = \underline{u}_E + (\delta \underline{x} \cdot \nabla)\underline{u}_E + O(\delta \underline{x}^2), \tag{1.16}$$

where $\underline{u}_L$ gives the Lagrangian surface velocity, $\underline{u}_E$ the Eulerian velocity and $\delta \underline{x}$ the change in position. The relationship between these variables is illustrated in Fig. 1.2. In spherical

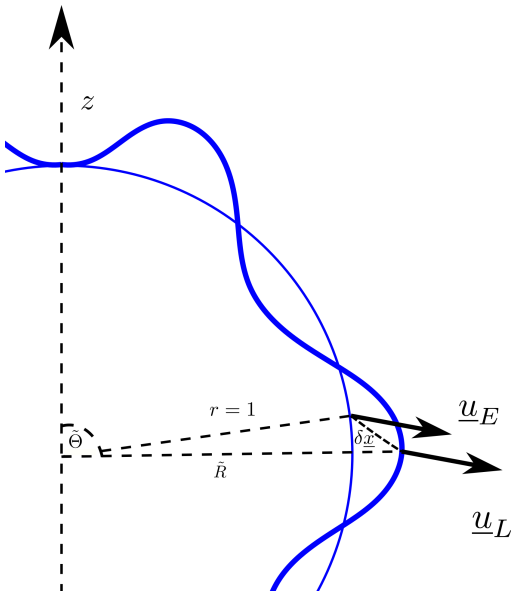

Figure 1.2: Comparing the Lagrangian and Eulerian boundary conditions

coordinates this gives

$$u_r|_{r=R} = u_r|_{r=1} + \Re\left[(\tilde{R}-1)\right]\Re\left[\left.\frac{\partial u_r}{\partial r}\right|_{r=1}\right] + \Re[(\tilde{\Theta}-\theta)]\Re\left[\left.\left(\frac{\partial u_r}{\partial \theta} - u_\theta\right)\right|_{r=1}\right] + O(\varepsilon^3), \quad (1.17)$$

and

$$u_\theta|_{r=R} = u_\theta|_{r=1} + \Re\left[(\tilde{R}-1)\right]\Re\left[\left.\frac{\partial u_\theta}{\partial r}\right|_{r=1}\right] + \Re[(\tilde{\Theta}-\theta)]\Re\left[\left.\left(\frac{\partial u_\theta}{\partial \theta} + u_r\right)\right|_{r=1}\right] + O(\varepsilon^3). \quad (1.18)$$

Looking for the dimensionless velocities and stream function as power series in ε as

$$u_r = \varepsilon u_r^{(1)} + \varepsilon^2 u_r^{(2)} + O(\varepsilon^3), \quad (1.19)$$

$$u_\theta = \varepsilon u_\theta^{(1)} + \varepsilon^2 u_\theta^{(2)} + O(\varepsilon^3), \quad (1.20)$$

$$\psi = \varepsilon \psi_1 + \varepsilon^2 \psi_2 + O(\varepsilon^2), \quad (1.21)$$

then at leading order Eq.1.17 and Eq.1.18 give

$$u_r^{(1)} = \sum_{n=0}^{\infty} V_n P_n(\mu) e^{it}, \quad (1.22)$$

$$u_\theta^{(1)} = -\sum_{n=1}^{\infty} W_n \left(\frac{\int_\mu^1 P_n(x)dx}{(1-\mu^2)^{\frac{1}{2}}} \right) e^{it}, \tag{1.23}$$

at $r = 1$ and for all values of θ. Similarly from Eq.1.17 and Eq.1.18 the $O(\varepsilon^2)$ boundary condition can be calculated. However, due to the non-linear terms arising from the Taylor expansions, the first-order flow needs to be first evaluated in order to determine the $O(\varepsilon^2)$ boundary conditions explicitly. This will be discussed in §1.3.1.

1.2 First-order Asymptotic solution

1.2.1 General solution

Based on the oscillatory nature of the boundary condition at first order, Eq.1.22–1.23, we look for a solution $\psi_1 \propto e^{it}$. At leading order the governing equation reduces to

$$\left(\frac{\partial}{\partial t} - \frac{\delta^2}{2} D^2 \right) (D^2 \psi_1) = 0. \tag{1.24}$$

This is easily solved using separation of variables $D^2\psi_1 = f(r)g(\mu)e^{it}$ to find $D^2\psi_1$ as

$$D^2\psi_1 = e^{it} \left[\sum_{n=1}^{\infty} \left(\int_\mu^1 P_n(x)dx \right) \left(B_n \sqrt{r} K_{n+\frac{1}{2}}(\alpha r) \right) \right], \tag{1.25}$$

where $K_a(x)$ is the modified Bessel function of the second kind of order a.

We then use separation of variables with the definition of the operator Eq.1.4 to solve Eq.1.25 for ψ_1 noting that Eq.1.25 gives the particular solution of ψ_1. Hence we finally obtain

$$\begin{aligned} \psi_1 = e^{it} \Bigg[& \left(A_0 \frac{\sqrt{r}}{\alpha^2} I_{\frac{1}{2}}(\alpha r) + B_0 \frac{\sqrt{r}}{\alpha^2} K_{\frac{1}{2}}(\alpha r) + C_0 r + D_0 \right) \left(\int_\mu^1 P_0(x)dx + e_0 \right) + \\ & \sum_{n=1}^{\infty} \left(A_n \frac{\sqrt{r}}{\alpha^2} I_{n+\frac{1}{2}}(\alpha r) + B_n \frac{\sqrt{r}}{\alpha^2} K_{n+\frac{1}{2}}(\alpha r) + C_n r^{n+1} + D_n r^{-n} \right) \left(\int_\mu^1 P_n(x)dx \right) \Bigg], \end{aligned} \tag{1.26}$$

where $\alpha = (1+i)\delta^{-1}$, $I_a(x)$ is the modified Bessel function of the first kind of order a, and A_n, B_n, C_n, D_n are constants to be determined using the boundary conditions.

1.2.2 Enforcing the boundary conditions

Since $I_n(\alpha r)$ increases to infinity exponentially as $r \to \infty$, we first see that the boundary conditions at infinity impose that $A_n = 0$ for all n and similarly $C_n = 0$ for $n > 0$.

Secondly, singularities in the velocity profile should be removed. This is not a problem for u_r but it is for u_θ. Indeed, we have the scaling $u_\theta \sim (1-\mu^2)^{-\frac{1}{2}} \left(\int_\mu^1 P_n(x)dx \right)$, which has formal singularities at $\mu = \pm 1$. Using the identity

$$\int_\mu^1 P_n(x)dx = \frac{(1-\mu^2)P_n'(\mu)}{n(n+1)} \quad \text{for } n \neq 0, \tag{1.27}$$

we see that the singularities are removable for $n > 0$ but not for $n = 0$. Since e_0 provides only one degree of freedom, it can be used to remove at most one singularity. Therefore, in order to prevent any singularity in u_θ at $\mu = \pm 1$, it is required that $C_0 = B_0 = 0$. The only term remaining in ψ_1 containing e_0 is proportional to $e_0 D_0$, which is an arbitrary constant and hence e_0 can be set to 0.

With these results, ψ_1 is reduced to

$$\psi_1 = e^{it} \left[\left(D_0 \int_\mu^1 P_0(x)dx \right) + \sum_{n=1}^{\infty} \left(B_n \frac{\sqrt{r}}{\alpha^2} K_{n+\frac{1}{2}}(\alpha r) + D_n r^{-n} \right) \left(\int_\mu^1 P_n(x)dx \right) \right]. \tag{1.28}$$

Applying the two first-order boundary conditions, Eq.1.22 and Eq.1.23, finally allows the determination of the remaining constants B_n, D_n and D_0. This solution for the constants B_n, D_n and D_0 is a closed-form solution, which has dependence on δ. However, a δ expansion is required for our second order calculation, to calculate the streaming flow. Thus, we expand this closed-form solution in powers of δ, and this form of the constants B_n, D_n and D_0 is expressed below in Eq.1.29-1.31. For the standard second order calculation, only the two leading orders terms in δ for each constant (B_n and D_n) are required, but three are included here as the third is necessary to calculate the in-phase streaming around a bubble discussed in §1.14, due to the significant cancellation of terms in that case so that the leading order streaming flow occurs at a higher order of δ. The Bessel function factor evaluated at α has been left formally in the definition of the constants, as Bessel function terms will appear in the second-order streaming equations and the expansion of that term has to be performed careful (as discussed in §1.3.3), which is simpler when this Bessel function term is left in B_n. We obtain the solution for B_n, D_n and D_0 as

$$B_n = \frac{-1}{K_{n+\frac{1}{2}}(\alpha)} \left(\frac{1}{\delta}(1+i) + n + \delta \frac{(i-1)n^2}{4} \right) (W_n + nV_n)$$

$$+O\left(\frac{\delta^2}{K_{n+\frac{1}{2}}(\alpha)}\right) \quad \text{for } n \geq 1, \tag{1.29}$$

$$D_n = V_n + \delta\frac{(1-i)}{2}(W_n + nV_n) - \delta^2\frac{in}{2}(W_n + nV_n) \tag{1.30}$$
$$+O(\delta^3) \quad \text{for } n \geq 1,$$

$$D_0 = V_0. \tag{1.31}$$

For simplicity of notation in what follows, we define $W_0 = 0$ so that Eq.1.29 and similarly Eq.1.30 remain valid for $n = 0$.

1.3 Second-order asymptotic solution

At $O(\varepsilon^2)$, a net fluid motion will arise and from this we will obtain the streaming flow. The first-order solution determines the explicit second order boundary conditions (§1.3.1) and provides a non-zero forcing term (§1.3.2) at $O(\varepsilon^2)$. Unfortunately, the governing equation with this forcing is too complex to solve explicitly analytically. We will thus employ asymptotic matching in order to solve for the flow inside the boundary layer of size $\eta = 1 + \delta r$ (§1.3.3) and for the flow in the far field (§1.3.4) where exponential decay of this forcing leads to a Stokes flow. Upon matching these two solutions (§1.3.5) the outer solution will give the Eulerian streaming flow around the body.

1.3.1 Second-order boundary conditions

Eqs.1.28–1.31 give the full solution for ψ_1. Using Eq.1.17 and Eq.1.18 we can now time-average the boundary conditions at order ε^2. Note that the product of two terms of the form fe^{it} and ge^{it} time average to $f\overline{g}/2$ or $\overline{f}g/2$ where the real part is assumed and overbars denote complex conjugates. Simplifying the μ dependence of the result to a sum over the appropriate basis functions, i.e. $(1-\mu^2)^{-\frac{1}{2}}\int_\mu^1 P_n(x)dx$ for u_θ and $P_n(\mu)$ for u_r and using the classical identities

$$xP_n'(x) = P_{n+1}'(x) - (n+1)P_n(x), \tag{1.32}$$

$$P_{n+1}'(x) = P_{n-1}'(x) + (2n+1)P_n(x), \tag{1.33}$$

we explicitly obtain time-averaged boundary conditions

$$\langle u_r^{(2)}\rangle\Big|_{r=1} = \sum_{k=1}^{\infty}\left\{\frac{i}{2}\left[2V_0\bar{V}_k - \sum_{n=0}^{\infty}\sum_{m=1}^{\infty} g_{knm}\bar{V}_n\left(W_m - 2V_m\right)\right.\right.$$
$$\left.\left. + \sum_{n=1}^{\infty}\sum_{m=1}^{\infty} f_{knm}\left(\bar{V}_n n(n+1) - \bar{W}_n\right)W_m \frac{1}{n(n+1)m(m+1)}\right]\right\} P_k(\mu), \quad (1.34)$$

and

$$\langle u_\theta^{(2)}\rangle\Big|_{r=1} = \sum_{k=1}^{\infty}\left\{\sum_{n=0}^{\infty}\sum_{m=1}^{\infty} a_{knm}\frac{i}{2}\left[2V_n\bar{W}_m - \frac{1}{\delta}\bar{V}_n\left(W_m + mV_m\right)(1+i) + \bar{V}_n V_m m\right.\right.$$
$$\left.\left. - \bar{V}_n W_m(m+1) - W_n\bar{W}_m + \sum_{j=1}^{\infty}\frac{C_{nj}}{j(j+1)}\bar{W}_m W_j\right]\right\}\left(\frac{\int_\mu^1 P_k(x)dx}{(1-\mu^2)^{\frac{1}{2}}}\right), \quad (1.35)$$

where we have used triangular brackets to indicate time-averaging.

In these equations, the series of coefficients C_{nj}, a_{knm}, f_{knm} and g_{knm} are defined by

$$C_{nj} = \begin{cases} 0 & \text{if } (j<n) \text{ or } (n \text{ and } j \text{ have different parity}), \\ n & \text{if } j = n, \\ (2n+1) & \text{otherwise}, \end{cases} \quad (1.36)$$

and

$$P_n(\mu)\left(\int_\mu^1 P_m(x)dx\right) = \sum_{k=1}^{\infty} a_{knm}\left(\int_\mu^1 P_k(x)dx\right), \quad (1.37)$$

$$P_n^1(\mu)P_m^1(\mu) = \sum_{k=0}^{\infty} f_{knm}P_k(\mu), \quad (1.38)$$

$$P_n(\mu)P_m(\mu) = \sum_{k=0}^{\infty} g_{knm}P_k(\mu), \quad (1.39)$$

where $P_n^1(\mu)$ is the associated Legendre polynomial of degree n and order 1. Recall that associated Legendre polynomials of degree n and order m are defined by

$$P_n^m(x) = (1-x^2)^{\frac{m}{2}}\frac{d^m P_n(x)}{dx^m}, \quad (1.40)$$

and have the useful orthogonality property

$$\int_{-1}^{1} P_n^m(x) P_{n'}^{m'}(x) dx = \frac{2}{(2n+1)} \frac{(n+m)!}{(n-m)!} \delta_{nn'} \delta_{mm'}. \tag{1.41}$$

Using the orthogonality property together with Eq.1.27, the formulae for a_{knm} in Eq.1.37, f_{knm} in Eq.1.38 and g_{knm} in Eq.1.39 can be rearranged into a more useful form to calculate their numerical value

$$a_{knm} = \frac{k(k+1)}{m(m+1)} \frac{\int_{-1}^{1} P_n(x) P_m^1(x) P_k^1(x) dx}{\int_{-1}^{1} P_k^1(x) P_k^1(x) dx}, \tag{1.42}$$

$$= \frac{(2k+1)}{2m(m+1)} \int_{-1}^{1} P_n(x) P_m^1(x) P_k^1(x) dx, \tag{1.43}$$

$$f_{knm,} = \frac{(2k+1)}{2} \int_{-1}^{1} P_n^1(x) P_m^1(x) P_k(x) dx, \tag{1.44}$$

$$g_{knm} = \frac{(2k+1)}{2} \int_{-1}^{1} P_k(x) P_n(x) P_m(x) dx. \tag{1.45}$$

The constants a_{knm}, f_{knm} and g_{knm} are Gaunt Coefficients, which have been extensively studied due to their appearance in theoretical physics. Gaunt's formula [58] for the triple product integral and fast numerical algorithms [59] exist to evaluate such coefficients.

1.3.2 Nonlinear Forcing

The governing equation at order ε^2 is given by

$$\frac{\delta^2}{2} \left(D^4 \psi_2 \right) - \frac{\partial (D^2 \psi_2)}{\partial t} = \frac{1}{r^2} \left(\frac{\partial (\psi_1, D^2 \psi_1)}{\partial (r, \mu)} + 2L\psi_1 D\psi_1 \right). \tag{1.46}$$

Time averaging equation (1.46) leads to

$$\frac{\delta^2}{2} D^4 \langle \psi_2 \rangle = \frac{1}{r^2} \left\langle \frac{\partial (\psi_1, D^2 \psi_1)}{\partial (r, \mu)} + 2L\psi_1 D\psi_1 \right\rangle. \tag{1.47}$$

A general second order solution that is valid throughout the domain, cannot be found due to the complexity of the right-hand side of Eq.1.47. However, for small values of δ, solutions can be found separately within the viscous boundary layer and in the far field, and they can be asymptotically matched to provide a full outer solution. This is the method we will be using in this chapter. In either case, an indication of the form of the non-linear forcing is required.

The term $D^2\psi_1$ is given in Eq.1.25. We also have

$$L\psi_1 = e^{it}\left[\sum_{n=1}^{\infty}\left(\frac{B_n}{2\alpha^2\sqrt{r}}K_{n+\frac{1}{2}}(\alpha r)+B_n\frac{\sqrt{r}}{\alpha}K'_{n+\frac{1}{2}}(\alpha r)-D_n n r^{-(n+1)}\right)\left(\frac{\mu P'_n(\mu)}{n(n+1)}\right)\right.$$
$$\left.-\frac{D_0}{r}P_0(\mu)-\sum_{n=1}^{\infty}\left(\frac{B_n}{\sqrt{r}\alpha^2}K_{n+\frac{1}{2}}(\alpha r)+D_n r^{-(n+1)}\right)P_n(\mu)\right], \quad (1.48)$$

and

$$\left\langle\frac{\partial(\psi_1,D^2\psi_1)}{\partial(r,\mu)}\right\rangle = -\frac{1}{2}\sum_{n=0}^{\infty}\sum_{m=1}^{\infty}\left(\frac{\bar{B}_nB_m}{\alpha^2}\bar{K}_{n+\frac{1}{2}}(\alpha r)K_{m+\frac{1}{2}}(\alpha r)\right.$$
$$+2\frac{\bar{B}_nB_m r}{\alpha}\bar{K}_{n+\frac{1}{2}}(\alpha r)K'_{m+\frac{1}{2}}(\alpha r)-\bar{B}_nD_m m\bar{K}_{n+\frac{1}{2}}(\alpha r)r^{-(m+\frac{1}{2})}$$
$$\left.-\frac{\bar{D}_nB_m}{2}r^{-(n+\frac{1}{2})}K_{m+\frac{1}{2}}(\alpha r)-\bar{D}_nB_m\alpha r^{-(n-\frac{1}{2})}K'_{m+\frac{1}{2}}(\alpha r)\right)P_n(\mu)\left(\int_{\mu}^{1}P_m(x)dx\right). \quad (1.49)$$

Using the coefficient a_{knm} defined in Eq.1.37, Eq.1.49 can then be transformed to the appropriate (integral polynomial) basis. Similarly the quantity given by $2\times$ Eq.1.48 $\times$ Eq.1.25 can have its basis transformed using a_{knm} and C_{nj} defined in Eq.1.36. These two quantities can then be added, which gives the total non-linear forcing as

$$\left\langle 2L\psi_1D^2\psi_1+\frac{\partial(\psi_1,D^2\psi_1)}{\partial(r,\mu)}\right\rangle = \sum_{k=1}^{\infty}\left[\sum_{n=0}^{\infty}\sum_{m=1}^{\infty}a_{knm}\times\right.$$
$$\left(\bar{B}_nB_m\frac{1}{2\alpha^2}\bar{K}_{n+\frac{1}{2}}(\alpha r)K_{m+\frac{1}{2}}(\alpha r)-\frac{3}{4}\bar{D}_nB_m r^{-(n+\frac{1}{2})}K_{m+\frac{1}{2}}(\alpha r)\right.$$
$$-\bar{B}_nB_m\frac{r}{\alpha}\bar{K}_{n+\frac{1}{2}}(\alpha r)K'_{m+\frac{1}{2}}(\alpha r)+\frac{1}{2}\bar{B}_nD_m m\bar{K}_{n+\frac{1}{2}}(\alpha r)r^{-(m+\frac{1}{2})}$$
$$+\frac{1}{2}\bar{D}_nB_m\alpha r^{-(n-\frac{1}{2})}K'_{m+\frac{1}{2}}(\alpha r)$$
$$+\sum_{j=1}^{\infty}\left(\frac{C_{nj}}{j(j+1)}\right)\left(-B_m\bar{B}_j\frac{1}{2\alpha^2}K_{m+\frac{1}{2}}(\alpha r)\bar{K}_{j+\frac{1}{2}}(\alpha r)\right.$$
$$\left.\left.\left.+B_m\bar{B}_j\frac{r}{\bar{\alpha}}K_{m+\frac{1}{2}}(\alpha r)\bar{K}'_{j+\frac{1}{2}}(\alpha r)-B_m\bar{D}_jjK_{m+\frac{1}{2}}(\alpha r)r^{-(j+\frac{1}{2})}\right)\right)\right]\left(\int_{\mu}^{1}P_k(x)dx\right). \quad (1.50)$$

1.3.3 Solution inside the boundary layer

The rest boundary is located at $r = 1$ with a boundary layer of size δ. We thus define an inner variable η related to r by $r = 1 + \delta\eta$. The boundary layer is small, $\delta \ll 1$, and within the boundary layer the inner variable η varies from 0 to 1. We now write the second-order equation in terms of η and expand in ascending powers of δ.

First consider expanding the right-hand side of Eq.1.47, i.e. Eq.1.50 divided by r^2. When the first-order boundary conditions were applied above, we obtained in Eq.1.29-1.31 Taylor expansions of the coefficients D_k and B_k in terms of δ. The powers of r can also be Taylor expanded about $r = 1$ to also obtain a powers series in δ.

However, the Taylor expansions of the Bessel functions have to be done more carefully. A useful identity [60] for expanding the Bessel function is that, for non-negative integer n we have

$$K_{n+\frac{1}{2}}(z) = \sqrt{\frac{\pi}{2}}\frac{e^{-z}}{\sqrt{z}}\sum_{j=0}^{n}\frac{(j+n)!}{(n-j)!j!}(2z)^{-j}. \tag{1.51}$$

Next, notice that when the expansions for D_k and B_k are substituted into Eq.1.47, the Bessel functions always appear in ratios of the form

$$\frac{\hat{K}_{n+\frac{1}{2}}(\alpha r)}{K_{n+\frac{1}{2}}(\alpha)}, \tag{1.52}$$

where $\hat{K}$ represents a derivative or complex conjugate of the Bessel function. As such, taking $f(r)$ as the appropriate power series in r gives

$$\frac{\hat{K}_{j+\frac{1}{2}}(\alpha r)}{K_{j+\frac{1}{2}}(\alpha)} = e^{-\tilde{\alpha}(r-1)}f(r) = e^{-(1\pm i)\eta}f(1+\delta\eta), \tag{1.53}$$

where $\tilde{\alpha}$ can be α or its complex conjugate. The exponential part of the Bessel function can clearly not be Taylor expanded in powers of δ. Hence to obtain the correct expansion, the power series part of the Bessel function should be Taylor expanded in powers of δ and the negative exponential part should only have the appropriate η substitution carried out.

Upon completion of the substitution and expansion in δ, we obtain inside the boundary layer

$$\frac{1}{r^2}\left\langle 2L\psi_1 D^2\psi_1 + \frac{\partial(\psi_1, D^2\psi_1)}{\partial(r,\mu)}\right\rangle = \sum_{k=1}^{\infty}\sum_{n=0}^{\infty}\sum_{m=1}^{\infty} a_{knm}\times$$
$$\left\{\frac{3}{4}\frac{1}{\delta}\bar{V}_n(W_m + mV_m)(1+i)e^{-(1+i)\eta} + \frac{1}{\delta}(\bar{W}_n + n\bar{V}_n)(W_m + mV_m)(1-i)e^{-2\eta}\right.$$

$$-\frac{1}{2}\frac{1}{\delta}(\bar{W}_n+n\bar{V}_n)V_m(1-i)me^{-(1-i)\eta}+\frac{1}{2}\left[\frac{2}{\delta^2}\bar{V}_n i+\frac{1}{\delta}(-2V_n in\eta+\right.$$
$$\left.\bar{V}_n m(1+i)-(\bar{W}_n+n\bar{V}_n)(1-i)+\frac{1}{2}\bar{V}_n(1+i)-4V_n i\eta\right)\Bigg](W_m+mV_m)e^{-(1+i)\eta}$$
$$+\sum_{j=1}^{\infty}\left(\frac{C_{nj}}{j(j+1)}\right)\left[-\frac{1}{\delta}(W_m+mV_m)(\bar{W}_j+j\bar{V}_j)(1+i)e^{-2\eta}\right.$$
$$\left.+\frac{1}{\delta}(W_m+mV_m)\bar{V}_j j(1+i)e^{-(1+i)\eta}\right]+O(1)\Bigg\}\left(\int_{\mu}^{1}P_k(x)dx\right). \quad (1.54)$$

This expansion has been performed to the two leading orders in δ, order δ^{-2} and δ^{-1}. Two orders of δ will be required when the matching conditions are applied, to obtain the leading order streaming behaviour, similar to the work of Longuet-Higgins [44].

Inside the boundary layer, the D^4 operator on the left hand side of Eq.1.47 is asymptotically given by

$$D^4=\frac{1}{\delta^4}\frac{\partial^4}{\partial\eta^4}+O(\delta^{-2}), \quad (1.55)$$

and therefore Eq.1.47 finally simplifies to

$$\left\langle\frac{\partial^4\psi_2^i}{\partial\eta^4}\right\rangle=\sum_{k=1}^{\infty}\sum_{n=0}^{\infty}\sum_{m=1}^{\infty}a_{knm}\Bigg(\left\{\frac{3}{2}\delta\bar{V}_n(W_m+mV_m)(1+i)e^{-(1+i)\eta}+\right.$$
$$2\delta(\bar{W}_n+n\bar{V}_n)(W_m+mV_m)(1-i)e^{-2\eta}-\delta(\bar{W}_n+n\bar{V}_n)V_m m(1-i)e^{-(1-i)\eta}+$$
$$\left[\delta\left(-2\bar{V}_n in\eta+\bar{V}_n m(1+i)-(\bar{W}_n+n\bar{V}_n)(1-i)+\frac{1}{2}\bar{V}_n(1+i)-4\bar{V}_n i\eta\right)+2\bar{V}_n i\right]\times$$
$$(W_m+mV_m)e^{-(1+i)\eta}+\sum_{j=1}^{\infty}\left(\frac{C_{nj}}{j(j+1)}\right)\left[-2\delta(W_m+mV_m)(\bar{W}_j+j\bar{V}_j)(1+i)e^{-2\eta}\right.$$
$$\left.\left.+2\delta(W_m+mV_m)\bar{V}_j j(1+i)e^{-(1+i)\eta}\right]\right\}+O(1)\Bigg)\left(\int_{\mu}^{1}P_k(x)dx\right), \quad (1.56)$$

where ψ_2^i is the second order stream function inside the boundary layer.

Using the elementary indefinite integrals (where c is the constant of integration)

$$\int_y\int_{\tilde{y}}\int_{\tilde{\tilde{y}}}\int_{\tilde{\tilde{\tilde{y}}}}e^{ax}dx d\tilde{y}d\tilde{\tilde{y}}d\tilde{\tilde{\tilde{y}}}=\frac{e^{ay}}{a^4}+c, \quad (1.57)$$

$$\int_y\int_{\tilde{y}}\int_{\tilde{\tilde{y}}}\int_{\tilde{\tilde{\tilde{y}}}}xe^{ax}dx\,d\tilde{y}\,d\tilde{\tilde{y}}\,d\tilde{\tilde{\tilde{y}}}=\frac{ye^{ay}}{a^4}-\frac{4e^{ay}}{a^5}+c, \quad (1.58)$$

allows us to integrate Eq.1.56 explicitly. We take the resulting solution to its first two leading orders, of order 1 and δ (as will be required for calculating the leading order outer streaming

flow), giving the general inner solution of

$$\begin{aligned}\langle \psi_2^i \rangle = \sum_{k=1}^{\infty} \Bigg\{ \sum_{n=0}^{\infty}\sum_{m=1}^{\infty} a_{knm} \Bigg[& -\frac{3}{8}\delta \bar{V}_n (W_m + mV_m)(1+i)e^{-(1+i)\eta} \\ & + \frac{1}{8}\delta(\bar{W}_n + n\bar{V}_n)(W_m + mV_m)(1-i)e^{-2\eta} + \frac{1}{4}\delta(\bar{W}_n + n\bar{V}_n)V_m m(1-i)e^{-(1-i)\eta} \\ & - \Bigg\{ \delta \left[-\frac{1}{2}\bar{V}_n i(n+2)\left(\eta + 2(1-i)\right) + \frac{1}{4}\bar{V}_n m(1+i) - \frac{1}{4}(\bar{W}_n + n\bar{V}_n)(1-i) + \frac{1}{8}\bar{V}_n(1+i) \right] \\ & + \frac{1}{2}\bar{V}_n i \Bigg\} (W_m + mV_m)e^{-(1+i)\eta} + \sum_{j=1}^{\infty} \left(\frac{C_{nj}}{j(j+1)} \right) \Bigg(-\frac{1}{8}\delta(W_m + mV_m)(\bar{W}_j + j\bar{V}_j)(1+i)e^{-2\eta} \\ & - \frac{1}{2}\delta(W_m + mV_m)\bar{V}_j j(1+i)e^{-(1+i)\eta} \Bigg) + O(\delta^2) \Bigg] + (L_k + M_k\eta + N_k\eta^2 + Q_k\eta^3) \Bigg\} \times \\ & \left(\int_{\mu}^{1} P_k(x)dx \right), \end{aligned} \tag{1.59}$$

where L_k, M_k, N_k and Q_k are constants of integration to be determined. Of those, two will be determined by enforcing the two second-order boundary conditions Eq.1.34 and Eq.1.35, namely L_k and M_k. Since these boundary conditions must hold for all $-1 \leq \mu \leq 1$, the coefficient of each basis function (i.e. $P_n(\mu)$ or $\int_{\mu}^{1} P_n(x)dx$) must obey these boundary conditions term by term, giving a countably infinite number of equations with solution

$$\begin{aligned} L_k = \; & \Re \Bigg\{ \Bigg[\sum_{n=0}^{\infty}\sum_{m=1}^{\infty} a_{knm}\bar{V}_n(W_m + mV_m) + 2V_0\bar{V}_k - \\ & \sum_{n=0}^{\infty}\sum_{m=1}^{\infty} g_{knm}\bar{V}_n(W_m - 2V_m) + \sum_{n=1}^{\infty}\sum_{m=1}^{\infty} f_{knm} \times \\ & (\bar{V}_n n(n+1) - \bar{W}_n) W_m \frac{1}{mn(n+1)(m+1)} \Bigg] \frac{i}{2} \Bigg\} + O(\delta),\ k > 0, \end{aligned} \tag{1.60}$$

$$\begin{aligned} M_k = \; & \delta \Bigg(\sum_{n=0}^{\infty}\sum_{m=1}^{\infty} a_{knm} \Bigg\{ -\frac{1}{2}(\bar{W}_n + n\bar{V}_n)V_m im + \frac{1}{2}\bar{V}_n(W_m + mV_m)i(4 + 3n - m) \\ & + \frac{1}{4}(\bar{W}_n + n\bar{V}_n)(W_m + mV_m)(3-i) + \frac{1}{2}\bar{V}_n W_m(m+3)i - \frac{1}{2}\bar{V}_n V_m mi \\ & + \frac{1}{2}W_n\bar{W}_m i - \sum_{j=1}^{\infty} \left(\frac{C_{nj}}{j(j+1)} \right) \Bigg[\frac{1}{4}(W_m + mV_m)(\bar{W}_j + j\bar{V}_j)(1+i) \\ & + (W_m + mV_m)\bar{V}_j ij + \frac{1}{2}\bar{W}_m W_j i \Bigg] \Bigg\} \Bigg) + O(\delta^2), \quad k > 0. \end{aligned} \tag{1.61}$$

Both L_k and M_k are given to leading order in δ, and although their order in δ is different, both contribute their leading order behaviour to the leading order outer streaming flow. Asymptotic

matching will determine the values of the remaining coefficients.

1.3.4 Solution Outside the Boundary Layer

Looking at equation Eq.1.50, we see that all the terms in the non-linear forcing are multiples of modified Bessel functions of the second kind or their derivatives. As such, this forcing decays away exponentially fast as $r \to \infty$ and can be neglected outside the boundary layer. In the outer region we therefore have an unforced Stokes flow and the governing equation for the outer stream function, ψ_2^o, is

$$D^2 D^2 \langle \psi_2^o \rangle = 0, \tag{1.62}$$

with exponentially small errors.

Given the form of the inner solution Eq.1.59, and anticipating the asymptotic matching, we can look for the outer solution with a known μ dependence as

$$\langle \psi_2^o \rangle = \sum_{n=1}^{\infty} f_n(r) \left(\int_\mu^1 P_n(x) dx \right) + f_0(r) \left(\int_\mu^1 P_0(x) dx + e_0 \right). \tag{1.63}$$

The value of $\langle D^2 \psi_2^o \rangle$ can be found by differentiating Eq.1.63 as well as by solving Eq.1.62 for $\langle D^2 \psi_2^o \rangle$ using separation of variables. Equating these gives a second order differential equation for f with power-law solutions. The general outer solution is thus given by

$$\begin{aligned} \langle \psi_2^o \rangle = \left(R_0 + T_0 r + Y_0 r^2 + S_0 r^3 \right) \left(\int_\mu^1 P_0(x) dx + e_0 \right) \\ + \sum_{n=1}^{\infty} \left(R_n r^{n+3} + T_n r^{-n} + Y_n r^{n+1} + S_n r^{-(n-2)} \right) \left(\int_\mu^1 P_n(x) dx \right). \end{aligned} \tag{1.64}$$

Applying the boundary condition at infinity gives $R_n = Y_n = 0$ for $n \geq 1$ and $S_0 = Y_0 = 0$. Furthermore, in order to avoid a singularity in u_θ at $\mu = \pm 1$ it is required $T_0 = 0$, and as $\langle \psi_2^o \rangle$ is a stream function it can be set that $e_0 = 0$ without affecting u_r or u_θ. Hence we obtain the outer solution as

$$\langle \psi_2^o \rangle = R_0 \left(\int_\mu^1 P_0(x) dx \right) + \sum_{n=1}^{\infty} \left(T_n r^{-n} + S_n r^{-(n-2)} \right) \left(\int_\mu^1 P_n(x) dx \right). \tag{1.65}$$

1.3.5 Matching

The final part of determining the solution for the flow consists of carrying out the asymptotic matching between the inner Eq.1.59 and outer solutions Eq.1.65. We first need to evaluate the inner solution, Eq.1.59, in the limit $\eta \gg 1$ which, because of the negative exponentials, simplifies to

$$\left\langle \psi_2^i \right\rangle = \sum_{k=1}^{\infty} \left(L_k + M_k\eta + N_k\eta^2 + Q_k\eta^3\right) \left(\int_{\mu}^{1} P_k(x)dx\right). \tag{1.66}$$

The outer solution, Eq.1.65, then needs to be evaluated in the limit $r \to 1$. Writing the outer solution in terms of the inner variable η and Taylor expanding the expression about $\eta = 0$ then gives

$$\begin{aligned}\left\langle \psi_2^o \right\rangle = R_0 \left(\int_{\mu}^{1} P_0(x)dx\right) + \sum_{n=1}^{\infty} \Bigg[&(T_n + S_n) - \delta(nT_n + (n-2)S_n)\eta \\ &+ \delta^2 \left(\frac{n(n+1)}{2}T_n + \frac{(n-2)(n-1)}{2}S_n\right)\eta^2 \\ &- \delta^3 \left(\frac{n(n+1)(n+2)}{6}T_n + \frac{n(n-1)(n-2)}{6}S_n\right)\eta^3 + O(\eta^4)\Bigg] \left(\int_{\mu}^{1} P_n(x)dx\right).\end{aligned} \tag{1.67}$$

Here $\left\langle \psi_2^o \right\rangle$ has been given to its four leading orders in η. The first two orders are required for the matching conditions, to calculate the outer streaming flow. The third and fourth orders can be used to explicitly determine N_k and Q_k, which are used in §1.10.

Equating the two highest orders of η gives

$$L_k = T_k + S_k \quad (k \geq 1), \tag{1.68}$$

$$M_k = -\delta\left[kT_k + (k-2)S_k\right] \quad (k \geq 1), \tag{1.69}$$

$$R_0 = 0. \tag{1.70}$$

If we use $M_k^{(\delta)}$ to denote the $O(\delta)$ term of M_k, the outer constants are thus given by

$$T_k = \frac{(2-k)}{2}L_k^{(1)} - \frac{1}{2}\frac{1}{\delta}M_k^{(\delta)} + O(\delta) \quad (k \geq 1), \tag{1.71}$$

$$S_k = \frac{k}{2}L_k^{(1)} + \frac{1}{2}\frac{1}{\delta}M_k^{(\delta)} + O(\delta) \quad (k \geq 1). \tag{1.72}$$

Notice that T_k and S_k are now known so they can be used to determine N_k and Q_k by matching to third and fourth order; if one carries out this matching, one obtains that N_k and Q_k are $O(\delta^2)$ and $O(\delta^3)$ respectively.

1.4 Lagrangian streaming

The solution derived so far has focused on the Eulerian streaming, i.e. the time-averaged Eulerian velocity field at a fixed position in the laboratory frame of reference. In order to compare with future experimental results tracking the motion of passive tracers in the flow, it is necessary to calculate the Lagrangian streaming instead. The difference between the Eulerian and the Lagrangian streaming is the so-called Stokes drift, which arises because the Lagrangian particles are advected by the Eulerian velocities at all the positions the particles move through, and not just fixed positions in the laboratory frame, and thus velocity gradients need to be accounted for.

Longuet-Higgins [44, 61] showed that the stream function for the non-dimensional time averaged Stokes drift $\langle \varphi_S \rangle$ at $O(\varepsilon^2)$ is given by

$$\langle \varphi_S \rangle = \left\langle \frac{1}{r^2} \int \frac{\partial \psi_1}{\partial r} dt \frac{\partial \psi_1}{\partial \mu} \right\rangle. \tag{1.73}$$

Ignoring exponentially-decaying terms, the outer solution for the Stokes drift is thus

$$\langle \varphi_S \rangle = -\varepsilon^2 \frac{i}{2} \sum_{k=1}^{\infty} \left(\sum_{n=0}^{\infty} \sum_{m=1}^{\infty} a_{knm} \bar{V}_n V_m m r^{-(n+m+3)} \right) \left(\int_{\mu}^{1} P_k(x) dx \right) + O(\delta). \tag{1.74}$$

Adding this expression to the outer time-averaged Eulerian solution ψ_2^o from Eq.1.65 leads to the final expression for the outer leading order time averaged Lagrangian streaming as

$$\langle \psi_L \rangle = \sum_{k=1}^{\infty} \left(T_k r^{-k} + S_k r^{-(k-2)} - \sum_{n=0}^{\infty} \sum_{m=1}^{\infty} Y_{knm} r^{-(n+m+3)} \right) \left(\int_{\mu}^{1} P_k(x) dx \right), \tag{1.75}$$

where

$$Y_{knm} = \Re \left(\frac{1}{2} a_{knm} \bar{V}_n V_m i m \right), \tag{1.76}$$

and the coefficients S_k and T_k are given by

$$\begin{aligned} S_k = \Re \Bigg\{ \sum_{n=0}^{\infty} \sum_{m=1}^{\infty} \Bigg(a_{knm} \Bigg\{ & \frac{1}{4} \bar{V}_n (W_m + m V_m) i k \\ & - \frac{1}{4} (\bar{W}_n + n \bar{V}_n) V_m i m + \frac{1}{4} \bar{V}_n (W_m + m V_m)(4 + 3n - m) i \\ & + \frac{1}{8} (\bar{W}_n + n \bar{V}_n)(W_m + m V_m)(3 - i) + \frac{1}{4} \bar{V}_n W_m (m+3) i - \frac{1}{4} \bar{V}_n V_m m i \\ & + \frac{1}{4} W_n \bar{W}_m i - \sum_{j=1}^{\infty} \left(\frac{C_{nj}}{j(j+1)} \right) \Bigg[\frac{1}{8} (W_m + m V_m)(\bar{W}_j + j \bar{V}_j)(1 + i) \end{aligned}$$

$$+\frac{1}{2}(W_m+mV_m)\bar{V}_j ij+\frac{1}{4}\bar{W}_m W_j i\Bigg]\Bigg\}-\frac{1}{4}g_{knm}\bar{V}_n\left(W_m-2V_m\right)ik\Bigg)$$
$$+\sum_{n=1}^{\infty}\sum_{m=1}^{\infty}\left[\frac{1}{4}f_{knm}\left(\bar{V}_n n(n+1)-\bar{W}_n\right)W_m\frac{ik}{mn(n+1)(m+1)}\right]+\frac{1}{2}V_0\bar{V}_k ki\Bigg\}+O(\delta), \quad (1.77)$$

and

$$T_k=\Re\Bigg\{\sum_{n=0}^{\infty}\sum_{m=1}^{\infty}\Bigg(a_{knm}\Bigg\{\frac{1}{4}\bar{V}_n(W_m+mV_m)i(2-k)$$
$$+\frac{1}{4}(\bar{W}_n+n\bar{V}_n)V_m im-\frac{1}{4}\bar{V}_n(W_m+mV_m)(4+3n-m)i$$
$$-\frac{1}{8}(\bar{W}_n+n\bar{V}_n)(W_m+mV_m)(3-i)-\frac{1}{4}\bar{V}_n W_m(m+3)i+\frac{1}{4}\bar{V}_n V_m im$$
$$-\frac{1}{4}W_n\bar{W}_m i+\sum_{j=1}^{\infty}\left(\frac{C_{nj}}{j(j+1)}\right)\Bigg[\frac{1}{8}(W_m+mV_m)(\bar{W}_j+j\bar{V}_j)(1+i)$$
$$+\frac{1}{2}(W_m+mV_m)\bar{V}_j ij+\frac{1}{4}\bar{W}_m W_j i\Bigg]\Bigg\}-\frac{1}{4}g_{knm}\bar{V}_n\left(W_m-2V_m\right)(2-k)i\Bigg)$$
$$+\sum_{n=1}^{\infty}\sum_{m=1}^{\infty}\left[\frac{1}{4}f_{knm}\left(\bar{V}_n n(n+1)-\bar{W}_n\right)W_m\frac{i(2-k)}{mn(n+1)(m+1)}\right]+\frac{1}{2}V_0\bar{V}_k(2-k)i\Bigg\}$$
$$+O(\delta). \quad (1.78)$$

Since the inner solutions is only valid in a δ-sized region about the spherical body this gives the Lagrangian solution in the bulk of the fluid.

We note that in the far field, the flow will be dominated by the slowest spatially decaying term. In the stream function Eq.1.75 this is the $\langle\psi_L\rangle\sim S_1 r$ term. The velocities associated with this term decay as $\sim 1/r$ and are associated with a net force acting on the fluid (stokeslet). This will be further discussed §1.10 in the context of force generation and propulsion.

1.5 Special case: squirming

As discussed in the introduction, the squirmer model of low-Reynolds number swimming is a popular mathematical model to address the motion of nearly spherical ciliated cells (e.g. Opalina, Volvox) [34, 36]. The array of deforming cilia is modelled as a continuous envelope where the effective tangential component is deemed far more significant than the radial component of motion. As such, the position of the surface can be modelled as fixed at its average position, and imposing steady velocities along it. Models of this form have been used

to study nutrient uptake by microorganisms [62], interaction of microorganisms [63], optimal locomotion and were recently generalised [37, 40]. Some versions of the squirming model do also allow a radial velocity to be applied through the fixed boundary as a model for a porous surface with normal jets of fluid through it [64].

The squirming approximation significantly increases the ease of theoretical calculations. However, and as expected, it has its limitations. A prescribed forcing through the boundary cannot be used to accurately model a moving boundary. If there is a non-zero radial velocity at the fixed boundary, the streaming flow will become one order of magnitude larger since the boundary conditions are no longer cancelling the leading-order term. In the very specific case of solely radial motion where all the radial modes are exactly $\pi/4$ out of phase with each other the solution will be at the right order, but other important terms will still be missing from the streaming. This demonstrates that the physical movement of the boundary, and hence the physical displacement of the fluid in that region, is as important as the prescribed velocities it is imparting to the fluid around it.

For angular motion alone, however, the squirmer streaming is identical to the full solution, demonstrating such an approximation is valid. Furthermore, in that situation the Lagrangian and Eulerian streamings are the same since the Stokes drift depends only on the radial motion of the surface. We thus focus on the standard tangential squirmer model where there is no radial motion at leading-order and $V_n = 0$ for all n. In that setup, the generated streaming is of the same form as has already been derived, Eq.1.75, but the constants are much simpler with $Y_{knm} = 0$ and

$$S_k = \Re\left\{\sum_{n=0}^{\infty}\sum_{m=1}^{\infty} a_{knm}\left[\frac{3}{8}\bar{W}_n W_m(1-i) - \sum_{j=1}^{\infty}\left(\frac{C_{nj}}{j(j+1)}\right)\frac{1}{8}\bar{W}_j W_m(1-i)\right] + \sum_{n=1}^{\infty}\sum_{m=1}^{\infty}\left[-\frac{1}{4}f_{knm}\bar{W}_n W_m\frac{ik}{mn(n+1)(m+1)}\right]\right\} + O(\delta), \quad (1.79)$$

and

$$T_k = \Re\left\{\sum_{n=0}^{\infty}\sum_{m=1}^{\infty} a_{knm}\left[-\frac{3}{8}\bar{W}_n W_m(1-i) + \sum_{j=1}^{\infty}\left(\frac{C_{nj}}{j(j+1)}\right)\frac{1}{8}W_m\bar{W}_j(1-i)\right] + \sum_{n=1}^{\infty}\sum_{m=1}^{\infty}\left[-\frac{1}{4}f_{knm}\bar{W}_n W_m\frac{(2-k)i}{mn(n+1)(m+1)}\right]\right\} + O(\delta). \quad (1.80)$$

1.6 Allowing slip on the boundary

In previous sections we assumed that the fluid satisfied the no-slip boundary condition and thus exactly matched the motion of our deforming body. Slip can however be systematically incorporated into this model through a small change of boundary conditions. The general form of the solution remains the same but the constants of integration gain an extra contribution. This will then extend the model to include other spherical bodies, in particular bubbles.

In the case of no-slip, the motion of the boundary was described by its radial position, $\tilde{R}$, and angular position, $\tilde{\Theta}$. Our new, more general, R and Θ can be interpreted as describing the motion of the fluid on the boundary of the spherical body. If we allow streaming at second order on the boundary, we can then write

$$R = 1 - \varepsilon \sum_{n=0}^{\infty} V_n P_n(\mu) e^{i(t+\frac{\pi}{2})} + \varepsilon^2 \sum_{n=0}^{\infty} G_n P_n(\mu) g(t) + O(\varepsilon^3), \tag{1.81}$$

$$\Theta = \theta + \varepsilon \sum_{n=1}^{\infty} W_n \left(\frac{\int_{\mu}^{1} P_n(x)dx}{(1-\mu^2)^{\frac{1}{2}}} \right) e^{i(t+\frac{\pi}{2})} + \varepsilon^2 \sum_{n=0}^{\infty} F_n \left(\frac{\int_{\mu}^{1} P_n(x)dx}{(1-\mu^2)^{\frac{1}{2}}} \right) f(t) + O(\varepsilon^3), \tag{1.82}$$

which now has the extra second-order contributions where F_n and G_n are known constants determined by the motion of the spherical body and $f(t)$ and $g(t)$ are unknown functions of time. This new R and Θ are a more general form of $\tilde{R}$ and $\tilde{\Theta}$ since imposing no-slip boundary conditions sets $G_n = F_n = 0$, which reduces R and Θ to $\tilde{R}$ and $\tilde{\Theta}$. The equations relating R and Θ to the velocities u_r and u_θ are the same as those relating $\tilde{R}$ and $\tilde{\Theta}$ to these velocities (Eq.1.14 -1.18), hence the form of the final solution is similar to before with the addition, at second order, of terms containing F_n and G_n .

The new definition of R is equivalent to the previous one since the fluid and spherical body cannot encompass the same space. Therefore, V_n is still determined by the shape of the surface oscillation and there is still no net motion of the boundary, we thus have $G_n = 0$ for all n. The new definition of Θ does, however, allow for net motion of the fluid along the surface of the body, and the coefficients W_n are then chosen so that the appropriate surface boundary condition is obeyed at first order. Similarly the value of F_n is determined by ensuring that this same surface boundary condition is obeyed at second order. As such F_n may be nonzero and without loss of generality we assume that $\partial f/\partial t$ time averages to one.

The addition of the coefficients F_n is a second-order contribution so ψ_1 is unchanged from Eq.1.28. The form of the second-order inner solution Eq.1.59 is unchanged with L_k as in Eq.1.60 but M_k now has an extra F_k contribution so we obtain the revised equation

$$M_k = \delta\left(\sum_{n=0}^{\infty}\sum_{m=1}^{\infty} a_{knm}\left\{-\frac{1}{2}(\bar{W}_n+n\bar{V}_n)V_m mi+\frac{1}{2}\bar{V}_n(W_m+mV_m)(4+3n-m)i\right.\right.$$
$$+\frac{1}{4}(\bar{W}_n+n\bar{V}_n)(W_m+mV_m)(3-i)+\frac{1}{2}\bar{V}_n W_m(m+3)i-\frac{1}{2}\bar{V}_n V_m im$$
$$+\frac{1}{2}W_n\bar{W}_m i-\sum_{j=1}^{\infty}\left(\frac{C_{nj}}{j(j+1)}\right)\left[\frac{1}{4}(W_m+mV_m)(\bar{W}_j+j\bar{V}_j)(1+i)\right.$$
$$\left.\left.\left.+(W_m+mV_m)\bar{V}_j ij+\frac{1}{2}\bar{W}_m W_j i\right]\right\}-F_k\right)+O(\delta^2) \text{ for } k>0. \quad (1.83)$$

The new boundary condition considered, such as that of no angular stress along the surface of a bubble, would now be applied to this new second order inner solution allowing us to determine the value of the coefficients F_k.

Similarly the form of the outer solution Eq.1.75 remains the same but through the asymptotic matching there is an extra contribution to its constants of integration so that the revised formulae for the S_k and T_k coefficients are now

$$S_k = \Re\left\{\sum_{n=0}^{\infty}\sum_{m=1}^{\infty}\left[a_{knm}\left\{\frac{1}{4}\bar{V}_n(W_m+mV_m)ik\right.\right.\right.$$
$$-\frac{1}{4}(\bar{W}_n+n\bar{V}_n)V_m im+\frac{1}{4}\bar{V}_n(W_m+mV_m)(4+3n-m)i$$
$$+\frac{1}{8}(\bar{W}_n+n\bar{V}_n)(W_m+mV_m)(3-i)+\frac{1}{4}\bar{V}_n W_m(m+3)i-\frac{1}{4}\bar{V}_n V_m mi$$
$$+\frac{1}{4}W_n\bar{W}_m i-\sum_{j=1}^{\infty}\frac{C_{nj}}{j(j+1)}\left[\frac{1}{8}(W_m+mV_m)(\bar{W}_j+j\bar{V}_j)(1+i)\right.$$
$$\left.\left.+\frac{1}{2}(W_m+mV_m)\bar{V}_j ij+\frac{1}{4}\bar{W}_m W_j i\right]\right\}-\frac{1}{4}g_{knm}\bar{V}_n(W_m-2V_m)ik\Bigg]$$
$$+\sum_{n=1}^{\infty}\sum_{m=1}^{\infty}\left[\frac{1}{4}f_{knm}(\bar{V}_n n(n+1)-\bar{W}_n)W_m\frac{ik}{mn(n+1)(m+1)}\right]+\frac{1}{2}V_0\bar{V}_k ki-\frac{1}{2}F_k\Bigg\}$$
$$+O(\delta), \quad (1.84)$$

and

$$T_k = \Re\left\{\sum_{n=0}^{\infty}\sum_{m=1}^{\infty}\left[a_{knm}\left\{\frac{1}{4}\bar{V}_n(W_m+mV_m)(2-k)i\right.\right.\right.$$
$$+\frac{1}{4}(\bar{W}_n+n\bar{V}_n)V_m im-\frac{1}{4}\bar{V}_n(W_m+mV_m)(4+3n-m)i$$
$$-\frac{1}{8}(\bar{W}_n+n\bar{V}_n)(W_m+mV_m)(3-i)-\frac{1}{4}\bar{V}_n W_m(m+3)i+\frac{1}{4}\bar{V}_n V_m mi$$

$$-\frac{1}{4}W_n\bar{W}_m i+\sum_{j=1}^{\infty}\frac{C_{nj}}{j(j+1)}\left[\frac{1}{8}(W_m+mV_m)(\bar{W}_j+j\bar{V}_j)(1+i)\right.$$
$$\left.+\frac{1}{2}(W_m+mV_m)\bar{V}_j ij+\frac{1}{4}\bar{W}_m W_j i\right]\Bigg\}-\frac{1}{4}g_{knm}\bar{V}_n(W_m-2V_m)\,i(2-k)\Bigg]+$$
$$\sum_{n=1}^{\infty}\sum_{m=1}^{\infty}\left[\frac{1}{4}f_{knm}(\bar{V}_n n(n+1)-\bar{W}_n)W_m\frac{(2-k)i}{n(n+1)m(m+1)}\right]+\frac{1}{2}V_0\bar{V}_k(2-k)i+\frac{1}{2}F_k\Bigg\}$$
$$+O(\delta), \quad (1.85)$$

with the coefficients Y_{knm} remaining the same as in Eq.1.76. Naturally, through the asymptotic matching outlined above, as T_k and S_k have an extra contribution, the inner constants N_k and Q_k will also include a contribution proportional to the constants F_k.

1.7 Special case: free surfaces

In the case of an oscillating bubble, the extra boundary condition is that of no tangential stress on the bubble surface

$$\underline{n}\cdot\underline{\underline{\sigma}}\cdot\underline{\Gamma}=0 \quad \text{at } r=R\,\theta=\Theta, \quad (1.86)$$

where $\underline{\Gamma}$ is the tangent vector in the plane through the axis of axisymmetry, $\underline{n}$ is the normal vector and $\underline{\underline{\sigma}}$ is the Newtonian stress tensor. There is still no penetration on the bubble surface and the shape of the bubble oscillation (via the coefficients V_n) is prescribed. Ensuring that the no-tangential stress conditions holds at first order and at second order (when time averaged) determines the values of W_n and F_n. This calculation is quite involved and its details are given in the appendices of §1.13 and §1.14 with the main results quoted in what follows.

1.7.1 General case

In this subsection we calculate the leading-order streaming provided the result is non-zero (in which case see §1.7.2). The generated streaming is of the same form as the one already derived, Eq.1.75, with Y_{knm} defined as in Eq.1.76 and $R_0=0$, with the difference that the constants T_k and S_k now take new values

$$T_k=\Re\left\{V_0\bar{V}_k\frac{(1-k^2)i}{(2k+1)}+\sum_{n=1}^{\infty}\sum_{m=1}^{\infty}f_{knm}\bar{V}_nV_m\frac{\left(k^2-k-1\right)(n+2)i}{2(2k+1)(n+1)(m+1)}\right.$$
$$+\sum_{n=0}^{\infty}\sum_{m=1}^{\infty}g_{knm}\bar{V}_nV_m\frac{3(1-k^2)i}{2(2k+1)}+\sum_{n=0}^{\infty}\sum_{m=1}^{\infty}\frac{a_{knm}}{2(2k+1)}\Big[\bar{V}_nV_m mi\left(n^2-4nm-4n\right.$$

$$+m^2-m-3)+\sum_{j=1}^{\infty}\left(\frac{C_{nj}}{j+1}\right)V_m\bar{V}_j m(3m+5)i\Bigg]\Bigg\}+O(\delta), \quad (1.87)$$

and

$$S_k=\Re\Bigg\{V_0\bar{V}_k\frac{ik(k+2)}{(2k+1)}-\sum_{n=1}^{\infty}\sum_{m=1}^{\infty}f_{knm}\bar{V}_nV_m\frac{ik(n+2)\,(2k+4)}{4(n+1)(m+1)\,(2k+1)}$$
$$+\sum_{n=0}^{\infty}\sum_{m=1}^{\infty}g_{knm}\bar{V}_nV_m\frac{3k(k+2)i}{2(2k+1)}-\sum_{n=0}^{\infty}\sum_{m=1}^{\infty}\frac{a_{knm}}{2(2k+1)}\Bigg[\bar{V}_nV_mmi\left(n^2-4nm-4n\right.$$
$$\left.+m^2-m-3)+\sum_{j=1}^{\infty}\left(\frac{C_{nj}}{j+1}\right)V_m\bar{V}_j m(3m+5)i\Bigg]\Bigg\}+O(\delta). \quad (1.88)$$

This solution is derived in detail in the appendix of §1.13.

1.7.2 Special case - In-phase motion

If the V_n coefficients are chosen such that the real part of $iV_n\bar{V}_m=0$ for all valued of n and m (i.e. all modes are in phase or π out-of-phase with each other) then $T_k=S_k=Y_{knm}=0$ and the steady streaming is identically zero at $O(1)$. This of course includes the case where only one mode is being forced. The net streaming in that case occurs at order δ. In order to determine this streaming the solution derived in §1.1 needs to be taken to third order, to give one more power of δ, and then have the no-stress condition applied to it. The details for this calculation are in the appendix of §1.14. The generated streaming is still of the same form as has already been derived, Eq.1.75 but with $Y_{knm}=0$, $R_0=0$ and with the constants T_k and S_k now taking new values as

$$T_k=\delta\Re\Bigg\{\sum_{n=1}^{\infty}\sum_{m=1}^{\infty}f_{knm}\bar{V}_nV_m\frac{(1-k^2)(n+2)}{2(2k+1)(n+1)}-\sum_{n=0}^{\infty}\sum_{m=0}^{\infty}g_{knm}\bar{V}_nV_m\frac{(1-k^2)m(m+2)}{2(2k+1)}$$
$$+\sum_{n=0}^{\infty}\sum_{m=1}^{\infty}a_{knm}\Bigg[\bar{V}_nV_m\left(\frac{n^2}{4}+\frac{9n}{4}-\frac{5m^2}{4}-\frac{5m}{4}+1+\frac{1}{2}k^2+\frac{3}{2}k\right)\frac{m(m+2)}{2(2k+1)}$$
$$-\bar{V}_nV_m\frac{nm(n+2)\,(2m+1)}{2(2k+1)}-\sum_{j=1}^{\infty}\frac{C_{nj}}{j(j+1)}\left(V_m\bar{V}_j\frac{mj(2m+j+6)}{2(2k+1)}\right)\Bigg]\Bigg\}, \quad (1.89)$$

and

$$S_k=\delta\Re\Bigg\{\sum_{n=1}^{\infty}\sum_{m=1}^{\infty}f_{knm}\bar{V}_nV_m\frac{k(k+2)(n+2)}{2(n+1)(2k+1)}-\sum_{n=0}^{\infty}\sum_{m=0}^{\infty}g_{knm}\bar{V}_nV_m\frac{k(k+2)m(m+2)}{2(2k+1)}$$

$$+\sum_{n=0}^{\infty}\sum_{m=1}^{\infty} a_{knm}\left[-\bar{V}_n V_m\left(\frac{n^2}{4}+\frac{9n}{4}-\frac{5m^2}{4}-\frac{5m}{4}+\frac{1}{2}k(k-1)\right)\frac{m(m+2)}{2(2k+1)}\right.$$
$$\left.+\bar{V}_n V_m\frac{nm(n+2)(2m+1)}{2(2k+1)}+\sum_{j=1}^{\infty}\frac{C_{nj}}{j(j+1)}\left(V_m\bar{V}_j\frac{mj(2m+j+6)}{2(2k+1)}\right)\right]\Bigg\}. \quad (1.90)$$

1.7.3 Discussion

Our results thus show that a bubble, for any in-phase oscillation of its shape, generates a streaming of $O(\delta)$ or lower, and therefore at least one order of magnitude weaker than that of a deformable no-slip surface (such as an elastic membrane) undergoing the same sequence of shape change. Thus the net flows generated by the angular velocities are of similar magnitude to those induced by the radial velocities and they cancel at leading order.

Longuet-Higgins observed that a bubble undergoing translational oscillation produced a force of $O(\delta)$, one order of magnitude less than the out-of-phase translational and pulsating oscillations, which is $O(1)$ [44]. Our calculations allow us to generalise this result to all shape changes, and thus suggests that ensuring there are at least two modes of oscillation out of phase leads to stronger streaming flows.

For bubbles forced by external fields, this raises an interesting question of whether a resonance mode of oscillation, which is solely at one mode, would produce a weaker streaming flow than out-of-phase forcing, which excites multiple modes. From a practical standpoint, microbubbles are often fixed to a wall, which enforces that the centre of the bubble has to move and as such is naturally excited at a second mode.

1.8 Comparison with past work

Our calculations have allowed us to compute the streaming generated by any specified, fixed, oscillating spherical object (and in particular we solved for a bubble). Past work has characterized the streaming flow for simple shape oscillations of bubbles and rigid spheres, to which we can compare our model in order to validate it.

1.8.1 Translating Bubble

In the case of a bubble undergoing translational oscillations, we have $V_1 = 1$ and $V_n = 0$ for $n \neq 1$, The angular boundary conditions W_n and F_n are determined by the no stress boundary condition. This case was studied by Longuet-Higgins [44] and the solution we obtain here is

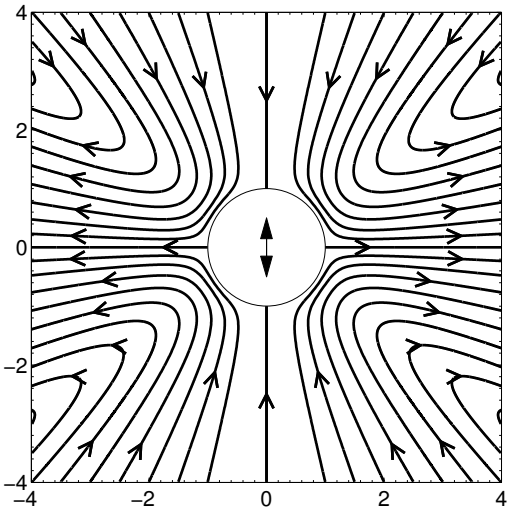

(a) Streaming from current model

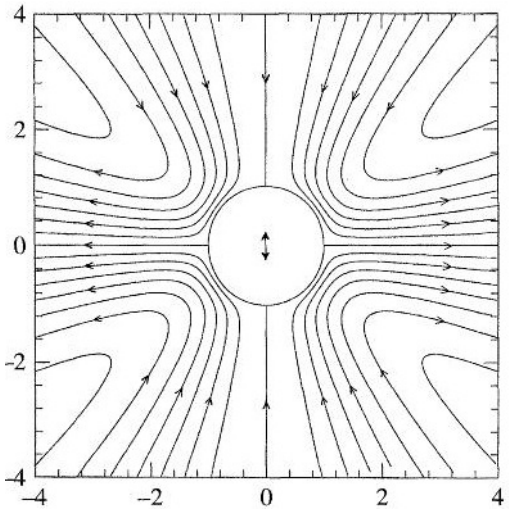

(b) Longuet-Higgins's streaming, reproduced by permission of the Royal Society from: M. S. Longuet-Higgins, "Viscous streaming from an oscillating spherical bubble", *Proc.Roy.Soc.A*, 1998, **454**, no.1970, pp.725-742. [44]

Figure 1.3: Streaming, in the form of a stresslet, generated by the translational oscillations of a bubble.

identical to his, namely

$$\langle \psi_L \rangle = \delta \frac{27}{20} \left(\frac{1}{r^2} - 1 \right) \int_\mu^1 P_2(x) dx, \tag{1.91}$$

as further illustrated in Fig.1.3. This streaming flow is a stresslet with fluid pulled in along the axis of oscillation and pushed out along the equator.

1.8.2 Translating Sphere

In the case of a solid sphere undergoing translational oscillations we have $V_1 = 1$, $V_n = 0$ for $n \neq 1$, $W_1 = 2$, $W_n = 0$ for $n \neq 1$, and $F_n = 0$. This case was studied by Riley [42] and the streaming we obtain is identical to his solution, namely

$$\langle \psi_2^o \rangle = -\frac{45}{16} \left(\frac{1}{r^2} - 1 \right) \int_\mu^1 P_2(x), \tag{1.92}$$

as further illustrated in Fig.1.4. Similarly to the oscillating bubble, this streaming flow is a stresslet but with opposite direction.

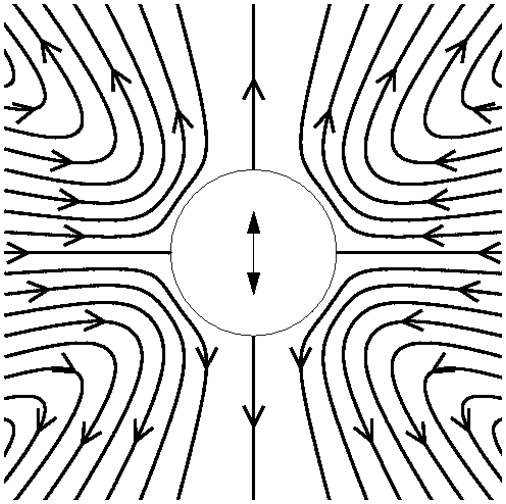

(a) Streaming from the current mode

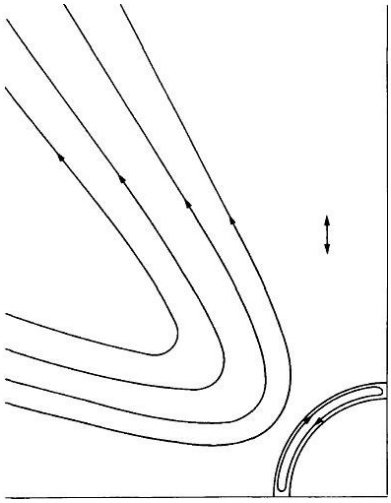

(b) Riley's streaming, reproduced by permission of Oxford University Press from: N. Riley, "On a sphere oscillating in a viscous fluid", *Q. J. Mech. Appl. Math.*, 1966, **19**, no.4, pp.461-472, [42]

Figure 1.4: Streaming, in the form of a stresslet, generated by the translational oscillations of a sphere.

1.8.3 Bubble Translating and Radially Oscillating

Finally, in the case of a bubble undergoing radial and lateral oscillations only V_0 and V_1 can be non-zero. Then the pairs W_n and F_n are determined by the no stress boundary condition. We obtain $W_1 = -V_1$, $W_n = 0$ for $n \neq 1$, $F_1 = 4i\bar{V}_0 V_1$ and $F_n = 0$ for $n \neq 1$. In this case there is a contribution from the Stokes drift with one non-zero component of Y, $Y_{101} = i\bar{V}_0 V_1/2$ leading to the final Lagrangian streaming as

$$\langle \psi_L \rangle = \Re\left(\bar{V}_0 V_1 i\right)\left(-\frac{1}{4r} + \frac{r}{2} - \frac{1}{4r^4}\right)(1-\mu^2), \tag{1.93}$$

which matches the result of Longuet-Higgins [44] (note that in Ref.[44], $\Re\left(i\bar{V}_0 V_1\right)$ is written as $\sin(\phi)$ with ϕ denoting the phase difference between modes 0 and 1). At leading order this streaming flow is a stokeslet, with direction parallel to the axis of axisymmetry, and with a sign determined by the phase difference between V_0 and V_1.

1.9 Illustration of steady streaming and far-field behaviour

With the calculations above, we can now illustrate the streaming patterns, which can be obtained from surface oscillations. We consider a range of surface boundary conditions (V_n and W_n) and assume for simplicity that the surface streaming is zero ($F_n = 0$). The steady streaming flow splits naturally into two regions with different behaviours: the fluid motion close to the spherical body, which often contains recirculation regions, and the far-field behaviour, which is dominated by the slowest decaying term in the velocity.

First we consider the streaming generated by a few simple surface shape oscillations. In Fig.1.5*a* we illustrate the streaming when only the mode $V_1 \neq 0$ is being forced. In all cases, the flow being axisymmetric, we only need to display streamlines in the plane of symmetry to illustrate the whole flow. Here $S_1 = 0$ so the slowest decaying term is S_2/r^2, which produces the pattern of flow coming in in the equatorial plane of the spherical body and pushed away along the vertical axis (stresslet, see below). Furthermore, as there are few higher order terms this behaviour in fact dominates the flow throughout the domain.

Differences between the far-field flow and the fluid motion close to the body can be seen with higher modes. This is illustrated in Fig.1.5*b*, which shows the streaming generated by forcing mode V_2 only. On the edge of the figure the dynamics seen in Fig.1.5*a* is apparent as the term S_2/r^2 is still dominant in the far field. However, close to the spherical body, we see circulation zones, which extend about one body diameter into the fluid. The number of these circulations regions increase as higher modes are being forced. A similar pattern is observed when only oscillating at one angular mode (i.e. $W_n \neq 0$ for one choice of n).

Let us now consider the behaviour in the far field. Far from the sphere, the steady streaming is dominated by the slowest decaying term. If $S_1 \neq 0$ then the slowest decaying flow is the stokeslet with the velocities decaying as S_1/r. This produces a non-zero force along the axis of rotational symmetry and this gives a clear movement of flow parallel to this axis - either in the positive (Fig.1.5c) or negative direction (Fig.1.5d). If $S_1 = 0$ the body has no force acting on it, as seen in Fig.1.5*a* and Fig.1.5*b* where the symmetry of the system prevents a net force from being induced. Generally, a net force is created only if two adjacent modes are non-zero, as otherwise a_{knm}, g_{knm}, f_{knm} are all zero and the $a_{knm}c_{nj}$ combinations cancel.

If the stokeslet coefficient, S_1, is zero the far field behaviour is dominated by a slower decaying term. In most cases it will be a stresslet with associated velocities decaying as S_2/r^2. This is the flow seen in Fig.1.5*a*. If $S_1 = S_2 = 0$ are both zero then the far-field behaviour is dominated by the $(T_k + S_{k+2})/r^{k+2}$ term for the lowest value of $k \geq 1$ such that $(T_k + S_{k+2})$ is non-zero.

Close to the spherical body, circulation regions will form. If there is a stokeslet, this term

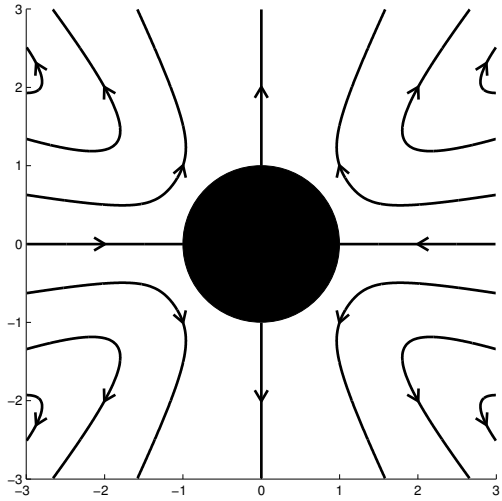

(a) Oscillating with $V_1 = 1$ only, corresponding to a translational oscillation.

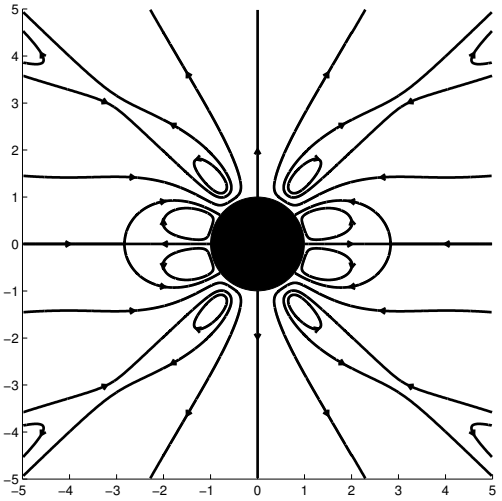

(b) Oscillating with $V_2 = 1$ only. This corresponds to the body oscillating between an oblate and prolate spheroid.

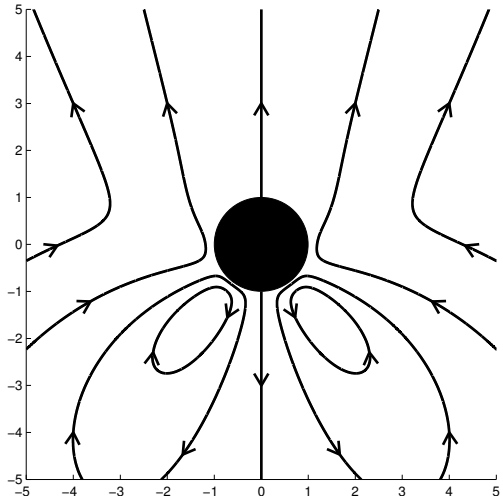

(c) Positive force by oscillating at two modes $V_1 = \frac{1}{\sqrt{2}}$, $V_2 = \frac{1}{\sqrt{2}}$, $W_1 = \frac{-3}{\sqrt{2}}$ and $W_2 = \frac{2}{\sqrt{2}}$. This oscillation shape is a combination of a translational oscillation and an oscillation between a prolate and oblate spheroid.

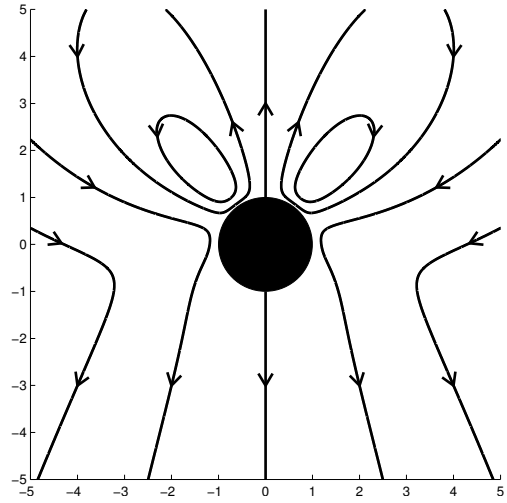

(d) Negative force by oscillating at two modes $V_1 = \frac{1}{\sqrt{2}}$ and $V_2 = \frac{1}{\sqrt{2}}$. This oscillation shape is a combination of a translational oscillation and an oscillation between a prolate and oblate spheroid.

Figure 1.5: Patterns of steady streaming for the first few surface oscillation modes.

tends to dominate the flow and even close to the body circulation regions rarely appear. The one exception is close to the axis of symmetry where a pair of large circulations will sometimes form, either just above or just below the sphere (see Fig.1.5c and Fig.1.5d). Since the flow is axisymmetric, this corresponds to a recirculation torus.

Intuitively, one would expect that the shape of the volume physically displaced by the spherical body (set by the modes V_n) would have a significant effect on the features of the flow field. But as discussed in §1.7, the angular motion on the surface can produce a flow of similar magnitude, and in fact it can change the direction of the circulations and the streaming flow (and hence the direction of the body force applied to the spherical object) as demonstrated in Fig.1.5d and Fig.1.5c. Another example of this, already seen in §1.8, displayed the streaming flow difference between a translating bubble (Fig.1.3) and a translating sphere in (Fig.1.4).

1.10 Application: force generation and propulsion

In our current setup, the sphere is held fixed, and the force exerted by the oscillations of the surface of the spherical body on the fluid is computed. However, by Newton's law, an equal and opposite force is being applied to the spherical body from the fluid. If the spherical body is not held in place then this would cause it to move. Mathematically, a net motion of the body is necessarily a second-order effect as all leading-order effects are oscillatory and produce no net motion or forces. Hence allowing the body to move will only slightly modify our mathematical approach. In this section we characterise the force induced by a fixed body and then adapt the calculation for the case where the body is free to move.

1.10.1 Force generation

Due to the axisymmetry of the system a net force can only be exerted along the axis of rotational symmetry, taken to be $\underline{e}_z$ using traditional notation from spherical coordinates. We thus write $\underline{F} = F\underline{e}_z$, for F the magnitude of $\underline{F}$.

The time averaged force on the spherical body is equal to the force across the boundary of our spherical object at $r = R$, i.e.

$$\underline{F} = \left\langle \int \left(\underline{\underline{\sigma}} \cdot \underline{n} \right) |_{r=R(\mu)} dS \right\rangle . \tag{1.94}$$

This force must match the force across the boundary "$r = \infty$" and thus

$$\underline{F} = -\left\langle \int \left(\underline{\underline{\sigma}} \cdot \underline{n} \right) |_{r=\infty} dS \right\rangle . \tag{1.95}$$

Across $r=\infty$, if the time average is taken then there will only be a contribution from the second order term as all first-order terms are oscillatory. Also, the region $r=\infty$ is now outside the boundary layer, where, due to the exponential decay of the non-linear terms, the time-averaged behaviour is a Stokes flow. Outside the boundary layer, the slowest decaying velocity is the $1/r$ term. This velocity field at leading order in r is

$$u_r = S_1 \frac{\cos\theta}{r} + O(r^{-3}), \tag{1.96}$$

$$u_\theta = -S_1 \frac{\sin\theta}{2r} + O(r^{-3}). \tag{1.97}$$

This is the stokeslet discussed above. Indeed a non-dimensional stokeslet due to a force $\underline{F}$ applied at the origin induces a flow $\underline{U}$ with components

$$U_j = \frac{F_i}{8\pi}\left(\frac{\delta_{ij}}{r} + \frac{x_i x_j}{r^3}\right). \tag{1.98}$$

With a force in the $\underline{e}_z$ direction this gives

$$U_r = \frac{F}{4\pi r}\cos\theta, \tag{1.99}$$

$$U_\theta = -\frac{F}{8\pi r}\sin\theta. \tag{1.100}$$

Equating these two forms of the stokeslet shows the non-dimensional force exerted on the spherical body by the surrounding fluid is

$$\underline{F} = -8\pi\varepsilon^2 \frac{S_1}{2}\underline{e}_z. \tag{1.101}$$

This force is the result of a dominant pressure field, thus the dimensional scaling for the pressure indicates the scaling for the force. The Navier-Stokes equations indicate that the pressure scales with time varying inertia so $p \sim \rho U a\omega \sim \rho a^2\omega^2$ implying that the dimensional force is

$$\underline{F} = -4\pi\varepsilon^2 S_1 \left(\rho a^4\omega^2\right)\underline{e}_z. \tag{1.102}$$

1.10.2 Force-free swimming

If the spherical body is no longer held in place but is free to move, it will translate with an $O(\varepsilon^2)$ velocity in the direction of this force. However, the constraint of force-free motion

needs to be carefully enforced at both $O(\varepsilon)$ and $O(\varepsilon^2)$ and being free to move will in general also impact the first-order oscillatory motion.

1.10.2.1 Force-free motion at $O(\varepsilon)$

At $O(\varepsilon)$ the motion of the spherical body is completely determined by the constants V_n and W_n. Up to now these coefficients could be chosen arbitrarily to represent any surface motion. The extra constraint of force-free motion will now restrict the allowed motion of the spherical body, therefore restricting choices of V_n and W_n.

Mathematically, force-free motion is written as

$$\underline{F} = \int \left(\underline{\underline{\sigma}} \cdot \underline{n}\right)|_{r=R(\mu,t)} dS = 0. \tag{1.103}$$

The normal vector to the surface of the spherical body is

$$\hat{\underline{n}} = \underline{e}_r - \frac{\partial R}{\partial \theta}\underline{e}_\theta + O(\varepsilon^2). \tag{1.104}$$

Knowing that the direction of $\underline{F}$ is in the $\underline{e}_z$ direction by symmetry, this becomes

$$\underline{F} = \left[\int \left(\sigma_{rr}\cos\theta - \sigma_{\theta r}\sin\theta\right)|_{r=1} dS + O(\varepsilon^2)\right]\underline{e}_z. \tag{1.105}$$

This can then be non-dimensionalised and the integral expanded to give

$$\underline{F} = \left\{\int_0^{2\pi}\int_0^{\pi}\left[\left(-p + \delta^2\frac{\partial u_r}{\partial r}\right)\cos\theta - \frac{\delta^2}{2}\left(\frac{1}{r}\frac{\partial u_r}{\partial \theta} + \frac{\partial u_\theta}{\partial r} - \frac{u_\theta}{r}\right)\sin\theta\right]\times \right.$$
$$\left. \sin\theta\, d\theta\, d\phi \qquad + O(\varepsilon^2)\right\}\underline{e}_z. \tag{1.106}$$

The first-order pressure can be calculated by substituting the first-order solution for ψ_1, Eq.1.28, into the Navier-Stokes equation to obtain

$$p = e^{it}\sum_{n=0}^{\infty} P_n(\mu)\left(\frac{iD_n}{(n+1)r^{n+1}}\right). \tag{1.107}$$

Then notice, using integration by parts and Legendre identities, that

$$\int_0^{\pi} P_n(\mu)\cos\theta\sin\theta d\theta = \frac{2}{3}\delta_{1n} \text{ for } n \geq 0, \tag{1.108}$$

$$\int_0^{\pi}(1-\mu^2)^{-\frac{1}{2}}\left(\int_\mu^1 P_n(x)dx\right)\sin^2\theta\, d\theta = \frac{2}{3}\delta_{1n} \text{ for } n \geq 1. \tag{1.109}$$

Therefore the force-free condition will only affect the $n = 1$ mode. Then as we have the scalings

$$\frac{\partial u_r}{\partial r} \sim O(1), \quad \frac{\partial u_r}{\partial \theta} \sim O(1), \quad \frac{\partial u_\theta}{\partial r} \sim O(\delta^{-1}), \quad u_\theta \sim O(1), \quad p \sim O(1), \tag{1.110}$$

at the two leading orders in δ only pressure and the viscous stress $\sim \partial u_\theta / \partial r$ will contribute to the force, leading to

$$\underline{F} = \frac{4\pi}{3} e^{it} \left[-\frac{i}{2} V_1 + \delta \frac{(1+i)}{4} (W_1 + V_1) + O(\delta^2) \right] \underline{e}_z. \tag{1.111}$$

For the spherical body to be force-free we thus need $V_1 = W_1 = 0$. In other words, if the boundary conditions are such that $V_1 \neq 0$ and $W_1 \neq 0$ for a fixed sphere, then the force-free sphere will undergo additional oscillatory motion to compensate and lead to $V_1 = W_1 = 0$ overall. Physically the V_1 mode corresponds to the sphere undergoing translational oscillations. So for the body to be force free the translational oscillations are suppressed. At $O(\varepsilon)$, since the behaviour is linear, for most angular surface boundary conditions, W_1 will be directly dependent on the value of V_1 so a condition restricting translational oscillations would be anticipated to effect the angular motion at this mode too.

1.10.2.2 Force-free motion at $O(\varepsilon^2)$

In order for the motion of the sphere at $O(\varepsilon)$ to be force-free, we saw that two of the surface coefficients become zero. Beyond that, the model has not fundamentally changed. We can thus use our mathematical framework to calculate the velocity of translation at $O(\varepsilon^2)$ in terms of the force generated by the oscillating body, which was force-free at first order.

We use $\tilde{V}$ to denote the non-dimensional time-averaged velocity of the body at order ε^2. In order to use the same formulation as above, we move into a frame of reference where the body undergoes no net motion at $O(\varepsilon^2)$ in the z direction. Mathematically, this keeps all the boundary conditions the same as above except now requires in the far field that

$$\psi \sim -\varepsilon^2 \tilde{V} \frac{r^2}{2} (1 - \mu^2), \quad r \to \infty. \tag{1.112}$$

As this is an outer boundary condition, the form of the second-order inner solution remains unchanged. Therefore, the main change is in the second-order outer solution. The general form of this outer streaming is still given by Eq.1.64 (which is still a Stokes approximation since the non-linear forcing term can be neglected due to its exponential decay rate). The

difference is that applying the new boundary condition Eq.1.112 allows one more term than before to be non-zero so we have

$$\langle \psi_2^o \rangle = \tilde{R}_0 \left(\int_\mu^1 P_0(x)dx \right) + (-\tilde{V} r^2 + \tilde{T}_1 r^{-1} + \tilde{S}_1 r) \left(\int_\mu^1 P_1(x)dx \right) + \sum_{n=2}^{\infty} \left(\tilde{T}_n r^{-n} + \tilde{S}_n r^{-(n-2)} \right) \left(\int_\mu^1 P_n(x)dx \right). \quad (1.113)$$

Then when comparing this outer solution to the inner solution Eq.1.68, Eq.1.69 and Eq.1.70 all still hold for $k \neq 1$ but for $k = 1$ we instead have

$$L_1 = \tilde{T}_1 + \tilde{S}_1 - \tilde{V}, \quad (1.114)$$

$$\frac{M_1}{\delta} = \tilde{S}_1 - \tilde{T}_1 - 2\tilde{V}. \quad (1.115)$$

In order to determine the value of $\tilde{V}$ we enforce that the time-averaged second-order solution be force-free so we have

$$\underline{F} = \left\langle \int \left(\underline{\underline{\sigma}} \cdot \underline{n} \right) |_{r=R(\mu,t)} dS \right\rangle = \underline{0}. \quad (1.116)$$

Contributions to this integral will come from linear terms involving the internal second-order solution, ψ_2^i, as well as non-linear terms involving the first order solution ψ_1.

As the form of the first-order solution has not changed, the contributions from those non-linear terms remain the same as when we restrict $\tilde{V} = 0$ (i.e. no second-order translation). However, the second-order internal solution will give a slightly different contribution as the values of the constants of integration N_k and Q_k have changed.

Looking at the second-order internal solution only the constants of integration L_k, M_k, N_k and Q_k could be different. But changes will only occur for $k = 1$ since for other values of k the outer solution is as before. Furthermore, the constants L_1 and M_1 are the same as before since their values were determined by the boundary conditions on the surface of the body, which are the same. We use the asymptotic matching in order to determine the values of T_1 and S_1 in terms of the known values L_1 and M_1 and this is then used to calculate the new values of N_1 and Q_1.

In this new system we have

$$L_1 = \left(\tilde{T}_1 + \frac{\tilde{V}}{2} \right) + \left(\tilde{S}_1 - \frac{3\tilde{V}}{2} \right), \quad (1.117)$$

$$\frac{M_1}{\delta} = \left(\tilde{S}_1 - \frac{3\tilde{V}}{2}\right) - \left(\tilde{T}_1 + \frac{\tilde{V}}{2},\right), \tag{1.118}$$

$$\frac{N_1}{\delta^2} = \tilde{T}_1 - \tilde{V} = \left(\tilde{T}_1 + \frac{\tilde{V}}{2}\right) - \frac{3\tilde{V}}{2}, \tag{1.119}$$

$$\frac{Q_1}{\delta^3} = -\tilde{T}_1 = -\left(\tilde{T}_1 + \frac{\tilde{V}}{2}\right) + \frac{\tilde{V}}{2}\cdot \tag{1.120}$$

Compared to S_1 and T_1 in the first-order force-free case, $T_1 = \tilde{T}_1 + \tilde{V}/2$ and $S_1 = \tilde{S}_1 - 3\tilde{V}/2$. Therefore, the drag force on the sphere will be the same as before, $-4\pi\mu S_1 \underline{e}_z$ plus an extra contribution from the $-3\tilde{V}/2$ extra term in N_1 and the $\tilde{V}/2$ term in Q_1.

Knowing $\hat{\underline{n}}$ from Eq.1.104 and that the direction of $\underline{F}$ is still in the $\underline{e}_z$ direction means we have

$$\underline{F} = \left\langle \int \left[\left(\sigma_{rr} - \varepsilon \frac{\partial R}{\partial \theta}\sigma_{\theta r}\right)\cos\theta - \left(\sigma_{\theta r} - \varepsilon \frac{\partial R}{\partial \theta}\sigma_{\theta\theta}\right)\sin\theta \right] |_{r=R(\mu,t)} dS \right\rangle \underline{e}_z. \tag{1.121}$$

We see that the extra contributions to F can only come from the linear terms evaluated at $r = 1$ (so $\eta = 0$) i.e.

$$\sigma_{rr}\cos\theta - \sigma_{\theta r}\sin\theta = \left[\left(-p + \delta^2 \frac{\partial u_r}{\partial r}\right)\cos\theta - \frac{\delta^2}{2}\left(\frac{1}{r}\frac{\partial u_r}{\partial \theta} + \frac{\partial u_\theta}{\partial r} - \frac{u_\theta}{r}\right)\sin\theta \right]. \tag{1.122}$$

In $\sigma_{\theta r}$ there will only be an extra N_1 contribution arising from the $\partial u_\theta/\partial r$ term. Any extra contribution from σ_{rr} will come from the pressure term. The non-dimensional second-order equation for the pressure is

$$\varepsilon \langle \underline{u} \cdot \nabla \underline{u} \rangle = -\nabla \langle p \rangle + \frac{\delta^2}{2}\mu \nabla^2 \langle \underline{u} \rangle, \tag{1.123}$$

where the pressure scales as $p \sim \rho a U \omega$. Then $\langle \underline{u} \cdot \nabla \underline{u} \rangle$ gives a contribution in terms of ψ_1 only. There is however an extra contribution coming from $\nabla^2 \langle \underline{u} \rangle$. By looking at the θ component of this equation, and noticing that we are evaluating at $r = 1$ in the integral, we see we are only interested in terms with no dependence of η. Then it can be found that the additional contribution comes from Q_k only (with none from N_k), and is given by

$$p = \frac{3}{2}\delta^2 \left(\frac{Q_1}{\delta^3}\right) P_1(\mu). \tag{1.124}$$

The extra contribution to F coming from the $\partial u_\theta/\partial r$ term in $\sigma_{\theta r}$ and from the pressure is

$$\delta^2 \int_0^{2\pi} \int_0^{\pi} \left[\left(-\frac{3\tilde{V}}{4} \right) \sin^3\theta - \left(\frac{3\tilde{V}}{4} \right) \cos^2\theta \sin\theta \right] d\theta d\phi = -3\pi\delta^2 V. \tag{1.125}$$

Therefore, the total non-dimensional force on the spherical body is

$$\underline{F} = \varepsilon^2 \left(-4\pi S_1 - 3\pi\delta^2 \tilde{V} \right) \underline{e_z}. \tag{1.126}$$

For the body to be force free its dimensional velocity must therefore be

$$\tilde{V} = -\frac{4}{3\delta^2}(a\omega) S_1, \tag{1.127}$$

which we can use to calculate a numerical value for $\tilde{V}$.

The relationship between the force on the body and its velocity is given by substituting this value of S_1 into Eq.1.102 giving

$$\underline{F} = 3\pi\varepsilon^2\delta^2\tilde{V}(\rho a^3\omega)\underline{e_z}. \tag{1.128}$$

Then substituting the scaling for δ^2 given by Eq.1.8 finally leads to

$$\underline{F} = 6\pi\varepsilon^2\tilde{V}\,(a\rho\nu)\,\underline{e_z}. \tag{1.129}$$

We recognise the standard result for a solid sphere translating at speed $\varepsilon^2\tilde{V}$ in a Stokes flow. Since outside the boundary layer the flow is a Stokes flow, such a similarity was in fact expected (corrections for non-sphericity are expected at higher orders in ε).

1.11 Conclusion

In this chapter we have mathematically derived the steady streaming flow generated by arbitrary axisymmetric shape oscillations of a spherical body. The final solution, and thus the main result of this chapter, is quantified in Eqs.1.75 – 1.78.

Our model, which agrees with classical results, shows that a net force is generated in the far field only when two adjacent surface modes are excited. If the body is free to move, this force will cause the body to move with a net velocity, which we derived, given by a balance between that streaming force and the Stokes drag (Eq.1.127).

Having kept the boundary forcing arbitrary makes our model applicable to a wide range of microorganisms and microfluidic devices. Future work could involve determining the impact

of inertia on the optimal swimming shape and associated efficiency of larger microorganisms (such as *Spirostomum* [57]), which may swim in regimes with non-negligible convective inertia. In addition, using this framework the study of active colloids could be extended to inertial regimes, from the extensively studied low Reynolds number regimes [65].

Recent experimental work has used bubbles embedded in free-moving hollow bodies to generate propulsion [46] and our formalism will be directly applicable to this new class of synthetic swimmers. In particular, in Chapter 2 we use our calculations to determine the streaming flow induced by such micron-sized "Armoured Microbubbles". Our analysis could be extended to a wider range of experimental parameters and could help improve future designs.

Since this model calculates the streaming flow around a spherical body, it could be used to study collective flows of these "Armoured Microbubbles" or other spherical bodies with complex surface shape oscillations where inertia is non-negligible, by linearly superposing their individual flows and correcting for other close bodies where necessary, using methods similar to Faxen's corrections for example. However, this model would need adapting to allow the spherical body to move rather than holding it stationary. The main problem, which may prevent this model being used to study (in particular, dense) collective flows, is in determining the effects when two bodies become close enough so that they significantly effect each others non-linear boundary layer (such as during collisions), and that scenario may require a different model to study it.

1.13 Appendix A: Out-of-phase streaming around a bubble

In order to apply the general steady streaming model Eq.1.75 specifically to a bubble the boundary condition of tangential stress on the boundary of the spherical body,

$$\underline{n}\cdot\underline{\underline{\sigma}}\cdot\underline{\Gamma}=0 \quad \text{at} \quad r=R,\ \theta{=}\Theta, \tag{1.130}$$

needs to be applied. This will determine the angular motion on the surface of the bubble W_n and F_n in terms of a prescribed radial motion V_n.

1.13.1 Boundary condition

We denote the unit tangent vector to the body's surface in the plane through the axis of symmetry, $\underline{\Gamma}$, and the normal vector $\underline{n}$. Both can be calculated in terms of $\underline{e}_r$ and $\underline{e}_\theta$ measured from

the centre of the rest position of the body giving

$$\underline{\Gamma} = \underline{e}_\theta + \frac{\partial R}{\partial \theta}\underline{e}_r + O(\varepsilon^3), \tag{1.131}$$

$$\underline{n} = \underline{e}_r - \frac{\partial R}{\partial \theta}\underline{e}_\theta + O(\varepsilon^3). \tag{1.132}$$

Using these equations the no stress condition can be expanded in terms of ε giving the first two terms as

$$\sigma_{\theta r} + \frac{\partial R}{\partial \theta_0}(\sigma_{rr} - \sigma_{\theta\theta}) + O(\varepsilon^3) = 0 \quad \text{at} \quad r = R,\ \theta{=}\Theta, \tag{1.133}$$

becoming

$$\sigma_{\theta r} + (R-1)\frac{\partial \sigma_{\theta r}}{\partial r} + (\Theta - \theta_0)\frac{\partial \sigma_{\theta r}}{\partial \theta} + (\sigma_{rr} - \sigma_{\theta\theta})\frac{\partial R}{\partial \theta} + O(\varepsilon^3) = 0$$
$$\text{at} \quad r = 1,\ \theta = \theta_0. \tag{1.134}$$

1.13.2 Leading-order solution

At $O(\varepsilon)$, Eq.1.134 reduces to the non-dimensional equation

$$\left(\frac{1}{r}\frac{\partial u_r}{\partial \theta} + \frac{\partial u_\theta}{\partial r} - \frac{u_\theta}{r}\right) = 0 \quad \text{at} \quad r = 1,\ \theta = \theta_0. \tag{1.135}$$

By substituting in the known first-order solution ψ_1, Eq.1.28, this equation can be used to determine W_n giving

$$W_n = -nV_n + \delta\frac{2n(n+2)}{(1+i)}V_n + \delta^2 in(n+2)^2 V_n + O(\delta^3). \tag{1.136}$$

1.13.3 Second-order solution

At $O(\varepsilon^2)$, after Taylor expansion of $\sigma_{\theta r}$ Eq.1.134 reduces to the non-dimensional equation

$$\sigma_{\theta r}^{(\varepsilon^2)} = -(R-1)\frac{\partial \sigma_{\theta r}^{(\varepsilon)}}{\partial R} - (\Theta - \theta_0)\frac{\partial \sigma_{\theta r}^{(\varepsilon)}}{\partial \theta} - \frac{\partial R}{\partial \theta_0}\left(\sigma_{rr}^{(\varepsilon)} - \sigma_{\theta\theta}^{(\varepsilon)}\right) \quad \text{at} \quad r = R,\ \theta{=}\Theta, \tag{1.137}$$

where superscripts indicate the order at which each term is to be taken. Upon substitution of R , Θ and σ, Eq.1.137 becomes

$$\left((1-\mu^2)\frac{\partial^2\psi_2^i}{\partial\mu^2}+2\frac{\partial\psi_2^i}{\partial r}-\frac{\partial^2\psi_2^i}{\partial r^2}\right)=\Re\left[i\sum_{n=0}^{\infty}V_nP_n(\mu)e^{it}\right]\times$$
$$\Re\left[(1-\mu^2)\frac{\partial^3\psi_1}{\partial\mu^2\partial r}+3\frac{\partial^2\psi_1}{\partial r^2}-\frac{\partial^3\psi_1}{\partial r^3}-3(1-\mu^2)\frac{\partial^2\psi_1}{\partial\mu^2}-4\frac{\partial\psi_1}{\partial r}\right]+$$
$$\Re\left[\varepsilon i\sum_{n=1}^{\infty}W_n\left(\int_{\mu}^{1}P_n(x)dx\right)e^{it}\right]\Re\left[\frac{\mu}{(1-\mu^2)}\left((1-\mu^2)\frac{\partial^2\psi_1}{\partial\mu^2}+2\frac{\partial\psi_1}{\partial r}-\frac{\partial^2\psi_1}{\partial r^2}\right)\right.$$
$$\left.+\frac{\partial}{\partial\mu}\left((1-\mu^2)\frac{\partial^2\psi_1}{\partial\mu^2}\right)+2\frac{\partial^2\psi_1}{\partial r\partial\mu}-\frac{\partial^3\psi_1}{\partial r^2\partial\mu}\right]$$
$$-\Re\left[\varepsilon i\sum_{n=0}^{\infty}n(n+1)V_n\left(\int_{\mu}^{1}P_n(x)dx\right)e^{it}\right]$$
$$\times\left[6\frac{\partial\psi_1}{\partial\mu}-4\frac{\partial\psi_1}{\partial r\partial\mu}-2\frac{\mu}{(1-\mu^2)}\frac{\partial\psi_1}{\partial r}\right]\quad\text{at}\quad r=1,\ \theta=\theta_0.\quad(1.138)$$

The forcing on the right-hand side of Eq.1.138 can be calculated explicitly from the derivatives of ψ_1, Eq.1.28, simplifying the equation to

$$\left\langle(1-\mu^2)\frac{\partial^2\psi_2^i}{\partial\mu^2}+2\frac{\partial\psi_2^i}{\partial r}-\frac{\partial^2\psi_2^i}{\partial r^2}\right\rangle=\frac{i}{2}\sum_{k=0}^{\infty}\sum_{n=0}^{\infty}\sum_{m=1}^{\infty}a_{knm}\left\{-\bar{V}_nV_mm(m^2+2)+\right.$$
$$\bar{V}_nW_m(m+2)^2-4\bar{W}_nV_mm(m+1)+\bar{V}_n(W_m+mV_m)\left[2i\frac{1}{\delta^2}+\frac{1}{\delta}(m+3)(1+i)+\right.$$
$$\left.\frac{1}{2}m(2m+3)\right]-\frac{1}{\delta}(\bar{W}_n+n\bar{V}_n)W_m(1-i)+\bar{V}_nW_mn(n+2)-\bar{W}_nW_m(n+2)$$
$$+\sum_{j=1}^{\infty}\frac{C_{nj}}{j(j+1)}\left[\frac{1}{\delta}W_m\left(\bar{W}_j+j\bar{V}_j\right)\frac{(1-i)}{j(j+1)}+W_m\left(\bar{W}_j-j\bar{V}_j\right)\frac{(j+2)}{j(j+1)}\right.$$
$$\left.\left.+2V_m\bar{W}_jm(m+1)\right]\right\}\int_{\mu}^{1}P_k(x)dx.\quad(1.139)$$

The left hand side of Eq.1.138 can be evaluated using ψ_2^i from Eq.1.59 and the value of the three constants of integration, L_k, M_k and N_k, are needed. The constants L_k and M_k were calculated in Eq.1.60 and Eq.1.61. From the asymptotic matching L_k and M_k are known in terms of T_k and S_k, Eq.1.68 and Eq.1.69. Matching at one higher order determines N_k in terms

of T_k and S_k, then using Eq.1.68 and Eq.1.69, N_k can be written in terms of L_k and M_k giving

$$N_k = \left[\frac{(2-k)k}{2}L_k + \frac{(1-2k)}{2}\frac{M_k}{\delta}\right]\delta^2. \tag{1.140}$$

Using Eq. 1.138 leads to an equality for $\sum_{k=1}^{\infty} F_k\left(\int_{\mu}^{1} P_k(x)dx\right)$ at leading order, $O(1)$. As this must hold for all $\mu \in [-1,1]$, the coefficients of $\left(\int_{\mu}^{1} P_k(x)dx\right)$ must equate for each k, and thus this will give an equation for every F_k separately. Upon substitution of Eq.1.136 the equation for F_k at order δ reduces to

$$\begin{aligned}\frac{1}{\delta}F_k^{(\delta)} = &-\sum_{n=0}^{\infty}\sum_{m=1}^{\infty} a_{knm}\left[\frac{1}{2}\bar{V}_n V_m m(m+4+n)i + \sum_{j=1}^{\infty}\left(\frac{C_{nj}}{j+1}\right)\frac{1}{2}\bar{V}_m V_j mi\right]\\ &- V_0\bar{V}_k\frac{3ki}{(2k+1)} - \sum_{n=0}^{\infty}\sum_{m=1}^{\infty} g_{knm}\bar{V}_n V_m\frac{9ki}{2(2k+1)}\\ &+\sum_{n=1}^{\infty}\sum_{m=1}^{\infty} f_{knm}\bar{V}_n V_m\frac{3k(n+2)i}{2(2k+1)(n+1)(m+1)}\\ &+\sum_{n=0}^{\infty}\sum_{m=1}^{\infty}\frac{a_{knm}}{(2k+1)}\left[\bar{V}_n V_m\left(n^2-4nm-4n+m^2-m-3\right)mi\right.\\ &\left.+\sum_{j=1}^{\infty}\left(\frac{C_{nj}}{j+1}\right)V_m\bar{V}_j m(3m+5)i\right].\end{aligned} \tag{1.141}$$

Then substituting $F_k^{(\delta)}$ into Eq.1.77 and Eq.1.78 finally gives

$$\begin{aligned}T_k = \Re\Bigg\{&V_0\bar{V}_k\frac{(1-k^2)i}{(2k+1)} + \sum_{n=1}^{\infty}\sum_{m=1}^{\infty} f_{knm}\bar{V}_n V_m\frac{\left(k^2-k-1\right)(n+2)i}{2(2k+1)(n+1)(m+1)}\\ &+\sum_{n=0}^{\infty}\sum_{m=1}^{\infty} g_{knm}\bar{V}_n V_m\frac{3(1-k^2)i}{2(2k+1)} + \sum_{n=0}^{\infty}\sum_{m=1}^{\infty}\frac{a_{knm}}{2(2k+1)}\left[\bar{V}_n V_m\left(n^2-4nm-4n\right.\right.\\ &\left.\left.+m^2-m-3\right)im + \sum_{j=1}^{\infty}\left(\frac{C_{nj}}{j+1}\right)V_m\bar{V}_j m(3m+5)i\right]\Bigg\} + O(\delta),\end{aligned} \tag{1.142}$$

and

$$\begin{aligned}S_k = \Re\Bigg\{&V_0\bar{V}_k\frac{k(k+2)i}{(2k+1)} - \sum_{n=1}^{\infty}\sum_{m=1}^{\infty} f_{knm}\bar{V}_n V_m\frac{(2k+4)\,k(n+2)i}{4\,(2k+1)\,(n+1)(m+1)}\\ &+\sum_{n=0}^{\infty}\sum_{m=1}^{\infty} g_{knm}\bar{V}_n V_m\frac{3k(k+2)i}{2(2k+1)} - \sum_{n=0}^{\infty}\sum_{m=1}^{\infty}\frac{a_{knm}}{2(2k+1)}\left[\bar{V}_n V_m mi\left(n^2-4nm-4n\right.\right.\end{aligned}$$

$$+m^2-m-3)+\sum_{j=1}^{\infty}\left(\frac{C_{nj}}{j+1}\right)V_m\bar{V}_j m(3m+5)i\Bigg]\Bigg\}+O(\delta), \quad (1.143)$$

which with Eq.1.76 gives the value of all the constants in the streaming solution Eq.1.75.

1.14 Appendix B: In-phase streaming around a bubble

Notice, from the solution of the steady streaming around a bubble given in Appendix A (§1.13), that all terms in Eq.1.143, Eq.1.142 and Eq.1.76 are multiplies of $iV_m\bar{V}_k$ for some integers $m,k\geq 0$. As such Appendix A (§1.13) only gives the solution for out-of-phase motion of the bubble, as otherwise that solution is identically zero. Therefore, for these cases, the steady streaming needs to be calculated to the next order, namely $O(\delta)$.

Since here the analysis is to one higher order in δ this could require more stringent conditions than $\varepsilon\ll\delta\ll 1$ relationship. However, the order change is due to terms being identically zero, which we expect to continue at higher orders in ε so the same relationship should hold.

Inner-solution at third order in δ

In order to find the steady streaming at $O(\delta)$, the asymptotic matching must be carried out at one higher order. As such the inner second-order solution must be calculated to an extra order in δ. Therefore, more terms will be required in the δ expansions, so we first return to the second-order, inner governing equation

$$\frac{\delta^2}{2}\langle D^4\psi_2^i\rangle=\frac{1}{r^2}\left\langle\frac{\partial(\psi_1,D^2\psi_1)}{\partial(r,\mu)}+2L\psi_1 D\psi_1\right\rangle. \quad (1.144)$$

When expanding the left hand side in δ, the $O(1)$ terms in δ now contribute to the streaming as well as the $O(\delta^{-2})$ term so we have

$$\frac{\delta^2}{2}\langle D^4\psi_2^i\rangle=\frac{1}{2\delta^2}\frac{\partial^4\langle\psi_2^i\rangle}{\partial\eta^4}+(1-\mu^2)\frac{\partial^4\langle\psi_2^i\rangle}{\partial\eta^2\partial\mu^2}+O(\delta). \quad (1.145)$$

From Eq.1.59, the $O(1)$ (leading-order) solution of $\langle\psi_2^i\rangle$ is known. The second term in Eq.1.145 will only make an $O(1)$ or lower contribution from this term so the governing equa-

tion for the first three orders of $\langle \psi_2^i \rangle$ can be simplified to

$$\frac{\partial^4 \langle \psi_2^i \rangle}{\partial \eta^4} = \frac{2\delta^2}{r^2} \left\langle \frac{\partial(\psi_1, D^2\psi_1)}{\partial(r,\mu)} + 2L\psi_1 D\psi_1 \right\rangle + \delta^2 \sum_{k=1}^{\infty} \sum_{n=0}^{\infty} \sum_{m=1}^{\infty} a_{knm} \left[2\bar{V}_n (W_m + mV_m) k(k+1) e^{-(1+i)\eta} \right] \left(\int_\mu^1 P_k(x)dx \right) + O(\delta^3). \quad (1.146)$$

Expanding the term $\langle \partial(\psi_1, D^2\psi_1)/\partial(r,\mu) + 2L\psi_1 D\psi_1 \rangle$ to $O(\delta^2)$ and then substituting into Eq.1.146 gives an equation for $\langle \partial^4 \psi_2^i / \partial \eta^4 \rangle$, which can be integrated twice to find that the $O(\delta^2)$ (only) term in $\langle \partial^2 \psi_2^i / \partial \eta^2 \rangle$ is

$$\begin{aligned} \left\langle \frac{\partial^2 \psi_2^i}{\partial \eta^2} \right\rangle^{(\delta^2)} = \sum_{k=1}^{\infty} \sum_{n=0}^{\infty} \sum_{m=1}^{\infty} a_{knm} \Bigg\{ & -(\bar{W}_n + n\bar{V}_n) V_m m i \left(\frac{n}{2} - m - 3 \right) \\ & + (\bar{W}_n + n\bar{V}_n)(W_m + mV_m) \left(\frac{i}{2}(1 - m + n) - 2 - \frac{n}{2} \right) \\ & + \bar{V}_n (W_m + mV_m)\, i \left(-\frac{5n^2}{4} - \frac{21n}{4} + nm + m + \frac{m^2}{4} - 3 - t^2 - t \right) \\ & + \sum_{j=1}^{\infty} \left(\frac{C_{nj}}{j(j+1)} \right) \Bigg[(W_m + mV_m)(\bar{W}_j + j\bar{V}_j) \left(1 + i - \frac{m}{2} - \frac{ij}{2} + j \right) \\ & + (W_m + mV_m)\bar{V}_j i j (2j + 6 - m) \Bigg] \Bigg\} \int_\mu^1 P_k(x)dx. \quad (1.147) \end{aligned}$$

The $O(\delta^2)$ contribution to$\langle \psi_2^i \rangle$ can be calculated by integrating twice more but in order to satisfy the no tangential stress boundary condition only $\langle \partial^2 \psi_2^i / \partial \eta^2 \rangle$ is required at $O(\delta^2)$.

Notice that every term in $\langle \psi_2^i \rangle$ up to and including $O(1)$ is a multiple of $W_n + nV_n$ for some n so every term will drop an order when the first order stress condition $W_n = -nV_n + O(\delta)$ is applied. Similarly, higher-order terms in $\langle \psi_2^i \rangle$ will also be multiples of $W_n + nV_n$ since in $\langle \partial(\psi_1, D^2\psi_1)/\partial(r,\mu) + 2L\psi_1 D\psi_1 \rangle$ every term is a multiple of $B_n \propto (W_n + nV_n)$ and in $\langle D^4 \psi_2^i \rangle$ extra terms in its delta expansion will be in terms of lower orders of $\langle \psi_2^i \rangle$, which are also proportional to $W_n + nV_n$. Therefore, even when calculating the streaming to $O(\delta)$ for a bubble, only the first three terms up to $O(1)$ are needed in the equation for the inner streaming.

Constants of integration

The second order inner solution $\langle \psi_2^i \rangle$ is of the form

$$\langle \psi_2^i \rangle = \sum_{k=1}^{\infty} \left[f_k(\eta) + \delta g_k(\eta) + \delta^2 h_k(\eta) + L_k + M_k \eta + N_k \eta^2 + O(\delta^3) \right] \times \left(\int_\mu^1 P_k(x) dx \right), \quad (1.148)$$

where f and g are known from Eq.1.59 and h could be found by integrating Eq.1.147. The no-tangential stress boundary condition then gives

$$\left\langle (1-\mu^2) \frac{\partial^2 \psi_2^i}{\partial \mu^2} + 2 \frac{\partial \psi_2^i}{\partial r} - \frac{\partial^2 \psi_2^i}{\partial r^2} \right\rangle = \sum_{k=1}^{\infty} \left\{ -\frac{1}{\delta^2} \frac{\partial^2 f_k}{\partial \eta^2} + \frac{1}{\delta} \left(2 \frac{\partial f_k}{\partial \eta} - \frac{\partial^2 g_k}{\partial \eta^2} \right) + \left[-k(k+1) f_k(\eta) + 2 \frac{\partial g_k}{\partial \eta} - \frac{\partial^2 h_k}{\partial \eta^2} + 2 \frac{1}{\delta} M_k - 2 \frac{1}{\delta^2} N_k - k(k+1) L_k \right] \right\} \times \left(\int_\mu^1 P_k(x) dx \right). \quad (1.149)$$

The $O(\delta^{-2})$ terms will cancel with the $O(\delta^{-2})$ quantity in Eq.1.139. The $O(\delta^{-1})$ terms do not cancel exactly but when taking $W_n = -nV_n + O(\delta)$ (the first order bubble condition) they do. Therefore, the $O(1)$ terms will give the leading-order behaviour for which the value of the constants L_k, M_k and N_k are needed. The constants L_k and M_k were calculated in Eq.1.60 and Eq.1.61 and N_k can be written in terms of L_k and M_k, Eq.1.140.

Next, Eq.1.149 can then be equated with Eq.1.139 to give the algebraic condition for no tangential stress. This will give a condition on M_k and L_k but L_k is uniquely determined by the boundary condition: the radial velocity of the bubble equals the radial velocity of the fluid adjacent to the bubble. The constant M_k was also determined but is a function of the unknown F_k, which this no tangential stress condition will determine. However, F_k uniquely determines M_k so this equation can be considered as just determining M_k giving

$$\begin{aligned} -\frac{1}{\delta} M_k (2k+1) = -3L_k k + \sum_{n=0}^{\infty} \sum_{m=1}^{\infty} a_{knm} \Bigg(& \frac{1}{\delta} \Bigg\{ \frac{1}{2} (\bar{W}_n + n\bar{V}_n)(W_m + mV_m)(i-1) \\ & + \frac{1}{2} \bar{V}_n (W_m + mV_m)(1-i)(2n+3) + \sum_{j=1}^{\infty} \frac{C_{nj}}{j(j+1)} \Bigg[\frac{1}{2} (W_m + mV_m)(\bar{W}_j + j\bar{V}_j)(1+i) \\ & - (W_m + mV_m) \bar{V}_j j (1-i) - \frac{1}{2} W_m \left(\bar{W}_j + j\bar{V}_j \right) \frac{(1+i)}{j(j+1)} \Bigg] \Bigg\} + \\ & \Bigg\{ (\bar{W}_n + n\bar{V}_n) V_m \left(\frac{n}{2} - m - 2 \right) mi - \frac{1}{2} (\bar{W}_n + n\bar{V}_n)(W_m + mV_m)(in - im + n - 1) \\ & - \bar{V}_n (W_m + mV_m) i \left[-\frac{5n^2}{4} - \frac{9n}{4} + nm + \frac{m^2}{4} + 1 - \frac{3}{2} k(k+1) + \frac{1}{4} (2m^2 + 3m) \right] \end{aligned}$$

$$
\begin{aligned}
&-\frac{1}{2}\bar{V}_n W_m n(n+2)i+\frac{1}{2}\bar{W}_n W_m(n+2)i\\
&+\frac{1}{2}\bar{V}_n V_m m(m^2+2)i-\frac{1}{2}\bar{V}_n W_m(m+2)^2 i+2\bar{W}_n V_m m(m+1)i\\
&+\sum_{j=1}^{\infty}\frac{C_{nj}}{j(j+1)}\left[-(W_m+mV_m)(\bar{W}_j+j\bar{V}_j)\left(\frac{1}{2}(1+i)-\frac{1}{2}(m+ij)+j\right)-\right.\\
&\left.\left.(W_m+mV_m)\bar{V}_j ij(2j+4-m)-V_m\bar{W}_j m(m+1)i-\frac{1}{2}W_m\left(\bar{W}_j-j\bar{V}_j\right)\frac{(j+2)i}{j(j+1)}\right]\right)\\
&+O(\delta). \quad (1.150)
\end{aligned}
$$

When applying the first-order stress boundary condition of Eq.1.136, all terms drop by one order in δ. Then assuming the $O(1)$ terms cancel (which is required for the result in the first appendix of §1.13 not to give the solution) this gives M_k at $O(\delta)$. Then L_k can be calculated at $O(\delta)$ by applying Eq.1.34 at $O(\delta)$ to $\langle\psi_2^i\rangle$ of Eq.1.59. This gives

$$
\begin{aligned}
L_k=\delta\left\{\sum_{n=0}^{\infty}\sum_{m=1}^{\infty}\frac{1}{2}a_{knm}\bar{V}_n V_m m(m+2)(1+i)-\sum_{n=0}^{\infty}\sum_{m=0}^{\infty}\frac{1}{2}g_{knm}\bar{V}_n V_m m(m+2)(1+i)\right.\\
\left.+\sum_{n=1}^{\infty}\sum_{m=1}^{\infty}\frac{1}{2}f_{knm}\bar{V}_n V_m\frac{(n+2)(m+2)(1+i)}{(n+1)(m+1)}-\sum_{n=1}^{\infty}\sum_{m=1}^{\infty}\frac{1}{2}f_{knm}\bar{V}_n V_m\frac{(n+2)(1-i)}{(n+1)(m+1)}\right\}, \quad (1.151)
\end{aligned}
$$

and the simplified M_k expression

$$
\begin{aligned}
\frac{1}{\delta}M_k=L_k\left(\frac{3k}{2k+1}\right)-\delta\sum_{n=0}^{\infty}\sum_{m=1}^{\infty}\frac{a_{knm}}{(2k+1)}\left\{-\bar{V}_n V_m nm(n+2)\,(2m+1)\,(1-i)\right.\\
+\frac{1}{4}\bar{V}_n V_m\left(n^2+9n-5m^2+6t(t+1)-5m\right)(1+i)m(m+2)\\
\left.+\sum_{j=1}^{\infty}\left(\frac{C_{nj}}{j(j+1)}\right)V_m\bar{V}_j mj\left[(m+1)(j+2)(1-i)-(m+2)(j+4)(1+i)\right]\right\}. \quad (1.152)
\end{aligned}
$$

Outer streaming constants

Using the matching conditions Eq.1.71 and 1.72 gives

$$
T_k=\delta\Re\left(\sum_{n=1}^{\infty}\sum_{m=1}^{\infty}f_{knm}\bar{V}_n V_m\frac{(1-k^2)(n+2)\left[(m+2)(1+i)-(1-i)\right]}{2(2k+1)(n+1)(m+1)}\right.
$$

$$
\begin{aligned}
&-\sum_{n=0}^{\infty}\sum_{m=0}^{\infty} g_{knm}\bar{V}_n V_m \frac{(1-k^2)m(m+2)(1+i)}{2(2k+1)} \\
&+\sum_{n=0}^{\infty}\sum_{m=1}^{\infty} \frac{a_{knm}}{2(2k+1)}\left\{\frac{1}{4}\bar{V}_n V_m\left(n^2+9n-5m^2-5m+4\right.\right. \\
&\left.+2k^2+6k\right)(1+i)m(m+2)-\bar{V}_n V_m n(n+2)m(2m+1)(1-i) \\
&\left.\left.+\sum_{j=1}^{\infty}\left(\frac{C_{nj}}{j+1}\right)V_m\bar{V}_j\left[m(m+1)(j+2)(1-i)-m(m+2)(j+4)(1+i)\right]\right\}\right), \quad (1.153)
\end{aligned}
$$

and

$$
\begin{aligned}
S_k = \delta\Re\Bigg(&\sum_{n=1}^{\infty}\sum_{m=1}^{\infty} f_{knm}\bar{V}_n V_m \frac{k(k+2)(n+2)\left[(m+2)(1+i)-(1-i)\right]}{2(n+1)(m+1)(2k+1)} - \\
&\sum_{n=0}^{\infty}\sum_{m=0}^{\infty} g_{knm}\bar{V}_n V_m \frac{m(m+2)k(k+2)(1+i)}{2(2k+1)} + \sum_{n=0}^{\infty}\sum_{m=1}^{\infty}\frac{a_{knm}}{2(2k+1)}\left\{-\frac{1}{4}\bar{V}_n V_m m(m+2)\right. \\
&\times\left[n^2+9n\ -5m^2-5m+2k(k-1)\right](1+i)+\bar{V}_n V_m n(n+2)m(2m+1)(1-i) \\
&\left.\left.-\sum_{j=1}^{\infty}\left(\frac{C_{nj}}{j+1}\right)V_m\bar{V}_j\left[m(m+1)(j+2)(1-i)-m(m+2)(j+4)(1+i)\right]\right\}\Bigg), \quad (1.154)
\end{aligned}
$$

which, with $Y_{knm}=0$, give the value of all the constants in the Lagrangian streaming solution of Eq.1.75.

Chapter 2

Resonances and streaming of an armoured microbubble

The main results presented in this chapter have been published in: "Bubble-based acoustic micro-swimmers", Nicolas Bertin, Tamsin A. Spelman, Olivier Stephan, Laetitia Gredy, Michel Bouriau, Eric Lauga and Philippe Marmottant, Physical Review Applied, 4:064012, 2015 [48] (copyright 2015 by the American Physical Society). The work on double and triple multipropulsors is included in our published paper: "Bubble-based acoustic micropropulsors: active surfaces and mixers", Nicolas Bertin, Tamsin A. Spelman, Thomas Combriat, Hervé Hue, Olivier Stéphan, Eric Lauga and Philippe Marmottant, Lab on a Chip, 17:1515-1528 , 2017 [66] (adapted by permission of the Royal Society of Chemistry).

This chapter focuses on studying the Armoured Microbubble (AMB) built by our experimental collaborators Nicolas Bertin and Philippe Marmottant, based at the University Grenoble Alpes, studying its resonances and streaming flow. We will first give details of the experiments in §2.1, then discuss the resonances of the AMB in §2.2. We then use the streaming model from Chapter 1 to calculate the streaming flow around the AMB in §2.3 and finally look at the streaming flow and resonances of multipropulsor compounds in §2.4.

2.1 Experiments

An AMB is a hollow partial sphere inside which a microbubble can be caught, see Fig.2.1a. Therefore, the surface of the device is mostly solid with a spherical bubble cap. Under ultrasound forcing, the spherical bubble cap oscillates applying a net force to the surrounding fluid, which generates a streaming flow in the fluid.

The capsule is constructed using two-photon polymerisation, attached to a wall by a tower of height H, see Fig.2.1a. If the AMB is being used for free-swimming, it can then be disattached from the tower. When a liquid is poured over the capsule, an air bubble can become trapped inside. In deionised water the AMB lasted approximately 15 min without ultrasound and 1 min under ultrasound forcing. Thus, experiments were conducted in $25 - wt\%\ NaCl$ solution, which increased the life-span of the AMBs to hours. (It was also later discovered that salianising the capsule improved bubble lifespan.)

The minimum shell thickness a capsule can be fabricated with is approximately $0.5\,\mu$m. However, we generally used capsules with shell thicknesses of $1\,\mu$m, for the additional strength provided by the thicker shell. The standard experimental AMB had a radius $a = 9 - 10\,\mu$m and aperture opening $b = 5\,\mu$m. These dimensions can be changed but these sizes were experimentally found to be good for bubble life-span. In the extreme when b/a becomes too large the bubble either never becomes trapped or escape very quickly.

The streaming flow around the AMB was experimentally observed by tracking the motion of $2\,\mu$m spherical particles in the flow using a Phantom v2511 high-speed camera. We assume the paths of the tracer particles are the streamlines of the flow, but we note that the tracer particle has a non-zero size so due to the interactions between themselves and the AMB or the wall when they are close, the tracer particle paths will not perfectly match the streamlines of the flow. You observe this effect when tracer particles become stuck on the AMB surface, particularly on the bubble interface. However, in the bulk of the flow, we expect these effects to be small due to the small size of the tracer particles. In theoretical calculations, Faxon's corrections can be used to calculate corrections to the particle velocity due to interactions with a nearby sphere or wall. Also, this disparity between particle paths and streamlines can be used to sort particles based on their size, such as in the work of Thameem et. al. [67], but their particles were much larger than our tracer particles with diameters of $5\,\mu$m and $10\,\mu$m.

Experimental ease and accuracy were increased by keeping the AMB attached to its tower of height $H = 10\,\mu$m, $20\,\mu$m or $30\,\mu$m. For these experiments the AMB was forced at an ultrasound frequency close to its resonance frequency, as the AMB only generates significant streaming at a driving frequency close to its resonance. For an AMB on a $H = 30\,\mu$m tower (where wall effects are minimal) the AMB generates a streaming pattern with flow being pulled in from behind and then pushed away in a strong jet in front of the orifice, see Fig.2.1b. When separated from the tower, the net force causing the strong jet propels the AMB.

Our aim was to model these experiments in order to validate and better physically understand the observed behaviour of the AMB, focusing particularly on their generated streaming flow and resonances.

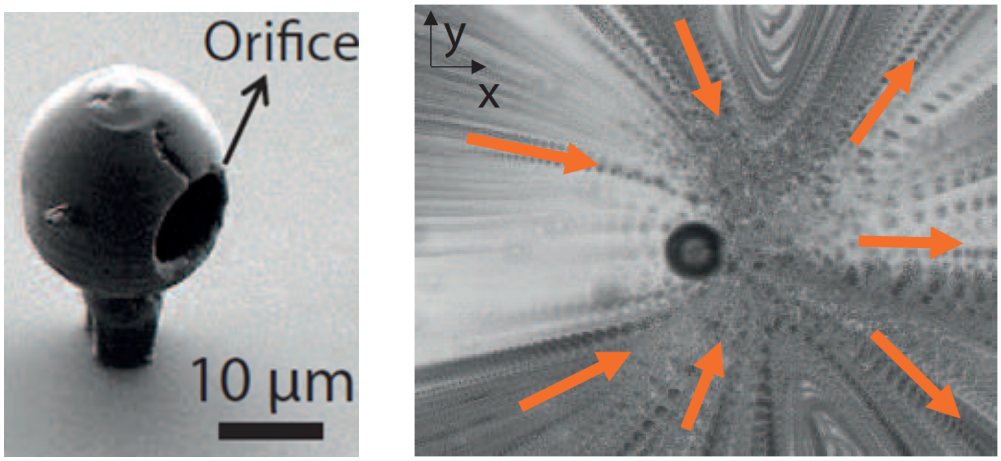

(a) A scanning-electron-microscopy image of the AMB.

(b) Streaming around the AMB with $H = 30\,\mu m$.

Figure 2.1: The Armoured Microbubble (by Nicolas Bertin)

2.2 Resonant modes

In this section, using a potential flow model, we will calculate the resonant modes of the AMB by applying mixed boundary conditions and solving the resulting eigenvalue problem. Our potential model will apply boundary conditions at the surface and in the far-field, thus assuming the validity of the model throughout the entire space, in contrast to our streaming analysis, which has a boundary layer and is performed in the limit as the size of the boundary layer tends to zero. Additionally, due to parameter limits, angular boundary conditions cannot be captured by the potential model. However, we expect the potential model to provide a good approximation to the resonances, since we focus on behaviour close to the AMB surface, and expect the radial surface motion to be most significant. We will specifically consider these modes for the preferred experimental AMB with inner radius $a = 10\,\mu$m and opening radius $b = 5\,\mu$m.

Before performing that analysis, we will estimate the importance of the surface tension forces and the volume forces using a scaling argument, to determine which is dominant. In an isentropic scenario, $P_1/P_2 = (V_1/V_2)^\kappa$ for P_1 and P_2 pressures at two stages of the oscillation; V_1 and V_2 the associated volumes and $\kappa = 1.4$ is the adiabatic index (in this chapter). Thus, assuming P_2 and V_2 are small perturbations of their respective quantities when the AMB is at

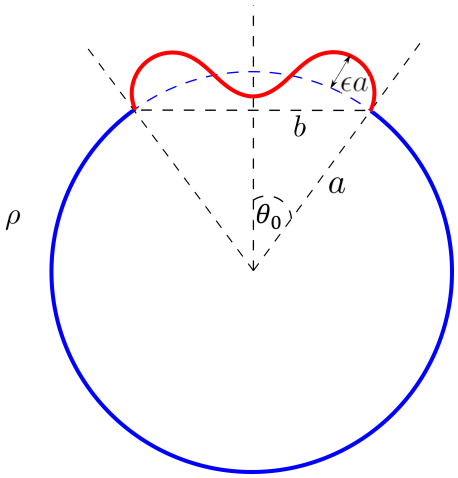

Figure 2.2: Setup for calculating the resonances of the AMB

rest, Taylor expanding gives the change in pressure as

$$\delta P \sim \frac{\kappa(\delta V)P_0}{V} \sim \frac{\kappa(\frac{\pi}{2}b^2\varepsilon a)P_0}{\frac{4}{3}\pi a^3}, \tag{2.1}$$

where δP is the change in pressure from the rest state to the perturbed state, δV the equivalent change in volume, V the volume of the capsule and P_0 atmospheric pressure. We can estimate the pressure change coming from the surface tension as

$$\delta P \sim \frac{2\pi\gamma(\varepsilon a)}{\pi b^2}. \tag{2.2}$$

Inserting values for our experimental AMB gives the pressure from the surface tension as being approximately four times bigger than that from the change in volume. (The basis of this analysis was done by our collaborators and details of it are included in [48].)

2.2.1 Setup

We will use a spherical coordinate system centred on the AMB with radial coordinate r and azimuthal angle θ. This setup is shown in Fig.2.2. The AMB is modelled as a axisymmetric spherical body, where for azimuthal angles $\theta \geq \theta_0$ the body has a solid stationary surface but for $\theta < \theta_0$ the body has a free surface. We assume the AMB thickness is negligible and take the AMB radius as a and the radius of the capsule opening as b, so $b = a\sin\theta_0$. We assume that the fluid density of the air inside the spherical body is negligible relative to the liquid outside the body where the density is ρ. The surface tension of the fluid-fluid interface is γ. We

are looking to identify the resonances so the AMB will be oscillating at the resonant angular frequency ω, which is the dominant time scale to the problem. The resonance frequency f is then $f = \omega/2\pi$. We assume small amplitude oscillations and thus that $\varepsilon \ll 1$ (where εa is the amplitude of oscillation as in Chapter 1).

2.2.2 Governing equations

As with the classical Lamb calculation for the resonances around a bubble [68], we assume the flow is potential so our governing equation is

$$\nabla^2 \phi = 0, \tag{2.3}$$

where ϕ is a velocity potential, with a spherical axisymmetric solution of the form

$$\phi(r,\theta) = \sum_{n=0}^{\infty} \left(a_n r^n + b_n r^{-(n+1)} \right) P_n(\cos(\theta)). \tag{2.4}$$

The spherical body undergoes small amplitude oscillations so the surface's radial position R is of the form

$$R = a\left(1 - \varepsilon i \sum_{n=0}^{\infty} V_n P_n(\cos(\theta)) e^{i\omega t}\right), \tag{2.5}$$

where V_n are constants to be determined. As the Legendre polynomials are an orthogonal basis this incorporates all axisymmetric oscillatory surface motions.

There are three boundary conditions for the problem. Firstly, that the radial motion of the fluid matches the radial motion of the body's surface (at leading order in ε)

$$\frac{\partial \phi}{\partial r} = \frac{\partial R}{\partial t} \text{ at } r = a. \tag{2.6}$$

Secondly, that the system has finite energy

$$\phi \to 0 \text{ as } r \to \infty. \tag{2.7}$$

Finally there are the mixed boundary conditions: in $\theta < \theta_0$ the normal surface stress is balanced by surface tension (at leading order in ε)

$$\left[\underline{n} \cdot \underline{\underline{\sigma}} \cdot \underline{n}\right]_-^+ = \gamma(\nabla \cdot \underline{n}) \text{ at } r = a \text{ when } 0 \leq \theta < \theta_0, \tag{2.8}$$

and when $\theta \geq \theta_0$ the body's surface does not move (at leading order in ε)

$$\frac{\partial \phi}{\partial r} = 0 \text{ at } r = a \text{ when } \theta_0 \leq \theta \leq \pi. \tag{2.9}$$

Applying the boundary conditions in Eq.2.6 and Eq.2.7 reduces Eq.2.4 to

$$\phi = -\varepsilon \sum_{n=0}^{\infty} \frac{a^2 \omega V_n}{(n+1)} \left(\frac{a}{r}\right)^{n+1} P_n(\mu) e^{i\omega t}. \tag{2.10}$$

Then applying the mixed boundary conditions of Eq.2.8 and Eq.2.9 to Eq.2.10 gives the eigenvalue equations of

$$\begin{cases} \sum_{n=0}^{\infty} iV_n P_n(\mu) e^{i\omega t} \left[\frac{\Omega}{(n+1)} - (n-1)(n+2)\right] = 0 & \text{when } 0 \leq \theta < \theta_0, \\ \sum_{n=0}^{\infty} V_n P_n(\mu) e^{i\omega t} = 0 & \text{when } \theta_0 \leq \theta \leq \pi, \end{cases} \tag{2.11}$$

where Ω is the non-dimensional quantity $\Omega = \rho a^3 \omega^2 / \gamma$, which are the eigenvalues we aim to determine (to determine the resonance angular frequencies ω).

Using the same method as used for some other Legendre polynomial mixed boundary value problems [69] , by using the integral form of the Legendre polynomial these equations can be simplified to

$$\begin{cases} \sum_{n=0}^{\infty} V_n \cos\left[(n+\frac{1}{2})\theta\right] \left[\frac{\Omega}{(n+1)} - (n-1)(n+2)\right] = 0 & \text{when } 0 \leq \theta < \theta_0, \\ -\sum_{n=0}^{\infty} V_n \frac{1}{(2n+1)} \cos\left[(n+\frac{1}{2})\theta\right] = 0 & \text{when } \theta_0 \leq \theta \leq \pi. \end{cases} \tag{2.12}$$

This system cannot be solved analytically so a numerical approach will be taken.

2.2.3 Solving numerically

Numerically Eq.2.12 can be solved by taking the inner product (multiplying by $\cos\left((m+\frac{1}{2})\theta\right)$ for $\forall m$) and integrating over θ. Rearranging, then reduces this to the generalised eigenvalue equation.

$$A_{mn} V_n = \Omega B_{mn} V_n, \tag{2.13}$$

with

$$A_{m+1,n+1} = \begin{cases} \frac{\left((n-1)(n+2)+\frac{1}{2n+1}\right)}{2}\left[\frac{\sin((n+m+1)\theta_0)}{(n+m+1)}+\frac{\sin((n-m)\theta_0)}{(n-m)}\right] & \text{if } n \neq m, \\ \frac{\left((n-1)(n+2)+\frac{1}{2n+1}\right)}{2}\left[\frac{\sin((n+m+1)\theta_0)}{(n+m+1)}+\theta_0\right]-\frac{\pi}{2(2n+1)} & \text{if } n = m, \end{cases} \tag{2.14}$$

$$B_{m+1,n+1} = \begin{cases} \frac{1}{2(n+1)}\left(\frac{\sin((n+m+1)\theta_0)}{(n+m+1)}+\frac{\sin((n-m)\theta_0)}{(n-m)}\right) & \text{if } n \neq m, \\ \frac{1}{2(n+1)}\left(\frac{\sin((n+m+1)\theta_0)}{(n+m+1)}+\theta_0\right) & \text{if } n = m, \end{cases} \tag{2.15}$$

where our eigenvalues are Ω.

This is a system of infinitely many equations in infinitely many unknowns so to solve numerically it needs to be truncated. However, information is lost in truncation. But $\theta = \theta_0$ is an important angle as it marks the sharp change from no motion to the free surface moving cap, so it is useful to retain information about this point. Therefore, when this system is truncated at size N the highest order resonance equation (the N^{th} equation) will be replaced with the condition of no motion at $\theta = \theta_0$

$$\sum_{n=0}^{N} V_n P_n(\cos(\theta_0) = 0. \tag{2.16}$$

This finite generalised eigenvalue problem will then be solved numerically using the *QZ* algorithm through Matlab's eig function, which uses the LAPACK library routine ZGGEV.

2.2.4 Resonant frequency and mode shape

For the experimental AMB $\theta_0 = 0.52$ radians, which we use throughout this subsection.

2.2.4.1 Convergence of eigenvalues and eigenvectors

As N is increased the eigenvalues converge. As seen in Fig.2.3a for the first eigenvalue this convergence is smooth and consistent, although for larger eigenvalues larger truncation sizes are necessary to obtain an accurate estimate.

The eigenvector convergence is shown in Fig.2.3b. Here v_N is the N^{th} eigenvector. The quantity $|1 - v_N \cdot v_{N+1}|$ is analysed for increasing N, since $|1 - v_N \cdot v_{N+1}|$ tends to zero as the eigenvectors converge and become parallel. There is a power law convergence giving $|1 - v_N \cdot v_{N+1}| \sim N^{-1.7}$. Therefore, this convergence is slow but consistent. Looking at the mode shapes (see Fig.2.5) there is slow convergence near $\theta = \pi$ and $\theta = \theta_0$.

The rate of convergence changes depending on θ_0, with slower convergence at smaller

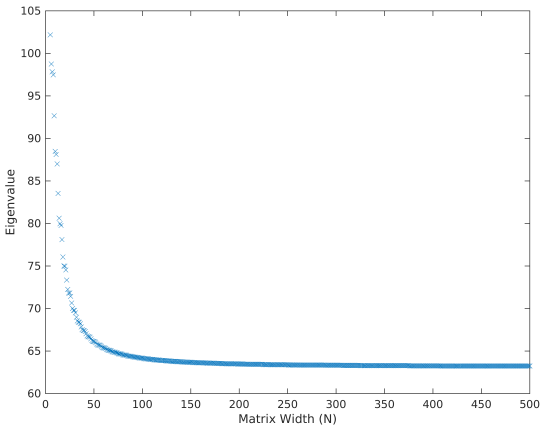

(a) Convergence of the smallest eigenvalue with truncation size

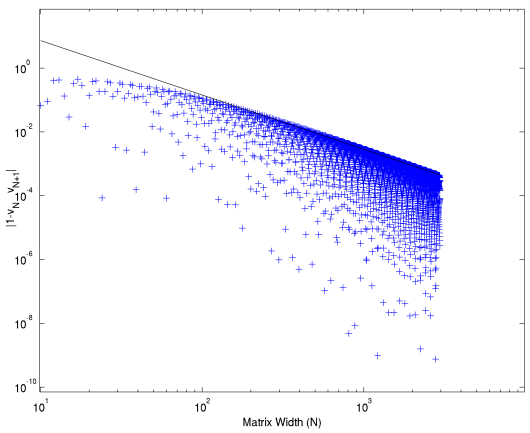

(b) Log-log convergence of the first eigenvector. Numerical results are $+$. An analytic power law fit of the local maxima for $N > 100$ is the solid straight line with a gradient of -1.704

Figure 2.3: Convergence of the first eigenvalue and eigenvector

values of θ_0 (see Fig.2.4). However, even for $\theta_0 = 0.1$ the first eigenvalue has converged to at least one significant figure by $N = 500$.

2.2.4.2 Mode Shapes

The non-dimensional eigenvalues for $\theta_0 = 0.52$ are obtained numerically to be $\Omega = 63.2$, 987, 4060, 10600, 21800, 39100.

For the experiments $\rho = 10^3\,\mathrm{kgm}^{-3}$, $\gamma = 69.7 \times 10^{-3}\,\mathrm{Nm}^{-1}$ and $a = 10 \times 10^{-6}\,\mathrm{m}$ and as $f = \sqrt{\Omega\gamma/\rho a^3}/2\pi$, this gives the first six resonance frequencies as $f = 334\,\mathrm{kHz}$, 1320 kHz, 2680 kHz, 4330 kHz 6200 kHz, 8310 kHz with the mode shapes displayed in Fig.2.5.

The first resonance frequency of 334 kHz agrees well with the experimentally identified resonance of 320 kHz, giving a 4% error.

2.2.4.3 Range of θ_0

We will now analyse the eigenvalue dependence on the size of the capsule opening, θ_0. The correlation for the four smallest eigenvalues are shown in Fig.2.6a. As θ_0 increases away from 0, the eigenvalues decrease, initially very rapidly away from infinity. This rate of decrease lessens sharply until very close to $\theta_0 = \pi$ where it becomes steeper again. These larger gradi-

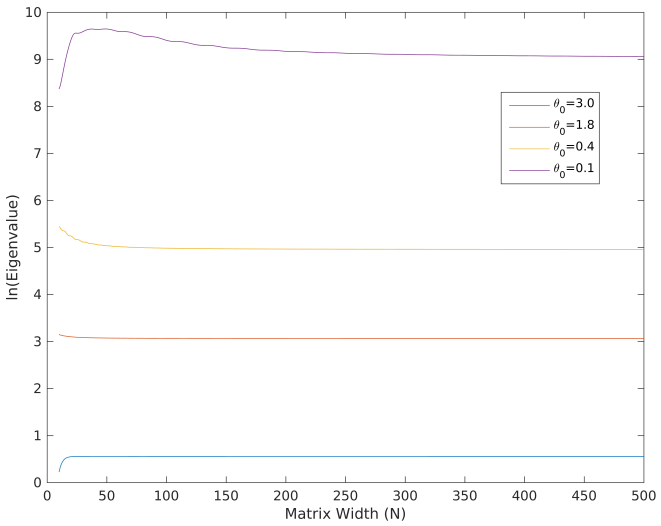

Figure 2.4: Convergence of the first eigenvalue with θ_0.

ents near the two extremes can be physically explained as the results are tending towards the resonances at the two limits of a completely solid surface and a complete bubble, but these are physically quite different systems to our mixed boundary system.

Fitting a curve of the form $\Omega = A/\theta_0^k$ indicates a good correction in Fig.2.6a . The log-log plot in Fig.2.6b indicates $\Omega \sim \theta_0^{-3}$ is an accurate scaling. The log-log plot in Fig.2.7 indicates the coefficient A scales with mode number n such that $A \sim n^3$. Therefore,

$$f \sim \left(\frac{n^3 \gamma}{\rho a^3 \theta_0^3} \right)^{\frac{1}{2}}. \tag{2.17}$$

2.3 Streaming around AMBs

In this section, we will calculate the streaming flow around the AMB using our model from Chapter 1. For this we need to know the surface motion of the AMB. The motion in §2.2 provides the radial motion of the surface near each resonant mode but this can be improved by applying our mixed boundary conditions directly to our streaming model from Chapter 1 to additionally obtain the angular surface motion. We will then compare the numerically obtained streaming flow to experiments and consider the effects of a nearby wall.

(a) 334 kHz (b) 1320 kHz

(c) 2680 kHz (d) 4330 kHz

(e) 6200 kHz (f) 8310 kHz

Figure 2.5: First six resonant mode shapes of the AMB. Blue marks the solid capsule and the red the bubble's free surface. The radial lines mark the edge of the cap at an angle $\theta_0 = 0.52$ from the axis of symmetry.

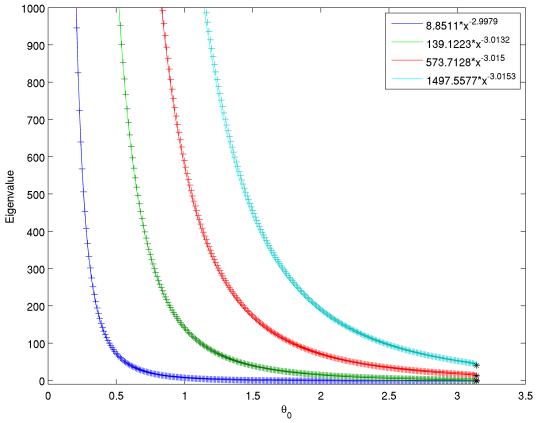

(a) The lowest four eigenvalues and the lines of best fit for a relation to θ_0 fitted for $\theta_0 \leq \frac{\pi}{2}$

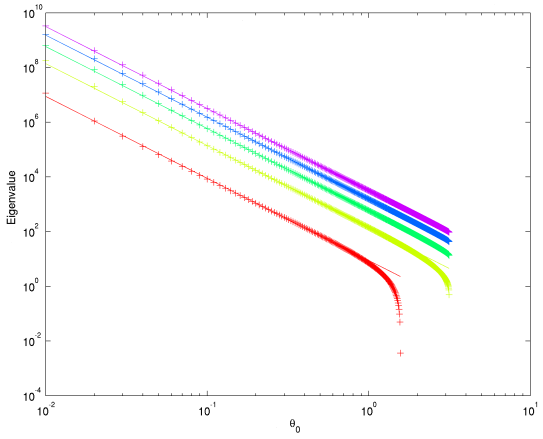

(b) Displaying the fit for $\Omega \sim \theta_0^{-3}$ for the first five eigenvalues. Numerical results are in $+$. The straight line was the line of best fit for $\theta_0 < \pi/4$ for the smallest eigenvalue and $\theta_0 < \pi/2$ for the remainder eigenvalues. Each colour refers to a different eigenvalue.

Figure 2.6: Analysing the dependence of the non-dimensional eigenvalue Ω with θ_0

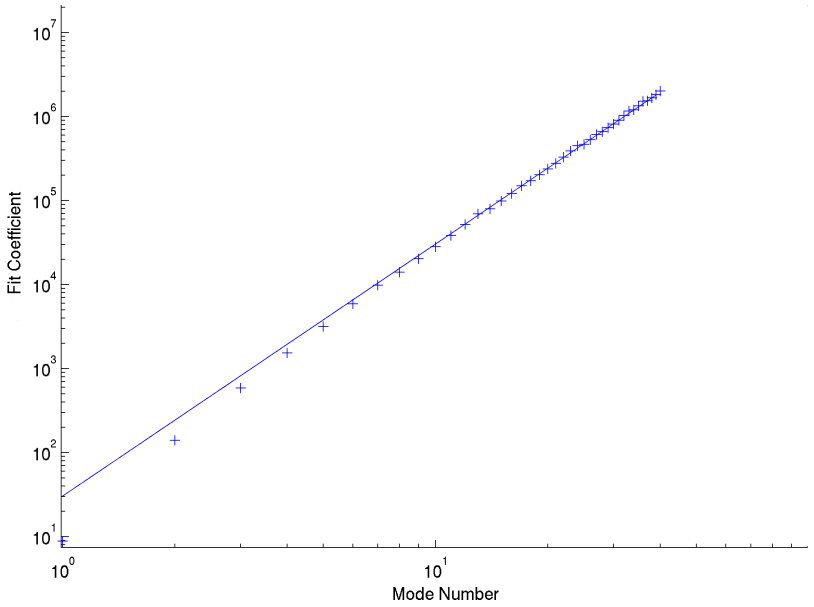

Figure 2.7: Coefficient A with increasing mode number n. Numerical results are $+$. The theoretical line is fitted for mode numbers > 10 with a gradient of 3.

2.3.1 Viscous approximation of the surface motion of the AMB

Our two radial boundary conditions are the same as for the resonant modes: normal stress balanced by surface tension on the bubble cap (when $\theta < \theta_0$) and the radial velocity zero on the solid shell (when $\theta \geq \theta_0$)

$$\underline{n} \cdot \underline{\underline{\sigma}} \cdot \underline{n} = \gamma(\nabla \cdot \underline{n}) \text{ for } \theta < \theta_0, \tag{2.18}$$

$$u_r = 0 \text{ for } \theta \geq \theta_0. \tag{2.19}$$

An external pressure forcing is included inside Eq.2.18. However, now that we are using our viscous streaming model, we can also apply the angular boundary conditions: no tangential stress on the bubble cap (when $\theta < \theta_0$) and no angular velocity on the solid shell (when $\theta \geq \theta_0$)

$$\underline{n} \times \underline{\underline{\sigma}} \cdot \underline{n} = 0 \text{ for } \theta < \theta_0, \tag{2.20}$$

$$u_\theta = 0 \text{ for } \theta \geq \theta_0. \tag{2.21}$$

These conditions are all applied on the surface of the AMB at $r = R$.

2.3.1.1 Pressure field

In order to calculate the radial stress in Eq.2.18 the pressure field needs to be evaluated in terms of the boundary constants V_n and W_n.

The non-dimensional Navier-Stokes equation is

$$\left(\frac{\partial \underline{u}}{\partial t}\right) + \varepsilon\left(\underline{u} \cdot \nabla \underline{u}\right) = \frac{p}{\rho a U \omega}\left(-\nabla p\right) + \frac{\delta^2}{2}\left(\nabla^2 \underline{u}\right). \tag{2.22}$$

Pressure p can either scale with the viscosity or the time dependent inertia but inertia is important close to the AMB.

We evaluate the r and θ component of Eq.2.22 at leading order in ε using our solution for ψ_1 in Eq.1.28. There is significant cancellation of terms so at $O(\varepsilon)$ this gives

$$p = e^{it}\left(\sum_{n=0}^{\infty} P_n(\mu)\left(\frac{iD_n}{(n+1)r^{n+1}}\right)\right) + f(\theta), \tag{2.23}$$

for $f(\theta)$ an unknown function of θ. Then similarly evaluating the θ component of Eq.2.22 gives $f(\theta)$ as a constant, which must be zero.

2.3.1.2 Radial boundary conditions

The two radial boundary conditions can now be written in terms of the constants V_n and W_n. Using Eq.1.28 for ψ_1 (and hence u_r) reduces the radial boundary condition (see Eq.2.18) to

$$\sum_{n=0}^{\infty} V_n P_n(\mu) = 0. \tag{2.24}$$

To apply the boundary condition in Eq. 2.19 we require the direction of the normal away from the AMB, which is calculated using the radial position of the AMB surface R given in Eq 1.12 . Then $\underline{n} = \nabla(r-R)$ and thus the non-dimensional surface curvature is

$$\nabla \cdot \underline{n} = 2 - \sum_{n=0}^{\infty} \varepsilon(n-1)(n+2)V_n P_n(\mu) e^{i(t+\frac{\pi}{2})} + O(\varepsilon^2). \tag{2.25}$$

Using Eq. 2.23 (with $f = 0$) and Eq. 1.28 the LHS of Eq. 2.19 can be evaluated since in the fluid

$$\underline{n} \cdot \underline{\underline{\sigma}} \cdot \underline{n} = -p + 2\frac{\partial u_r}{\partial r} + O(\varepsilon^2). \tag{2.26}$$

The external ultrasound pressure forcing is included through a $\Delta p e^{it}$ forcing term. Therefore, at $O(\varepsilon)$ we obtain

$$\sum_{n=0}^{\infty} P_n(\mu) \left(-\delta^2 \frac{3B_n}{2\alpha^2} K_{n+\frac{1}{2}}(\alpha r) + \delta^2 \frac{B_n}{\alpha} K'_{n+\frac{1}{2}}(\alpha r) - \delta^2 (n+2) D_n - \frac{iD_n}{(n+1)} \right) + \Delta p = -\frac{\gamma}{\rho a^3 \omega^2} \sum_{n=0}^{\infty} i(n-1)(n+2)V_n P_n(\mu), \tag{2.27}$$

which, upon Taylor expansion, gives the leading order behaviour in δ as

$$\sum_{n=0}^{\infty} P_n(\mu) \left(\frac{i}{(n+1)} V_n \right) - \Delta p = \frac{\gamma}{\rho a^3 \omega^2} \sum_{n=0}^{\infty} i(n-1)(n+2)V_n P_n(\mu). \tag{2.28}$$

2.3.1.3 Angular boundary conditions

Similar to the previous subsection, using Eq.1.28 reduces Eq.2.21 to

$$-\sum_{n\in\mathbb{N}} W_n \frac{\int_\mu^1 P_n(x)dx}{(1-\mu^2)^{\frac{1}{2}}} = 0. \tag{2.29}$$

The tangential stress condition of Eq. 2.20 reduces at $O(\varepsilon)$ to $\sigma_{r\theta} = 0$, which (at leading order in δ) gives

$$\sum_{n\in\mathbb{N}} (W_n + nV_n)\left(\frac{2i}{1+i}\right)\left(\frac{\int_\mu^1 P_n(x)dx}{(1-\mu^2)^{\frac{1}{2}}}\right) = 0. \tag{2.30}$$

2.3.1.4 Leading-order surface conditions

Therefore, having the same non-dimensional quantity as before of $\Omega = \rho a^3\omega^2/\gamma$ at leading order in δ we have

$$\sum_{n=0}^{\infty} V_n P_n(\mu) = 0 \text{ on } \theta_0 \le \theta \le \pi, \tag{2.31}$$

$$\sum_{n=0}^{\infty} V_n \left(\frac{i}{(n+1)} - \frac{1}{\Omega} i(n-1)(n+2)\right) P_n(\mu) = \Delta p, \text{ on } 0 \le \theta < \theta_0, \tag{2.32}$$

$$-\sum_{n\in\mathbb{N}} W_n \left[\frac{P_n^1(\mu)}{n(n+1)}\right] = 0, \text{ on } \theta_0 \le \theta \le \pi, \tag{2.33}$$

$$\sum_{n\in\mathbb{N}} (W_n + nV_n)\frac{2i}{(1+i)}\left[\frac{P_n^1(\mu)}{n(n+1)}\right] = 0. \text{ on } 0 \le \theta < \theta_0. \tag{2.34}$$

To solve these equations, the first pair of equations can be solved for V_n, which then provides the forcing for the second pair of equations to solve for W_n. We can multiply Eq.2.34 through by $(1+i)/2i$ to reduce it to a real equation. Similarly we can multiply Eq.2.32 through by $-i$ which gathers the complex part, physically the phase change, into the pressure forcing term Δp. Since the only effect of this is on the phase of the pressure forcing, which is arbitrary, the phase of the pressure forcing can be adapted so that the quantity is real. We note this suggests the response is then $\pi/2$ out of phase with the pressure forcing but this is not the case as a $\pi/2$ phase difference is included in the definition of the radial position R in Chapter 1 (which we used here). This then reduces the system to a set of real equations. This therefore implies that out-of-phase surface motion is not a leading order effect, and will also not effect the steady streaming.

Thus our equations reduce to the real pair of equations to solve for the radial motion

$$\begin{cases} \sum_{n=0}^{\infty} V_n P_n(\mu) = 0 & \text{on } \theta_0 \leq \theta \leq \pi, \\ \sum_{n=0}^{\infty} V_n \left(\frac{1}{(n+1)} - \frac{1}{\Omega}(n-1)(n+2) \right) P_n(\mu) = \Delta p & \text{on } 0 \leq \theta < \theta_0, \end{cases} \tag{2.35}$$

and the real pair of equations to solve for the angular motion

$$\begin{cases} -\sum_{n=1}^{\infty} W_n \left[\frac{P_n^1(\mu)}{n(n+1)} \right] = 0 & \text{on } \theta_0 \leq \theta \leq \pi, \\ \sum_{n=1}^{\infty} (W_n + nV_n) \left[\frac{P_n^1(\mu)}{n(n+1)} \right] = 0 & \text{on } 0 \leq \theta < \theta_0. \end{cases} \tag{2.36}$$

2.3.1.5 Radial surface motion

This radial motion is solved from Eq.2.35, similarly to with the resonant modes, by taking inner products and then truncating a size N, then many numerical routines exist to solve a finite series of $N+1$ linear equations in $N+1$ unknowns.

The constant Ω was calculated for the experimental parameter of $f = 320\,\text{kHz}$ (giving ω through $\omega = 2\pi f$), $\gamma = 69.7 \times 10^{-3}\,\text{Nm}^{-1}$ $\rho = 10^3\,\text{kgm}^{-3}$ and $a = 9 \times 10^{-6}\,\text{m}$. We took the non-dimensional change in pressure as $\Delta p = 1$. Numerically this non-dimensional value only effects the amplitude of the oscillation, not the shape of the oscillation. Thus, the same shape will be obtained whatever value Δp takes, and once the shape has been obtained, the coefficients can be scaled to give the appropriate amplitude.

The predicted radial surface motion for this forcing is shown in Fig.2.8a. As expected it is a very similar shape to the first resonant mode predicted by the potential model shown in Fig.2.5a. For a fixed maximum number of modes N we observe $|V_n|$ oscillates in size as $n \to N$ but its amplitude of oscillation decreases on the order of $n^{-1.5}$. This justifies the accuracy of truncating our system at N coefficients. Similarly, the quantity $\left| 1 - V^{(N)} \cdot V^{(N+1)} \right| \to 0$ as $N \to \infty$, with its amplitude decaying like $N^{-2.4}$, which indicates convergence (where here $V^{(N)}$ indicates the predicted radial modes V of length N). We also note this is faster than the eigenvalue solution of our potential model converged in § 2.2.4.1.

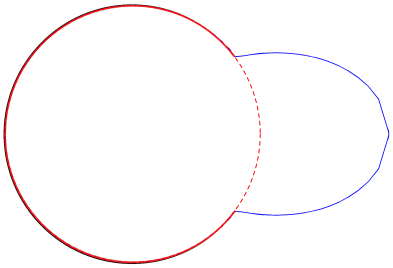

(a) Shape of the radial oscillation.

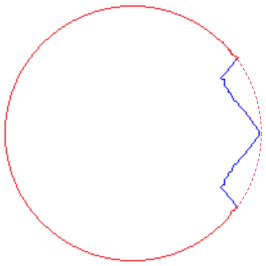

(b) u_θ on the spherical body. The amplitude away from the rest position $r = 1$ indicates the relative strength and direction of u_θ.

Figure 2.8: Surface motion of the AMB. The solid line gives the surface shape, with red indicating the solid capsule surface and blue the bubble surface The red dotted line indicates the rest position of the AMB.

2.3.1.6 Angular surface motion

The angular motion can now be solved using Eq. (2.36). Similar to before, taking the inner product of Eq. (2.36) reduces to a set of linear equations

$$\left(\frac{2}{2n+1}\right) W_n \delta_{nm} = -\sum_{n=1}^{\infty} V_n \left[\frac{\int_{\cos(\theta_0)}^{1} P_n^1(\mu) P_m^1(\mu)}{(n+1)}\right] \quad \forall m, \tag{2.37}$$

where again we solve numerically by truncating the sum at $n = N$ and consider equations up to $m = N$.

This gives the angular motion indicated in Fig. 2.8b. Here we do not observe a decrease in $|W_n|$but instead $\frac{|W_n|}{n}$oscillates as $n \to N$ with the amplitude of oscillation decreasing on the order of $n^{-0.6}$. Since W_n is a cofactor of $P_n^1(\mu)/[n(n+1)]$ this still corresponds to larger coefficients having a smaller impact on the surface angular velocity and hence the steady streaming, justifying the accuracy of truncating our system at N coefficients. Similar to V we observe that $\left|1 - W^{(N)} \cdot W^{(N+1)}\right| \to 0$, with its amplitude decaying like $N^{-0.9}$, as $N \to \infty$. The order of convergence of $\frac{|W_n|}{n}$ is thus lower than V_n and similarly $\left|1 - W^{(N)} \cdot W^{(N+1)}\right|$ decays more slowly than $\left|1 - V^{(N)} \cdot V^{(N+1)}\right|$.

2.3.2 Streaming around the AMB

Now that we have both the angular and radial motions on the AMB surface, we will calculate the acoustic streaming of $O(\varepsilon^2)$.

2.3.2.1 Second-order boundary conditions

When using this model to study the streaming generated by a bubble we obtained an $O(1)$ in δ steady streaming, which was a result of the $O(\delta^{-2})$ and $O(\delta^{-1})$ terms cancelling out when calculating F_k (or equivalently the matching coefficients M_k) . But here, because of the mixed boundary conditions, this does not occur. The $O(\delta^{-2})$ terms still cancel but the $O(\delta^{-1})$ term does not.

Here we will refer to determining the matching coefficient M_k, which is equivalent to calculating F_k as the two are dependent on each other, but we note that the explanations in Chapter 1 were performed using F_k. As the $O(\delta^{-1})$ term does not cancel,when applying the boundary conditions the motion is dominated by the value of M_k where it obeys the mixed boundary conditions

$$\begin{aligned}\sum_{k=1}^{\infty}(2k+1)\left(\frac{M_k}{\delta}\right)\frac{\left(\int_\mu^1 P_k(x)dx\right)}{(1-\mu^2)^{\frac{1}{2}}} = -\sum_{k=1}^{\infty}\sum_{n=0}^{\infty}\sum_{m=1}^{\infty}a_{knm}\left(\frac{1}{\delta}\left\{(W_m+mV_m)(\bar{W}_n+n\bar{V}_n)\frac{(i-1)}{2}\right.\right.\\ +(W_m+mV_m)\frac{\bar{V}_n}{2}(1-i)(2n+3)+\sum_{j=1}^{\infty}\left(\frac{C_{nj}}{j(j+1)}\right)\left[(\bar{W}_j+j\bar{V}_j)(W_m+mV_m)\frac{(1+i)}{2}\right.\\ \left.\left.\left.-(W_m+mV_m)\bar{V}_j j(1-i)-\frac{W_m\left(\bar{W}_j+j\bar{V}_j\right)(1+i)}{2j(j+1)}\right]\right\}\frac{\left(\int_\mu^1 P_k(x)dx\right)}{(1-\mu^2)^{\frac{1}{2}}} \quad \text{for } 0\le\theta<\theta_0,\end{aligned} \tag{2.38}$$

and

$$\sum_{k=1}^{\infty}\left(\frac{M_k}{\delta}\right)\frac{\left(\int_\mu^1 P_k(x)dx\right)}{(1-\mu^2)^{\frac{1}{2}}}=0 \quad \text{for } \theta_0\le\theta\le\pi. \tag{2.39}$$

This is one order higher than L_k and other streaming terms, and as such this value will dominate the streaming flow. At leading order in δ, this means $S_k=-T_k=M_k/2\delta$ so our streaming is of the simpler form

$$\langle\psi_L\rangle = S_k\sum_{k=1}^{\infty}\left(r^{-(k-2)}-r^{-k}\right)\left(\int_\mu^1 P_k(x)dx\right). \tag{2.40}$$

The pair of equations for M_k can be transferred to associated Legendre polynomials and then

by taking the inner product with $P_m^1(x)$ this gives the set of linear equations

$$\sum_{k=1}^{\infty} M_k \delta_{kq} \left(\frac{2}{2k+1}\right) + \sum_{k=1}^{\infty} (2k) M_k \frac{1}{k(k+1)} \left[\int_{cos(\theta_0)}^{1} P_k^1(\mu) P_q^1(\mu) d\mu\right]$$
$$= -\sum_{k=1}^{\infty}\sum_{n=0}^{\infty}\sum_{m=1}^{\infty} a_{knm} \left(\left\{ (W_m + mV_m)(\bar{W}_n + n\bar{V}_n) \frac{(i-1)}{2} \right.\right.$$
$$+ (W_m + mV_m)\frac{\bar{V}_n}{2}(1-i)(2n+3) + \sum_{j=1}^{\infty}\left(\frac{C_{nj}}{j(j+1)}\right)\left[(\bar{W}_j + j\bar{V}_j)(W_m + mV_m)\frac{(1+i)}{2}\right.$$
$$\left.\left.\left. -(W_m + mV_m)\bar{V}_j j(1-i) - \frac{W_m\left(\bar{W}_j + j\bar{V}_j\right)(1+i)}{2j(j+1)}\right]\right\} \frac{\left[\int_{cos(\theta_0)}^{1} P_k^1(\mu) P_q^1(\mu) d\mu\right]}{k(k+1)} \quad \forall q. \quad (2.41)$$

Similar to first order, this is truncated at $k = K$ and $q = K$ to give K equations to find the first K coefficients M_k. The constants are then used to calculate S_k and T_k, which gives the acoustic streaming flow shown in Fig. 2.9. We observed 5 coefficients for M_k were sufficient to display the main features of the streaming flow.

2.3.2.2 Streaming around a single AMB

We have now calculated the numerical streaming flow around a single, stationary AMB in free space, which is shown in Fig. 2.9. The flow shows fluid being pulled in towards the AMB slowly from behind and the sides, and then pushed away from the AMB at the front, where the aperture opening is located, in the form of a strong jet. Small circulations are also visible close to the AMB.

We next compare this numerical model to the experimental streaming flow for an AMB held on a $H = 30\,\mu$m tower, where we focus the microscope on a plane parallel to the wall and through the centre of the AMB. This experimental streaming flow is shown in Fig. 2.9. The experimental streaming image is obtained by stacking the frames of a video showing the motion of the $2\,\mu$m tracer particles when the AMB is forced under ultrasound. Here we see flow being pulled in from a wide region behind the AMB and pushed out in a wide region in front of the AMB.

The overall flow shape of the numerical and experimental streaming patterns agree. However, there are differences. Circulations close to the AMB are only seen numerically, which is likely due to errors in the numerical model since neglected higher order terms make a greater contribution close to the AMB. The exact shape of the jet also differs slightly. This additional difference could be attributed to the tower and tracer particles impacting the experimental flow or the neglecting of higher order terms in the numerical flow. Nevertheless the good overall agreement in flow shape indicates that wall effects are small for a tower of height $H = 30\,\mu$m.

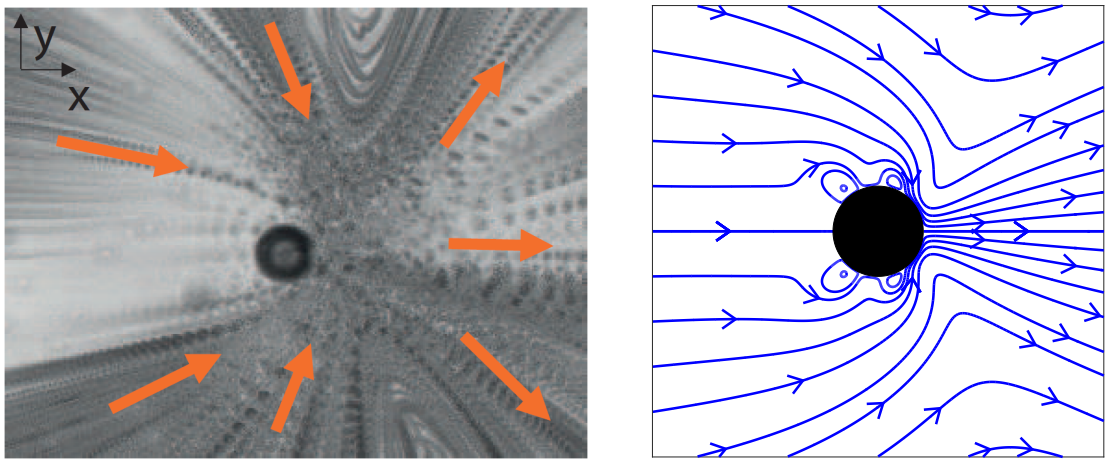

(a) Experimental Streaming (by Nicolas Bertin) (b) Numerical Streaming

Figure 2.9: Comparing numerical and experimental streaming around an AMB

Indeed, this is supported by the fact that if we include leading order wall effects in our numerical model (see §2.3.3) for a tower of height $H = 30\,\mu$m there were minimal changes to the numerical streaming pattern.

2.3.3 AMB near a Wall

For towers of height of $H = 30\,\mu$m the effect of the wall on the flow was small, however, we expect wall effects to be more significant for smaller towers of heights $H = 10\,\mu$m and $H = 20\,\mu$m. This is reflected by changes in the experimental streaming patterns for these lower heights. At $H = 20\,\mu$m small circulations have started to appear behind the AMB (see Fig. 2.10a). The general flow shape is otherwise similar to $H = 30\,\mu$m although the shape of the bend in the flow as it moves from behind the capsule to in front is sharper. At $H = 10\,\mu$m a very different flow field has been established with two circulations in front of the AMB and two behind, although the strong jet at the capsule opening, seen at larger tower heights, is still visible (Fig. 2.11a). Comparing the sharp clear flow fields of $H = 30\,\mu$m and $H = 10\,\mu$m, to that of $H = 20\,\mu$m we see that the $H = 20\,\mu$m flow has flow features that are similar to those observed at $H = 30\,\mu$m, such as flow being pulled around the AMB with a sharp jet but no circulations at the front, and, more weakly, similar to those observed at $H = 10\,\mu$m, such as an area of back flow behind the AMB. This giving the impression that at $H = 20\,\mu$m the flow is in a transitional state between these two flow fields.

We incorporated the wall computationally by adding the image system for the leading-order Stokeslet flow decaying as $1/r$ [70] and next order Stresslet decaying as $1/r^2$ [71], which both have well known image systems. This wall approximation will become less accurate very close to the wall since the $1/r^3$ and higher order terms are then relevant. The computational flow for a $20\,\mu$m tower is similar to that with no wall, although the circulations behind the AMB are slightly larger (see Fig. 2.10b). However, for $H = 10\mu$m we see significant changes in the flow computationally (see Fig. 2.11b). Two large circulations have formed out the front of the AMB, and behind the AMB there are small circulations still but with the flow being bent more strongly behind the AMB.

Comparing the computational and experimental flow fields for a $H = 20\,\mu$m tower, we see the overall shape of the flow fields are very similar, with flow being pulled in from behind and pushed out in a strong jet in front. The small pair of circulations seen behind the AMB experimentally is seen numerically, however, more circulations are seen numerically, and given these circulations were present numerically when there was no wall it is unlikely the numerical and computational cause are the same. Also there is a definite change experimentally in the flow field from a $30\,\mu$m to a $20\,\mu$m tower, but numerically the flow fields at these two wall heights are more similar. For $H = 10\,\mu m$, the pair of circulations near the opening of the AMB are seen numerically and computational. This is a very significant flow feature given that the flow velocities are largest here, in front of the capsule opening. However, the flow behind the capsule does not agree computationally and experimentally, with a large pair of circulations seen only experimentally. One explanation for this is that the flow velocities are low here and thus the higher order terms neglected in our numerical model are more significant behind the capsule than in front. Thus, for $10\,\mu$m tower, there is agreement between the computational model and experiments for the flow field at the front of the AMB, near the opening, but disagreement in flow shape behind the AMB.

When the tower height is $0\,\mu$m, so the AMB is sitting on the wall, our computational wall approximation becomes invalid but experimentally there are also problems with tracer beads getting stuck. As such towers of lower than $10\,\mu$m have not been studied.

2.4 Combining AMBs

Up until this point only single AMBs have been studied. We will now consider combinations of AMBs first by considering two multipropulsor compounds (created by attaching together equally sized AMBs) and then briefly discussing combining different sized AMBs to build a

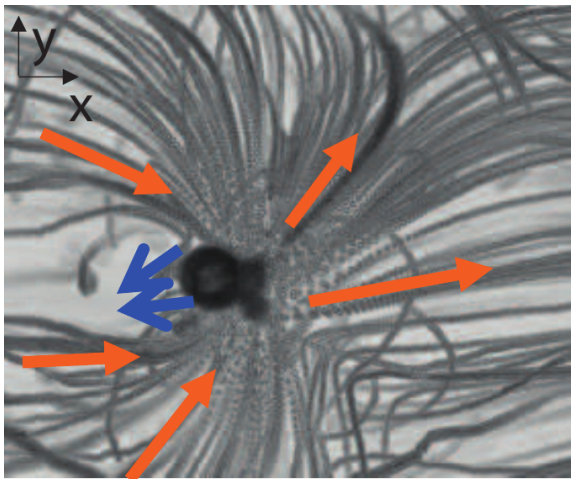

(a) Experimental Streaming (by Nicolas Bertin)

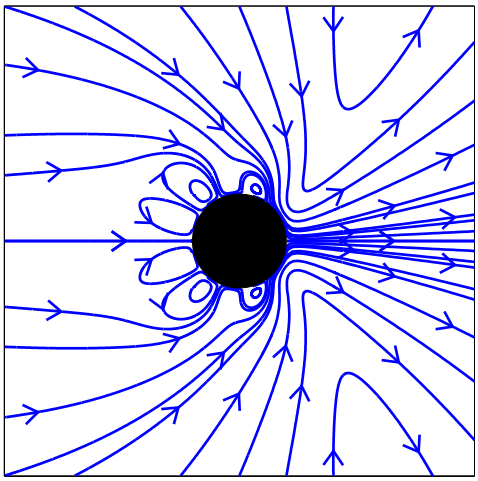

(b) Numerical Streaming

Figure 2.10: Comparing numerical and experimental streaming around an AMB with a $H = 20\,\mu$m tower

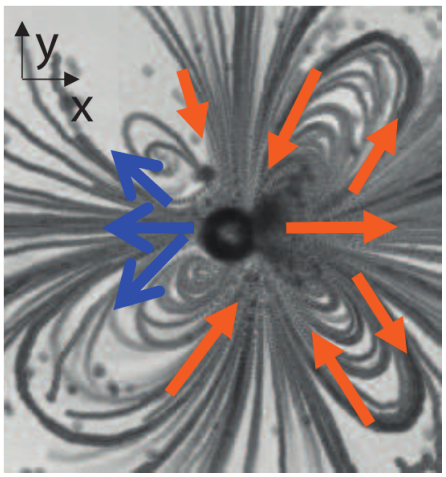

(a) Experimental Streaming (by Nicolas Bertin)

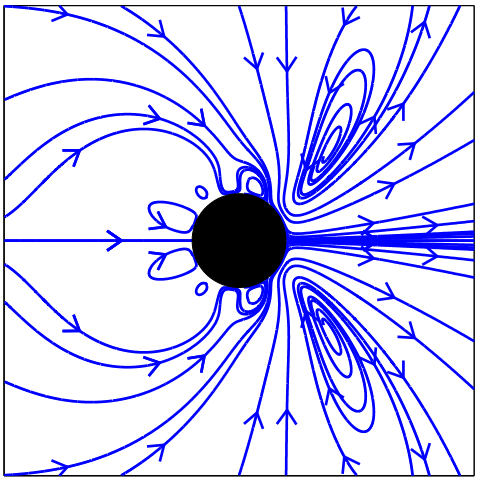

(b) Numerical Streaming

Figure 2.11: Comparing numerical and experimental streaming around an AMB with a $H = 10\,\mu$m tower

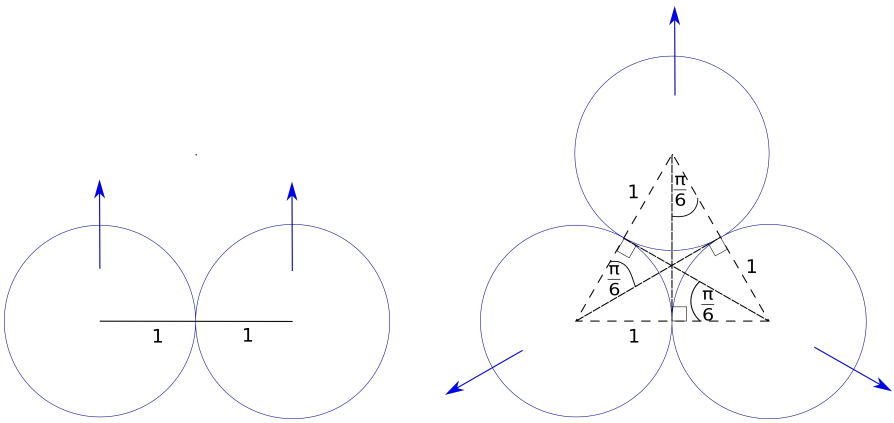

(a) Double AMBs (b) Triple AMBs

Figure 2.12: Set up of double and triple capsule configurations. Blue arrows indicate the direction of the aperture opening.

multi-directional swimmer.

2.4.1 AMB Compounds

Experimental work has been conducted studying pairs and triples of AMBs (see Fig.2.12) and the streaming flow they generate in the surrounding fluid (Fig.2.13a and 2.14a respectively). Double propulsors consist of two AMBS attached to each other, built on the same tower, with their aperture opening pointing in the same direction perpendicular to the line joining their centres (see Fig.2.12a). Triple propulsors consist of three capsules arrayed in a triangle with aperture openings pointing outwards at 0^o, 120^o and 240^o from each other (see Fig. 2.12b). The constituent parts of both setups are standard capsules of inner radius $a = 9\,\mu$m and aperture opening $b = 5\,\mu$m.

To model these multipropulsors compounds we use our previous model describing the streaming flow around one AMB (see §2.3). We note that applying a rotation or translation to our original flow field generated by one AMB gives the streaming around an AMB at any position and orientation. To approximate the flow field around the double and triple propulsors, we linearly superpose the flow fields generated by each AMB individually. However, this introduces errors since we are superposing individual solutions, which only obey the boundary conditions on their own AMB, and thus the resulting streaming flow approximation is not valid close to where the AMBs meet. In the external Stokes flow, adding two solutions obeying the same boundary conditions will produce a third solution, however within the boundary layer convective inertia is important so in the boundary layer using linear superposing to obtain new

solutions does not work. Within the boundary layer there are additional contributions to the flow field, beyond linear superposition, from the flow of one AMB affecting the boundary layer of a different AMB. This in turn will affect the boundary layer matching conditions and the external Stokes flow, thus providing additional contributions to the flow field beyond linear superposition, which is not accounted for by our method.

Additional errors are added close to the AMBs due to the importance of inertia in the boundary layer close to the AMBs. But outside the boundary layer the streaming flow is a Stokes flow and so a short distance from the AMBs our approximation is valid.

The comparisons of experimental and numerical streamlines for the double AMB is shown in Fig.2.13. Experimentally the double propulsors showed a pair of circulations in front of the opening and a pair of circulations behind, similar to a single AMB on a $10\,\mu$m tower. However, the jet in front of the aperture openings is wider than the jet seen for a single AMB. All the double AMBs in Fig. 2.13a show the circulations in front of the opening, but the circulations behind the AMB are not always clear due to the slower velocities behind the AMB and the positioning of the tracer beads. This experimental streaming flow compares well to the numerical streaming flow in front of the double AMB, where the wide jet and frontal circulations are seen numerically. However, behind the AMB no pair of circulations are observed numerically, in disagreement with experiments. This was unsurprising as our model for a single AMB also did not capture this feature of circulations behind the AMB.

The comparison between experiments and numerics for the triple AMB is shown in Fig. 2.14. Experimentally, the triple propulsor shows three pairs of circulations around itself, with each capsule opening having one pair of AMBs, one circulation on either side of a strong jet. Not all the circulations are the same size, which could be attributed to small variation in the hole strengths due to tracer particles becoming stuck near the capsule openings. This experimental flow agrees well with the numerical streamlines, which show six pairs of circulations (although all equally sized) with a strong jet in front of each opening. The better agreement can be attributed to the flow behind the AMBs having a smaller overall effect on the flow field, and this was the portion of flow the numerics modelled badly

2.4.2 Multidirectional swimmer

The AMBs free swim when detached from their tower. This was studied experimentally (by our collaborators). Initially there were issues with the AMBs sinking to the bottom of the tank or floating to the top. This was dealt with by attaching the AMB to a ring on a tower.

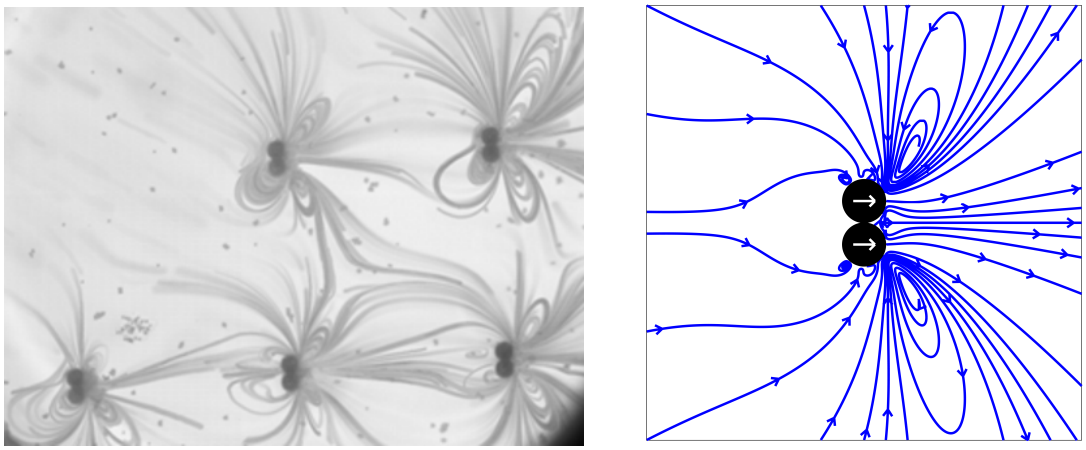

(a) Experimental results (by Nicolas Bertin). (b) Computational prediction.

Figure 2.13: Flow field around the double AMB configuration

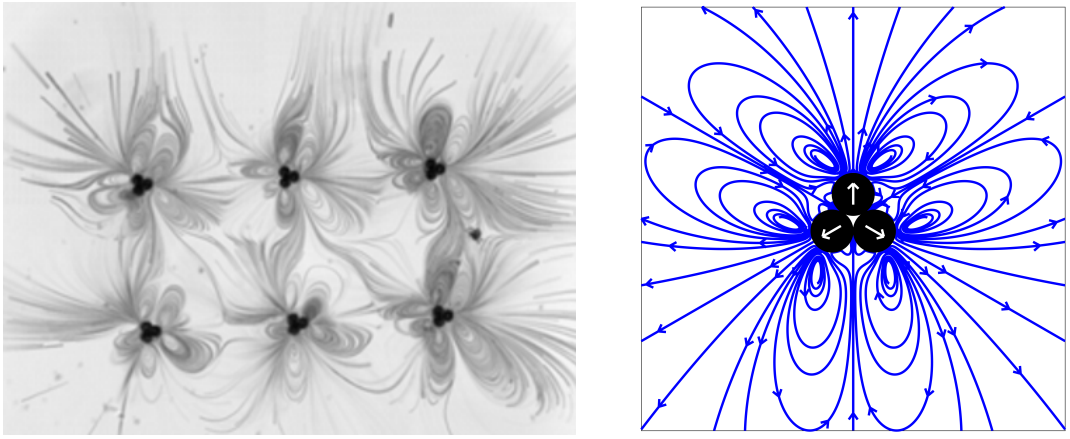

(a) Experimental results (by Nicolas Bertin) (b) Computational prediction

Figure 2.14: Flow field around the triple AMB configuration

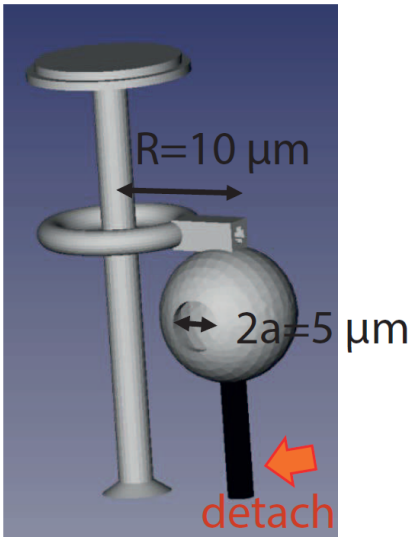

(a) AMB on the ring/tower setup for circular swimming

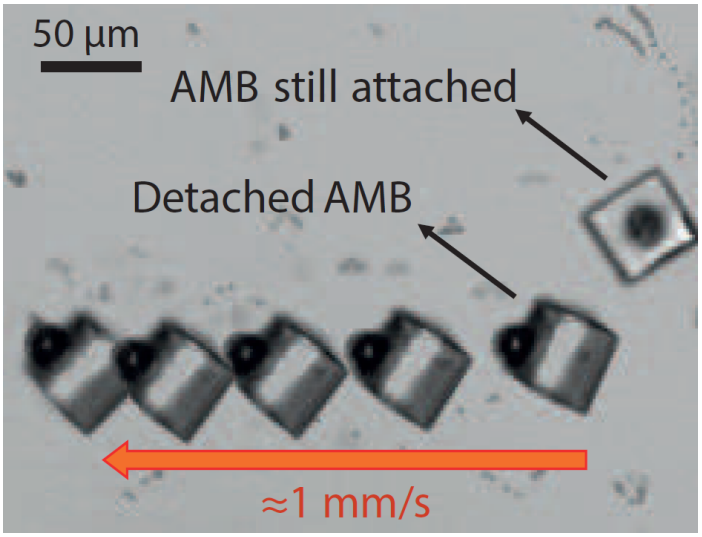

(b) Free swimming AMB with additional weight for buoyancy and stability

Figure 2.15: Free swimming AMB (by Nicolas Bertin)

The AMB then swims around the tower at a constant distance maintained by the ring, and the "hat" on the tower stopped the AMB from floating away (Fig.2.15a). Using this setup the force generated by the AMBs was estimated, but due to friction with the tower this is believed to be an underestimate. Free-swimming was later demonstrated by attaching the AMB to a $40\,\mu\text{m} \times 40\,\mu\text{m} \times 30\,\mu\text{m}$ cuboid so it was neutrally buoyant (Fig.2.15b).

Experiments then moved to building multidirectional swimmers from AMBs of different sizes by containing AMBs in different sides of a cuboid (Fig.2.16). Upon applying an ultrasound field, a significant response is generated only by the AMBs (if any) whose resonance is close to the frequency of the ultrasound field, pushing the device away from the active AMB. As such AMBs with sufficiently separated resonances were required so they could be be separately activated.

For this purpose, additional sizes of AMBs were studied, two in particular. Both had radius $a = 9\,\mu\text{m}$ with an aperture opening radius of $b = 7.5\,\mu\text{m}$ and $b = 3\,\mu\text{m}$. We can use our AMB resonance model from §2.2 to predict the resonances for these cases under the same physical conditions. For $b = 7.5\,\mu\text{m}$ our resonance model predicts the first resonance at 133 kHz , whereas it has an experimentally observed resonance frequency of 160 kHz. This gives a higher error than for our standard capsule size of 17%. However, as the aperture opening gets larger our approximation of a spherical rest position becomes less accurate.

For the $b = 3\,\mu\text{m}$ capsule our resonance model predicts 725 kHz whereas the experimental

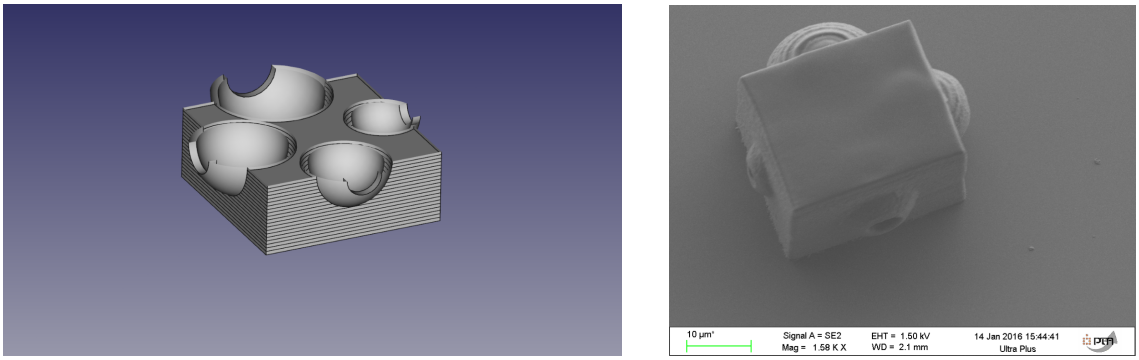

(a) Schematic (b) Actual Swimmer

Figure 2.16: Multidirectional Swimmer created by combining AMBs (by Nicolas Bertin)

resonance was 510 kHz, which is a percentage error of 42%. This large error can be explained by noticing that for small openings, slight changes in θ_0 have large effects on the resonance (as seen in Fig.2.6a). To illustrate, for $b = 5\,\mu$m if the AMB radius a is increased from $a = 9\,\mu$m to $a = 10\,\mu$m the difference in resonance is of the order of 10 kHz, whereas the difference in resonance between an AMB of size $b = 2.8\,\mu$m and $a = 8.8\,\mu$m compared to one of size $b = 3.2\,\mu$m and $a = 9.2\,\mu$m is of the order of 200 kHz. Therefore, a numerically sensitive resonance combined with small experimental inaccuracies could account for differences in the experimental and theoretical results.

2.5 Conclusion

For the AMB, we have determined the resonance frequency dependence on the aperture opening size, $f \sim \theta_0^3$, and found the exact resonances. For the preferred experimental AMB size the theoretical prediction of 334 kHz was in good agreement with experiments. Applying mixed boundary conditions, to our streaming model introduced in Chapter 1 we calculated the streaming around the experimental AMB in free space, predicting the strong frontal jet in good agreement with experiments. By adding the two leading-order images for the wall and linearly superposing the effects of multiple AMBs we accurately calculated: the frontal circulations generated close to a wall; the wider jet produced by double propulsors and the three pairs of circulations produced by triple propulsors.

Chapter 3

Streaming flows around AMB arrays

The main results from this chapter are included in our published paper: "Bubble-based acoustic micropropulsors: active surfaces and mixers", Nicolas Bertin, Tamsin A. Spelman, Thomas Combriat, Hervé Hue, Olivier Stéphan, Eric Lauga and Philippe Marmottant, Lab on a Chip, 17:1515-1528 , 2017 [66] (adapted by permission of the Royal Society of Chemistry).

In this chapter we will study the flow fields generated by Armoured Microbubbles (AMBs), introduced in Chapter 2, placed in a pattern short distances apart, inside a confined channel. We are interested in such arrays as they generate large collective flows, which can be used for mixing, although their mixing potential is not considered in this chapter. In §3.1 we introduce the experimental setup and experimentally studied AMB arrays, which we will focus our theoretical analysis on. We will first consider the effect of the confined channel by analysing the L-array when just one wall is present (§3.2) before extending this analysis to two walls in §3.3, and discussing the effects of the additional wall. In §3.4 we will use this two wall numerical model to discuss the numerical flow fields generated by the five experimental arrays and how they change as the relative strength of the AMBs is decreased, comparing to experimental results. In §3.5 we will briefly discuss how our results validate our estimate of the AMB strength.

3.1 Experimental arrays

Our experimental collaborators Nicolas Bertin and Philippe Marmottant constructed a microchannel with an AMB array printed on its base. To do this, they first printed an array of AMBs, each on $10\,\mu$m poles, onto a glass coverslip, which they drew marker lines on. The microchannel was then placed on top after plasma treatment. Plasma treatment is a technique used to change the surface properties of a material. Here it is used to change the polydimethylsiloxane (PDMS) channel from a hydrophobic to a hydrophilic material, which prevents

bubbles becoming stuck on the surface of the channel and interfering with the fluid flow. The channel cross section was 80 μm in height and 1 mm in width (although 0.5 mm wide channels were also considered experimentally only). The channel had a Y shaped entrance (Fig.3.1). This allows fluid dyed different colours to enter from the two entrances so this setup can be used for microfluidic mixing (although this use is not discussed further in this chapter). This size of channel is not expected to cause any cell streaming as the observed resonant frequencies in other microchannels are on the order of megahertz [72], whereas these experiments used a driving frequency of 350 kHz. Additionally, significant cell streaming would have been noticeable experimentally when ultrasound was applied to the channel and any AMBs contained no air. A driving frequency of 350 kHz corresponds to an ultrasound wavelength of 4.2 mm, four times the width of the channel. The acoustic beam width is the same order of magnitude as the wavelength. Thus, multiple AMBs in the channel can be actuated by our generated ultrasound wave. A different experimental setup of a circular tank with one or two confining walls was also used for the L-array only to observe the effects of confinement on the flow field.

For the microchannel experiments, the ultrasound was produced by a focussed transducer. The voltage applied to the transducer was steadily increased and this corresponds to a rise in the acoustic pressure. A separate experiment was performed with a hydrophone inside a ring of PDMS, where the PDMS thickness was similar to that of the microchannel, so the loss of pressure from transmitting sound through water to PDMS to PBS could be determined. This experiment measured P_{ac} and thus determined the relationship between the driving voltage and the acoustic pressure, so comparison to driving pressure rather than voltage could be made in the results.

Experimentally, they studied five AMB configurations in detail (see Fig.3.2): a L , a V, a straight line perpendicular to the flow, a short line parallel to the base flow with half the AMBs pointing in opposite directions and a diagonal line with half of the AMBs pointing in opposite direction. The AMBs are in general separated by gaps of 50 μm centre-to-centre. The exception is for the two arrays where half the AMBs point in different directions, then between the two AMBs where the direction changes the gap is 100 μm centre-to-centre. The AMBs have an inner radius of 9 μm and are 1 μm thick so have an outer radius of 10 μm.

It was experimentally observed that these AMB arrays produce large collective flows, such as for the L-array shown in Fig.3.3. Here the L-array is positioned closer to one of the side walls than the L-array design in Fig. 3.2, where the L-array is centred in the middle of the channel. The confining effects caused by both walls has the largest impact on the flow but

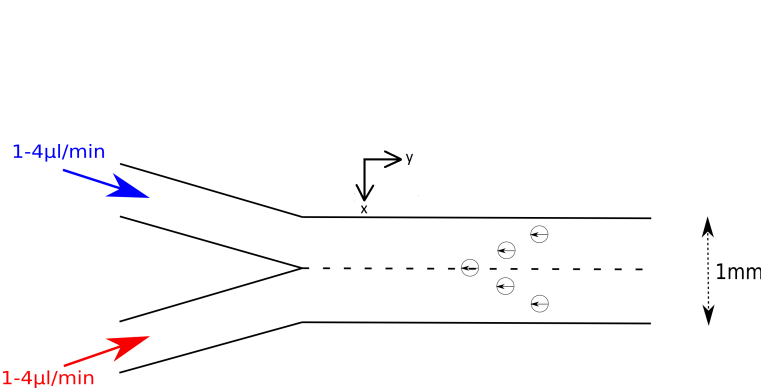

(a) Top-down view of the channel containing a small v-array

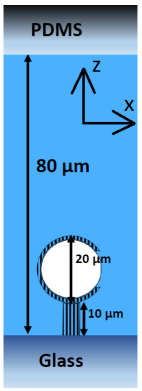

(b) Vertical arrangement in channel cross section (by Nicolas Bertin)

Figure 3.1: Experimental setup

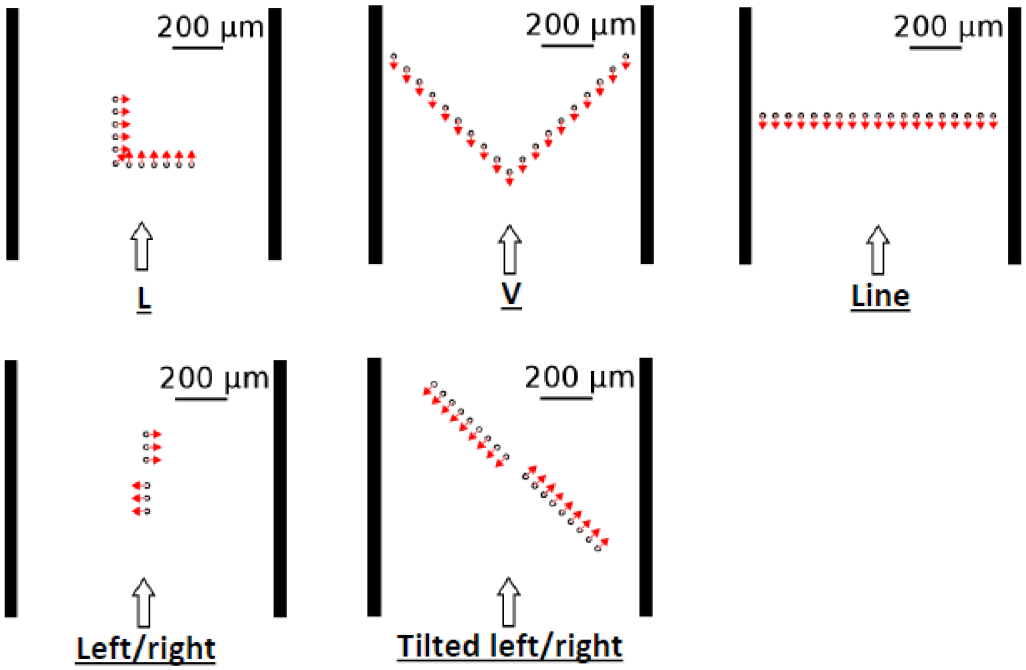

Figure 3.2: Configuration of the 5 experimental arrays in 1 μm wide and 80 μm high microchannel (adapted from original figure by Nicolas Bertin)

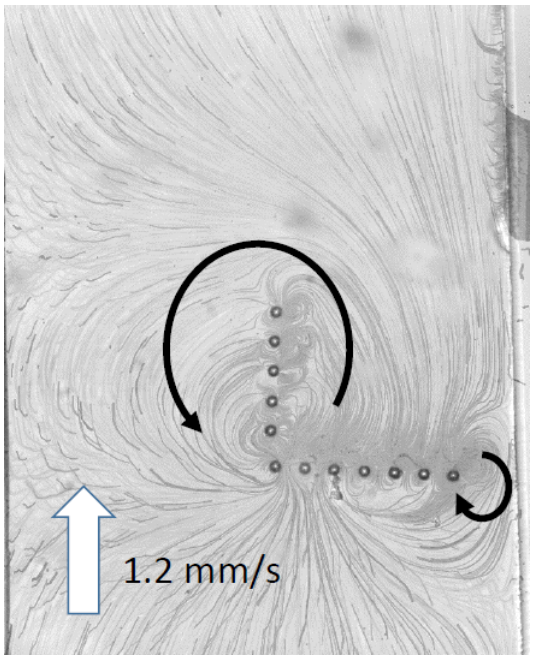

Figure 3.3: Experimental streaming around the L-array, in a confined channel 1 μm wide and 80 μm high, when $P_{ac} = 216$ kPa (by Nicolas Bertin)

smaller differences, such as the right hand circulations being smaller than the left, are likely attributed to the array being closer to one wall than the other. It can be difficult experimentally to position the array in the centre of the microchannel, this is why the straight line array was the first array to be studied since a longer line of capsules could be built and the microchannel placed over a subset of capsules.

In Fig. 3.3 there are two circulations (with the right one smaller than the other likely due to the closer right hand wall). The circulations are far larger than those seen around single AMBs in Chapter 2 and it is these large flow features, generated by the AMB arrays, which we will build a model to study in this chapter.

3.2 Flow field with only one wall

The arrays are contained with a microchannel, but three of the walls are a long distance away from most of the AMBs. The wall they are closest to is the base they are attached to, which is only 20 μm away fro the AMB centre. Therefore, we will initially model the AMBs adjacent to just one plane wall to see if this generates the large collective flows. .

3.2.1 Numerical model for an array near one wall

For the arrays of AMBs considered in this section, the length scales of the relevant patterns are $O(100\,\mu\text{m})$ as opposed to $O(10\,\mu\text{m})$ for the individual AMBs in Chapter 2, and therefore we approximate each AMB as its leading order flow in the far field, namely a Stokeslet. The next order correction is a Stresslet, which we will include here when modelling one wall.

We then model the flow induced by each AMB above a flat plate using the regularised version [73, 74] of the well known Blake solution for a Stokeslet above a no-slip wall [70] plus the Stresslet with its known solution near one wall [73, 74]. The Stokeslet strength for an AMB, f_t, was chosen so the flow velocity $\approx 10\ \mu$m from the Stokeslet was of the order of $1-100$ mms^{-1}, the range of velocities observed in front of an AMB experimentally (we discuss this in more detail in §3.3.1). The flow field of the Stresslet is determined by a tensor, that for an AMB pointing in the x direction, is modelled at leading order by a Stokeslet of strength f_t in the x-direction, is given by

$$f_t \begin{pmatrix} -8/3 & 0 & 0 \\ 0 & 4/3 & 0 \\ 0 & 0 & 4/3 \end{pmatrix}. \tag{3.1}$$

This form and relative strength of the Stresslet is given by the full solution of the flow field around the AMB, calculated in Chapter 1. To regularise, the delta function is replaced by a smoothed finite function, of similar shape. We used a standard algebraic blob of

$$\Phi = \frac{15\Delta^4}{8\pi(r^2+\Delta^2)^{\frac{7}{2}}}, \tag{3.2}$$

taking the regularisation factor as $\Delta = 10^{-5}$, the radius of the AMB. The blob Φ tends to the delta function as $\Delta \to 0$ and thus with a non-zero Δ is used as a non-singular approximation to the delta function.

To obtain the full flow field around the AMB array, we then linearly superpose the flow field generated by each AMB individually. Additionally if there is a base flow we linearly add it to the full flow field generated by the AMBs.

3.2.2 L-array with one wall

Using our one wall numerical model, we will now study the flow induced by the L-array when we account only for the wall it is closest to in the microchannel (i.e. the one it is attached to, $20\,\mu$m away from the AMB centre). The numerical flow field bends as it passes through the

array with a small circulation at the end of each line of AMBs (see Fig.3.4a). This numerically obtained flow field does not contain the large circulations we observe experimentally when the L-array is in the microchannel (see Fig.3.3). We note that the base flow in these compared numerical and experimental cases are different, but we would expect the additional base flow in the experimental case to reduce the size of the circulations, as happens numerically, so this base flow difference does not account for the absence of the large circulations numerically.

If we remove the first order Stresslet correction and modelled each AMB solely as their leading order Stokeslet, we see a similar numerical flow field to Fig.3.4a where the Stokeslet and Stresslet were included. However, we included the Stresslet correction, as the Stresslet incorporates the small circulations found locally near the AMB, which could have contributed to generating the large circulations seen experimentally in the microchannel. This suggests the errors from our approximation of the AMB flow field is not the reason why large collective flows are not observed with our current numerical model.

We can check whether the lack of large circulations is due to the walls rather than inaccuracies in the numerical model by comparing to an experiment where there was only one wall close to the array. When the L-array was placed in a circular tank with no base flow and only one wall (see Fig.3.4b), the flow shows fluid being pulled through the array with circulations off the ends of the two AMB rows, matching our numerical flow field (in Fig. 3.4a) for the L-array above one wall with no base flow. Thus, this suggests that the confinement effects caused by the second side wall of the microchannel is important for generating the large circulations.

3.3 Flow field with two walls

We will now consider building a numerical model for the array flow field which includes two confining walls. We will include the base of the channel (same as our previous model) and we will add the top wall to the channel, as for the majority of the AMB arrays this is the second closest wall and thus, we expect, the second most influential.

3.3.1 Model for an array between two walls

To model the AMBs between two walls, we approximate each AMB by its leading order Stokeslet only (so we ignore the Stresslet correction). Between two walls a Stokeslet has a well known solution [75]. To obtain the flow field in a vertical cross section of the channel,

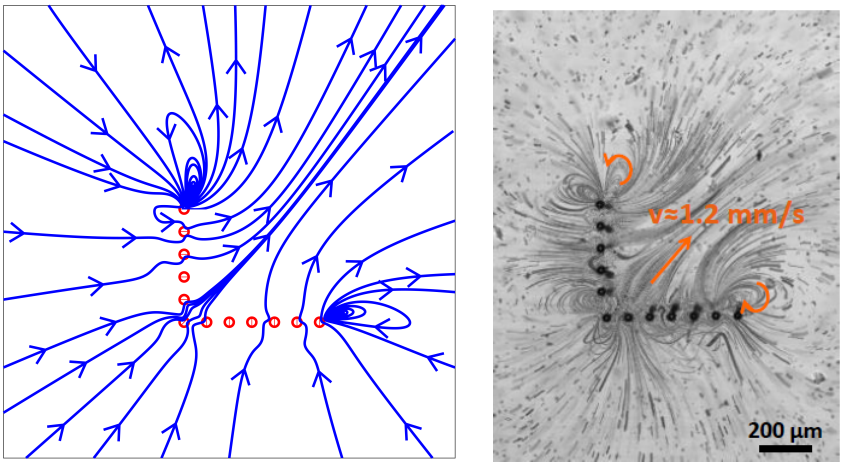

(a) Numerical streamlines around L array above a plane wall with no base flow

(b) Experimental streamlines above one wall with no base flow (by Nicolas Bertin)

Figure 3.4: Streamlines around the L-array with no side walls

we linearly superpose this individual solution for each AMB between two walls. However, this solution cannot be regularised, so the ODE solver breaks down near the singularities, thus streamlines may end abruptly and computational plotting time will be higher.

We can simplify this model, when we are not focusing on studying the vertical flow. The solution for a Stokeslet parallel to two confining walls has a vertical component of velocity, which decays exponentially, whereas the planar component of the velocity decays as a power law. Therefore, in the far field, the vertical velocity component is negligible. The horizontal velocity is then given by

$$\underline{u}(x,y) = \frac{4}{h^2} z(h-z)\underline{\tilde{u}}(x,y), \tag{3.3}$$

where $z = 0$ is the bottom plate, $z = h$ is the position of the top plate, and $\underline{\tilde{u}}$ is the 2D Stokes Doublet that for an AMB pointing in the x direction is

$$\tilde{u}_j^1 \sim -\frac{3f_t}{4\pi\mu} H(1-\frac{H}{h})\frac{1}{\rho^2}\left[\frac{1}{2}\delta_{j1} - \frac{r_j r_1}{\rho^2}\right], \tag{3.4}$$

where $j = 1,2$, H is the height of the Stokeslet above the bottom plate, μ is the dynamic viscosity of the fluid, (y_1, y_2, H) is the position of the Stokeslet, $\rho = \sqrt{(x-y_1)^2 + (y-y_2)^2}$ is the distance in the plane from the Stokeslet, and $r_1 = (x-y_1)$, $r_2 = (y-y_2)$ is the straight line distance from the Stokeslet in the x and y direction. We see that in the far field the flow is equal to a 2D Stokes Doublet (Eq. 3.4) with a magnitude, which varies quadratically across the

channel as in Eq. 3.3 [75]. We can then regularise this Stokes Doublet to remove singularities using the technique described in Refs. [73, 76]. We then linearly superpose this individual solution for each AMB to obtain the total flow field around the AMB array. Note that the result in Eq.3.3 shows that the choice of horizontal plane (i.e. the value of z) only affects the total magnitude of the flow field, thus the flow field is structurally the same in every plane (at leading order). The flow field is similar to those in a Hele-Shaw cell (where Poiseuille base flows are standard) however, such an approximation would be insufficient close to the AMB where inertia is important.

When there is a base flow of strength $4v_0/h^2$ (for constant v_0), we assume it is a traditional 2D Poiseuille flow with velocity field

$$\underline{U_0} = \frac{4v_0}{h^2} z(h-z)\underline{e_y}. \tag{3.5}$$

This has the same quadratic dependence across the channel as the flow generated by the AMB array, so when we linear superpose it the flow generated by the AMB array it is still structurally the same in each plane.

The flow structure in the horizontal plane will depend on the non-dimensional quantity of the ratio of the strength of the AMBs (which is equal for all of them) to that of the base flow, U_0, which we denote τ,

$$\tau = \frac{f_t}{\mu H U_0}. \tag{3.6}$$

To quantify τ experimentally we require values for U_0 and f_t. Experimental base flow velocities were $1.2\,\mathrm{mms}^{-1}$ (for most experiments). The strength of the AMBs is harder to identify experimentally, and the experimental measurements which were taken underestimate the force due to friction. However, it is known the velocity field in front of the AMB was $1-100\,\mathrm{mms}^{-1}$ so our Stokeslet strength was chosen so the flow velocity $\approx 10\,\mu$m from the Stokeslet was at the upper end of this on the order of $10-100\,\mathrm{mms}^{-1}$. Although we approximate the Stokeslet strength this way we acknowledge limitations of our numerical model which may impact its validity: a Stokeslet evenly distributes force in front and behind itself unlike the AMB; the regularisation size can effect the velocity magnitude close to the AMB and the Stokeslet is a far field model for the AMB. We approximate the force at about $f_t \approx 1-10\,$nN. Therefore, for experiments, $\tau \approx 40-400$. (We will discuss if this choice is validated by our results in §3.5).

3.3.2 Vertical flow field and collective flow features of the L-array with two walls

We will first consider the significance of adding the additional wall by comparing the flow in vertical cross-sections around the L-array for our one wall model (see Fig.3.5) and our two wall numerical model, (see Fig.3.6). Fig. .3.5 shows the array layout with the relative position of the modelled cross sections marked. Around this layout, the cross-sectional flow fields are shown for the numerical model with one wall. In Fig.3.6 streamlines from the numerical model incorporating two walls is shown for the cross section at $y = 0$ (where the plane this corresponds to is marked on the layout in Fig. .3.5). These streamline pictures are plotted from the in-plane velocity fields.

With the unconstrained flow (one wall) there is significant motion through the second imaginary boundary, pulling flow into the array and pushing flow out once it has passed through the array. The second plane restricts this 3D motion, so within the vertical cross section, flow is approximately parallel to the top and bottom walls, except close to the AMBs. To compensate for this additional confinement caused by the second wall, we observe the appearance of two large in-plane vortices (see Fig. 3.7).

These large vortices are the significant collective flow features from Fig.3.3. There is evidence the side-walls are impacting the flow in the microchannel as in Fig.3.3 the right-hand vortex is relatively small. However, when the experiment is undertaken in an open tank with a low base flow rate, the two vortices are similar sizes and match those seen in our numerical model when there is no base flow rate (see Fig.3.7a). We note that the experiments have a higher base flow rate than the numerical model and we expect higher base flow rates to suppress flow features generated by the array, as we will see in §3.4.1. However, the aim of the experiments was to understand the array flow features, so the experiments were performed in a regime where the array dominates over the base flow, which justifies our comparison of the numerics and experiments despite the different base flow rates . Overall, our model is capturing the main flow features, as was the aim, and we will now use this model to examine flow fields around arrays.

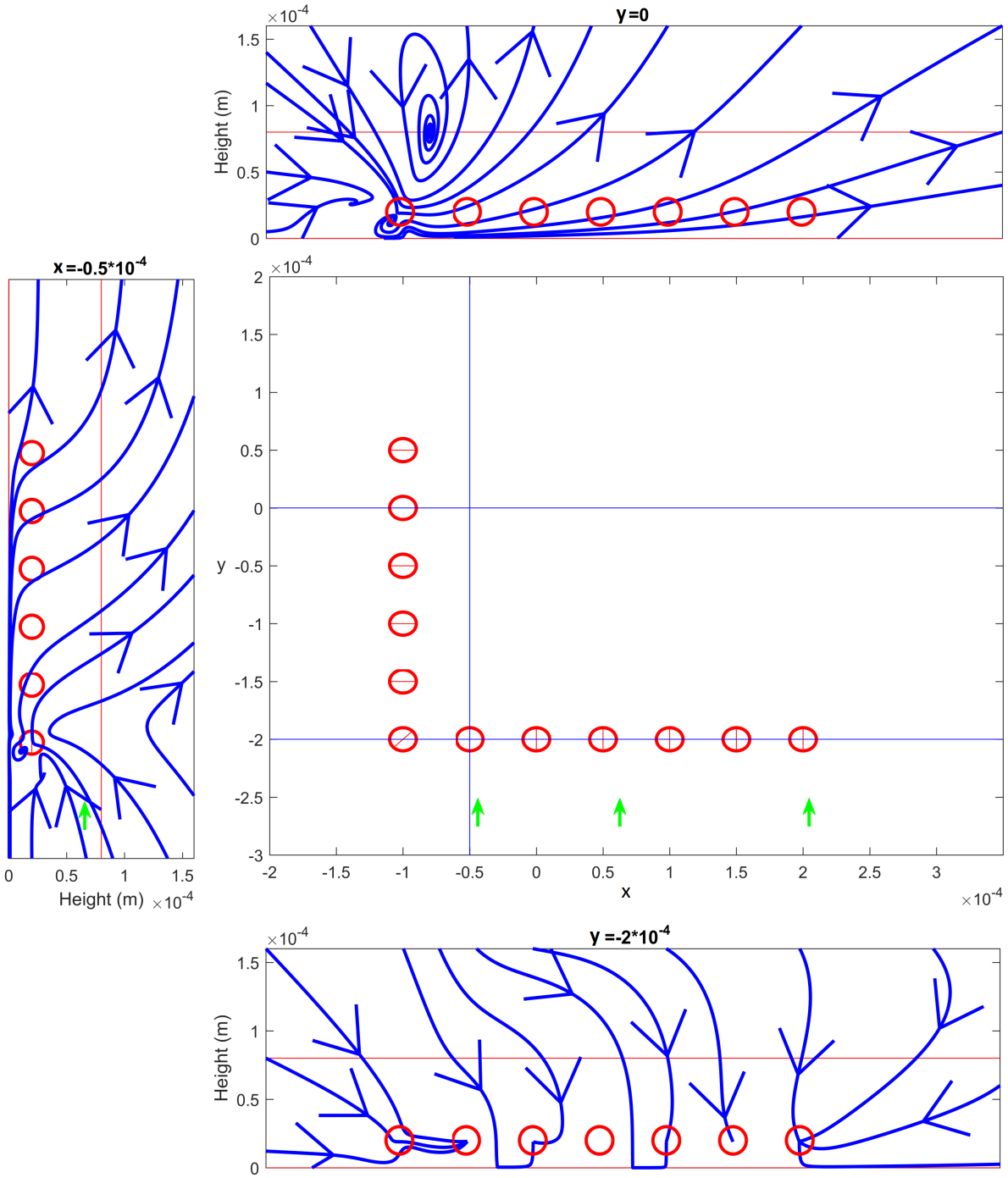

Figure 3.5: Streamlines around the L-array in vertical planes using our one wall numerical model. Green arrows indicate the direction of the base flow. The red line at $H = 0$ marks the base wall of the channel and the red line at $H = 80\,\mu$m marks the position of the channel top wall, which is neglected by our model so the numerical model shows flow through this top wall.

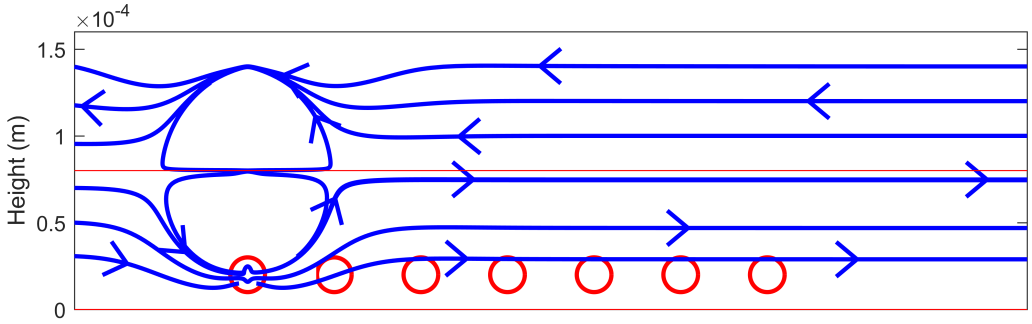

Figure 3.6: Vertical motion at $y = 0$ (as marked on Fig.3.5) using our numerical model with two confining walls. The red line at $H = 0$ marks the base wall of the channel and the red line at $H = 80\,\mu$m marks the position of the channel top wall, both of which are incorporated in the numerical model (unlike in Fig. .3.5).

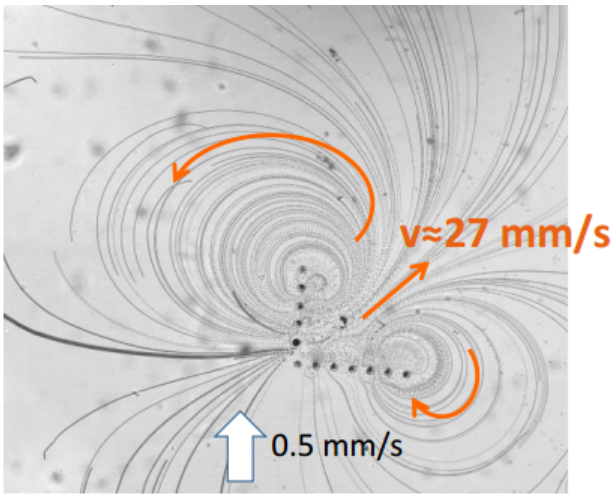

(a) Experiments at $P_{ac} = 1.53$ MPa with a base flow of $0.5\,\mathrm{mm s}^{-1}$ (by Nicolas Bertin)

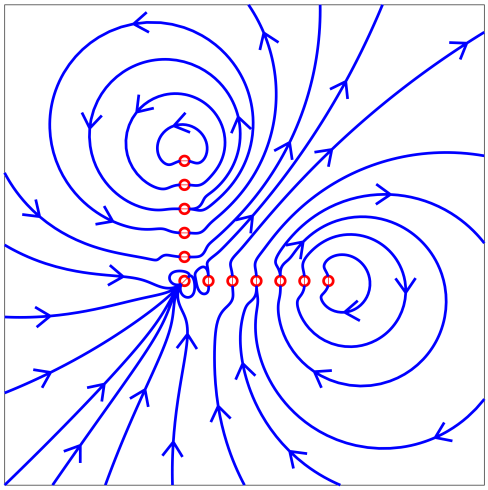

(b) Numerics with no base flow, $\tau = \infty$.

Figure 3.7: Streaming around the L-array at low base flow

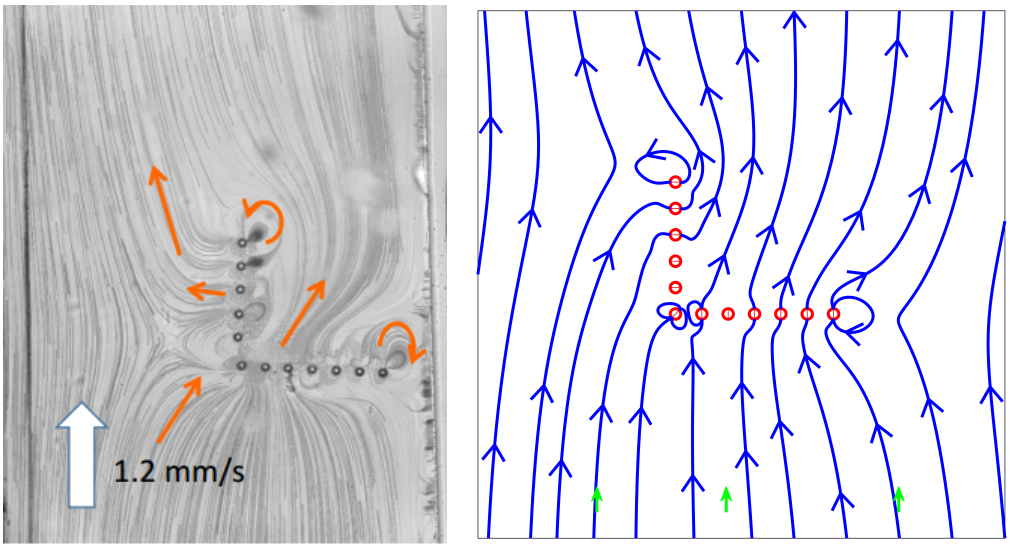

(a) Experiments at $P_{ac} = 93\,\text{kPa}$ (by Nicolas Bertin)

(b) Numerical streamlines for L for $\tau \approx 187.5$

Figure 3.8: Streamlines showing the flow around the L-array, at low AMB strength.

3.4 Numerical flow structure development of the experimental arrays

In this section, we will numerically examine the development of the flow fields for the five experimental arrays, as τ is increased. These will be compared to experimentally obtained flow fields. With the exception of the L-array, all these experimental flow fields were obtained during mixing experiments, thus concentration fields are shown with flow direction arrows added afterwards, using the associated videos to determine the direction of the flow manually.

3.4.1 L-array

Our first array is the L-array. The L-array is not symmetric and thus non-symmetric flow fields are expected and observed (see Fig. 3.7). The main changes in flow shape as τ decreases (corresponding to increasing strength of background flow) are:

- $\tau = \infty$ (corresponding to $U_0 = 0$), plotted in Fig. 3.7b. There are two large circulations on both sides of the L, in agreement with experiments performed at a small but non-zero U_0(which could correspond to τ as large as 800), Fig. 3.7. However, in channel experiments, due to the side walls these circulations are different sizes (Fig.3.3). Another

difference with these experiments, likely due to the non-zero U_0 in the experiments, is that there is a change in behaviour from flow being caught by the left hand vortex to flow escaping downstream.

- $\tau \approx 1900$. The circulations start to be suppressed within a 1mm width here;
- $\tau \approx 190$ plotted in Fig. 3.8b. A saddle is now clearly apparent to the left of the array behind the circulations. The two circulations have shrunk significantly and become more elongated, but survive off the edge of the two straight sections of the array. These features all agree with those observed experimentally when the driving acoustic pressure is $P_{ac} = 93\,\text{kPa}$ and there is a $1.2\,\text{mms}^{-1}$ base flow (Fig. 3.8). Numerically our features are noticeable closer to the two end points of the array than those experimentally, and this is true even at slightly higher τ where the circulations are bigger. Since these differences are small, they are likely due to our approximation to the AMB flow field. We also have a saddle to the right of the array, next to the right hand circulation, which is not observed experimentally, but experimentally that end of the array is very close to the wall. The major additional experimental feature is the presence of an additional saddle to the left of the AMB array separating flow into the bottom of the array, flow past the array and backflow behind the array. Numerically, there is no backflow close to the AMBs, which means the saddle is not seen numerically, so this suggests the AMB flow approximation may explain the difference between the numerical and experimental flow feature.
- $\tau \approx 40$. Both circulations have disappeared completely.

The structural changes with decreasing τ agree well with experiments as seen when comparing Fig.3.3 and Fig.3.7b and in Fig.3.8.

Less experimental analysis has been undertaken for the other four experimental array, but we will still study their structurally changes and compare to the available experimental data.

3.4.2 V-array

The main changes in flow shape as τ decreases (corresponding to U_0 increasing) are:

- $\tau = \infty$ (corresponding to $U_0 = 0$), plotted in Fig. 3.9a. As shown in Fig.3.9a, the V-array pushes fluid away from its point, around the outside and into the pointed ends of the V from behind. A saddle exists between the V opening. Flow at the two ends of the V is pushed down a very narrow channel close to the AMB lines, but they can the be pulled into the many small circulations pushing flow back to the V ends. Since the array is vertically symmetric, the flow it generates is also symmetric;

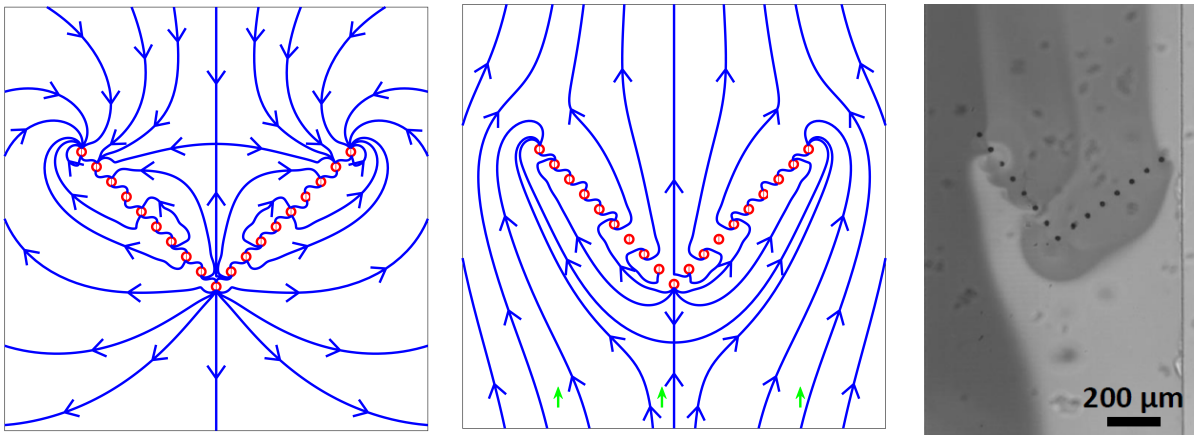

(a) Numerical streamlines, $\tau = \infty$

(b) Numerical streamlines, $\tau = 187.5$

(c) Experiments for $P_{ac} = 224\,\text{kPa}$ (by Nicolas Bertin)

Figure 3.9: Flow around the V-array

- $\infty > \tau \gtrsim 50$ plotted at $\tau = 187.5$ in Fig. 3.9b. As τ decreases down to $\tau \approx 380$, the saddle in the V of the array is pushed further away from the array. It is rapidly approached (as τ decreases) by a different saddle, which starts (at $\tau = \infty$) on the centre line at $y = \infty$, until they are nearly on top of each other. Around $\tau \approx 380$ they both move away, towards either end of the V. The saddles separate flow caught by the array and that passing around the outside. A saddle also appears upstream, approaching the array as τ decreases. This saddle separates the region where the saddle is pulling in flow from behind as seen in Fig. 3.9a and the base flow pushing flow around and away from the array. As τ decreases from infinity more flow is pushed around the array, although some is still caught and pulled into the array. Many of these features are visible in Fig.3.9b for $\tau = 187.5$;

- $\tau \approx 50$. The array is having minimal effect on the flow field.

In experiments, when the AMBs were pointing into the flow, the AMBs degraded and had a significantly shorter life span, making experimental data harder to obtain. This was particularly a problem at higher acoustic pressures. However, fluid being circulated close to the line of AMBs is visible in Fig. 3.9c along with fluid escaping around the outside of the array, which we identified numerically. But the flow is not symmetric, in contrast with what we saw numerically, probably due to AMBs degrading as well as manufacturing variability, meaning the two rows of AMBs are not of exactly equal strengths.

3.4.3 Straight-line array

The straight line array contains 19 AMBs stretching across the channel width and pointing (downwards) against the base flow (as shown in Fig. 3.2). The main changes in flow shape as τ decreases (corresponding to U_0 increasing) are:

- $\tau = \infty$ (corresponding to $U_0 = 0$), plotted in Fig. 3.10a. There are two circulations, an anticlockwise one to the right of the line of AMBs and a clockwise one to the left of the line of AMBs, with each circulation centred slightly off the edge of the line of AMBs (see Fig.3.10a);

- $\infty > \tau > 130$ plotted at $\tau = 375$ in Fig. 3.10b. As τ decreases from ∞, saddles appear in front and behind the array and start moving towards the array. Simultaneously the circulations elongate squeezing in close to the line of AMBs, reducing the size of the backflow region. Decreasing τ further causes the base flow to break through in the middle of the AMB line leaving a saddle to either side each bordering a smaller circulation centred near the line's end, as can be seen in Fig.3.10 for $\tau = 375$;

- $\tau = 130$. The circulations have reduced in size and the AMB line does no more than cause a slight bending of the flow away from its centre.

This simulation gives the worst experimental agreement of all five arrays (see 3.10). The experiment shows a large anti-clockwise circulation on the right-hand side of the channel and a partial clockwise circulation on the left-hand side. The partial circulation is missing any rotation beyond the array, as is seen on the right-hand side. To the far right and the far left of the channel, near the side walls, there is evidence of flow proceeding past the array with minimal interference from the array. The presence of the circulations and regions where the flow passes straight past the array agrees with the numerical model. However, the major difference is that numerically the flow passes straight through the middle of the array separating the circulations rather than having the circulations in the middle with the flow passing around both sides. We hypothesise this is an effect of not including the side walls in our numerical model, which we expect to be particularly significant since this array stretches the entire width of the channel. The missing half of the left circulation experimentally could be a wall effect or more likely, due to practical differences between experiments and numerics (line not completely horizontal, air trapped in AMBs) so the idealised symmetric numerics is not realised in the physical world.

As such with this array we should be most sceptical about drawing conclusions about how the flow structure changes with τ.

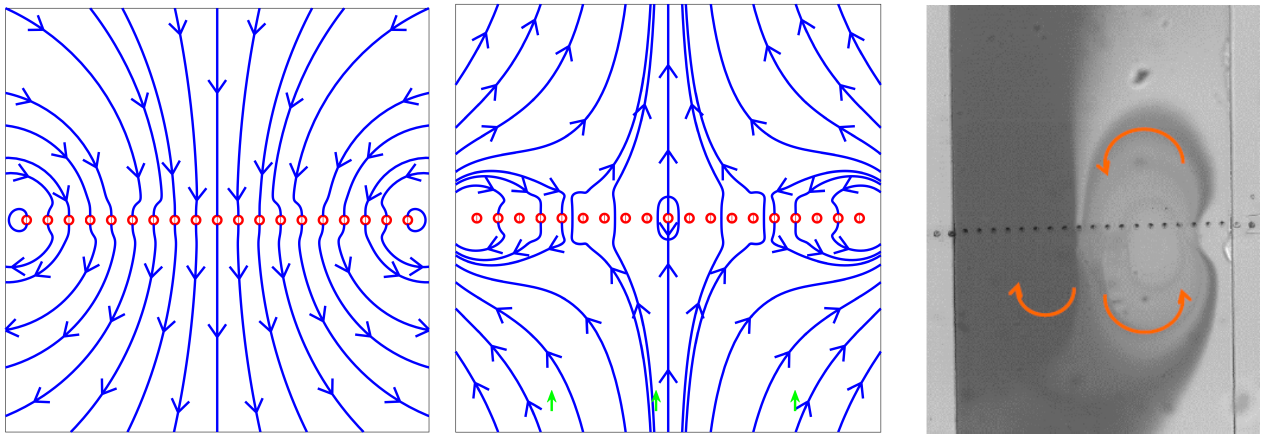

(a) Numerical streamlines, $\tau = \infty$

(b) Numerical streamlines, $\tau = 375$

(c) Experiments at $P_{ac} = 1.45\,\text{MPa}$ (by Nicolas Bertin)

Figure 3.10: Flow around the straight-line array

3.4.4 Tilted left/right array

The tilted left/right array consists of a diagonal line of AMBs across the channel, with 9 AMBs on the left, pointing perpendicular to the line against the base flow, and 9 AMBs on the right, pointing perpendicular to the line with the base flow (as shown in Fig. 3.2). The main changes in flow shape as τ decreases (corresponding to U_0 increasing) are:

- $\tau = \infty$ (corresponding to $U_0 = 0$), plotted in Fig. 3.11a. There is a large anticlockwise circulation at the centre of the AMB line, with two other large clockwise circulations with oppose directions centred just off both ends of the AMB line (see Fig. 3.11a);
- $\infty > \tau > 50$ plotted at $\tau = 187.5$, in Fig. 3.11b. Decreasing τ from infinity causes fluid to push through, between the circulations on the right hand of the array where the direction of the component of the AMBs force parallel to the channel matches the base flow. This separates the right-hand end clockwise circulation from the other two, which shrinks far more quickly than the other two circulations. Saddles move in from infinity, one for each circulation, separating flow that escapes from the array and that which is caught in the vortices. The two circulations become linked so flow can do half a rotation with one circulation before passing into the other circulation, doing half a rotation and escaping. Decreasing τ further increases this interplay between the two circulations and shrinks all the array features. The flow for $\tau = 187.5$ is shown in Fig.3.11;
- $\tau \approx 50$. Most array effects are unnoticeable by this stage.

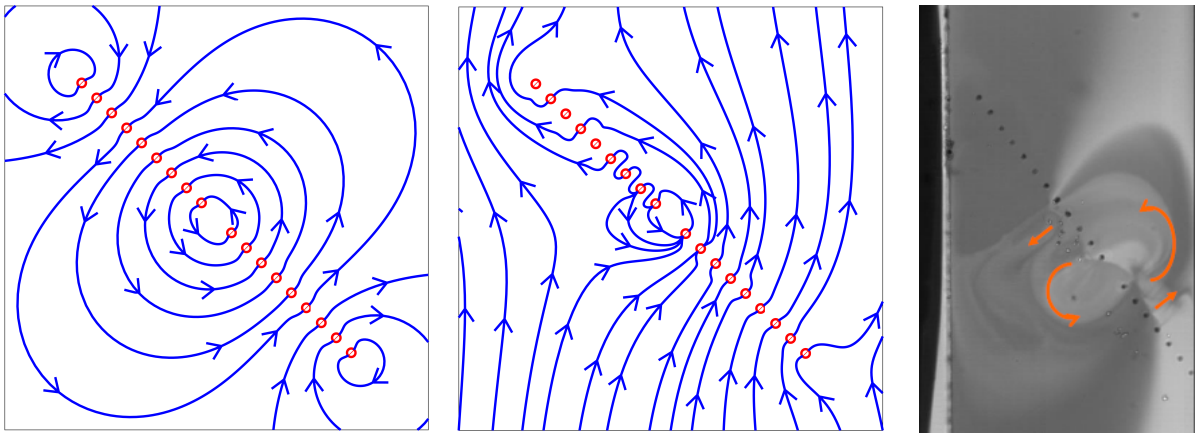

(a) Numerical streamlines, $\tau = \infty$

(b) Numerical streamlines, $\tau = 187.5$

(c) Experiments with $P_{ac} = 1.82\,\text{MPa}$ (by Nicolas Bertin)

Figure 3.11: Flow around the tilted left/right array

Experimentally, we observe a central anticlockwise circulation as the major flow feature. This main flow feature is observed numerically as well but this circulation dominates more than is observed theoretically (see Fig.3.11), which we again expect to be due to side wall effects.

3.4.5 Vertical left/right array

The vertical left/right array consists of a line of 6 AMBs positioned down the centre of the channel with the 3 at one end pointing towards one side-wall and the 3 at the other end pointing towards the other side wall (as shown in Fig. 3.2). The main changes in flow shape as τ decreases (corresponding to U_0 increasing) are:

- $\tau = \infty$ (corresponding to $U_0 = 0$), plotted in Fig. 3.12a. There is a long wide central circulation exchanging flow between the top AMBs to the bottom AMBs, as well as two large oblong circulations above and below the array (see Fig. 3.12a). We note that like the tilted left/right array, the flow is symmetric under a π radian rotation;

- $\infty > \tau > 15$ plotted at $\tau = 375$ in Fig. 3.12b. Decreasing τ, the left half of the centre circulation, (which has a component of its flow in the direction of the base flow), maintains its size (even temporarily growing in size vertically) and the right hand side of the centre circulation, (with a flow direction with the base flow), shrinks in size. The other two circulations reduce in size (far faster than the large circulation) and elongate, with the additional space between the circulations allowing flow to be pulled in from

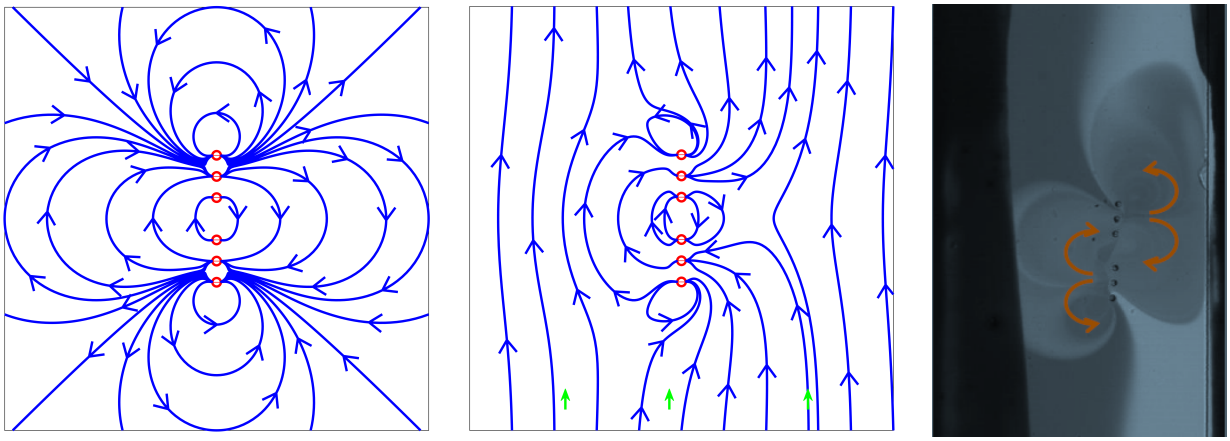

(a) Numerical streamlines, $\tau = \infty$

(b) Numerical streamlines, $\tau = 375$

(c) Experiments with $P_{ac} = 1.34\,\text{MPa}$ (by Nicolas Bertin)

Figure 3.12: Flow around the vertical left/right array

up channel and pushed out down channel. Some flow escapes around the outside of the array and by $\tau \approx 940$ this occurs within a 1mm wide channel. One saddle approach from infinity for each of the circulations, separating this laminar flow and circulation. Many of these features are visible in Fig.3.12b for $\tau = 375$;

- $\tau = 15$. Most of these array features are almost unnoticeable by $\tau \approx 15$, but the longest surviving major feature is the gentle bending of flow as it passes through the array.

Experimentally, at $P_{ac} = 1.34\,\text{MPa}$, we observe four circulations. Two on the right, the one further upstream clockwise and the one further downstream anticlockwise, and two on the left, the one further upstream anticlockwise and the one further downstream clockwise. In good comparison, we numerically saw the four distinct flow circulations, however their alignment and relative sizes differed from these experimental observations (Fig. 3.12). We anticipate this being partly due to the approximations we made in our AMB flow model, since the differences in the flows occur close to the AMBs. Also, the circulations in the experiments stretch across the width of the channel so the side walls may have an impact.

3.5 Force strength and τ

We have observed that the array has minimal effects as τ is reduced long before τ equals 1. Thus the strength of the AMBs needs to be orders of magnitude stronger than that of the base flow to have an effect. This agrees with experiments where the stronger AMBs generate

velocities of roughly $10-100\,\mathrm{mms}^{-1}$ in front of themselves, whereas base flows used were $1.2\,\mathrm{mms}^{-1}$. This can be explained as the AMB force is maintained in one location whereas the base flow is uniform in the plane.

We can now consider whether the observed flow fields validate our choice of force strength of $f_t = 1-10\,\mathrm{nN}$. A comparison is made more difficult as the driving pressures for the flow fields vary experimentally, and its effect vary between the experimental setups of a circular tank and a microchannel. However, the excellent agreement in Fig.3.8 in terms of shape and size of features suggests $f_t = 4.5\,\mathrm{nN}$ for the strength of the Stokeslets is appropriate for a driving pressure of $P_{ac} \approx 100\,\mathrm{kPa}$, well within our force range based on AMB velocities.

At higher P_{ac} the comparison becomes harder as the agreement between the theoretical and experimental results are not as good. Similar features are observed (see Fig.3.12) but experimentally the features extend across the width of the channel. At that point the side walls become important, which are not captured theoretically. However, forces 10 times stronger are required to get some features stretching across the channel suggesting much stronger forces are being produced under the stronger driving pressures P_{ac}, and this strength is then of a similar order of magnitude but outside our original force range (although side walls may reduce the necessary strength to obtain these effects).

3.6 Conclusion

We first modelled the AMBs as Stokeslets above one wall and then separately in a confined channel as Stokeslets between two plane walls identifying that the top wall of the channel is essential to the structure of the flow field in the channel. Using this channel model we observed similar structural changes in the flow to that observed experimentally for the L-array where we have the most experimental results to compare with. For all the arrays there are flow differences between experiments and numerics (particularly for the straight line array) which we hypothesise are mainly due to the absence of side walls in the numerical model. Further work could include adding side walls to our numerical model, by using the method of images to calculate the effect of these additional walls on our leading order 2D Stokes doublet approximation of the AMB between the top and bottom wall, and then linearly superposing the flow fields of all the AMBs within the array.

Chapter 4

Optimising AMB arrays for mixing

The main results from this chapter are included in our published paper: "Bubble-based acoustic micropropulsors: active surfaces and mixers", Nicolas Bertin, Tamsin A. Spelman, Thomas Combriat, Hervé Hue, Olivier Stéphan, Eric Lauga and Philippe Marmottant, Lab on a Chip, 17:1515-1528 , 2017 [66] (adapted by permission of the Royal Society of Chemistry).

In this chapter we will analyse the mixing potential of our AMB arrays in our microchannel. Ultimately, diffusion will cause two fluids to mix on a molecular scale and generate a homogeneous fluid. However, at high Reynolds numbers, diffusion is assisted by turbulence, which can inter-disperse fluids quickly, rapidly increasing the surface area [77, 78]. Numerical models by E. Lunasin et. al. have ignored diffusion and looked for the optimal flow field to inter disperse multiple fluids, to identify optimal mixing [79]. A different numerical model uses probabilistic methods, where the concentration is taken as a probability density function (PDF) and its mean value and the mean values of its moments are analysed [80, 81]. This PDF can also be used to analyse particular mixing protocols, such as stirring a blob of dye with a flapping plate [82]. On the theoretical side, the Batchelor scale, named after George Batchelor, describes the smallest length scale of flow variation before diffusion dominates [83].

On the microscale flows are laminar, so turbulence will not help mixing, and diffusion plays a larger role. However, the mixing process can be sped up by exploiting shear effects, for example, through Taylor-Aris dispersion [84, 85], or at high Reynolds number, through shear instabilities [86]. Microfluidic mixers [87, 88] are largely broken up into two types: active and passive mixers. In active mixers, a moving part such as an oscillating bubble actuates the flow to cause mixing [50, 89]. In a passive mixer, the channel geometry splits and folds the flow to increase the effects of diffusion [90–92]. In these microfluidic mixers, there are multiple methods for measuring the mixing experimentally [93] including: using two fluid streams with one or both dyed different colours [94]; using two chemicals that interact with each other [95] and using photometric and fluorescent methods (or Raman techniques) to study

the concentration change directly in 1D [96].

Here, we will analyse the mixing potential of the AMB arrays introduced in Chapter 3 for mixing two streams of fluid in a confined channel, focusing on variations of the experimental arrays introduced in Fig.3.2. Most theoretical studies of mixing use detailed numerical simulations [90, 97] or scaling arguments [98, 99]. Here we present an alternative approach, namely a numerical method applied to a simplified array-channel setup. The advantage of our method is that, due to its simplicity, it can analyse hundreds of AMB arrays a day, and is designed to identify groups of good arrays, which can then undergo further numerical and experimental study. In §4.1 we describe the experimental motivation, in §4.2 we outline our mixing measure, in §4.3 we discuss the effect of the fluid-fluid boundary line position on mixing and boundary lines becoming caught in vortices, in §4.4 the best arrays identified by our model are discussed and finally in §4.5 we compare two of these best arrays for mixing with experimental results.

4.1 Experiments

Our mixing analysis was motivated by experiments undertaken by our collaborators. They used the experimental setup introduced in Chapter 3 §3.1, to analyse the ability of the five armoured microbubble (AMB) arrays, introduced in Fig.3.2, to mix two continuous streams of fluid within a confined channel of dimensions 80 μm in height and 1 mm in width (although they have also considered a thinner channel of width 0.5 mm but we do not study that case in this thesis). The experimental protocol involved actuating the array under ultrasound for 2 seconds, and then turning the ultrasound off for 2 seconds. Experimentally, mixing was quantified using the Relative Mixing Index (RMI) [100], which compares the standard deviation of the light intensity from the fluid in the mixed and unmixed states. Mathematically, RMI is calculated from a video frame as

$$\mathrm{RMI} = 1 - \frac{\sigma}{\sigma_0} = 1 - \frac{\sqrt{\frac{1}{N}\sum_{i=1}^{N}(I_i - \langle I\rangle)^2}}{\sqrt{\frac{1}{N}\sum_{i=1}^{N}(I_{0i} - \langle I\rangle)^2}}, \tag{4.1}$$

where σ is the standard deviation of the light intensity, σ_0 is the standard deviation in the unmixed state light intensity, N is the number of pixels in the analysis box, i is the pixel number, I_i is the grey scale intensity of the pixel, $\langle I\rangle$ is the average light intensity in the analysis box and I_{0i} is the intensity of the i^{th} pixel in the unmixed state. RMI=100% corresponds to

perfect mixing and RMI= 0 corresponds to no mixing. The RMI was measured in an 'analysis box', which spanned the width of the channel, and was positioned sufficiently far downstream so as to not be significantly effected by the AMB array. The RMI was analysed at a range of driving pressures P_{ac}. Experimentally, the L-array was the best for mixing at higher driving pressures and obtained nearly perfect mixing at a lower driving pressure of $P_{ac} = 1$ MPa than the other arrays (if they reached perfect mixing). At lower driving pressures the V-array was best reaching an RMI of 59% at $P_{ac} = 224$ kPa but the L-array performed particularly poorly. Experimentally, problems arose with AMBs pointing into the flow having very short bubble lifespans. This interfered with experiment using the straight-line and V-array, with greater problems at higher driving pressures.

In this experimental setup the Reynolds number is low so the mixing is caused solely by diffusion [101]. To increase the rate of mixing between two fluids, the two-fluid boundary can be stretched, thus increasing the surface area for diffusion. Therefore, there is a correlation between the rate of mixing and the stretching of the two-fluid boundary. To numerically study the mixing ability of AMB arrays, we will ignore diffusive effects for simplicity and solely consider the stretching of the two-fluid boundary, which we expect to correlate with the rate of mixing.

4.2 Numerical mixing measure

Our numerical setup is different to the experimental setup in that: we will ignore side wall effects; focus our mixing analysis at the lower acoustic driving pressures and focus on the stretching (so mixing) of fluid, which starts outside the array when it is turned on. These differences are implemented for simplicity, but in §4.5 we will compare our results to experiments to demonstrate our theoretical work still has some physical correspondence.

For our numerical analysis we use the same model for the flow field as we introduced in Chapter 3. In summary, we model each AMB as the regularised far field solution of a Stokeslet between two plane walls, which is a regularised 2D Stokes Doublet. We linearly superpose the effects of each AMB and the background flow to obtain the total flow field. We identified in Chapter 3 that every plane within the channel was structurally the same in the far field, thus we will focus our mixing analysis on one plane.This is equivalent to depth averaging, because we have the same flow field in each plane so depth averaging gives a constant multiplied by the one plane flow field. This is a far field approximation and is inaccurate close to the AMBs where there is vertical motion of the fluid and vertical circulations can be seen, indicating different flow fields in each plane. However, this approximation will capture the larger flow fields, which cause the flow mixing. Separately, although the structure of each plane is similar,

the average speed varies between each plane so in slower planes diffusion will have had longer to smooth out the concentration field at the fluid-fluid boundary before it reaches the array. Thus behaviour in the near-field region of the original fluid-fluid boundary is more significant in these planes. This approximation also removes information about vertical shear, which can increase the mixing rate, although our measure of mixing does not account for shearing anyway.

Regularising the Stokes Doublet approximation for the AMB introduces difficulties for our mixing analysis, which were not problematic when we were only considering the streaming flow in Chapter 3. The regularisation breaks the Stokes Doublet into a source and sink, thus we choose our regularisation length of $\delta = 0.5 \times 10^{-5}$ such that these are contained well within the AMB radius. To prevent fluid non-physically becoming trapped in a sink, we add a small $Ae^{-B/(r-r_0)^2}$ velocity contribution in the direction of the Stokes Doublet within the AMB radius r_0 (where A, B are constants) to push flow from the sink to the source. The maximum velocity within the AMB increases from $0.02\,\mathrm{ms}^{-1}$ to $0.07\,\mathrm{ms}^{-1}$ due to this correction but is maintained at the same order of magnitude. This contribution is continuous at all derivatives on the boundary of the AMB and is added only within the AMB. The AMB strength is taken as 0.45 nN (which corresponds to a low experimental pressure forcing as we justified in Chapter 3 §3.3.1 and §3.5) with a base flow in the AMB plane of 1.2 mm/s to match experiments.

Diffusion ultimately causes the mixing but its effectiveness is dependent on the size of the surface area between the two fluids. As the fluid passes through the AMB array this two fluid boundary will be stretched, increasing in size, and thus improving mixing. Therefore, we measure mixing ability by considering the stretching of the fluid-fluid boundary. This ignores Taylor-Aris dispersion effects and the smoothing of the boundary caused by diffusion by the time the boundary has passed through the mixer. However, it will capture the increase in mixing caused by diffusion, due to the greater surface area between the two fluids.

In our plane, this fluid boundary will be a line extending down the channel, and we consider a section of line 3.2 mm in length. We measure mixing capability as Λ, the ratio of the length of line after it has partially passed through the array to its initial length at time $t = 0$ of 3.2 mm (similar to some measures for simple passive mixing such as for duct flow in a channel [101]). In general, Λ will be greater than one, indicating the boundary has stretched over time by the AMB array but it can be less than one if the boundary line contracts, such as if it is caught in a sink or the flow is slows down. We take our stretch of line starting a long distance away from the array (about 1 mm) where the base flow dominates, and thus we can assume that each point on the line follows the same path, only time delayed. We note this assumption ignores the possibility for chaotic advection on the fluid-fluid boundary to improve mixing. Chaotic

advection can occur in the flow, for example, when flow splits to go either way around a vortex. The analysis is terminated when the end of this line element reaches the starting position of the front of the line element, at which point the front of the line element will have well passed out the other side of the array (if not caught in an array circulation). Line lengths are calculated assuming straight lines between data points. We note that our measure takes the stretch of boundary line we analyse starting a long way from the array, and that this ignores effects such as chaotic advection, which will most prominently effect the boundary line starting within the array when the array is turned on. Experimentally, the ultrasound is turned on for two seconds then off for two seconds, which is a time modulation that introduces time dependence to the flow. This modulation would allow for chaotic advection, as often seen in 2D time dependent flows, as when the array is switched on fluid close to the array will behave differently to that further downstream, allowing fluid that starts close together to become widely separated very quickly. This could allow very good mixing of the fluid close to the array when the array is switched on, but this behaviour is not captured by our numerical model and mixing measure.

Using the experimental arrays as templates we considered variations on their design. Specifically, we consider three array designs: an L-array, a same direction V-array and an opposite direction V-array, as shown in Fig.4.1, maintaining the array centre at a similar distance downstream. We vary these designs by changing the parameters θ_1, θ_2 and θ_3. The parameter θ_3 always represents rotating the array around the centre of the array. For the L-array, θ_1 and θ_2 represent rotating the direction of the AMBs on the corresponding AMB line while keeping the centre of each AMB constant. For the same direction V-array and opposite direction V-array, θ_1 and θ_2 represent rotating the position of the corresponding rows of AMBs about the point of the V, while keeping the direction of the AMBs constant. This is explained in more detail in Fig. 4.1. We also vary the starting position of the two fluid boundary relative to the AMB array across the width of the channel (i.e. from Fig.3.1a, varying the x position of the boundary), considering Λ at every $10\,\mu$m position across a 1 mm width. We define $\bar{\Lambda} = \max(\Lambda)$ where we maximise over all these positions of the fluid boundary, and will use that to identify the best arrays for mixing.

4.3 Boundary line and vortices

We will first consider the effect of varying the x position of the two fluid boundary, and the effect of that boundary becoming trapped in vortices using the array shown in Fig.4.2a as an example.

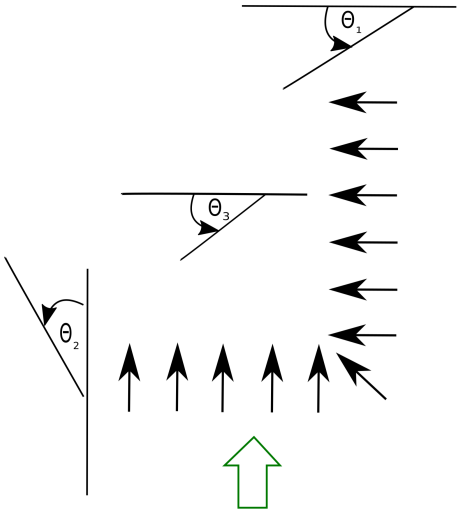

(a) Numerical L-array. The parameter θ_1 dictates the direction of the six AMBs in the column below it, where each of these AMBs is rotated around its own centre. The parameter θ_2 dictates the direction of the five AMBs in the adjacent row, where each AMBs is rotated around its own centre. The corner AMB points in a direction which is an average of the direction of its two adjacent AMBs. The position of the AMBs remain constant for all values of the parameters θ_1 and θ_2. We consider the mixing ability of all configurations of this array with $\theta_1, \theta_2, \theta_3 = 0, \pi/2, \pi, 3\pi/2$.

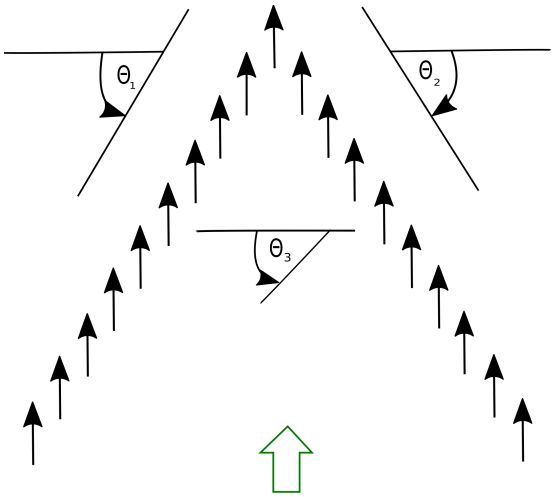

(b) Numerical same direction V-array. The parameter θ_1 rotates the position of the AMBs in the left hand line anticlockwise about the AMB at the point of the V while keeping the AMB direction constant. Similar to θ_1, θ_2 rotates the position of the AMBs in the right hand line clockwise about the AMB at the point of the V while keeping the AMB direction constant. The AMB at the point of the V remains stationary for all values of θ_1 and θ_2. We consider the mixing ability of all array configurations with $\theta_1, \theta_2 = 0, -\pi/4, -\pi/2$ and $\theta_3 = 0, \pi/2, \pi, 3\pi/2$.

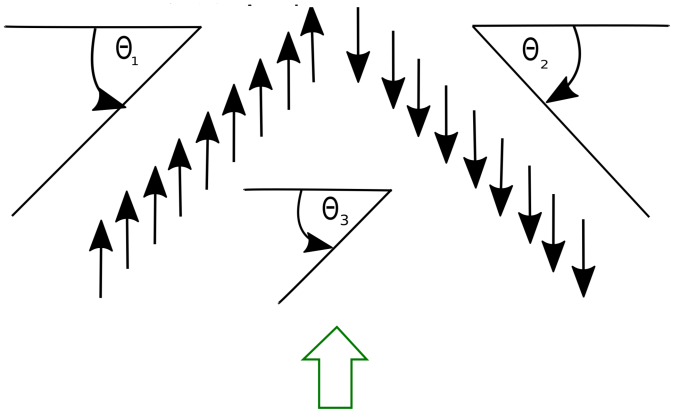

(c) Numerical opposite direction line array. The parameter θ_1 rotates the position of the AMBs in the left hand line anticlockwise about the (empty) point of the V while keeping the AMB direction constant (for example, a rotation of $-\pi/4$ would make the left hand line horizontal). Similar to θ_1, θ_2 rotates the position of the AMBs in the right hand line clockwise about the (empty) point of the V, while keeping the AMB direction constant. We consider the mixing ability of array configurations with $\theta_1, \theta_2 = 0, -\pi/4, -\pi/2$ and θ_3 ranging from 0 to $7\pi/4$ in divisions of $\pi/4$.

Figure 4.1: The three AMB array designs we analyse for their mixing ability. The centre of each black arrow marks the centre of an AMB and the arrow direction indicates the direction the AMB opening points. For each of the three designs, multiple values will be prescribed for the parameters θ_1, θ_2 and θ_3, so that we can study multiple variations of these three starting configurations. For all designs, θ_3 rotates the entire array (so all the AMBs) around a point in the centre of the array. The three designs in these sub figures correspond to $\theta_1 = \theta_2 = \theta_3 = 0$. The green arrow marks the direction of the base flow, which remains in this direction for all values of θ_1, θ_2 and θ_3.

Our theoretical results indicate that the position of the two fluid boundary relative to the AMB array affects the mixing efficiency. If there is a circulation in the flow, it will benefit mixing if it is able to pull in both fluids rather than just rotating one of them. The position of the boundary affects which local features stretch and contract and by how much (see Fig.4.2), although some arrays (like the long left/right array) do have wide bands of similar boundary stretching. The two biggest differences in behaviour is that either the boundary is stretched but passes out the other side of the array or it is pulled and caught in local vortices. These vortices are close to the AMBs and behave like sinks, which do not conserve mass. The sinks arise due to inaccuracies in our numerical model close to the AMBs (as we used the far-field approximation for the AMBs) and in this region, vertical motion in particular is more important so flow would have been able escape the circulation by moving out of plane, but this is not captured by our numerical model since it only evolves the material surface in a single plane.

We expect vortices to create the best mixing, particularly when the array is turned 'on' and 'off' as in the experiments. Local vortices can cause large stretching, however the boundary then became tightly wrapped (close to the AMBs where our model is weakest) so the diffusion length scale becomes significant. Using experimental values for the diffusivity D and the time T, the diffusion length scale $2\sqrt{DT} \approx 2\sqrt{10^{-9} \times 2} \sim 10^{-4}\,\mathrm{m}$ after two seconds, which is much larger than the gap size of order $10^{-6}\,\mathrm{m}$ between folds of the boundary in the tightly wrapped vortices (see Fig.4.2c). Thus for tightly wrapped vortices our mixing measure will overestimate the mixing ability. If the AMB strength is increased, corresponding to higher driving pressures, vortices would become larger in size thus potentially reducing this issue. However, unconstrained large vortices throw flow out sideways rather than capturing it thus the side walls became significant, but as these are not included in our model we do not consider higher driving pressures here.

Our analysis best compares the cases where the boundary passes completely through the array, which is particularly useful for a continuously actuated array as vortices trap fluid, delaying fluid from progressing out of the mixing region and down the channel even once it is mixed. In what follows we will focus on the cases where the boundary passes completely through the array by excluding any boundary lines where the front of the boundary remains within $30 \times 10^{-6}\,\mu\mathrm{m}$ of the last AMB in the array by the end of the simulation.

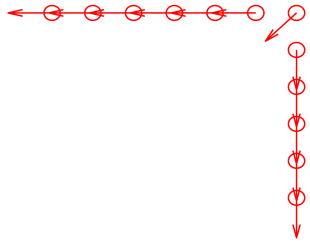

(a) The L-array with $\theta_1 = 3\pi/2, \theta_2 = \pi/2$ and $\theta_3 = \pi/2$. The circles indicates the AMB positions and the arrows the direction the bubble cap of the AMB points.

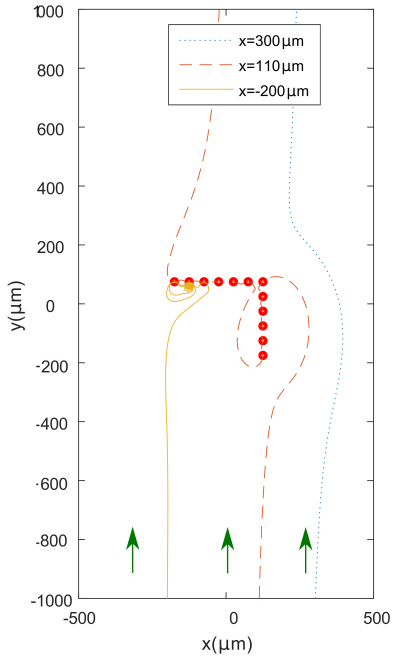

(b) Shape of the boundary as it passes through the array in (a) for three boundary starting positions.

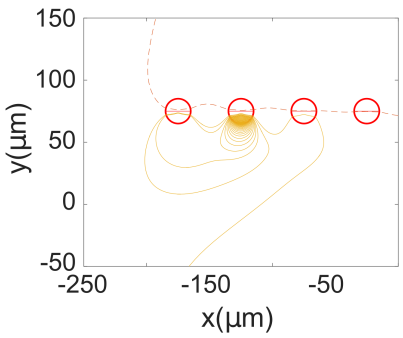

(c) Zoom in on the local vortex of b

Figure 4.2: Different line stretching around the AMB array.

4.4 Stretching to find best arrays

We will now use our mixing measure to study the mixing ability of the range of arrays in Fig.4.1. The time of each simulation will effect Λ since the boundary will spend more time away from the array. Therefore, the absolute value of Λ is unimportant but its relative size for different arrays and setups is important. Simulations ran for 2 s at a base flow rate of $1.2\,\mathrm{mms}^{-1}$ to best match experiments.

4.4.1 Local stretching

We first consider Λ for the experimental arrays for a range of boundary line positions (Fig.4.3).

In this scenario we found the best of the experimental arrays, from Fig.3.2, for mixing was a long left/right array followed closely by the tilted left/right array and then the experimental L-array. In addition the left/right array has a wide band of over $300\,\mu$m where a similar high level of stretching is observed, very useful for mixing when diffusion had smoothed out the concentration field at the fluid-fluid boundary.

The experimental V-array and line array, from Fig.3.2, have AMBs pointing into the flow, reducing the downstream flow speed and not significantly bending the flow (at this relatively low AMB strength), causing contraction of the boundary line. The V-array has a wide central band of $400\,\mu$m where the flow is caught in small local vortices. This might indicate a region of strong mixing (particularly for the case of the ultrasound turned on and off) since a wide band of fluid is caught there in local vortices. This does agree with experimental results where at low driving pressures the V-array is best. However, our numerical model cannot accurately analyse small local vortices (as discussed in §4.3) thus preventing rigorous comparison of the mixing effects of this feature with experiments.

As the starting position of the boundary line moves across the channel, the stretching mostly varies smoothly, with sharper spikes indicating sudden changes where the flow is caught by a new flow feature. The larger spikes further from the array distinguishes between the boundary line going through rather than around the array. Smaller spikes are caused by the boundary bending around local flow features differently (see Fig.4.4). Variations of $O(0.01)$ are errors arising from our numerical approach, namely the fineness of our line discretisation. This lack of smoothness of Λ impacts the optimisation of the mixers as experimentally the setup will vary from the theoretical optimal, and if that optimal is unstable because it is at one of the spikes so that small position perturbations significantly reduce the mixing, the experimental realisability of the theoretical optimal may be difficult. Also, experimentally diffusion causes the fluid-fluid boundary to become a region rather than a distinct line, thus stretching in a thin band could be physically important, so this is another reason why a theoretical optimum

at a spike could impact experimentally realising the optimum. Therefore, trying to identify an optimum with a band of good mixing is important but the best width of band to use would require further analysis.

4.4.2 Comparing arrays for mixing

Comparisons of the relative stretching for the orientations of the numerical configurations introduced in Fig.4.1 are shown in Fig.4.5, 4.6 and 4.7. We aim to identify groups of arrays that have large relative length, and thus we predict will produce better mixing. We will not specifically order the array origination from best to worst based off small variations in their stretching, as due to the number of assumptions with our model this cannot be justified.

The numerical L configuration reaches a maximum $\bar{\Lambda}$=1.45 (to 2dp), see Fig.4.5. A similar maximum is reached for each θ_3 when the two rows of AMBs point along their own line with both lines pointing towards their corner or away. (Although only one of these two orientations provides the maximum $\bar{\Lambda}$ at each θ_3 the other only has a slightly lower $\bar{\Lambda}$.) Two of these best L-arrays are shown in Fig.4.8. These arrays are optimum because the flow is pushed around the circulation created by one row of AMBs and then into the circulation of the other AMB row before continuing downstream. The minima occurs when the row of AMBs across the channel are pointing into the flow and the other row across the flow, so the flow is slowed by one row and only slightly bent by the other row.

The numerical V configuration obtains a slightly lower $\bar{\Lambda}$ than the numerical L configuration of $\bar{\Lambda} = 1.39$ (to 2dp). This occurs when the experimental or inverted V (see Fig.4.9a) is perpendicular to the base flow, and the flow pushes the boundary line down one of the rows of AMBs and across the channel. This is only slightly less with a jinked V (see Fig.4.9b) and the V jinked the other way so θ_1 and θ_2 are $-\pi/4$ smaller. (We note that due to the system symmetry $\theta_3 = \pi/2, 3\pi/2$ are analogous). Configurations perpendicular to the base flow on average produced better mixing . However, this setup has many cases where flow gets caught in small vortices close to the array, similar to the experimental V, for example when

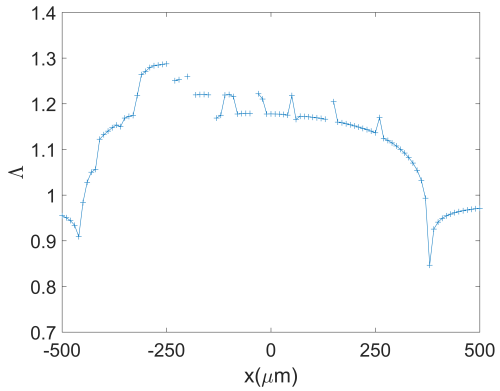

(a) Numerical L-array with $\theta_1 = \theta_2 = 0$ with $\theta_3 = \frac{3\pi}{2}$ corresponding to the experimental L-array.

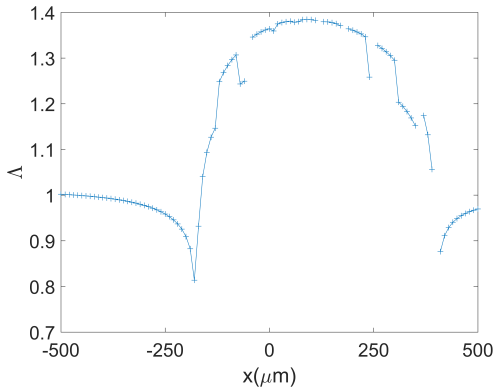

(b) Numerical opposite line mixer with $\theta_1 = -\frac{\pi}{4}$, $\theta_2 = -\frac{\pi}{4}$ and $\theta_3 = \frac{3\pi}{2}$ corresponding to the experimental left/right array.

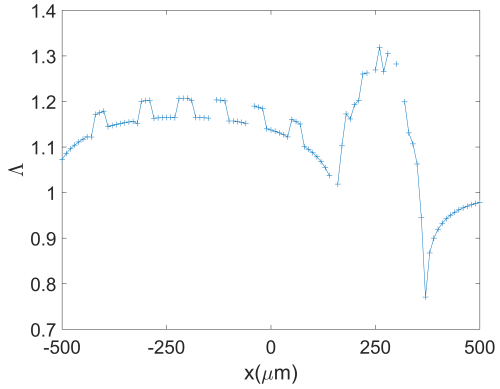

(c) Numerical opposite line mixer with $\theta_1 = -\frac{\pi}{4}$, $\theta_2 = -\frac{\pi}{4}$ and $\theta_3 = \frac{\pi}{4}$ corresponding to the experimental tilted left/right array.

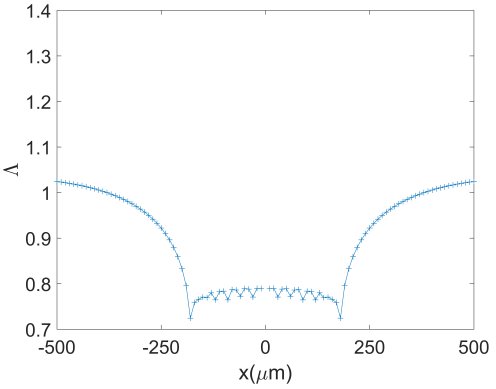

(d) Numerical V-array with $\theta_1 = -\frac{\pi}{4}$, $\theta_2 = -\frac{\pi}{4}$ and $\theta_3 = \pi$ corresponding to the experimental line array

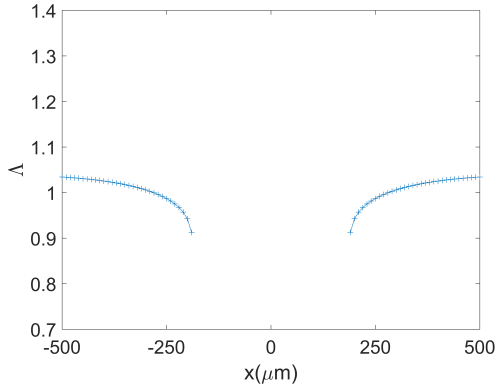

(e) Numerical V-array with $\theta_1 = 0$, $\theta_2 = 0$ and $\theta_3 = \pi$ corresponding to the experimental V-array.

Figure 4.3: Numerical mixing for each of the arrays studied experimentally.

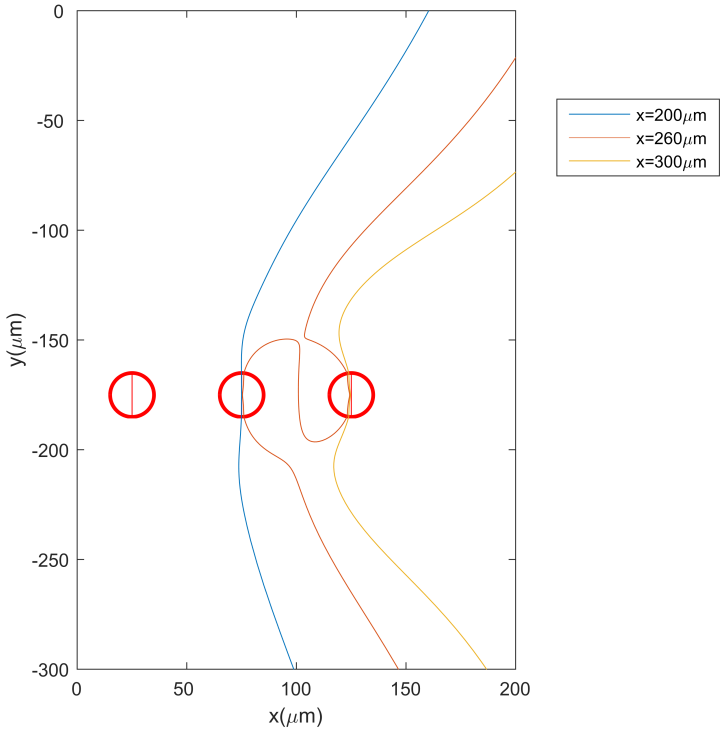

Figure 4.4: Example of variations causing a local spike

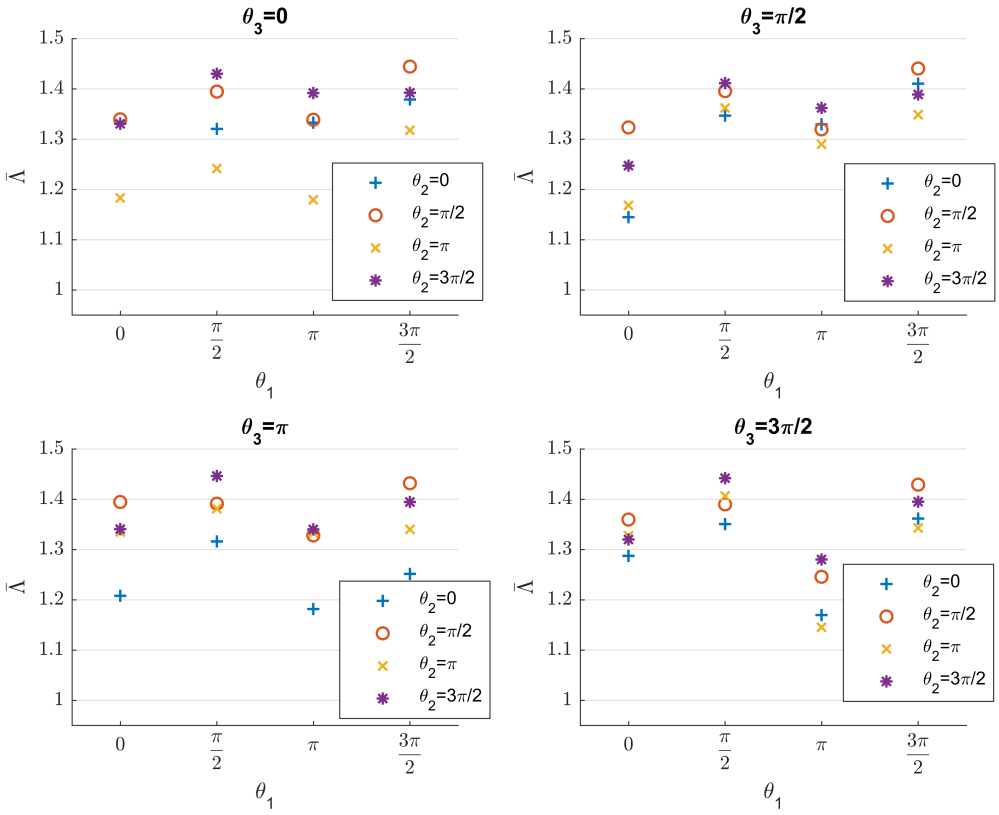

Figure 4.5: Line stretching for rotations of the numerical L-array

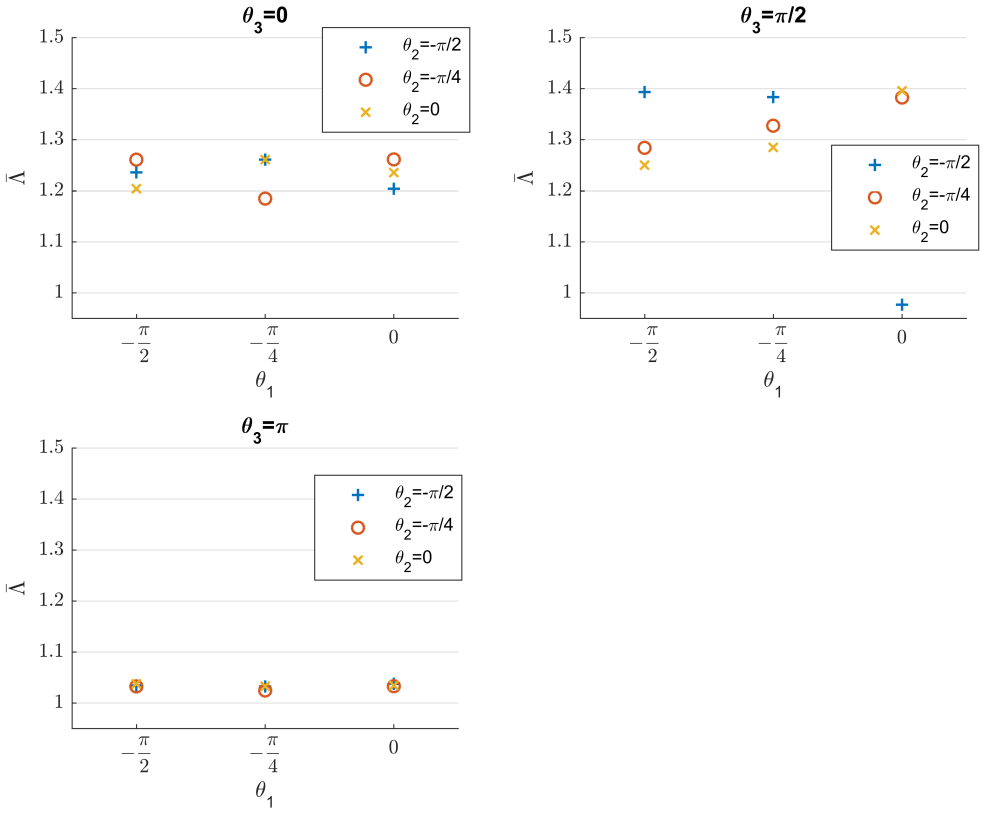

Figure 4.6: Line stretching for rotations of the numerical V-array. Then setting $\theta_3 = 3\pi/2$ is equivalent to $\theta_3 = \pi/2$ due to channel symmetry so is not shown here.

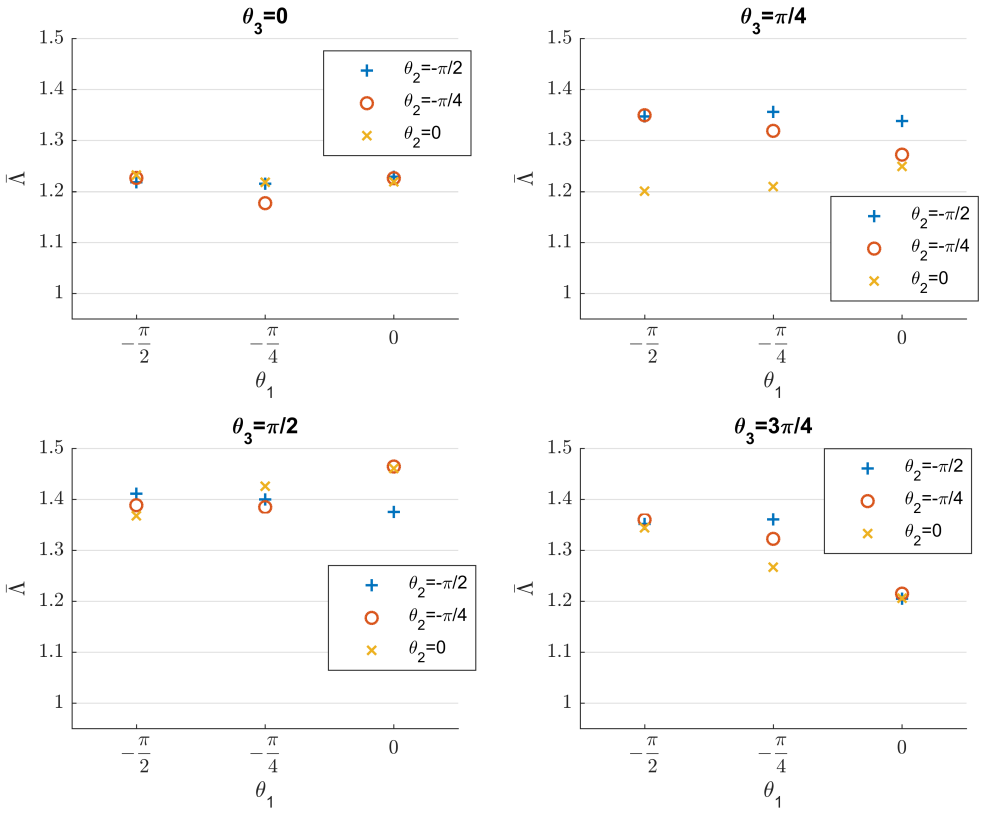

Figure 4.7: Line stretching for rotations of the numerical opposite direction array. Setting $\theta_3 = \pi$ is equivalent to $\theta_3 = 0$, $\theta_3 = 3\pi/2$ is equivalent to $\theta_3 = \pi/2$, $\theta_3 = 5\pi/4$ is equivalent to $\theta_3 = \pi/4$ and finally $\theta_3 = 7\pi/4$ is equivalent to $\theta_3 = 3\pi/4$ due to channel symmetry so are not shown here

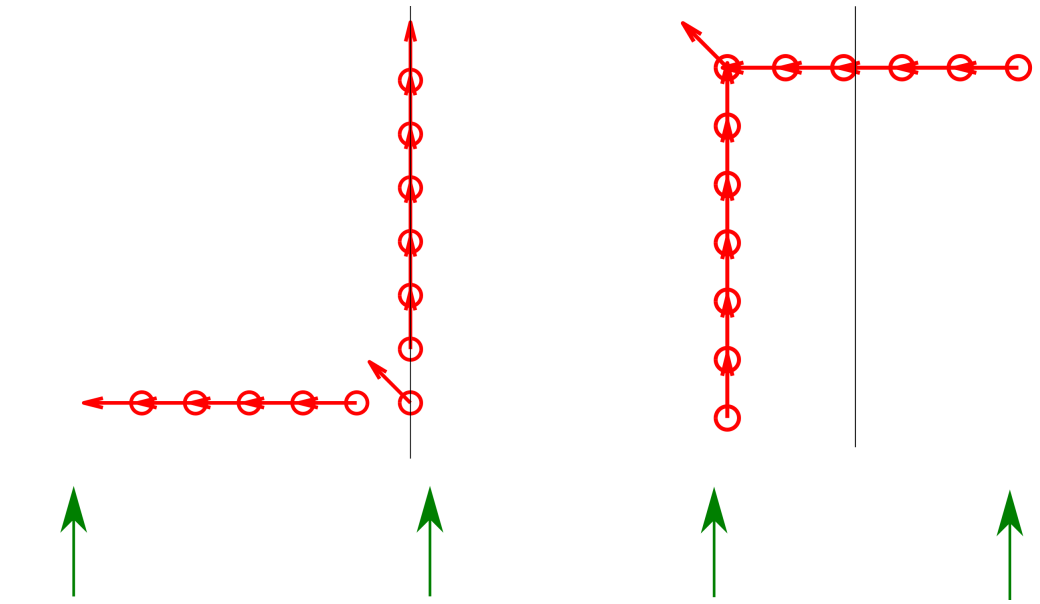

(a) Configuration corresponding to $\theta_3 = 0, \theta_1 = 3\pi/2, \theta_2 = \pi/2$

(b) Configuration corresponding to $\theta_3 = \pi, \theta_1 = \pi/2, \theta_2 = 3\pi/2$

Figure 4.8: The two L arrays producing the greatest stretching.

$\theta_1 = -\pi/2, \theta_2 = 0, \theta_3 = 3\pi/2$ for most boundary starting positions. Although, $\theta_3 = \pi$ has very low $\bar{\Lambda}$ for a different reason, in that the AMBs pointing into the flow slow the flow down and push incoming fluid (and the boundary line) around the array instead, and while there are small circulations close to the array, the downstream flow does not interact with these.

The opposite direction array has the largest $\bar{\Lambda}$ of $\bar{\Lambda} = 1.46$ (to 2dp). This maximum is obtained by a left/right V (see Fig.4.10a) and a jinked left/right V (see Fig.4.10b). In these cases, the boundary is pushed across the channel in one direction by the first row of AMBs and then across the channel in the opposite direction by the second row of AMBs pointing in the opposite direction. We note that due to the system symmetry $\theta_3 = \pi/2, 3\pi/2$ are analogous, as are $\theta_3 = 0, \pi$ and $\theta_3 = 5\pi/4, \pi/4$ and $\theta_3 = 7\pi/4, 3\pi/4$. In general, better mixing is obtained by having the AMBs pointing perpendicular to the direction of flow. The worst mixing is generally obtained when $\theta_3 = 0$, so the AMBs are pointing parallel to the direction of flow. Here the boundary is either sped up as it is pushed through the array where the AMBs are pointing with the flow, or the AMBs pointing against the flow slow the boundary down but push the boundary around this half of the array. Both cases only cause slight stretching and the movement around AMBs pointing into the flow suggest small circulations forming close to these AMBs.

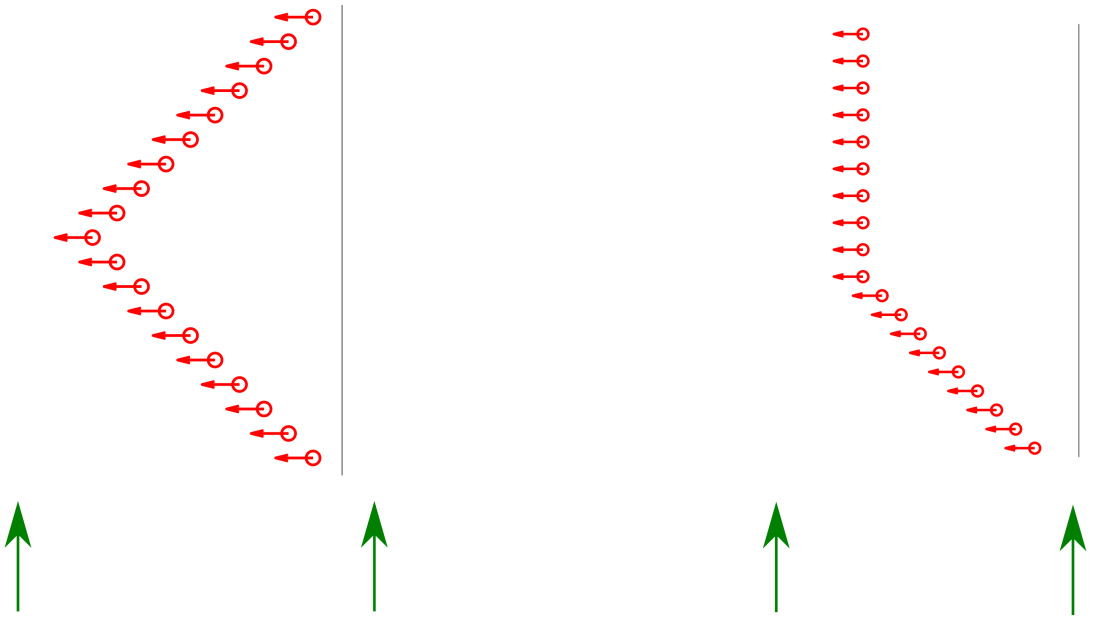

(a) Inverted V

(b) Configuration corresponding to $\theta_1 = 0, \theta_2 = -\pi/4, \theta_3 = \pi/2$.

Figure 4.9: Two better V-arrays.

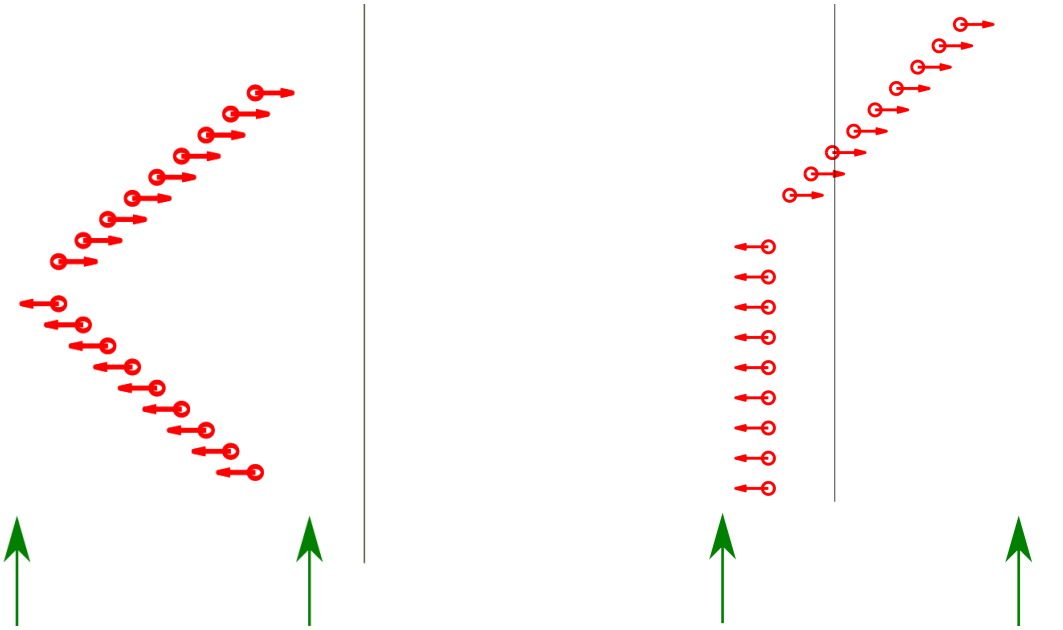

(a) Left/right V

(b) Jinked V: $\theta_1 = -\pi/2, \theta_2 = -\pi/4, \theta_3 = 3\pi/2$.

Figure 4.10: Two best opposite direction arrays

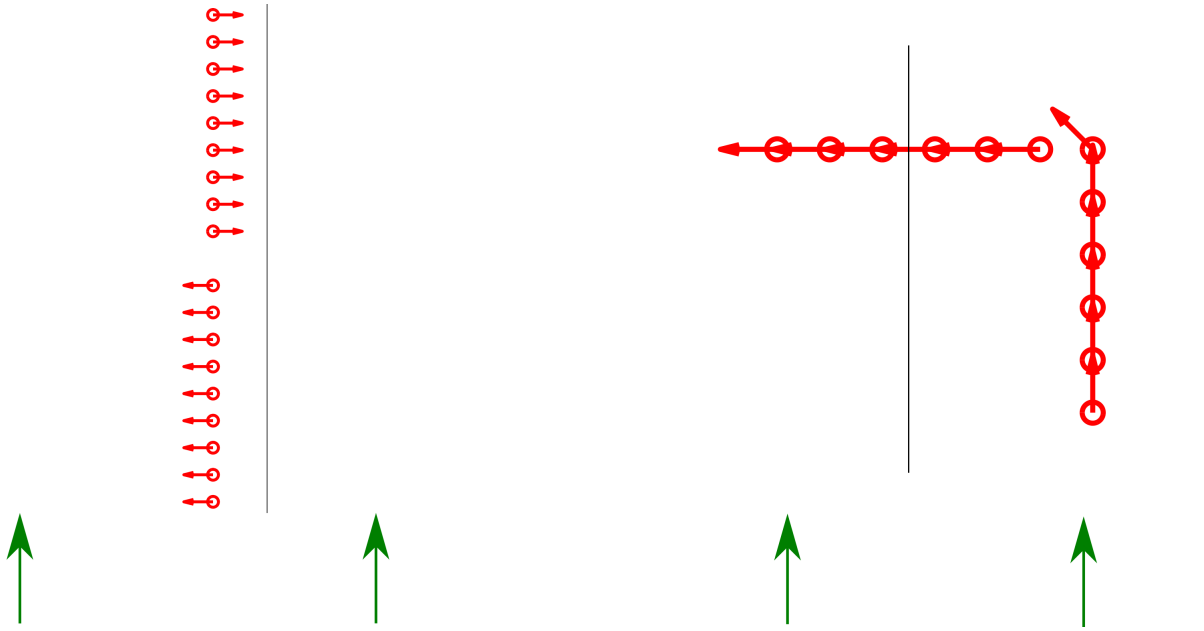

(a) Long left/right array

(b) Configuration corresponding to $\theta_1 = 3\pi/2, \theta_2 = 3\pi/2, \theta_3 = \pi/2$

Figure 4.11: Two best average arrays

Therefore, the best arrays, with similar levels of stretching, are obtained by the opposite direction arrays and the L array variations shown in Fig.4.8 and Fig.4.10.

In general these best arrays only obtain this maximum relative length within a small width of boundary position across the channel, with the stretching dropping off quickly away from the optimal boundary position or having the flow caught in local vortices instead. This is a problem once diffusion has smudged the boundary significantly and if, for example, these theoretically good mixing arrays were used as blueprints for constructing large arrays with high efficiency through replication. To analyse this we took an average of the stretching for boundary starting positions within a 100 μm band, for every band contained within the 1 mm channel, and compared this maximum average relative length for every configuration. The average maximum stretching is still achieved by the opposite direction and L arrays. The maximum stretching is 1.38 for the opposite direction array, with the long experimental left/right array. The maximum stretching by the numerical L-array is 1.39 obtained with both lines of AMBs pointing along their row length but in opposite direction (decreasing to 1.38 depending on which row points towards the centre and which away for each θ_3) see Fig.4.11.

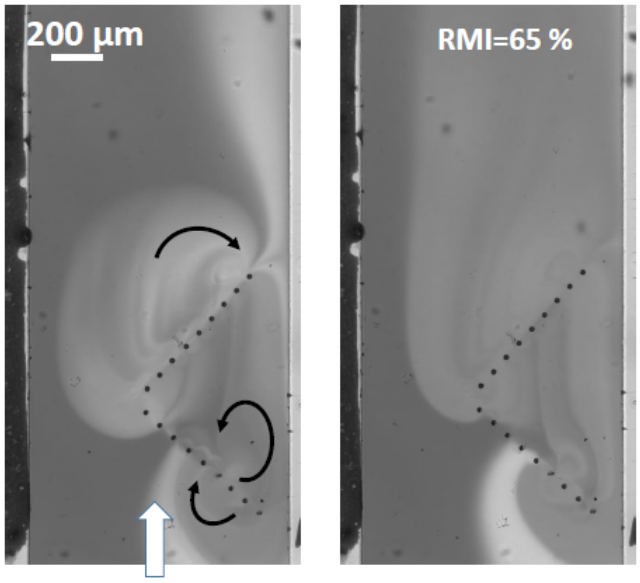

(a) Modified left/right array, $P_{ac} = 537$ kPa (by Nicolas Bertin)

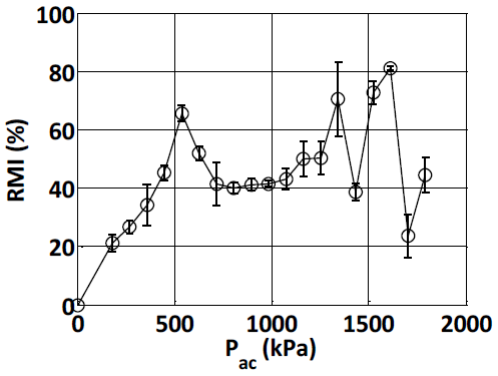

(b) Mixing efficiency against acoustic driving pressure P_{ac} (by Nicolas Bertin).

Figure 4.12: Mixing efficiency of the modified left/right array

4.5 Comparison to experiments

To demonstrate physical correspondence of this method, two of the best theoretical arrays were tested in the experimental setup discussed in §4.1. When choosing which of our theoretically best arrays to test experimentally, we chose ones where the AMBs did not point into the flow as experimentally AMBs pointing into the base flow had a shorted bubble lifespan. The experiments were performed for the left-right array of Fig.4.10a and an L-array with the AMBs pointing along each row of AMBs away from the corner, a 90 degree rotation of Fig.4.8a.

Experimentally, the modified left-right array demonstrated very strong mixing at low driving pressures (see Fig.4.12) reaching RMI= 65.5% at the low acoustic pressure of $P_{ac} = 537$ kPa. This is one of the highest RMIs of the experimental arrays at this driving pressure. However, at higher pressures the AMBs pointing to the right lost their bubbles. The modified L-array only reached RMI=37% at $P_{ac} = 448$ kPa (see Fig.4.13) but this is better than the original experimental L-array at low driving pressures. However, it suffered severely from the unexpected issue of the horizontal row of AMBs pointing across the channel having a short bubble lifespan.

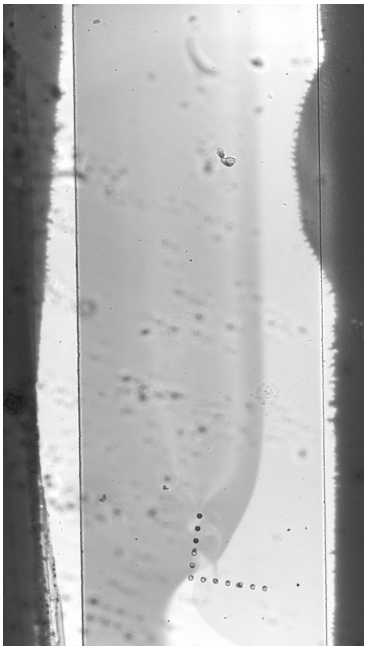

(a) Modified L-array (by Nicolas Bertin)

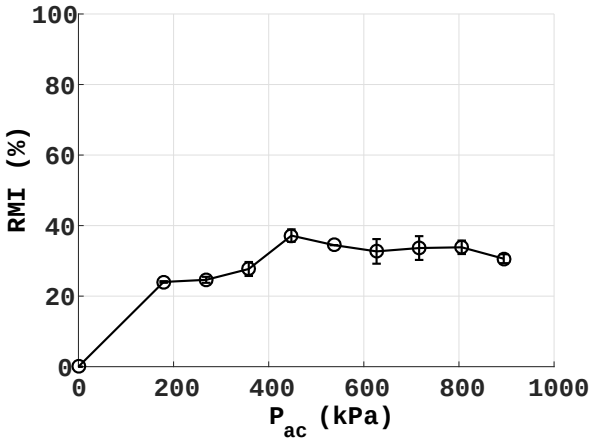

(b) Mixing efficiency against P_{ac}(by Nicolas Bertin).

Figure 4.13: Mixing efficiency of a modified L-array

4.6 Conclusions and future outlooks

In this chapter, we have presented a numerically method for analysing the mixing potential of AMB arrays by studying the stretching of the boundary between the two fluids. Our method is fast so can analyse many AMB arrays quickly. However, the flow field model ignores the concentration field and the side walls of the channel, which introduces inaccuracies, particularly at later times when diffusion has had longer to smooth out the fluid-fluid boundary and close to the side walls. Also, in our numerical model, vortices appear as sinks (due to out-of-plane motion being ignored), which is unphysical, thus we limited this study by ignoring all cases where the fluid-fluid boundary becomes trapped in vortices. Additionally, our simple mixing measure ignores shear near the fluid-fluid boundary and also the concentration field, and thus ignores multiple physical features, which contribute to the mixing. These inaccuracies mean only general trends and results should be drawn from the data, and small differences and variation should be ignored. From our results we identified groups of theoretically good arrays in Fig.4.8 and Fig.4.10. Two of these were tested experimentally to demonstrate physical correspondence of the numerical model, and the modified left/right array in particular, demonstrated very strong mixing experimentally at low driving pressures.

We have identified a number of weaknesses with our model, and future work could extend

the model to address some of these weaknesses and more accurately capture behaviour within vortices. Also, adding the side walls to our numerical flow field would additionally allow us to model the mixing at higher driving pressures, where the confining effects of the side walls are more noticeable. Also, the mixing measure could be adapted to incorporate fluid already within the AMB array when the ultrasound is turned on. Further experimental work may include making the printed capsules hydrophobic to tackle the bubble lifespan issues.

Part III

Artificial Cilium

Chapter 5

Magnetically actuated permanently magnetised cilium

In this chapter we model the motion and optimal working conditions of a permanently magnetised cilium driven by a magnetic field. We shall first present the experimental motivation for this work in §5.1. We shall then consider our cilium setup in §5.2 before discussing our force model in §5.3 followed by the equilibrium model and asymptotics we use primarily to validate it in §5.4. Finally in §5.5, we consider the force exerted by the beat pattern of the cilium on the surrounding fluid, as the two important non-dimensional parameters are varied.

5.1 Experimental motivation

The theoretical work in this chapter was motivated by an experimental cilium designed by Tsumori et. al [1]. They mixed pure iron powder filings (of diameter $4.3\,\mu$m) with liquid PDMS to reach 5 vol%, and then spread this mixture on a substrate to a make a $90\,\mu$m thick sheet. They then applied a magnetic field to the sheet so the iron filings became aligned in the same direction, and then cured it. Cilia of height and width $1.5\,\text{mm} \times 4\,\text{mm}$ were then cut from the sheet, and stuck to a substrate.

These cilia are not microscale so in order to reduce the Reynolds number, experiments were performed in glycerol at a Reynolds number of 2.6×10^{-3}. When a magnetic field is turned on, a force is applied to the iron filings pushing them to align with the magnetic field, causing the cilium to bend. Under a magnetic field rotating in a plane containing the cilium, the cilium undergoes a beat pattern (see Fig.5.1) similar to that observed in nature [27].

The iron filings can be aligned at any angle to the cilium tangent (within the plane of the rotating magnetic field). In Ref.[1] they specifically consider 3 different angles of $\pm 30^o$ and

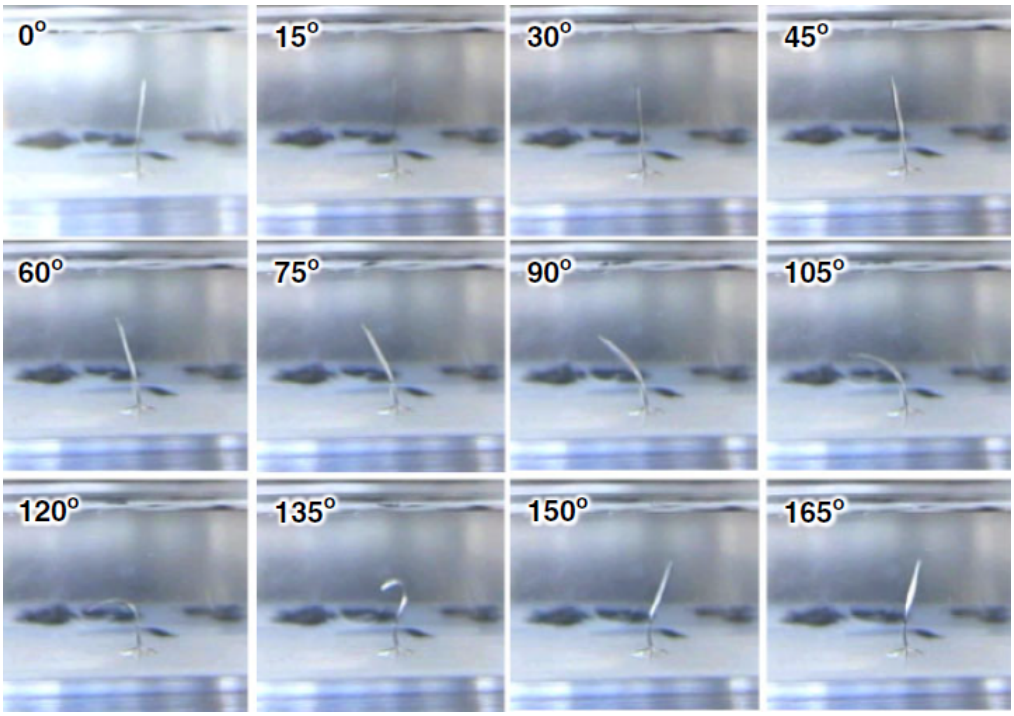

Figure 5.1: Actuation of the experimental artificial cilium reproduced from: Development of actuation system for artificial cilia with magnetic elastomer, F. Tsumori, A. Saijou, T. Osada and H. Miura, *Jpn. J Appl Phys.*, 2015, 54:06FP12 [1]. Copyright 2015 The Japan Society of Applied Physics.

0^o. The angle causes a phase delay in the response of the cilium to the rotating magnetic field. As such this provides an inbuilt mechanism to generate a metachronal wave with many adjacent cilia, by having the iron filings aligned at an increasing angle for cilia based further along the line, as demonstrated in Ref.[6].

There is further experimental work to be undertaken in improving the fabrication method and decreasing the cilium size. However, this is a new design for an artificial cilium, whose physical behaviour in different conditions is not known. We will now consider a similar cilium numerically and analytically, with the goal of determining its stroke shape and the net force the cilium applies to the surrounding fluid across the full range of ζ and Sp (the two important non-dimensional parameters).

5.2 Setup

In this section we will present the general setup for the problem and the important non-dimensional parameters. All the experiments with the discussed cilium design used iron fil-

ings, which are ferromagnetic [102]. However, in this analysis, we will consider embedded permanently magnetised powder.

The mathematics for a ferromagnetic cilium contains a singularity. The moment on an iron filing in a fixed magnetic field pushes the filing to align with the magnetic field. Mathematically the moment is $\underline{\mu} \times \underline{B}$, for $\underline{\mu}$ the magnetic dipole of the iron filing and $\underline{B}$ the magnetic field. Due to the geometry of an iron filing (long and thin), it can only be magnetised along its length, but which way along its length will change so that the magnetic dipole always has a positive component in the direction of the magnetic field. A cross product is theoretically maximal when the two vectors are perpendicular, so when the iron filing is perpendicular to the magnetic field. If the iron filing is perturbed clockwise away from this perpendicular position , the direction of the magnetic dipole will be in a direction such that the filing will continue rotating clockwise to align with the magnetic field, and if it is perturbed anti-clockwise the magnetic dipole will be in the opposite direction so the filing will continue rotating anti-clockwise to align with the magnetic field. Thus there is a singularity in the numerics whenever any of the iron filings in the cilium are perpendicular to the magnetic field., as such permanently magnetised powder (which has no such singularity) is a simpler first step, and future work could include extending this model to the experimental ferromagnetic cilium.

5.2.1 Cilium parametrisation

We will model our cilium in 2D, in the plane of the magnetic field rotation. We model a cilium of length L and of negligible width and depth, see Fig.5.2. We assume that the metal filings are at an additional anticlockwise angle χ to the cilium tangent, and that this angle is fixed for any one cilium. We assume the cilium has uniform elastic properties, despite it being a composite of metal filings and PDMS, with constant Young's modulus E. The moment of inertia of the cilium cross-section, I, is also assumed to be constant along the length of the cilium.

We define the vertical direction, $\underline{e}_y$, as the direction parallel to the cilium base and we define the horizontal direction, $\underline{e}_x$, as the direction perpendicular to the cilium base. These are shown in Fig.5.2.

The magnetic field $\underline{B}$ will force the cilium. At any time t it will be at an angle $\Phi(t)$ to the horizontal and it rotates with a fixed angular frequency ω. The magnetic field remains at constant magnitude and at any fixed time is taken to be uniform. The magnetic dipole, μ of the magnetic filings in the cilium, is in the direction of the metal filings, which is $\chi + \alpha$, and has strength μ_0 so

$$\underline{\mu} = \mu_0 \begin{pmatrix} \cos(\alpha+\chi) \\ \sin(\alpha+\chi) \end{pmatrix}. \tag{5.1}$$

We will then define $H = \mu_0|\underline{B}|/L$, which is the quantity determining the total strength of the magnetic field acting on our cilium.

This cilium is working at low Reynolds number so the hydrodynamic drag from the fluid can be estimated using C_N and C_T, the normal and tangential drag coefficients [103].

We parametrise the distance along the cilium by s and we define $\alpha(s,t)$ as the angle of the cilium tangent to the horizontal at time t. The position of the cilium given by $\underline{r}(s,t) = (x(s,t), y(s,t))$ is determined by α, where

$$x(s,t) = \int_0^s \cos(\alpha(s',t))\mathrm{d}s', \tag{5.2}$$

$$y(s,t) = \int_0^s \sin(\alpha(s',t))\mathrm{d}s', \tag{5.3}$$

where we assume the base of the filament is at the origin. Then, taking derivatives, gives the tangent

$$\underline{t} = \frac{\partial \underline{r}}{\partial s} = \begin{pmatrix} \cos(\alpha) \\ \sin(\alpha) \end{pmatrix}, \tag{5.4}$$

and normal

$$\underline{n} = \begin{pmatrix} -\sin(\alpha) \\ \cos(\alpha) \end{pmatrix}, \tag{5.5}$$

to the cilium, which are both shown in Fig.5.2. This parametrisation with respect to α is useful since it satisfies the condition of no-extension of the cilium length, so $\underline{t} \cdot \underline{t} = 1$.

5.2.2 Non-dimensional Parameters

There are three non-dimensional parameters important to this problem: ζ is the ratio of elastic to magnetic forces

$$\zeta = \frac{EI}{HL^2}; \tag{5.6}$$

the Sperm number is the ratio of elastic to drag forces

$$Sp = L\left(\frac{C_N \omega}{EI}\right)^{\frac{1}{4}}; \tag{5.7}$$

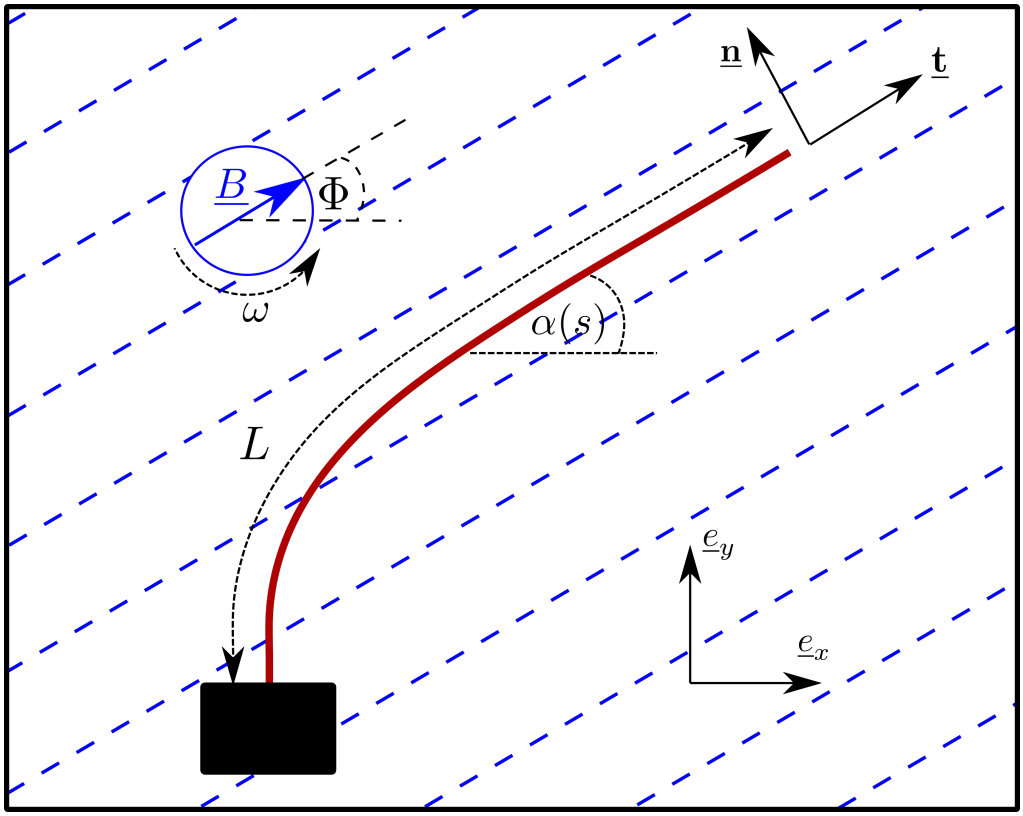

Figure 5.2: A cilium of length L and clamped at its base, parametrised by α, being bent under a magnetic field $\underline{B}$ which is at an angle Φ to the horizontal (at any fixed time) and rotating at an angular frequency ω. The coordinate system is defined by the normal $\underline{n}$ and the tangent $\underline{t}$ to the cilium.

and finally, the ratio of the normal to tangential drag coefficient

$$C_{NT} = \frac{C_N}{C_T}. \tag{5.8}$$

Throughout this chapter we will keep $C_{NT} = 2$. This is a standard approximation for a long thin filament [29, 103], although other values as low as 1.4 have also been used [30, 104].

5.2.3 Effect of the angle of the magnetic filings

The torque exerted on each magnetic filing individually by the magnetic field is given by $\underline{\mu} \times \underline{B}$. Multiplying out the cross product, rearranging and factorising gives

$$\underline{\mu} \times \underline{B} = \mu_0 \begin{pmatrix} \cos(\alpha+\chi) \\ \sin(\alpha+\chi) \end{pmatrix} \times \begin{pmatrix} |B|\cos(\Phi) \\ |B|\sin(\Phi) \end{pmatrix} \tag{5.9}$$

$$= \mu_0 \begin{pmatrix} \cos(\alpha) \\ \sin(\alpha) \end{pmatrix} \times \begin{pmatrix} |B|\cos(\Phi-\chi) \\ |B|\sin(\Phi-\chi) \end{pmatrix}. \tag{5.10}$$

Therefore, having the metal filings at an angle χ to the cilium when a magnetic force $\underline{B}$ is applied at an angle Φ is equivalent to having the metal filings parallel to the cilium and applying the magnetic field at an angle $\Phi - \chi$. So having the metal filings at an angle only causes a phase lag on the magnetic field direction. Since we are rotating the magnetic field at a constant speed and are interested in the steady state position of the cilium we will now assume $\chi = 0$ so the metal filings are aligned with the tangent of the cilium.

We are aware that the phase delay would also have affected the relative starting potion of the magnetic field when it is turned on so affects our initial condition, which could affect the speed and which steady state the cilium approaches. At small Sperm number we do not believe alternative steady states exist due to the equilibrium validation we will discuss in §5.4, and at high Sperm number it takes many rotations to settle to a steady state, so again we do not anticipate other stable states. Although it is a possibility we feel it is unlikely other steady states exist even at middle Sperm number and the existence of alternative cilium steady states is not considered here.

5.3 Force model

To determine the cilium motion we use a force model balancing the magnetic forces driving the cilium motion, the cilium elastic properties resisting bending and hydrodynamic drag forces. Our model is based on that derived by Hines et. al. [29] for a biological self-propelled

flagellum confined to a plane (as such the derivation will only be outlined below). Our variation is in choosing boundary conditions appropriate for a cilium fixed at its base (similar to [30]) and the addition of a magnetic forcing term, in place of a biological internal forcing mechanism.

5.3.1 Force model governing equations

5.3.1.1 Force, moment and velocity equations

The requirement that the cilium does not accelerate (due to the low Reynolds number) gives the force balance

$$\frac{\partial \underline{F}}{\partial s} = C_N V_N \underline{n} + C_T V_T \underline{t}, \tag{5.11}$$

where $\underline{F}$ is the force on the filament, V_N is the normal velocity and V_T is the tangential velocity.

The next requirement is that the cilium has no angular acceleration and thus the total torque acting on it is zero. We consider cutting the cilium at a distance s along its length and calculate the moment at its new end, around the out of plane axis. The moments acting at this new end can be separated into moments from the magnetic field M_m, drag M_d and the internal moment M (arising from the the stiffness of the cilium, which we define later in Eq. 5.26). To meet the torque free condition at the cut end, $M_m + M_t + M = 0$. On each magnetic filing within the cilium, the magnetic field applies a moment, pushing the filing to align with the magnetic field. We assume the centre of this rotation is the centre of the filing, thus the magnetic filing feels the effect of a couple, providing a total moment of $\underline{\mu} \times \underline{B}$ (where the magnetic filings are aligned along the cilium so $\underline{\mu} = \mu_0 \underline{t}$). Since the magnetic filings have a couple acting on them, this is the moment irrespective of where the moment is calculated around. Thus, the total moment generated by the magnetic field is a summation of the magnetic moments on all the filings within the cilium, but using a continuum assumption on the density of the filings gives the integral $\left[\frac{1}{L}\int_0^s \mu_0 (\underline{t} \times \underline{B}) ds'\right]$, so

$$\frac{\partial M_m}{\partial s} = \frac{\mu_0}{L} (\underline{t} \times \underline{B}) \cdot \underline{z}, \tag{5.12}$$

where $\underline{z}$ is the vector out of the plane (with direction given by the right-hand rule). Following the work of Hines et. al. [29], the moment from the drag coefficients can be calculated. We define $\underline{\phi} \delta s = -(C_N V_N \underline{n} + C_T V_T \underline{t}) \delta s$, so $\underline{\phi} = -\frac{\partial \underline{F}}{\partial s}$. The moment from the drag is then

$$M_t = \underline{z} \cdot \int_0^s \left[(r(s',t) - r(s,t)) \times \phi(s',t) \right] ds', \tag{5.13}$$

so that differentiating gives

$$\frac{\partial M_t}{\partial s} = (\underline{t} \times \underline{F}) \cdot \underline{z}. \tag{5.14}$$

Therefore, the moment balance equation is

$$\frac{\partial M}{\partial s} + \left[\underline{t} \times \underline{F} + \frac{\mu_0}{L} \underline{t} \times \underline{B}\right] \cdot \underline{z} = 0. \tag{5.15}$$

We can define the velocity of the cilium, alternatively to Eq. 5.11, as

$$\frac{\partial \underline{r}}{\partial t} = V_N \underline{n} + V_T \underline{t}, \tag{5.16}$$

and taking spatial derivatives (with respect to ds) of both sides gives

$$\frac{\partial \alpha}{\partial t} \underline{n} = \left(\frac{\partial V_N}{\partial s} + V_T \frac{\partial \alpha}{\partial s}\right) \underline{n} + \left(\frac{\partial V_T}{\partial s} - V_N \frac{\partial \alpha}{\partial s}\right) \underline{t}, \tag{5.17}$$

giving us two equations for V_N and V_T,

$$\frac{\partial V_T}{\partial s} = V_N \frac{\partial \alpha}{\partial s}, \tag{5.18}$$

$$\frac{\partial \alpha}{\partial t} = \frac{\partial V_N}{\partial s} + V_T \frac{\partial \alpha}{\partial s}. \tag{5.19}$$

This now gives us five equations Eq.5.15, Eq.5.11, Eq.5.18 and Eq.5.19 for five unknowns V_N,V_T, α and $\underline{F}$ (where $\underline{F}$ and Eq. 5.11 both have two components).

5.3.1.2 Rearranging to numerically solvable form

We decompose the force into its normal and tangential components

$$\underline{F} = F_N \underline{n} + \underline{F}_T \underline{t}. \tag{5.20}$$

The force balance, Eq.5.11, then becomes

$$\frac{\partial F_N}{\partial s} + F_T \frac{\partial \alpha}{\partial s} = C_N V_N, \tag{5.21}$$

$$\frac{\partial F_T}{\partial s} - F_N \frac{\partial \alpha}{\partial s} = C_T V_T. \tag{5.22}$$

Substituting these forms for V_N and V_T into Eq.5.18 and Eq.5.19 gives

$$\frac{\partial^2 F_T}{\partial s^2} = \left(1+\frac{C_T}{C_N}\right)\left(\frac{\partial F_N}{\partial s}\right)\left(\frac{\partial \alpha}{\partial s}\right) + \left(\frac{C_T}{C_N}\right) F_T \left(\frac{\partial \alpha}{\partial s}\right)^2 + F_N\left(\frac{\partial^2 \alpha}{\partial s^2}\right), \tag{5.23}$$

$$\frac{\partial^2 F_N}{\partial s^2} = C_N \frac{\partial \alpha}{\partial t} - \left(1+\frac{C_N}{C_T}\right)\left(\frac{\partial F_T}{\partial s}\right)\left(\frac{\partial \alpha}{\partial s}\right) + \left(\frac{C_N}{C_T}\right) F_N \left(\frac{\partial \alpha}{\partial s}\right)^2 - F_T \frac{\partial^2 \alpha}{\partial s^2}. \tag{5.24}$$

Rewriting the moment equation (Eq.5.15) in terms of Φ and α,

$$\frac{\partial M}{\partial s} + F_N + H\sin(\Phi-\alpha) = 0. \tag{5.25}$$

We can alternatively determine the moment in terms of the stiffness of the filament giving a relationship between the moment and the curvature of the filament κ (where the curvature is defined through the cilium tangent $\partial \underline{t}/\partial s = \kappa \underline{n}$ so $\kappa^2 = \left|\partial^2 r/\partial s^2\right|^2$) giving

$$\frac{\partial M}{\partial s} = EI\frac{\partial \kappa}{\partial s} = EI\frac{\partial \alpha^2}{\partial s}. \tag{5.26}$$

Then equating the two forms of the moment equation gives

$$-F_N = EI\frac{\partial \alpha^2}{\partial s^2} + H\sin(\Phi-\alpha). \tag{5.27}$$

Substituting Eq.5.27 into Eq.5.23 and Eq.5.24 gives two equation for F_T and α

$$\frac{\partial^2 F_T}{\partial s^2} = \left(1+C_{NT}^{-1}\right)\left(-EI\frac{\partial^3 \alpha}{\partial s^3} + H\frac{\partial \alpha}{\partial s}\cos(\Phi-\alpha)\right)\left(\frac{\partial \alpha}{\partial s}\right) + \left(C_{NT}^{-1}\right) F_T \left(\frac{\partial \alpha}{\partial s}\right)^2 + \left[-EI\frac{\partial^2 \alpha}{\partial s^2} - H\sin(\Phi-\alpha)\right]\left(\frac{\partial^2 \alpha}{\partial s^2}\right), \tag{5.28}$$

$$-EI\frac{\partial^4 \alpha}{\partial s^4} + H\frac{\partial^2 \alpha}{\partial s^2}\cos(\Phi-\alpha) + H\left(\frac{\partial \alpha}{\partial s}\right)^2 \sin(\Phi-\alpha) = C_N\frac{\partial \alpha}{\partial t} - (1+C_{NT})\times \left(\frac{\partial F_T}{\partial s}\right)\left(\frac{\partial \alpha}{\partial s}\right) + (C_{NT})\left[-EI\frac{\partial^2 \alpha}{\partial s^2} - H\sin(\Phi-\alpha)\right]\left(\frac{\partial \alpha}{\partial s}\right)^2 - F_T\frac{\partial^2 \alpha}{\partial s^2}, \tag{5.29}$$

which, after non-dimensionalising, we will solve simultaneously, using an implicit numerical

method.

5.3.1.3 Non-dimensionalising the governing equation

We assume distance scales with L and time scales with ω^{-1}. We have $F_N \sim H$, so from Eq.5.20 it is implicit that $F_T \sim F_N \sim H$ as it would not make physical sense for them to scale differently. Then Eq.5.28 becomes

$$\frac{\partial^2 F_T^*}{\partial s^{*2}} = (1+C_{NT}^{-1})\left(-\zeta\frac{\partial^3\alpha}{\partial s^{*3}}+\frac{\partial\alpha}{\partial s^*}\cos(\Phi-\alpha)\right)\left(\frac{\partial\alpha}{\partial s^*}\right) + C_{NT}^{-1}F_T^*\left(\frac{\partial\alpha}{\partial s^*}\right)^2+\left[-\zeta\frac{\partial^2\alpha}{\partial s^{*2}}-\sin(\Phi-\alpha)\right]\left(\frac{\partial^2\alpha}{\partial s^{*2}}\right), \quad (5.30)$$

where * indicates a non-dimensional parameter, and Eq.5.29 becomes

$$-\zeta\frac{\partial^4\alpha}{\partial s^{*4}}+\frac{\partial^2\alpha}{\partial s^{*2}}\cos(\Phi-\alpha)+\left(\frac{\partial\alpha}{\partial s^*}\right)^2\sin(\Phi-\alpha)=\zeta\times Sp^4\times\frac{\partial\alpha}{\partial t^*} -(1+C_{NT})\left(\frac{\partial F_T^*}{\partial s^*}\right)\left(\frac{\partial\alpha}{\partial s^*}\right)+C_{NT}\left[-\zeta\frac{\partial^2\alpha}{\partial s^{*2}}-\sin(\Phi-\alpha)\right]\left(\frac{\partial\alpha}{\partial s^*}\right)^2-F_T^*\frac{\partial^2\alpha}{\partial s^{*2}}. \quad (5.31)$$

The motion is now dependent solely on our three non-dimensional quantities Sp, ζ and C_{NT}. For the rest of this section all quantities will be non-dimensional but the stars will be dropped for notational convenience.

5.3.1.4 Boundary conditions

We are solving a fourth-order equation in α and a second order equation in F_T, thus we require 6 boundary conditions. The cilium is force-free at the distal end giving

$$F_N(1,t)=0, \quad (5.32)$$

$$F_T(1,t)=0. \quad (5.33)$$

No drag at the anchor of the cilium gives, from Eq.5.21 and Eq.5.22, that

$$\frac{\partial F_N}{\partial s}(0,t)+F_T(0,t)\frac{\partial\alpha}{\partial s}(0,t)=0, \quad (5.34)$$

$$\frac{\partial F_T}{\partial s}(0,t) - F_N(0,t)\frac{\partial \alpha}{\partial s}(0,t) = 0. \tag{5.35}$$

We assume the anchor of the cilium is vertical,

$$\alpha(0,t) = \frac{\pi}{2}. \tag{5.36}$$

There is also zero moment at the distal end,

$$\frac{\partial \alpha}{\partial s}(1,t) = 0. \tag{5.37}$$

5.3.1.5 Numerical particulars

These equations were solved numerically in MATLAB using the implicit in time Crank-Nicolson finite difference method. This implicit method was chosen since it is well known these equations have strict stability criteria with an explicit method [29]. We took $n = 121$ discretised points on the cilium (as will be justified in more detail in §5.5.2). For the rotating magnetic field we increased the angle in gaps of 0.03 radians, allowing for 1000 time steps for each magnetic field direction. The magnetic field was rotated multiple times until the cilium stroke had settled to its steady state, taken as when the norm (accounting for the number of discretised points) of the difference in the start and end cilium position (of one rotation) was less than 10^{-4}.

5.3.2 Cilium beat shape

The cilium beat pattern over one cycle changes as the Sperm number and ζ are varied and examples displaying some major features are given in Fig.5.3, where the cilium position is plotted at multiple time stamps. The blue cilia indicate the forward or effective stroke, where the cilium is moving anticlockwise, which we numerically distinguish as when the motion of the cilium at its base is anticlockwise. The red cilium positions indicate the recovery stroke, where the cilium is moving clockwise, which we numerically distinguish by clockwise motion at the cilium base.

The forward and backward stroke can be very similar, particularly at low ζ (see Fig.5.3a). Asymmetries can be introduced by higher ζ where the stronger magnet force causes the cilium

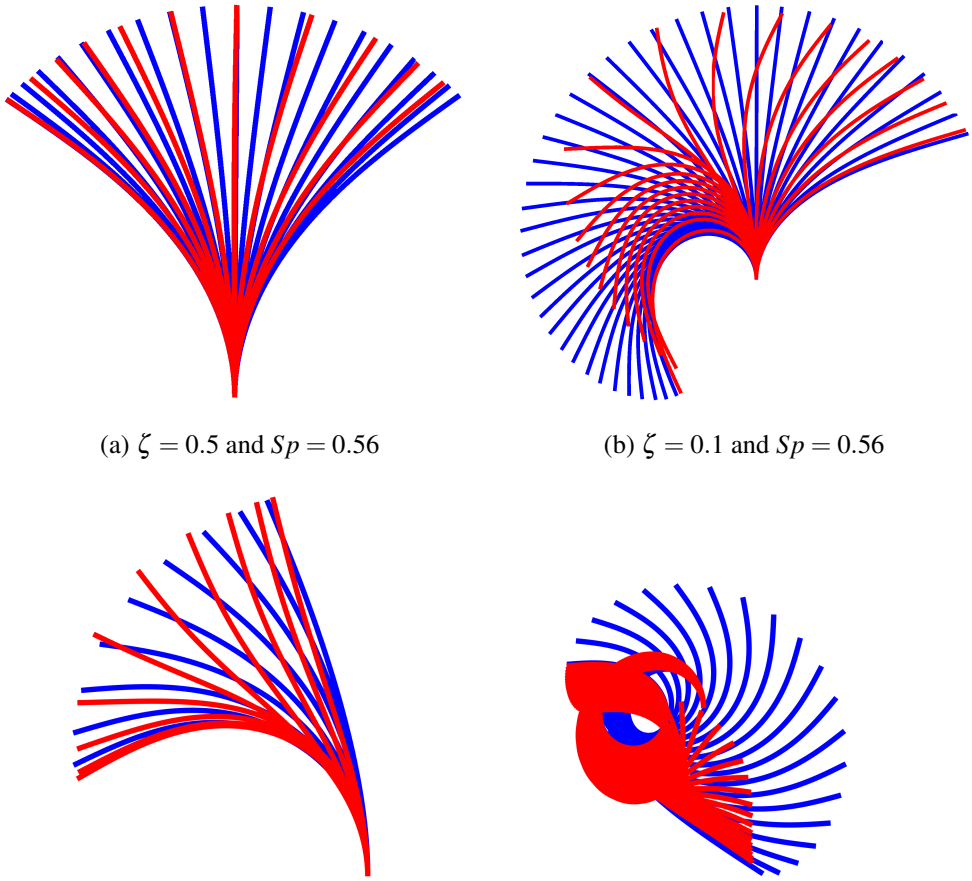

(a) $\zeta = 0.5$ and $Sp = 0.56$

(b) $\zeta = 0.1$ and $Sp = 0.56$

(c) $\zeta = 0.135$ and $Sp = 1.78$

(d) $\zeta = 0.018$ and $Sp = 3.16$

Figure 5.3: Examples of the range of cilium beat shapes at varying ζ and Sp. Blue cilia are part of the forward anticlockwise stroke and red cilia the clockwise recovery stroke.

to loop around itself and become temporarily trapped (see Fig.5.3b), or at higher Sperm number where the hydrodynamic drag contributes to asymmetries (see Fig.5.3c). The cilium steady state does not always centre around its starting vertical position (see Fig.5.3c and 5.3d). The cilium can also become wrapped around itself, maintaining a permanent, sometimes significant bend throughout the entire stroke (see Fig.5.3d). (However, at this extreme, issues of physical accuracy, and the accuracy of the model due to our assumption of small curvature should be noted.) In general, the recovery stroke is faster than the effective stroke, being particularly fast when the cilium becomes tightly wrapped (see Fig.5.3b and 5.3d) but there is a much smaller difference in speed when the effective and recovery stroke are similar (see Fig.5.3a).

5.4 Equilibrium model and asymptotics

In order to validate the force model and understand the behaviour of the cilium in the limit of low Sperm number we will compare our force model to an equilibrium model. This equilibrium model will balance magnetic forces against elastic forces to identify the minimal energy position and thus where the cilium would settle given an infinite amount of time and a fixed direction of the uniform magnetic field.

5.4.1 Equilibrium model governing equation

5.4.1.1 Elastic and magnetic energy formulations

The elastic energy held when the cilium is bent, assuming bending in one axis, no twist and small strain, is

$$\frac{1}{2}\int_0^L EI\kappa^2(s)ds, \tag{5.38}$$

where κ is the radius of curvature [105].

Magnetic energy is held when the magnetic dipoles (corresponding to the magnetic filings in the cilium) are not aligned with the magnetic field and the total magnetic energy of the cilium is

$$-\frac{1}{L}\int_0^L \left(\underline{\mu}\cdot\underline{B}\right) ds. \tag{5.39}$$

(We note this quantity can be negative due to ignoring an additional constant which will not affect our energy minimisation.) This energy is minimised when the magnetic dipole and magnetic field are parallel and pointing in the same direction. It is largest when they are parallel but in opposite directions.

5.4.1.2 Magnetic field equivalent to a point force

It is interesting to note that Eq.5.39 can be directly integrated since $\underline{\mu}\cdot\underline{B}=\mu_0\underline{t}\cdot\underline{B}=\mu_0(\partial\underline{r}/\partial s)\cdot\underline{B}$ giving the magnetic energy as

$$-\frac{\mu_0}{L}\underline{r}(L)\cdot\underline{B}, \tag{5.40}$$

if the base of the cilium is at the origin. As such the magnetic energy contained in a cilium in a uniform magnetic field is equivalent to the energy of a cilium with a point force on its end pointing in the same direction.

5.4.1.3 Minimising energy equation

The total energy contained in the cilium is

$$\int_0^L\left[-\frac{\mu_0}{L}\frac{\partial\underline{r}}{\partial s}\cdot\underline{B}+\frac{EI}{2}\left(\frac{\partial^2\underline{r}}{\partial s^2}\right)\cdot\left(\frac{\partial^2\underline{r}}{\partial s^2}\right)\right]ds. \tag{5.41}$$

This non-dimensionalises to

$$\int_0^1\left[-\frac{\partial\underline{r}^*}{\partial s^*}\cdot\underline{B}^*+\frac{\zeta}{2}\left(\frac{\partial^2\underline{r}^*}{\partial s^{*2}}\right)\cdot\left(\frac{\partial^2\underline{r}^*}{\partial s^{*2}}\right)\right]ds^*, \tag{5.42}$$

where stars represent non-dimensional quantities. Similar to previously, the stars will now be dropped but all quantities in the rest of this chapter will be non-dimensional.

Substituting the dependence on Φ and α this equation reduces to

$$\int_0^1-\left[\cos(\alpha-\Phi)+\frac{\zeta}{2}\left(\frac{\partial\alpha}{\partial s}\right)^2\right]\mathrm{ds}. \tag{5.43}$$

This is the energy function, which we are to minimise. We minimise it by applying standard calculus of variational methods, so the energy minima (and maxima) positions of the cilium solve

$$\zeta\frac{\partial^2\alpha}{\partial s^2}-\sin(\alpha-\Phi)=0, \tag{5.44}$$

subject to the boundary conditions that the cilium end is force free

$$\frac{\partial\alpha}{\partial s}(1)=0, \tag{5.45}$$

and the cilium is vertical at its base

$$\alpha(0)=\frac{\pi}{2}. \tag{5.46}$$

We numerically solved this boundary value problem by using 'bvp4c' in MATLAB. We take initial conditions first as the vertical cilium to obtain global energy minima.We also steadily increased Φ (the angle of the magnetic field) solving the boundary value problem for each Φ but using the position of the cilium at the previous slightly smaller value of Φ as the initial condition.

5.4.2 Comparison to the force model

The comparison of the cilium position from the force model and the equilibrium model are shown in Fig.5.4. In the force model the magnetic field direction is rotated in discrete increments, and the cilium is plotted, just prior to increasing the magnetic field by an increment. The two are in good agreement for the forward stroke of the cilium so the force model follows the local energetic minima of the cilium, as would be expected physically, thus validating the force model.

At high ζ the entire stroke follows the energetic global minima (see Fig.5.4a). This is because there is a continuous change in the position of the global minima as the magnetic field is rotated. This changes at $\zeta = 0.417$ where there is supercritical pitchfork bifurcation in the position of the cilium when the magnetic field is vertically downwards. For this magnetic field direction, at high ζ the energetically optimal cilium position is unbent. But as ζ is decreased, at $\zeta = 0.417$ this position becomes unstable and two global minima appear, one bent to the left and one to the right. Therefore, at low ζ, as the magnetic field is rotated past the vertically downwards position, the global minimum jumps from being bent to the left to being bent to the right. The existence of this bifurcation is well known since for a vertically downwards magnetic field our energy equation is the well known problem of a point weight on the end of a flexible rod [105].

At lower ζ the global minima are separated, see Fig.5.4b, but initially the jump between global minima occurs very soon after the angle of the magnetic field is rotated past vertically downwards. But at lower ζ a local energetic minimum becomes important as seen as in Fig.5.4c. Rather than immediately jumping between global minima there is a curled local minimum, which the cilium follows. This behaviour must be a local energy minimum due to the asymmetry, since the global minimum would give symmetric cilium positions. Therefore, the cilium stays in the local minimum till the magnetic field has rotated far enough, then it jumps to the global minimum for that magnetic field direction.

During the jump between energetic minima hydrodynamic forces become significant, allowing the forward and recovery strokes to become very different, see Fig.5.4c. Most of the cilia in the recovery stroke have not been plotted in Fig.5.4b and 5.4c since the stroke happens

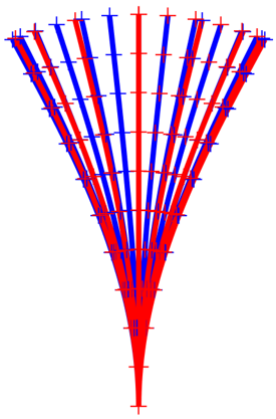

(a) $\zeta = 1$

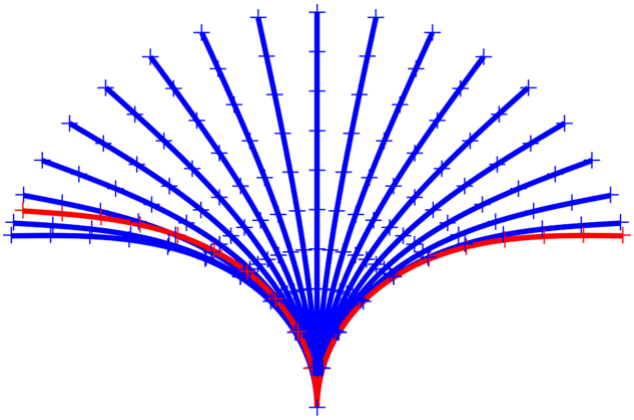

(b) ζ=0.3

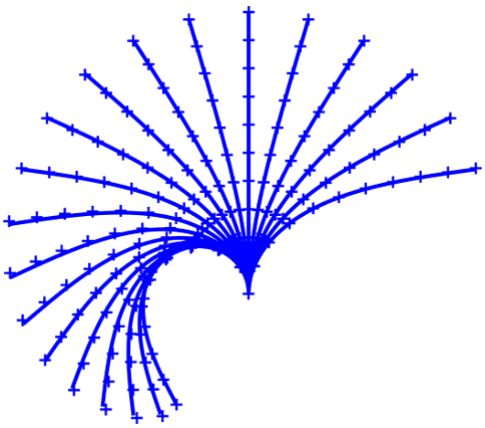

(c) $\zeta = 0.1$

Figure 5.4: Comparison between the force and equilibrium model during the stroke for increasing angle of the magnetic field. For the force model $Sp = 0.32$. For the equilibrium model the previous position of the cilium at a small magnetic field angle is used to update the position at the new magnetic field angle. Blue cilia are part of the forward anticlockwise stroke and red cilia the clockwise recovery stroke. The equilibrium model is represented by crosses and the force model by solid lines.

very quickly so the recovery stroke only represents a very small change of the magnetic field direction.

5.4.3 Asymptotics

In this limit of low Sperm number we can additionally study the the two cases $\zeta \to 0$ and $\zeta \to \infty$ analytically, to more explicitly determine the shape of the cilium in each limit and the total energy contained by the bent cilium.

5.4.3.1 Limit of $\zeta \to \infty$

In this limit Eq.5.44 reduces to

$$\frac{\partial^2 \alpha}{\partial s^2} = 0, \quad \alpha(0)=\tfrac{\pi}{2}, \quad \frac{\partial \alpha}{\partial s}(1) = 0, \tag{5.47}$$

which has the simple solution

$$\alpha = \frac{\pi}{2}, \tag{5.48}$$

so the cilium remains vertical at leading order.

We can calculate a first order correction by assuming $\alpha = \frac{\pi}{2} + \zeta^{-1}\alpha_1 + O(\zeta^{-2})$ so at next order in ζ

$$\frac{\partial^2 \alpha_1}{\partial s^2} - \cos(\Phi) = 0, \quad \alpha_1(0)=0, \quad \frac{\partial \alpha_1}{\partial s}(1) = 0, \tag{5.49}$$

with the solution

$$\alpha(s) = \frac{\pi}{2} + \zeta^{-1}\left[\frac{\cos(\Phi)}{2}s^2 - \cos(\Phi)s\right] + O(\zeta^{-2}), \tag{5.50}$$

and therefore the cilium position a distance $\hat{s}$ along the cilium is

$$y = \int_0^{\hat{s}} \sin\left(\alpha(s)\right) ds = \hat{s} + O(\zeta^{-2}), \tag{5.51}$$

$$x = \int_0^{\hat{s}} \cos(\alpha) ds = -\zeta^{-1}\left(\frac{\cos(\Phi)}{6}\hat{s}^3 - \frac{\cos(\Phi)}{4}\hat{s}^2\right) + O(\zeta^{-2}). \tag{5.52}$$

Therefore, the cilium remains vertical in this regime with the first order correction being of $O(\zeta^{-1})$ and determined by the magnitude of the horizontal magnetic force.

The natural logarithm of the total bending energy this cilium has is

$$\ln\left[\frac{1}{2}\int_0^1\left(\frac{\partial\alpha}{\partial s}\right)^2 ds\right] = \ln\left[\frac{(\zeta^{-1}\cos(\Phi))^2}{2}\int_0^1 (s^2-2s+1)ds\right]$$
$$= -2\ln(\zeta)+\ln\left[\frac{\cos(\Phi)^2}{6}\right]. \quad (5.53)$$

5.4.3.2 Limit of $\zeta \to 0$

In this limit (5.44) reduces to

$$\sin(\alpha-\Phi)=0, \quad (5.54)$$

with the solution $\alpha = \Phi + n\pi$ i.e. the cilium aligns with the magnetic field. However, although this obeys the boundary condition $\frac{\partial\alpha}{\partial s}(1)=0$, it does not obey $\alpha(0)=\frac{\pi}{2}$. As such we require a boundary layer about $s=0$.

We take a boundary layer length scale λ and a new boundary length-scale $\tilde{s}$ so $s=\lambda\tilde{s}$ which reduces Eq.5.44 to

$$\frac{\zeta}{\lambda^2}\frac{\partial^2\alpha}{\partial\tilde{s}^2}(\tilde{s})-\sin(\alpha(\tilde{s})-\Phi)=0, \quad (5.55)$$

where requiring both terms to be of the same order of magnitude in the boundary layers gives $\lambda\sim\zeta^{\frac{1}{2}}$. Therefore, in the boundary layer

$$\frac{\partial^2\alpha}{\partial\tilde{s}^2}-\sin(\alpha-\Phi)=0, \quad \alpha(0)=\frac{\pi}{2}, \quad \alpha(\infty)=\Phi. \quad (5.56)$$

This equation is similar to Eq.5.44 but the changed form of the boundary conditions means an analytic solution exists. Shifting α by defining $\hat{\alpha}=\alpha-\Phi-\frac{\pi}{2}$ gives

$$\frac{\partial^2\hat{\alpha}}{\partial\tilde{s}^2}-\cos(\hat{\alpha})=0, \quad \hat{\alpha}(0)=-\Phi, \quad \hat{\alpha}(\infty)=-\frac{\pi}{2}. \quad (5.57)$$

This equation has the known exact solution [105] of

$$\hat{\alpha}=\frac{\pi}{2}-4\tan^{-1}\left[\tanh\left(\frac{\tilde{s}+\tilde{s}_0}{2}\right)\right], \quad (5.58)$$

where

$$\tilde{s}_0 = 2\tanh^{-1}\left[\tan\left(\frac{\pi/2+\Phi}{4}\right)\right]. \tag{5.59}$$

Therefore,

$$\alpha = \pi + \Phi - 4\tan^{-1}\left[\tanh\left(\frac{\tilde{s}+\tilde{s}_0}{2}\right)\right]. \tag{5.60}$$

Eq.5.60 can be integrated using results from [105] to give the x and y position of the cilium in this sharply bent section

$$x(s) = \zeta^{\frac{1}{2}}\left[\cos\left(\frac{\pi}{2}+\Phi\right)\left(x_0 - 2\left(1+\frac{1}{\cosh(\zeta^{1/2}s+\tilde{s}_0)}\right)\right)\right.$$
$$\left. -\sin\left(\frac{\pi}{2}+\Phi\right)\left(y_0 + 2\tanh(\zeta^{1/2}s+\tilde{s}_0) - (s+\tilde{s}_0)\right)\right], \tag{5.61}$$

$$y(s) = \zeta^{\frac{1}{2}}\left[\sin\left(\frac{\pi}{2}+\Phi\right)\left(x_0 - 2\left(1+\frac{1}{\cosh(\zeta^{1/2}s+\tilde{s}_0)}\right)\right)\right.$$
$$\left. -\left(\frac{\pi}{2}+\Phi\right)\left(y_0 + 2\tanh(\zeta^{1/2}s+\tilde{s}_0) - (s+\tilde{s}_0)\right)\right], \tag{5.62}$$

where x_0 and y_0 are constants of integration chosen to fix the base of the rod. Therefore, over a small region the cilium bends significantly to line up with the magnetic field and the remainder of the cilium is straight.

The total bending energy this cilium generates can be approximated by only considering bending within the boundary layer, since outside the boundary layer the cilium is straight. Therefore, the natural logarithm of the total bending energy is

$$\ln\left(\frac{\zeta^{-1/2}}{2}\int_0^\infty\left(\frac{\partial\alpha}{\partial\tilde{s}}\right)^2 d\tilde{s}\right) = -\frac{1}{2}\ln(\zeta) + \ln\left[2-4\left(\frac{\tanh(\frac{\tilde{s}_0}{2})}{1+\tanh^2(\frac{\tilde{s}_0}{2})}\right)\right]. \tag{5.63}$$

5.4.4 Comparison of asymptotics to numerics

Fig.5.5 validates the equilibrium model against the asymptotic solutions for the two magnetic field directions of $\Phi = \pm 3\pi/8$. At both extremes of ζ the bending energy of the asymptotics and equilibrium model agree well and the shapes of the cilium obtained from the equilibrium model matches the shapes predicted by the asymptotics. At high ζ the x component of the magnetic field for both $\Phi = 3\pi/8$ and $\Phi = -3\pi/8$ tends towards the same cilium shape and

bending energy value, as was predicted by our asymptotics since the x component of the magnetic field is the same in both cases.

5.5 Force variation with non-dimensional parameters

We will now use our force model to analyse how the force applied to the surrounding fluid by the cilium during one cycle varies with the two non-dimensional parameters of ζ and Sperm number.

5.5.1 Calculating force

The non-dimensional force applied to the fluid by the cilium at any instance of time $\underline{\tilde{F}}(t)$ is

$$\underline{\tilde{F}}(t) = Sp^4 \times \zeta \times \int_0^1 \left(V_N \underline{\hat{n}} + \frac{1}{C_{NT}} V_T \underline{\hat{t}} \right) ds. \tag{5.64}$$

We then average over one cilium stroke to obtain the force in the x direction F_x, the force in the y direction F_y and the total force F imparted by the cilium to the surrounding fluid as

$$F_x = \frac{\sum_t \tilde{F}_x}{t_{tot}}, \; F_y = \frac{\sum_t \tilde{F}_y}{t_{tot}}, \; F = \sqrt{F_x^2 + F_y^2}, \tag{5.65}$$

for t_{tot} the total number of time steps.

5.5.2 Variation with number of discretised points

The number of points n to discretise the cilium by needs to be sufficient to accurately calculate the force but not excessive due to the increased computational time. At $\zeta = 0.1$ and $\log(Sp) = 0.85$, near the maximum F for changing Sperm number, Fig.5.6 shows as n increases there is clear convergence in the total applied force. Indeed the percentage error is

$$\frac{F_{121} - F_{271}}{F_{271}} = 0.0019, \tag{5.66}$$

which is an error of 0.2% (where here subscripts of F denote the truncation size).

For the ζ and Sperm number comparisons undertaken below, we take $n = 121$.

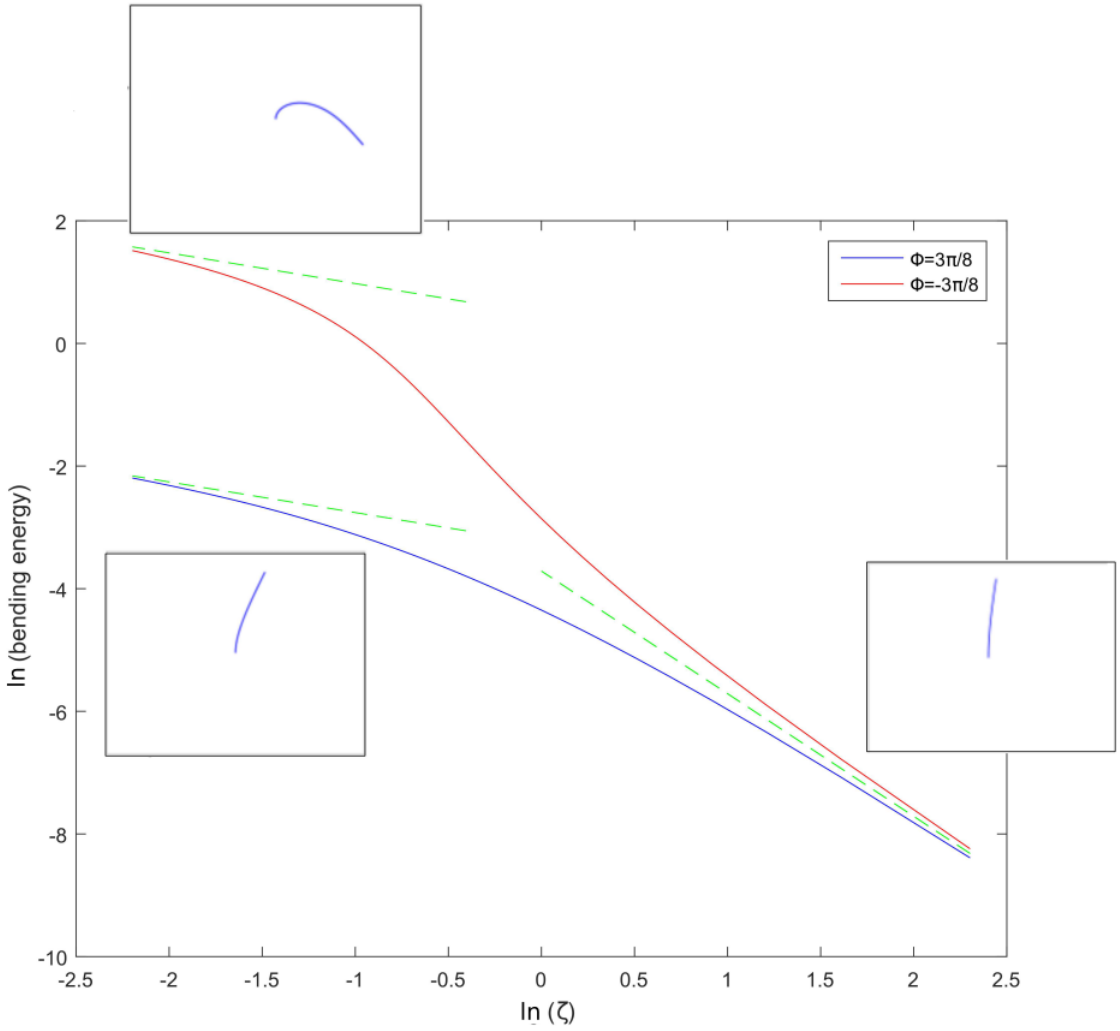

Figure 5.5: Comparison of the bending energy of the asymptotic and equilibrium numerical solution. The two green dashed lines are the asymptotics solutions in the limits $\zeta \to \infty$ and $\zeta \to 0$. The equilibrium models is plotted with solid lines. The inserts show the cilium shape at each extreme.

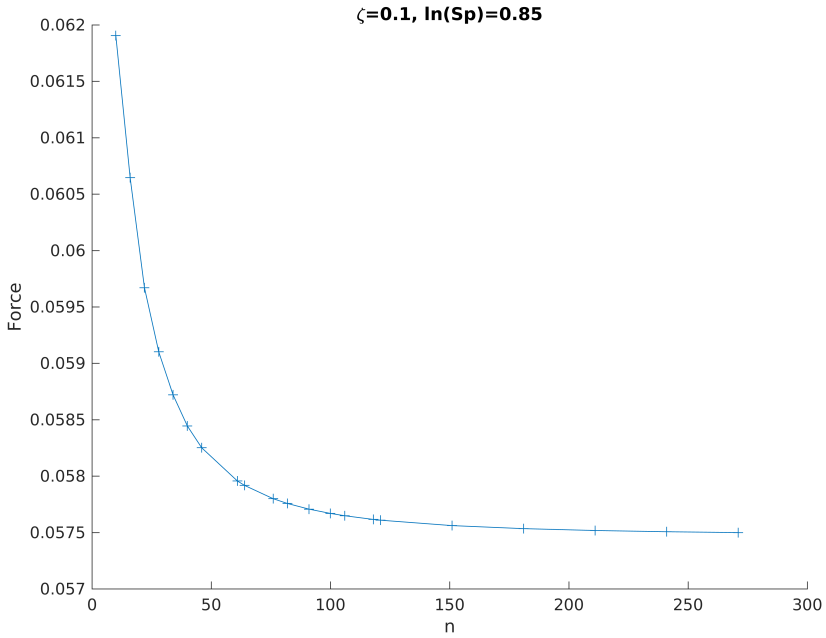

Figure 5.6: Variation in the numerically calculated force with the number of discretised points, n.

5.5.3 Varying ζ

The maximum magnitude of the force is observed at an intermediate $\ln(\zeta)$, decreasing to 0 force as $\ln(\zeta) \to \pm\infty$ (Fig.5.7a). This behaviour can be explained with a physical argument. The limit $\ln(\zeta) \to \infty$ corresponds to the relative magnetic driving force tending to zero. Thus in this limit the cilium will not move and hence generate no force. The limit $\ln(\zeta) \to -\infty$ corresponds to a very strong relative magnetic force. In this limit of $\ln(\zeta)$, the cilium will rotate while remaining completely straight, except for a small region of sharp curvature near the cilium base, keeping the base of the cilium vertical. Due to the symmetry of such a stroke shape, this stroke must generate negligible force. Stroke shapes containing a partial circle (and tending towards this limit) are visible in Fig.5.8. We also observe that the value of ζ at which the maximum force magnitude occurs, decreases with increasing Sperm number, since greater relative magnetic field strength is required to move the cilium.

In an engineering application we expect the cilium to be mounted on a wall and used to transport fluid, for which the applied horizontal force F_x will determine the effectiveness of the

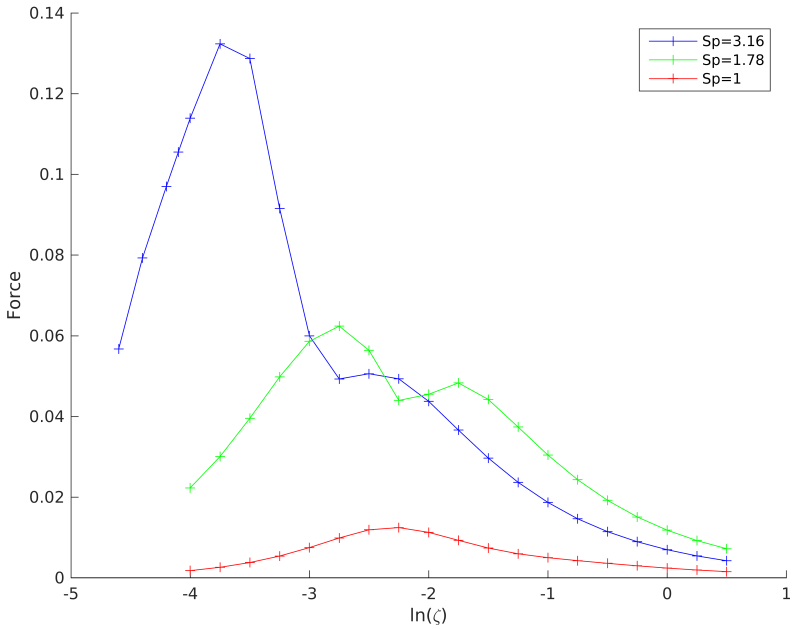

(a) Total force

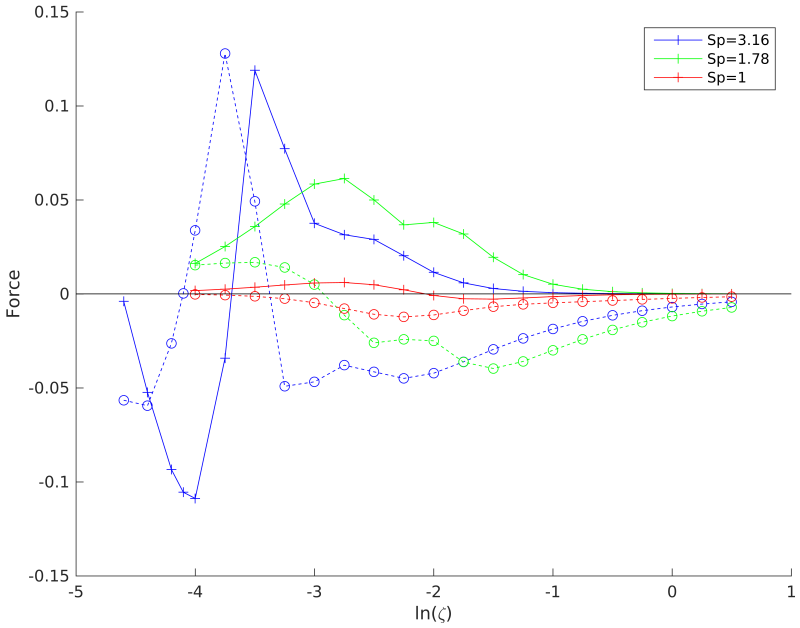

(b) Components of Force as ζ is varied . Solid lines with crosses represent F_x and dashed lines with circles represent F_y

Figure 5.7: Variation in force generated at a range of zeta at different Sperm number

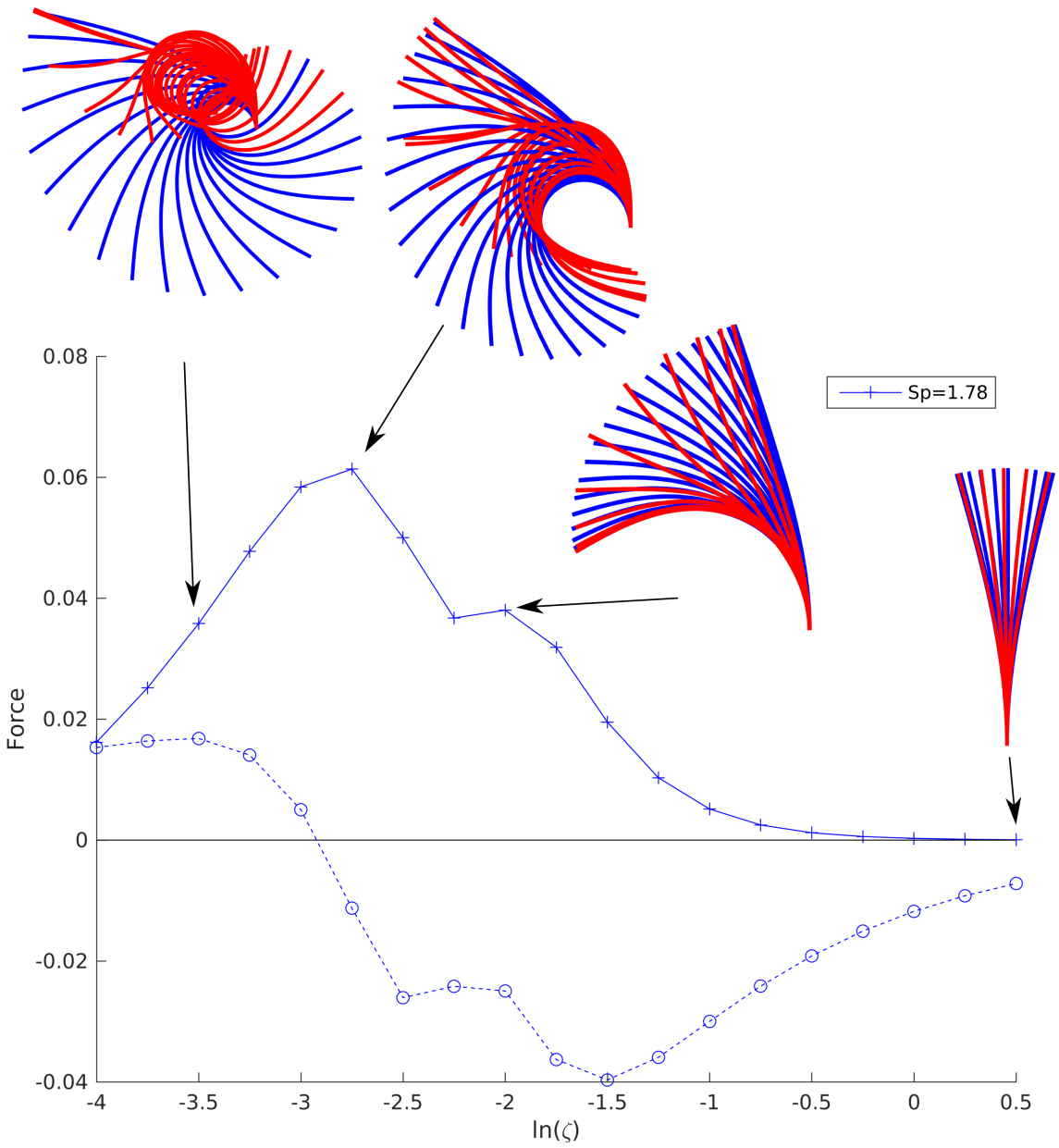

Figure 5.8: Stroke shape as ζ is varied at $Sp = 1.78$. Blue cilia are part of the forward anticlockwise stroke and red cilia the clockwise recovery stroke. The solid line with crosses represents F_x and the dashed line with circles represents F_y

cilium. The horizontal force, F_x, has its maximum at a similar intermediate $\ln(\zeta)$ as F. F_x is generally positive, which is unexpected considering the magnetic field rotates anticlockwise. However, this behaviour can be explained by the difference in area swept out by the effective stroke and recovery stroke (which is a common method for estimating the force applied by a cilium, as this area linearly corresponds to the volume of displaced fluid [54, 106]). Looking at this region where these two strokes differ in Fig.5.8(which we will call the swept out region difference), the effective stroke is pushing fluid to the right and thus suggests a positive F_x. This arises, particularly at large ζ, as our cilium firstly sweeps out a large segment of a circle and then uncurls during the recovery stroke. Therefore, the difference in the region swept out by the forward stroke and the recovery stroke, tends to be in that the effective stroke sweeps out extra area near the end of its stroke. Normally, this is in a quadrant below (or only just above) and to the left of the base of the cilium and it is pushing fluid in the $\underline{e}_x$ direction.

The relative position of the swept out region difference and the cilium can change significantly. This causes the sharp changes in F_x and F_y, as seen at low ζ and high Sperm number in Fig.5.7b for $Sp = 3.16$. A physical problem arising from the large curvature in the cilium at lower ζ is that it moves through itself. Also, our condition of small curvature, which allows us to use linear elasticity theory, starts to break down.

At high Sperm number, a secondary local maximum of force magnitude is visible. This maximum appears at a higher value of ζ than the global maximum (see Fig.5.7a). There is no significant feature in the cilium beat pattern to account for this secondary maximum, but we note that at higher Sperm number, smaller changes in beat pattern correspond to a greater change in force.

5.5.4 Varying Sperm number

The maximum magnitude of the force occurs at an intermediate Sperm number and decreases as $\ln(Sp) \to \pm\infty$ (see Fig.5.9a). This behaviour can be explained with a physical argument. The limit $\ln(Sp) \to \infty$ corresponds to a relative increase in the amount of drag. Thus, in this limit, the cilium will not move and so apply no force to the surrounding fluid. The limit $\ln(Sp) \to -\infty$ corresponds to a relative decrease in the amount of drag. Thus, although the cilium beat pattern sweeps out al larger region in this limit, there is less resistance so the cilium applies less force to the surrounding fluid. This change in beat pattern with increasing sperm number is visible in Fig.5.10. As ζ increases, the value of $\ln(Sp)$ at which the force is maximal, increases slowly (see Fig.5.9a).

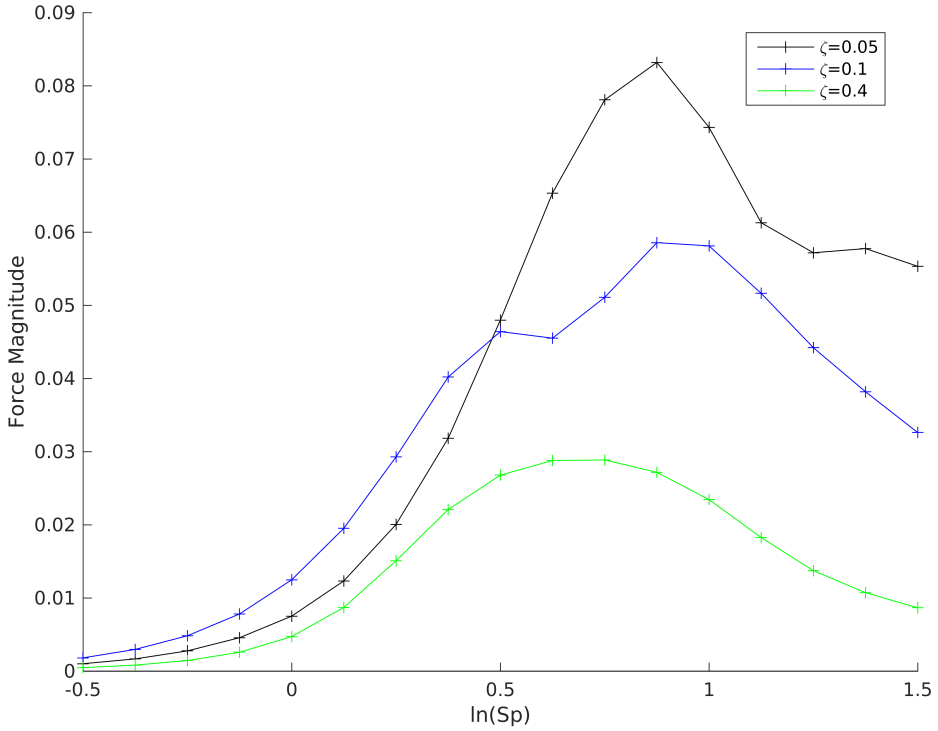

(a) Force magnitude

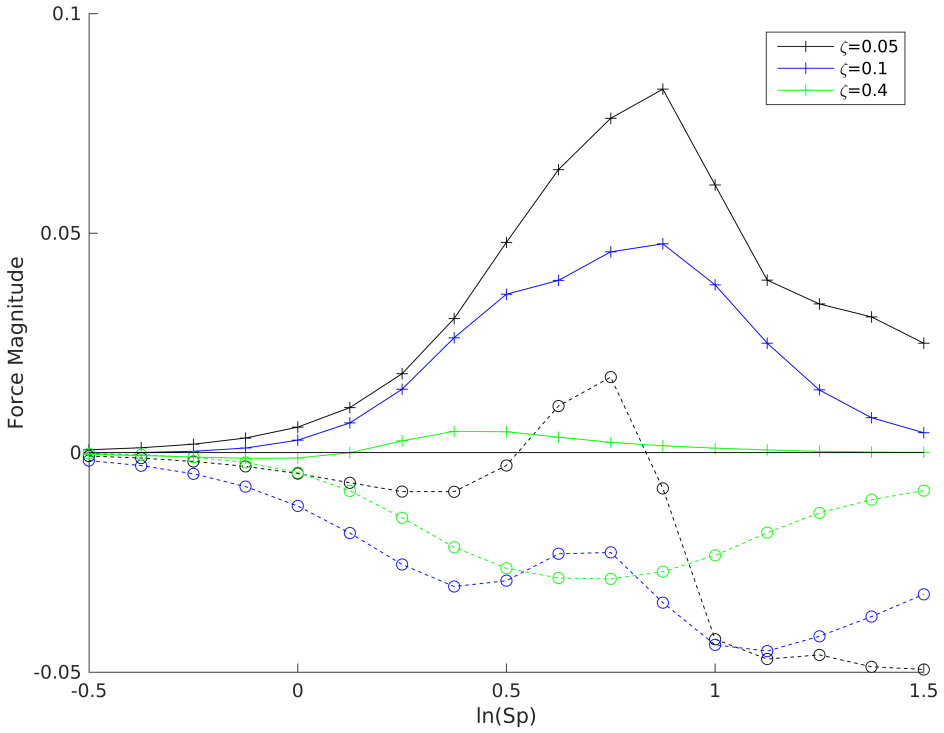

(b) Components of force (F_x and F_y) . Solid lines with crosses represent F_x and dashed lines with circles represent F_y.

Figure 5.9: Force as Sperm Number is varied for three fixed values of ζ.

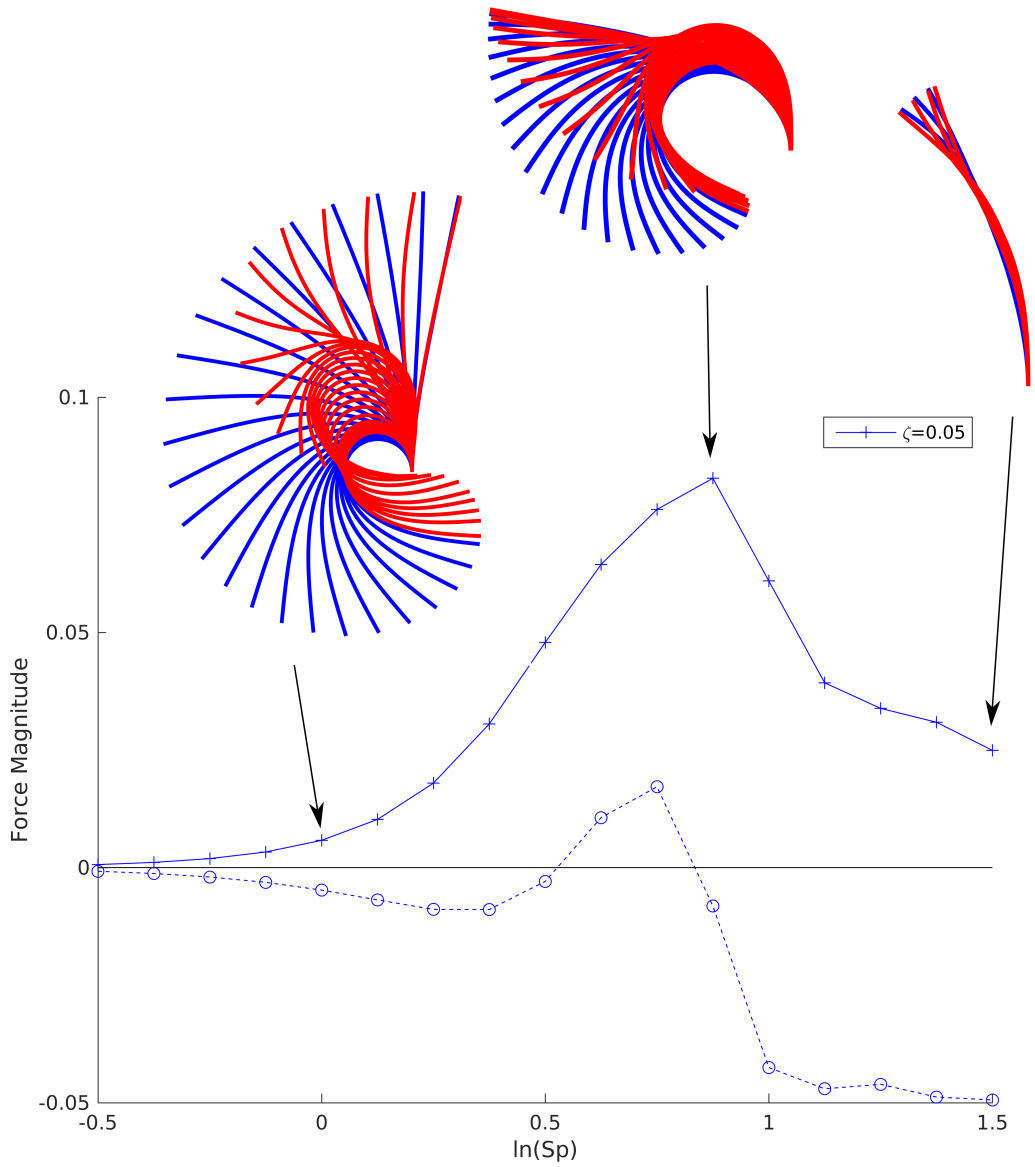

Figure 5.10: Cilium stroke when $\zeta = 0.05$ at a range of Sperm numbers. Blue cilia are part of the forward anticlockwise stroke and red cilia the clockwise recovery stroke. The solid line with crosses represent F_x and dashed line with circles represent F_y.

The magnitude of the horizontal force, F_x, varies in a similar way to the total force, with its maximum at a similar Sperm number (see Fig.5.9b). The horizontal force, F_x, is also primarily positive for the same reasons as discussed in §5.5.3. Similarly regions of sharp change in F_x and F_y are observed for the same reasons as in §5.5.3 and can be seen in Fig.5.10. Similar to §5.5.3, we see small secondary local maxima in F but there is no significant physical feature in the cilium pattern to explain these.

5.6 Conclusion

We have analysed the beat pattern of an artificial, permanently magnetised cilium actuated by a rotating magnetic field. At low Sperm number, we identified that the effective stroke was in energetic equilibrium, whereas for the recovery stroke, hydrodynamic effects are important when ζ is small enough. Using a force model, we observed that the cilium applies the largest total force (and horizontal force) to the surrounding fluid at an intermediate Sperm number and ζ. Unexpectedly, for an anticlockwise stroke, the force was generally to the right, due firstly to the cilium stroke encompassing a large circle sector, and secondly, due to the early uncurling of the cilium during the recovery stroke.

Part IV

Conclusion

This thesis was motivated by two sets of experimental work on armoured microbubbles and an artificial cilium.

For the armoured microbubbles (AMBs) we worked in direct collaboration with the experimentalists, Philippe Marmottant's group in Grenoble, France. We first built a general model using asymptotic matching to calculate the streaming generated by a spherical body undergoing known arbitrary small-amplitude oscillations, with the streaming given by Eq. (1.75) – (1.78). We found there was a net force on the spherical body only when it was forced at two adjacent modes.

Next, we focussed on the AMB explicitly in order to understand the motion of its surface. We used a potential flow model to analyse the resonances, identifying the relationship between its resonance frequency f and the size of the opening θ_0 as

$$f \sim \left(\frac{n^3 \gamma}{\rho a^3 \theta_0^3} \right)^{\frac{1}{2}}. \tag{5.67}$$

This gave a resonance frequency of 334 kHz for a standard bubble of radius 10 μm and opening of 5 μm, in good agreement with the experimental resonance of 320 kHz.

Using our previously derived general streaming model, and applying boundary conditions for the AMB we identified the streaming flow its generates, with the strong frontal jet (see Fig.2.9), in good agreement with experiments. By including the image of the leading order Stokeslet (and next order Stresslet correction), we identified the streaming for the AMB near a wall (see Fig.2.11), which correctly predicted the two large circulations in front of the AMB.

We next analytically studied the collective streaming flow generated experimentally by arrays of AMBs placed in a long channel with an 80 μm $\times$ 1 mm cross-section. We modelled this system by linearly superposing the leading order Stokeslet behaviour (with a Stresslet correction when only modelling one wall) for each AMB individually. We found the two closest channel walls (above and below) cause the large circulations seen experimentally (compare Fig.3.4 to Fig.3.7). We then analysed the development of the array's collective flow as the base flow strength was increased for the five experimental setups, demonstrating good experimental agreement for an L-array.

We next analysed the ability of AMB arrays to mix two streams of adjacent fluid in a channel, by analysing the extension of the streams' boundary line. The numerical simplicity allows fast testing of AMB arrays to determine which arrays should face more rigorous numerical and experimental analysis. Of the arrays identified by this method as good mixers, two were tested experimentally, with the left/right V array of Fig.4.10a showing very good mixing at low driving pressures (see Fig.4.12).

We concluded this thesis by studying a different microdevice: an artificial cilium. Our analysis studied a paramagnetic cilium actuated by a rotating magnetic field, motivated by a ferromagnetic cilium designed by Tsumori et. al. [1, 6]. We used a force model balancing magnetic, elastic and hydrodynamic forces to calculate the stroke shape (see Fig.5.3), which we validated using an equilibrium model (see Fig.5.4). At low Sperm number, the forward stroke is in energetic equilibrium, balancing magnetic and elastic forces, whereas the hydrodynamics effect the recovery stroke when we also have small ζ (the ratio of elastic to magnetic forces). We analysed the force the cilium applies to the surrounding fluid for a range of sperm numbers and ζ and identified that the force is highest for an intermediate sperm number and ζ, dropping off at very high and low ζ and Sperm number (see Fig.5.7a and 5.9a).

Building on the work presented in this thesis, there are opportunities for further work with both the AMB and the artificial cilium, both experimentally and numerically. Extending the numerical work on AMB array mixing includes adding the two side walls so a high pressure forcing can be modelled, as well as modelling the extension of the boundary within the array. Extending the experimental work using AMBs includes constructing a working multi-directional swimmer, and making AMBs within a channel more hydrophobic. For the cilium, further work includes extending the numerical study to a ferromagnetic cilium, while experimental further work involves miniaturising the cilium.

References

[1] F. Tsumori, A. Saijou, T. Osada, and H Miura. Development of actuation system for artificial cilia with magnetic elastometer. *Jpn. J Appl Phys.*, 54:06FP12, 2015.

[2] D. L. Polla, A. G. Erdman, D. T. Robbins, J. Diaz-Diaz, R. Rizq, Y. Nam, and H. T. Brickner. Microdevices in medicine. *Annu. Rev. Biomed. Eng.*, 2:551–576, 2000.

[3] Y. Chen and S. Lee. Manipulation of biological objects using acoustic bubbles: A review. *Integr. Comp. Biol.*, 54(6):1–10, 2014.

[4] Z. Wu, J. Li, B. E. de Avila, T. Li, W. Gao, Q. He, L. Zhang, and J. Wang. Water-powered cell-mimicking janus micromotor. *Adv. Funct. Mater.*, 25(48):7497–7501, 2015.

[5] J.M.J den Toonder, B. Femke, D. Broer, M.Gillies L. Filippii, J. de Goede, T. Mol, M. Reijme, W. Talen, H. Wilderbeek, V. Khatavkar, and P. Anderson. Artificial cilia for active micro-fluidic mixing. *Lab Chip*, 8:533–541, 2008.

[6] F. Tsumori, R. Marume, A. Saijou, K. Kudo, T. Osado, and H. Miura. Metachronal wave of artificial cilia array actuated by applied magnetic field. *Jpn. J Appl Phys.*, 55:06GP19, 2016.

[7] P. Marmottant and S. Hilgenfeldt. A bubble-driven microfluidic transport element for bioengineering. *Proc. Natl. Acad. Sci. USA*, 101:9523–9527, 2004.

[8] D. Ahmed, T. Baasch, B. Jang, S. Pane, J. Dual, and B. J. Nelson. Artificial swimmers propelled by acoustically activated flagella. *Nanno Lett.*, 16(8):4968–4974, 2016.

[9] X. Ding, P. Li, S. S. Lin, Z. S. Stratton, N. Nama, F. Guo, D. Slotcavage, X. Mao, J. Shi, F. Costanzo, and T. J. Huang. Surface acoustic wave microfluidics. *Lab Chip*, 13(18):3626–3649, 2013.

[10] H. A. Stone and S. Kim. Microfluidics: Basic issues, applications, and challenges. *AIChe J.*, 47(6):1250–1254, 2001.

[11] S. R. Gowda, A. L. Mohana, X. Zhan, and P. M. Ajayan. Building energy storage device on a single nanowire. *Nano. Lett.*, 11(8):3329–3333, 2011.

[12] B. Dai, J. Wang, Z. Xiong, X. Zhan, W. Dai, C. Li, S. Feng, and J. Tang. Programmable artificial phototactic microswimmer. *Nat. Nanotechnol.*, 11:1087–1092, 2016.

[13] A. Walther and A. H. E. Muller. Janus particles: Synthesis, self-assembly, physical properties, and applications. *Chem. Rev.*, 113(7):5194–5261, 2013.

[14] J. R. Howse, R. A. L. Jones, A. J. Ryan, T. Gough, R. Vafabakhsh, and R. Golestanian. Self-motile colloidal particles: From directed propulsion to random walk. *Phys. Rev. Lett.*, 99(4):048102, 2007.

[15] R. Di Leonardo, L. Angelani, D. Dell'Arciprete, G. Ruocco, V. Iebba, S. Schippa, M. P. Conte, F. Mecarini, F. De Angelis, and E. Di Fabrizio. Bacterial ratchet motors. *P. Natl. Acad. Sci. USA*, 107(21):9541–9545, 2010.

[16] P. Marmottant and S Hilgenfeldt. Controlled vesicle deformation and lysis by single oscillating bubbles. *Nature*, 453:153–156, 2003.

[17] F. Mekki-Berrada, P. Thibault, and P. Marmottant. Acoustic pulsation of a microbubble confined between elastic walls. *Phys. Fluids*, 28(3):032004, 2016.

[18] C. Wang, B. Rallabandi, and S. Hilgenfeldt. Frequency dependence and frequency control of microbubble streaming flows. *Phys. Fluids*, 25(2):022002, 2013.

[19] M. Kaynak, A. Ozcelik, A. Nourhani, P. E. Lammert, V. H. Crespi, and T. J. Huang. Acoustic actuation of bioinspired microswimmers. *Lab Chip*, 17:395–400, 2016.

[20] M. Kaynak, A. Ozcelik, N. Nama, A. Nourhani, P. E. Lammert, V. H. Crespi, and T. J. Huang. Acoustofluidic actuation of in situ fabricated microrotors. *Lab Chip*, 16:3532–3537, 2016.

[21] Y. Wang, Y. Gao, H. M. Wyss, P. D. Anderson, and J. M. J. den Toonder. Artificial cilia fabricated using magnetic fiber drawing generate substatial flow. *Microfluid Nanofluidics*, 2015.

[22] M. Vilfan, A. Potocnik, B. Kavcic, N. Osterman, I. Poberaj, A. Vilfan, and D. Babic. Self-assembled artificial cilia. *Proc. Natl. Acad. Sci. USA*, 107(5):1844–1847, 2010.

[23] H. Yu, T. Nguyen, S. H. Ng, and T. Tran. Mixing control by frequency variable magnetic micropillar. *RSC Adv.*, 6:11822–11828, 2016.

[24] E. M. Gauger, M. T. Downton, and H. Stark. Fluid transport at low reynolds number with magnmagnetic actuated artificial cilia. *Eur. Phys. J. E.*, 28(2):231–242, 2009.

[25] E. Lauga. Life around the scallop theorem. *Soft Matter*, 7:3060–3065, 2011.

[26] K. W. Wan and R. E. Goldstein. Rhythmicity, recurrence, and recovery of flagella. *Phys. Rev. Lett.*, 113:238103, 2014.

[27] M. J. Sanderson and M. A. Sleigh. Ciliary activity of cultured rabbit tracheal epithelium: beat pattern and metachrony. *J Cell Sci.*, 47(1):331–347, 1981.

[28] G. I. Taylor. Analysis of the swimming of microscopic organisms. *Proc. R. Soc. Lond. A.*, 209(1099):447–461, 1951.

[29] M. Hines and J. J. Blum. Bend propagation in flagella. 1. derivation of equations of motion. *Biophys. J.*, 23(1):41–57, 1978.

[30] S. Gueron and N. Liron. Ciliary motion modeling, and dynamic multicilia interactions. *Biophys. J.*, 63:1045–1058, 1992.

[31] K. Drescher, R. E. Goldstein, N. Michel, M. Polin, and I. Tuval. Direct measurement of the flow field around swimming microorganisms. *Phys. Rev. Lett.*, 105:168101, 2010.

[32] T. D. Montanegro-Johnson, D. A Gagnon, P. E. Arratia, and E. Lauga. Flow analysis of the low reynolds number swimmer c. elegans. *Phy. Rev. Fluids.*, 1:053202, 2016.

[33] A. A. Smith, T. D. Johnson, D. J. Smith, and J. R. Blake. Symmetry breaking cilia-driven flow in a zebrafish embryo. *J. Fluid. Mech.*, 705:26–45, 2012.

[34] J. R. Blake. A spherical envelope approach to ciliary propulsion. *J. Fluid Mech.*, 46:199–208, 1971.

[35] C. Brennen. An oscillating-boundary-layer theory for cilliary propulsion. *J. Fluid Mech.*, 65:799–824, 1974.

[36] M. J. Lighthill. On the squirming motion of nearly spherical deformable bodies through liquids at very small reynolds numbers. *Commun. Pur. Appl. Math.*, 5:109–118, 1952.

[37] O. Pak and E. Lauga. Generalized squirming motion of a sphere. *J. Eng. Math.*, 88:1–28, 2014.

[38] G. Li and A. M. Ardekani. Hydrodynamic interaction of microswimmers near a wall. *Phys. Rev. E*, 90:013010, 2014.

[39] S. E. Spagnolie and E. Lauga. Hydrodynamics of self-propulsion near a boundary: Predictions and accuracy of far-field approximations. *J. Fluid Mech.*, 700:105–147, 2012.

[40] K. Ishimoto and E. A. Gaffney. Swimming efficiency of spherical squirmer: Beyond the lighthill theory. *Phys. Rev. E*, 90:012704, 2014.

[41] N. Riley. Steady streaming. *Annu. Rev. Fluid Mech.*, 33:43–65, 2001.

[42] N. Riley. On a sphere oscillating in a viscous fluid. *Q. J. Mech. Appl. Math.*, 19:461–472., 1966.

[43] B. J. Davidson and N. Riley. Cavitation Microstreaming. *J. Sound Vib.*, 15:217–233, 1971.

[44] M. S. Longuet-Higgins. Viscous streaming from an oscillating spherical bubble. *Proc. Roy. Soc. Lond. A*, 454:725–742, 1998.

[45] A. O. Maksimov. Viscous streaming from surface waves on the wall of acoustically-driven gas bubbles. *Eur. J. Mech. B-Fluid*, 26:28–42, 2007.

[46] J. Feng, J. Yuan, and S. K. Cho. Micropropulsion by an acoustic bubble for navigating microfluidic spaces. *Lab. Chip*, 15:1554–1562, 2015.

[47] D. Ahmed, M. Lu, A. Nourhani, P.E. Lammert, Z. Stratton, H.S. Muddana, V.H. Crespi, and T. J. Huang. Selectively manipulable acoustic-powered microswimmers. *Sci. Rep.*, 5:9744, 2015.

[48] N. Bertin, T. A. Spelman, O. Stephan, L. Gredy, M. Bouriau, E. Lauga, and P. Marmottant. Propulsion of bubble-based acoustic microswimmers. *Phys. Rev. Applied*, 4:064012, 2015.

[49] S. A. Elder. Cavitation Microstreaming. *J. Acoust. Soc. Am.*, 31:54, 1958.

[50] D. Ahmed, X. Mao, B. K. Juluri, and T. J. Huang. A fast microfluidic mixer based on acoustically driven sidewall-trapped microbubbles. *Microfluid. Nanofluid.*, 7:727–731, 2009.

[51] S. S. Wang, Z. J. Jiao, X. Y. Huang, C. Yang, and N. T. Nguyen. Acoustically induced bubbles in a microfluidic channel for mixing enhancement. *Microfluid. Nanofluid.*, 6:847–852, 2009.

[52] J. Hussong, N. Schorr, J. Belardi, O. Prucker, J. Ruhe, and J. Westerweed. Experimental investigation of the flow induced by artificial cilia. *Lab Chip*, 11:2017–2022, 2011.

[53] M. T. Downton and H. Stark. Beating kinematics of magnmagnetic actuated cilia. *Europhys. Lett.*, 85(4):44002, 2009.

[54] S. N. Khaderi, M. G. H. M. Baltussen, P. D. Anderson, D. Ioan, J. M. J. den Toonder, and P. R. Onck. Nature-inspired microfluidic propulsion using magnetic actuation. *Phys. Rev. E.*, 79(4):046304, 2009.

[55] C. Chen, C. Lin, and Y. Hu. Inducing 3d vortical flow pattern with 2d asymmetric actuation of artificial cilia for high-performance active micromixing. *Exp Fluids*, 2014.

[56] B.K. Batchelor. *An Introduction to Fluid Mechanics*. Cambridge University Press, Cambridge, 1967.

[57] H. Ishida and Y. Shigenaka. Cell model contraction in the ciliate Spirostomum. *Cell Motil. Cytoskel.*, 9:278–282, 1988.

[58] J.A. Gaunt. The Triplets of Helium. *Phil. Trans. Roy. Soc. A*, 228, 1929.

[59] Yu-Lin Xu. Fast evaluation of the gaunt coefficients. *Math. Comp.*, 65:1601–1612, October 1996.

[60] E. Grosswald. *Bessel Polynomials*. Springer-Verlag Berlin Heidelberg, 1978.

[61] M. S. Longuet-Higgins. Mass Transport in Water Waves. *Phil. Trans. Roy. Soc. A*, 245:535–581, 1953.

[62] V. Magar and T. J. Pedley. Average nutrient uptake by a self-propelled unsteady squirmer. *J. Fluid Mech.*, 539:93–112, 2005.

[63] T. Ishikawa, M. P. Simmonds, and T. J. Pedley. Hydrodynamic interaction of two swimming model micro-organisms. *J. Fluid Mech.*, 568:119–160, 2006.

[64] S. R. Keller and T. Y. Wu. A porous prolate-spheroidal model for ciliated microorganisms. *J. Fluid Mech.*, 80:259–278, 1977.

[65] I.S.Aranson. Active colloids. *Physics-Uspekhi*, 56(1):79, 2013.

[66] N. Bertin, T. A. Spelman, T. Combriat, H. Hue, O. Stephan, E. Lauga, and P. Marmottant. Bubble-based acoustic micropropulsors: active surfaces and mixers. *Lab Chip*, 17:1515–1528, 2017.

[67] R. Thameem, B. Rallabandi, and S Hilgenfeldt. Particle migration and sorting in microbubble streaming flows. *Biomicrofluidics*, 10:014124, 2016.

[68] H. Lamb. *Hydrodynamics*. Dover Publications, Inc., 6 edition, 1932.

[69] Ian N. Sneddon. *Mixed Boundary Value Problems in Potential Theory*. North-Holland Publishing Company, 1966.

[70] J. R. Blake. A note on the image system for a Stokeslet in a no-slip boundary. *Math. Proc. Cambridge*, 70:303–310, 1971.

[71] J R Blake and A T Chwang. Fundamental singularites of viscous flow part i: the image systems in the vicinity of a stationary no-slip boundary. *J. Eng. Math*, 8(1):23–29, 1973.

[72] M. W. H. Ley and H. Bruus. Three-dimensional numerical modeling of acoustic trapping in glass capillaries. *Phy. Rev. Applied*, 8:024020, 2017.

[73] R. Cortez and D. Varela. A general system of images for regularized stokeslets and other elements near a plane wall. *J. Comput. Phys.*, 2015.

[74] J. Ainley, S. Durken, R. Embid, P. Boindala, and R. Cortez. The method of images for regularized stokeslets. *J. Comput. Phys.*, 2008.

[75] N. Liron and S. Mochon. Stokes flow for a stokeslet between two parallel flat plates. *J. Eng. Math*, 1976.

[76] R. Cortez. The method of regularized stokeslets. *SIAM J. Sci. Comput.*, 2001.

[77] P. E. Dimotakis. Turbulent mixing. *Annu. Rev. Fluid Mech.*, 37:329–356, 2005.

[78] I. H. Campbell and J. S. Turner. Turbulent mixing between fluids wiht different viscosities. *Nature*, 313, 1985.

[79] E. Lunasin, Z. Lin, A. Novikov, A. Mazzucato, and C.R. Doering. Optimal mixing and optimal stirring for fixed energy, fixed power, or fixed palenstrophy flows. *J. Math. Phys.*, 53(11):115611, 2012.

[80] N. Mole. The α-β model for concentration moments in turbulent flows. *Environmetrics*, 6(6):559–569, 1995.

[81] L. Clarke and N. Mole. Modelling the evolution of moments of contaminant concentration in turbulent flows. *Environmetrics*, 6(6):607–617, 1995.

[82] P. Meunier and E. Villermaux. How vorticies mix. *J. Fluid Mech.*, 476:213–222, 2003.

[83] R. S. Cant and E. Mastorakos. *An introduction to turbulent reacting flows*. Imperial college press, 2008.

[84] G. Taylor. Dispersion of soluble matter in solvent flowing slowly through a tube. *Proc. R. Soc. London A.*, 219(1137):186–203, 1953.

[85] R. Aris. On the dispersion of a solute in a fluid flowing through a tube. *Proc. R. Soc. London A.*, 235(1200):67–77, 1956.

[86] E. Villermaux and H. Rehab. Mixing in coaxial jets. *J. Fluid Mech.*, 425:161–185, 2000.

[87] V. Hessel, H. Lowe, and F. Schonfeld. Micromixers - a review on passive and active mixing principles. *Chemical Engineerin Science*, 8-9:2479–2501, 2005.

[88] Nam-Trung Nguyen and Zhigang Wu. Micromixers - a review. *J. Micromech. Microeng*, 15, 2005.

[89] K. S. Lu, L. Ryu and C. Liu. A magnetic microstirrer and array for microfluidic mixing. *J. Microelectromech. S.*, 11(5), 2002.

[90] K. Conlisk and G. M. O'Connor. Analysis of passive microfluidic mixers incorporating 2d and 3d baffle geometries fabricated using an excimer laser. *Microfluid. Nanofluid.*, 12(6):941–951, 2012.

[91] P. K. Sahu, A. Golia, and A. K. Sen. Analytical, numerical and experimental investigations of mixing fluids in microchannel. *Microsystem Technologies*, 18(6):823–832, 2012.

[92] L. Wang, D. Liu, X. Wang, and X. Han. Mixing enhancement of novel passive microfluidic mixers with cylindrical grooves. *Chem. Eng. Sci.*, 81:157–163, 2012.

[93] J. Aubin, M. Ferrando, and V. Jiricny. Current methods for characterising mixing and flow in microchannels. *Chem. Eng. Sci.*, 65(6):2065 – 2093, 2010.

[94] Seck Hoe Wong, Michael C.L. Ward, and Christopher W. Wharton. Micro t-mixer as a rapid mixing micromixer. *Sensor Actuat. B Chem*, 100(3):359 – 379, 2004.

[95] N. Schwesinger, T. Frank, and H. Wurmus. A modular microfluid system with an integrated micromixer. *J. Micromech. Microeng.*, 6(1):99, 1996.

[96] V. Hessel, S. Hardt, H. Lowe, and F. Schonfeld. Laminar mixing in different interdigital micromixers: I. experimental characterization. *A. I. Ch. E. J.*, 49(3):566–577, 2003.

[97] S. Wang, X. Huang, and C. Yang. Microfluidic bubble generation by acoustic field for mixing enhancement. *J. Heat Transfer.*, 134(5):051014, 2012.

[98] A. E. Kamholz and P. Yager. Molecular diffusive scaling laws in pressure-driven microfluidic channels: deviation from one-dimensional einstein approximations. *Sensor Actuat. B Chem*, 82(1):117 – 121, 2002.

[99] R. F. Ismagilov, A. D. Stroock, P. J. A. Kenis, G. Whitesides, and H. A. Stone. Experimental and theoretical scaling laws for transverse diffusive broadening in two-phase laminar flows in microchannels. *Appl. Phys. Lett.*, 76(17):2376–2378, 2000.

[100] A. Hashmi and J. Xu. On the quantification of mixing in microfluidics. *J. Lab. Autom.*, 19(5):488–491, 2014.

[101] J. M. Ottino and S. Wiggins. Introduction: mixing in microfluidics. *Phil. Trans. R. Soc. Lond. A*, 362(1818):923–935, 2004.

[102] L. Neel. Antiferromagnetism and ferrimagnetism. *Proc. Phys. Soc. A.*, 65(11):869, 1951.

[103] J. Gray and G. J. Hancock. The propulsion of sea-urchin spermatozoa. *J. Exp. Biol.*, 32(4):802–814, 1955.

[104] C. J. Brokaw. Bending moments in free-swimming flagella. *J. Exp. Biol.*, 53:445–464, 1970.

[105] B. Audoly and Y. Pomeau. *Elasticity and Geometry: From hair curls to the non-linear response of shells*. Oxford University Press, 2010.

[106] S. Sareh, J. Rossiter, A. Conn, K. Drescher, and R. E. Goldstein. Swimming like algae: biomimetic soft artificial cilia. *J. R. Soc. Interface*, 10(78):20120666, 2013.